



# THÈSE

En vue de l'obtention du

## DOCTORAT DE L'UNIVERSITÉ DE TOULOUSE

Délivré par :

Institut Supérieur de l'Aéronautique et de l'Espace (ISAE)

---

**Présentée et soutenue par :**

**Guillaume LELIAS**

le vendredi 8 juillet 2016

**Titre :**

Assemblages collés : modélisation, simulation et caractérisation expérimentale

Adhesively Bonded Joints: Modeling, Simulation and Experimental  
Characterization

---

**École doctorale et discipline ou spécialité :**

ED MEGeP : Génie mécanique, mécanique des matériaux

**Unité de recherche :**

Institut Clément Ader

**Directeur(s) de Thèse :**

M. Frédéric LACHAUD (directeur de thèse)

M. Joseph MORLIER (co-directeur de thèse)

**Jury :**

Éric MARTIN, Professeur des universités, ENSEIRB-MATMECA - Président

Marc SARTOR, Professeur des universités, INSA Toulouse - Examineur

Lucas F M DA SILVA, Professeur associé, Universidade do Porto - Rapporteur

Frédéric JACQUEMIN, Professeur des universités, Ecole Centrale de Nantes - Rapporteur

Frédéric LACHAUD, Professeur, ISAE-SUPAERO - Directeur de thèse

Joseph MORLIER, Professeur, ISAE-SUPAERO - Co-directeur de thèse

– This page has been voluntarily left blank –

*Bruce Benarman*

*“Un scientifique aguerri ne cherche pas à prouver que ce qu’il pense est vrai. Un scientifique aguerri cherche à prouver que ce qu’il pense est faux. Et c’est seulement en n’y arrivant pas suffisamment longtemps qu’il finit par se convaincre que ce qu’il pense est vrai.”*



## Acknowledgments

During the three years that have formed this PhD thesis, I have received encouragement and support from many different people. I would like to express my gratitude to all of those who have contributed in any way to the finalization of the following thesis.

First and furthermore, I would like to thank my thesis supervisors: Prof. Frédéric Lachaud, Prof. Joseph Morlier and Dr Eric Paroissien, respectively director, co-director and industrial supervisor, for their respective help and guidance during these three years. Their helpful advices as well as their support during the most difficult times of this project have certainly highly contributed to the finalization of the following thesis.

Then, I wish to express my gratitude to the thesis defense committee for the time and effort they devoted in reading and evaluating the following thesis: Prof. Eric Martin, Department of Mathematics and Mechanics, ENSEIRB-MATMECA, Bordeaux, France, Prof. Marc Sartor, Department of Modeling of Mechanical Systems and Microsystems Group, ICA, Toulouse, France, Prof. Lucas F. M. Da Silva, Department of Mechanical Engineering, University of Porto, Porto, Portugal, and Prof. Frédéric Jacquemin, Research Institute of Civil Engineering and Mechanics, Ecole Centrale de Nantes, Nantes, France.

Last but not least, I would also like to thank all my family, and particularly my parents for the endless love and support they provided me over years... Thank you both for giving me the strength and courage to become who I am now. This thesis is yours as much as mine.



## **Abstract**

As presented latter on in [Chapter 1](#), in structural components design, the choice of joining technology is essential. In this particular context, adhesive bonding may appear as an attractive joining process. Indeed, adhesive bonding offers the possibility of joining without damaging various combinations of materials, from plastics to metals including composite materials. However, the interest of adhesive bonding remains while the integrity of the joint is ensured. Accurate strength prediction are then required.

In the frame of an internal research program called JoSAT (Joint Stress Analysis Tool), Sogeti High Tech has suggested developing since 2008 a simplified tool for the stress analysis of adhesively bonded joints. This tool allows for the distribution of both the internal forces and displacements in the adherends as well as the adhesive stresses along the overlap to be estimated from specified loads and boundary conditions, and has the advantage of being extremely time saving compared to conventional Finite Element (FE) analyses.

In 2011, this tool was extended to support adhesive material nonlinearities in the form of specified adhesive stress-strain evolution laws. However the theory developed was demonstrated as valid for the Single-Lap Joint (SLJ) configuration only, and limited to small levels of adhesive material nonlinearities.

In this context, the objective of the thesis is double. First, extend and validate the simplified tool for the analysis of adhesively bonded joints in the case of nonlinear adhesive as well as adherends stress-strain constitutive behaviors. Then, suggest and develop experimental protocols for the characterization of the cohesive properties of thin adhesive layers so that the simplified tool can be sustained with relevant experimental data in terms of adhesive stress-strain constitutive relationships.

The following dissertation then falls into two parts. First, [Chapter 2](#) aims at presenting a method that extends the simplified tool to simultaneously account for various adhesive and adherend nonlinear constitutive behaviors with no restriction on the specimen geometry and (or) level of material nonlinearities. Secondly, [Chapter 3](#) aims at presenting a new and original protocol for characterizing the cohesive properties of thin adhesive layers based on the monitoring of the adherend-to-adherend displacement field nearby the adhesive crack tip. Finally, the results of a first experimental test campaign are provided so that it validates the newly introduced experimental protocols. Good agreement is shown.

– This page has been voluntarily left blank –

**Table of contents**

Abstract .....	7
Table of contents .....	9
<b><u>Chapter 1. Structural adhesive bonding</u></b> .....	13
1.1. Structural adhesive bonding: An efficient joining process .....	14
1.2. Selection of the adhesive material.....	15
1.3. Adhesive joint manufacturing .....	16
1.4. Adhesive joint geometries .....	17
1.5. The fracture of adhesive joints .....	20
1.6. Mechanical analyses of adhesively bonded joints.....	22
1.6.1. Closed-form stress analyses of adhesively bonded joints .....	22
1.6.2. Finite Element (FE) analyses of adhesively bonded joints .....	26
1.6.3. Analysis of adhesively bonded joints using macro-elements.....	26
1.7. Experimental characterization of adhesively bonded joints.....	27
1.7.1. Cohesive Zone Modeling (CZM).....	28
1.7.2. Determination of cohesive zone model parameters .....	29
1.8. Objectives of the thesis .....	31
<b><u>Chapter 2. Extension and validation of the simplified 1D-beam adhesive stress analysis</u></b> .....	33
2.1. Introduction .....	34
2.2. Organization of the chapter .....	34
2.3. Semi-analytical analysis of adhesively bonded joints using macro-elements.....	35
2.3.1. The simplified 1D-beam adhesive stress analysis: Overview .....	35
2.3.2. Formulation of the BBe macro-element.....	37
2.3.3. Formulation of the outer beam element .....	42
2.3.4. Resolution procedures .....	45

2.3.5. Comparison with existing sandwich type analyses .....	45
2.3.6. Comparison with Finite Element (FE) analyses.....	50
2.4. Introduction of adhesive material nonlinearities .....	53
2.4.1. Description of the interface models .....	53
2.4.2. Overview of the Newton-Raphson iteration procedure.....	62
2.4.3. Local equilibrium of the bonded overlap .....	63
2.4.4. Adaptation of the Newton-Raphson iteration procedure to the particular formulation of the BBe element .....	63
2.4.5. Comparison with existing sandwich type analyses .....	66
2.4.6. Comparison with Finite Element (FE) analyses.....	77
2.5. Introduction of adherend material nonlinearities .....	85
2.5.1. Adaptation of the classical theory of beam plasticization to the particular formulation of the BBe element .....	85
2.5.2. Comparison with Finite Element (FE) analyses.....	90
2.6. Conclusion and discussion .....	94
<b>Chapter 3. On the experimental characterization of thin adhesive layers .....</b>	<b>97</b>
3.1. Introduction .....	98
3.2. Organization of the chapter .....	98
3.3. Bulk material properties .....	99
3.3.1. Adherends.....	99
3.3.2. Adhesive.....	101
3.4. On the experimental characterization of CZM: Energetic methods.....	104
3.4.1. Overview .....	104
3.4.2. On the constitutive relationship of a thin adhesive layer loaded in pure shear (mode II) .....	105
3.4.3. On the constitutive relationship of a thin adhesive layer loaded in pure peel (mode I) .....	107
3.4.4. On the constitutive relationship of a thin adhesive layer loaded in mixed mode I/II.....	109
3.4.5. Confrontation with semi-analytical predictions .....	111
3.5. On the experimental characterization of CZM: The direct method .....	116

3.5.1. Overview .....	116
3.5.2. On the constitutive relationship of a thin adhesive layer loaded in pure shear (mode II) .....	117
3.5.3. On the constitutive relationship of a thin adhesive layer loaded in pure peel (mode I) .....	119
3.5.4. On the constitutive relationship of a thin adhesive layer loaded in mixed mode I/II .....	120
3.5.5. Confrontation with semi-analytical predictions .....	121
3.6. Experimental investigation on metal-to-metal adhesive joints .....	123
3.6.1. Data processing .....	123
3.6.2. Experimental setup, preparation of the specimens and instrumentation .....	136
3.6.3. Material description .....	140
3.6.4. Experimental results .....	141
3.7. Conclusion and discussion .....	147
<b><u>Chapter 4. Conclusion and perspectives</u></b> .....	151
References .....	155
List of PhD publications .....	163
<i><u>Appendix 1.</u></i> Non-exhaustive review of simplified closed-form stress analyses of adhesively bonded joints (Da Silva 2012) .....	165
<i><u>Appendix 2.</u></i> Supplementary materials on the adherends constitutive equations .....	166
<i><u>Appendix 3.</u></i> On the effective peel modulus of sandwiched adhesive layers .....	168
<i><u>Appendix 4.</u></i> Expressions of the adhesive shear (peel) stress distribution(s) depending on the nature of the roots of the characteristic polynomial .....	170
<i><u>Appendix 5.</u></i> Convergence of the numerical analyses .....	175
<i><u>Appendix 6.</u></i> Moore-Penrose pseudo inverse technique for solving linear least squares optimization problems .....	188
<i><u>Appendix 7.</u></i> Joint Stress Analysis Tool (JoSAT) .....	194

– This page has been voluntarily left blank –

## **Chapter 1. Structural adhesive bonding**

Chapter 1 aims at presenting structural adhesive bonding in industrial applications.

### **Table of contents**

- 1.1. 1.1. Structural adhesive bonding : An efficient joining process
- 1.2. Selection the adhesive material
- 1.3. Adhesive joint manufacturing
- 1.4. Adhesive joint geometries
- 1.5. The fracture of adhesive joints
- 1.6. Mechanical analyses of adhesively bonded joints
  - 1.6.1. Closed-form stress analyses of adhesively bonded joints
  - 1.6.2. Finite Element (FE) analyses of adhesively bonded joints
  - 1.6.3. Analysis of adhesively bonded joints using macro-elements
- 1.7. Experimental characterization of adhesively bonded joints
  - 1.7.1. Cohesive Zone Modeling (CZM)
  - 1.7.2. Determination of cohesive zone model parameters
- 1.8. Objective of the thesis

1.1.

S

### Structural adhesive bonding: An efficient joining process

In the frame of the design of structural components, the choice of the joining method is essential. A large range of joining methods exists for bringing together similar (or dissimilar) materials from plastics to metals including composite materials. In a large amount of industrial applications, conventional mechanical joints (e.g. bolted, riveted, etc) are preferred due to their simplicity and disassembly ability. However, when loaded, mechanical joints are limited by the local damage introduced at fastener holes (see Fig.1). This generally leads to the overweight design of mechanical joints structures (i.e. safe tolerant damage, etc).

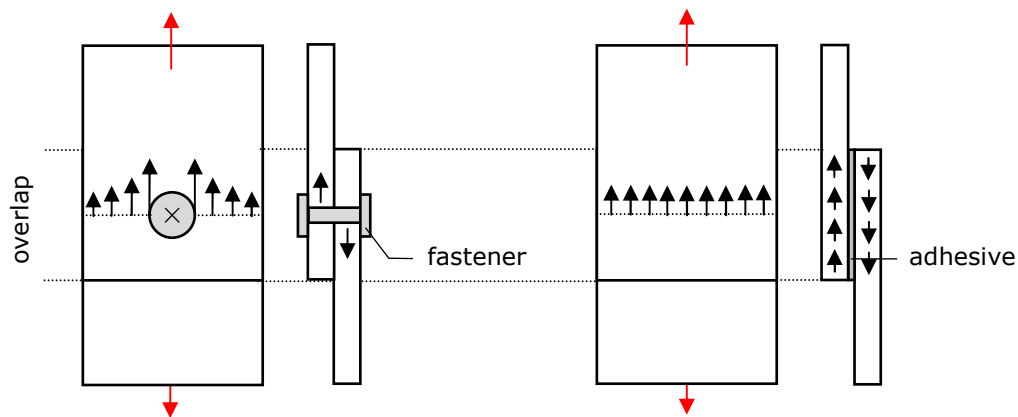


**Figure 1.** Schematic representation of the concentration of stresses nearby the fasteners holes. Structural adhesive bonding. An efficient joining process.

The demand for designing lightweight structures without any loss of strength and (or) stiffness has conducted many engineers (researchers) to seek for alternative joining methods. In this context, adhesively bonded joints may appear as an attractive joining method.

According to (Adams & Wake 1997, Hart-Smith 2002 and Anyfantis 2012), adhesively bonded joints have the advantage of: (i) allowing for the joining of thin substrates, (ii) providing high strength to weight ratios with three times higher the shearing force of riveted joints due to a continuous load transfer, (iii) providing a superior fatigue resistance up to twenty times higher than equivalent riveted joints, (iv) being generally sufficiently flexible to allow for the variation in coefficients of thermal expansion when joining dissimilar materials, (v) generally being an excellent electrical and (or) thermal insulation, (vi) improving aerodynamic/hydrodynamic smoothness and visual appearance and (vii) being usable as a seal or corrosion preventer when joining incompatible materials (i.e. galvanic corrosion).

However, adhesive bonding also involves: (i) a perfectly controlled joining process, (ii) clean and specifically prepared substrates to allow for optimal adhesion properties and (iii) adhesive potentially sensitive to harsh environmental conditions (e.g. temperature, ambient humidity, UV exposure, etc).

Another advantage of adhesive bonding is that since the amount of adhesive generally required for sustaining static as well as fatigue loads is very low it generally allows for significant weight benefits. Finally, another advantage of adhesive bonding is that, thanks to chemistry, adhesives can be specifically formulated to fit at best dedicated specifications (see [Section 1.2](#)).

Adhesive bonding for secondary load bearing structures has been introduced several decades ago and finds its roots in the field of aeronautics (see [Fig.2](#)). However, although numerous successful structural applications have been identified (e.g. De Havilland Mosquito, British Aerospace RJ series, Airbus A300, A380, Boeing 787, etc) the technology has always suffered from a general lack of confidence compared to conventional joining methods, such as bolting or riveting ([Higgins 2000](#)).

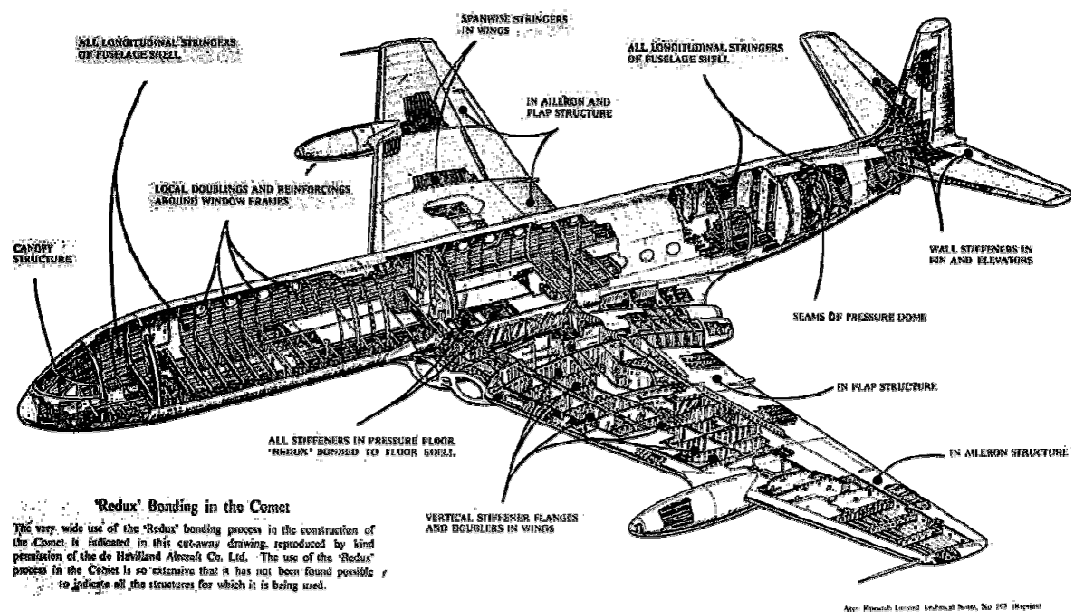
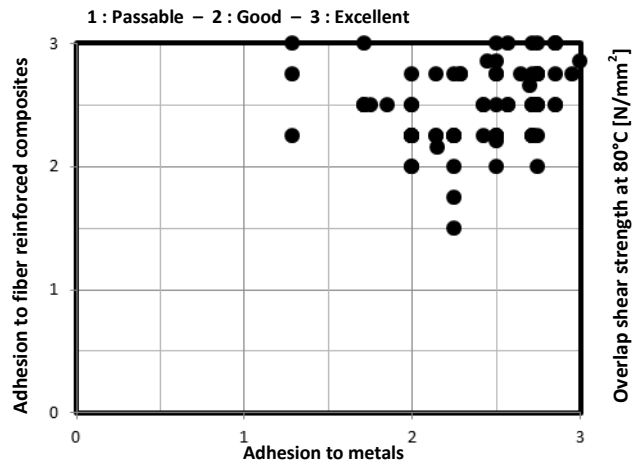


**Figure 2.** Blueprint of the DeHavilland Comet. Secondary load bearing structures bonded with Redux 775 in the DeHavilland Comet. Structural adhesive bonding. An efficient joining process. ([Higgins 2000](#)).

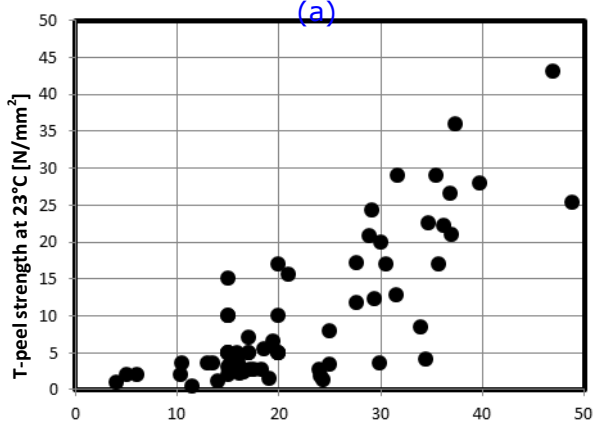
### 1.2. Selection of the adhesive material

In ([Anyfantis 2012](#)), the author suggests that most of today's structural adhesives can be classified into six groups that are: (i) epoxies, (ii) urethanes, (iii) acrylics, (iii) anaerobics, (iv) cynaoacrylates and (v) UV curable adhesives.

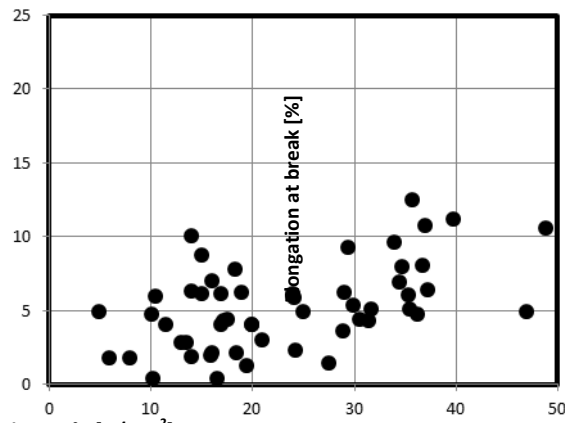
As a result, nowadays exists a large amount of different adhesive materials. Each one specified to fit at best dedicated specifications. In [Fig.3](#) is presented a non-exhaustive survey of some of the main structural properties of a representative number of today's industrial adhesives. Different characteristics were set out from numerous suppliers technical datasheets (i.e. 147) and compared from one to others. Different trends are set out.



Overlap shear strength at 23°C [N/mm<sup>2</sup>]



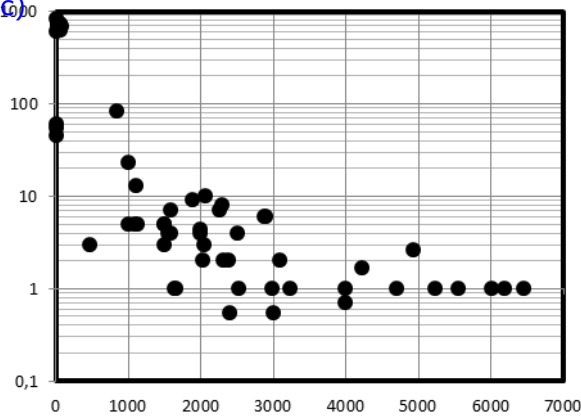
(b)



Overlap shear strength at 23°C [N/mm<sup>2</sup>]

Young's tensile modulus [MPa]

(c)



(d)

**Figure 3.** Survey of structural properties of a representative number of today's industrial adhesives. Adhesion to fiber reinforced composites versus adhesion to metals (a). T-peel strength at 23°C versus overlap shear strength at 23°C (c). Overlap shear strength at 80°C versus overlap shear strength at 23°C (b). Elongation at break versus Young's tensile modulus (d).

As an example, it is seen from Fig.3-(c) that today's adhesives are generally expected to sustain more efficiently shear loadings than peel loadings. As a result, investigations on adhesive peel strength have become an industrial concern of growing interest in terms of bonding efficiency.

### 1.3. Adhesive joint manufacturing

According to (Broughton 2001a), the reliability of an adhesive joint depends not only on the selected adhesive (adherend) material, but on the preparation of the adherends, the mixing of the adhesive, the joint assembly and the curing process. Indeed, always according to (Broughton 2001a), a significant percentage of adhesive joint failures can be attributed to poor manufacturing processes. The manufacturing process then appears as a key parameter involved in the overall performance (structural integrity) of adhesively bonded joints.

Surface preparation is commonly recognized as one of the most critical step in adhesive bonding. Indeed, inadequate surface preparation of the adherends generally results in the bond to fail unpredictably at the adhesive-to-adherend interface (see Section 1.5). As a result, a considerable attention has been given in optimizing existing (or developing new) surface treatments for increasing adhesive-to-adherend adhesion properties in the open literature (Broughton 2001a, Broughton 2001b).

According to (Broughton 2001b), the role of surface preparation is to remove all surface contaminants, favor mechanical micro-interlocking, and (or) modify the local chemistry of the bonding surface (see Fig.4). However it is important to ensure that the surface preparation does not affect significantly the constitutive relationships of the bonded adherends, so that those have to be characterized after the surface treatment.

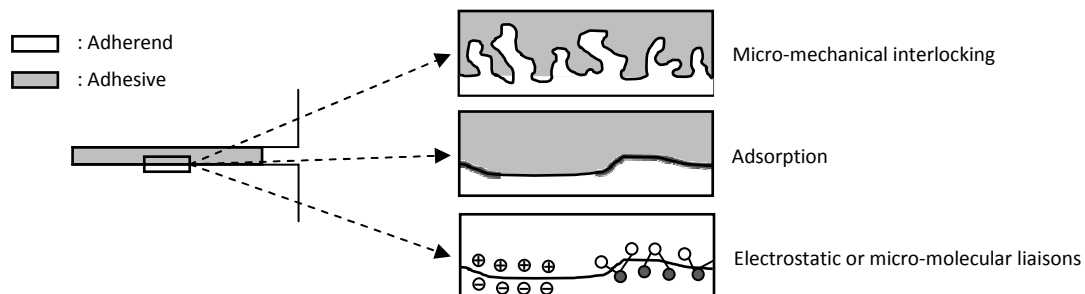


**Figure 4.** Schematic representation the mechanical interlocking, adsorption, covalent and (or) polar-covalent liaisons adhesive-to-adherend adhesion mechanisms. Adhesive joint manufacturing.

Several authors such as (Adams and Wake 1997, Wegman and Van Twisk 2012) have then suggested making a distinction between three types of surfaces treatments: (i) surface preparation, (ii) surface pre-treatment and (iii) surface post-treatment. Surface preparation covers cleaning (degreasing) and preparation (deburring) of the substrate surface. Surface pre-treatment refers to mechanical processes (e.g. grinding, jet-cleaning, etc), chemical processes (e.g. etching, gas phase fluorination, etc) and physical processes (e.g. low pressure plasma, etc) that alter the mechanical and (or) chemical composition of the surface to be bonded. Finally, surface post-treatment refers to all techniques that purposes to preserve the treated surface from later on contaminations (e.g. application of a primer, etc).

#### 1.4. Adhesive joint geometries

In (Anyfantis 2012), the author suggests defining adhesive bonding as a joining process in which an adhesive material, sandwiched between two adherends, solidifies to produce a bond. This definition is interesting since it clearly links an adhesive layer to its surrounding structure, so that the mechanical response of an adhesive layer cannot be dissociated from its surrounding structure.

As an example, a non-exhaustive list of existing adhesive joint geometries is provided in Fig.5. These geometries refer to in-plane loaded adhesive joint geometries, so that out-of-plane deformations of the adhesive layer are not addressed. The Single-Lap Joint (SLJ) is certainly the most common adhesive joint that is found in practice (see Fig.6). Firstly discussed in (Volkersen 1938), the SLJ design allows for the joining of similar (or dissimilar) thin (or thick) adherends with a simple manufacturing process. Moreover, the SLJ design has the advantage of transferring loads from one adherend to another so that the adhesive layer experiences shear loadings essentially (i.e. which is known as being the strongest way of loading an adhesive bond). However the SLJ causes the adhesive layer to be stressed also in peel. The misalignment of the axial loading directions (i.e. also referred as the load path eccentricity) resulting in the rise of significant bending moments at the overlap edges so that peel stresses appear at each end of the adhesive layer (see Fig.6).

To overcome this problem (i.e. load path eccentricity), (Lees 1987) suggested an alternative joint design. This alternative joint design is referred as the Double Joggle Joint (DJJ) and suggests bringing back the axial loading directions into alignment by stamping both of the surrounding adherends. The gain in terms of joint durability (i.e. due to the modified distributions of adhesive stresses along the overlap) is shown as significant (see Fig.7). However, although the DJJ is particularly well suited for bonding adherends that can endure stamping, this particular design remains difficult to manufacture.

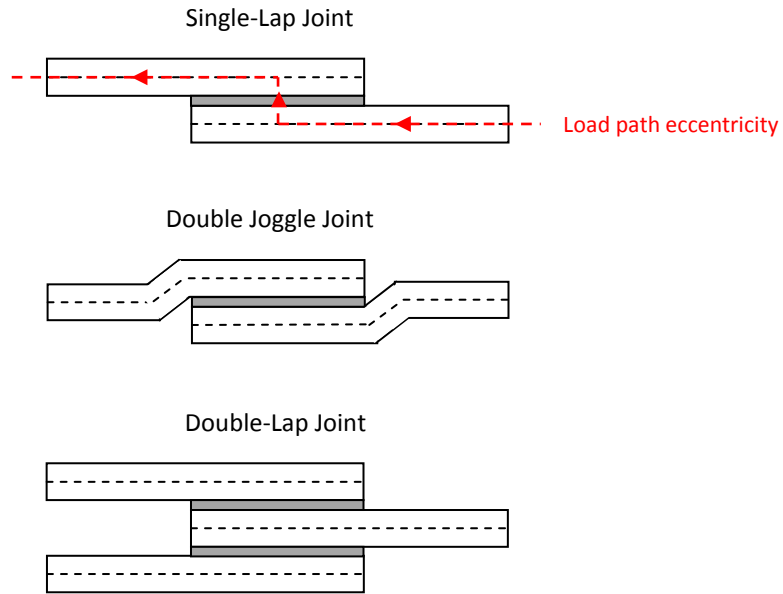


Figure 5. Schematic representation of the Single-Lap Joint (SLJ), the Double Joggle Joint (DJJ) and the Double-Lap Joint (DLJ). Adhesive joint geometries. Structural adhesive bonding.

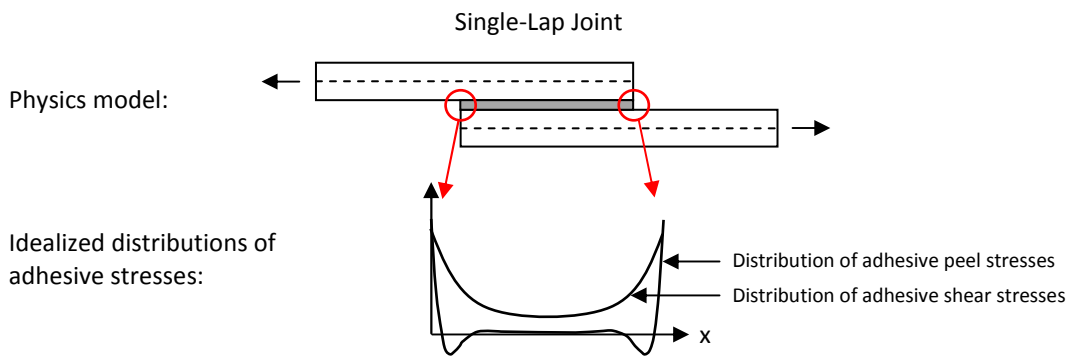


Figure 6. Schematic representation of the Single-Lap Joint (SLJ). Idealized distributions of adhesive stresses. Adhesive joint geometries. Structural adhesive bonding.

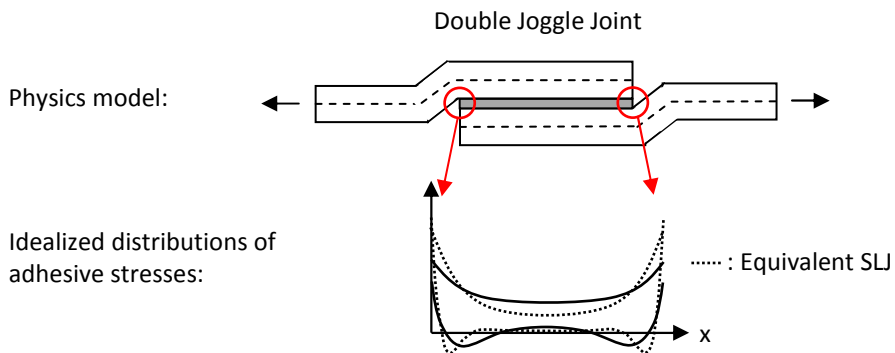
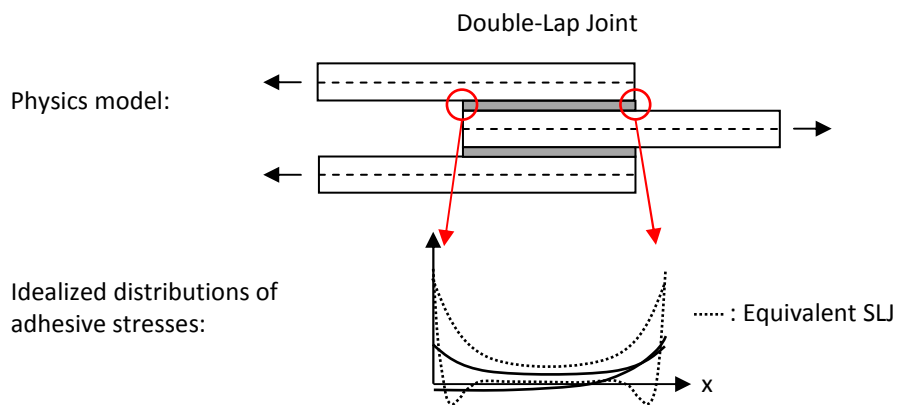


Figure 7. Schematic representation of the Double Joggle Joint (DJJ). Idealized distributions of adhesive stresses. Adhesive joint geometries. Structural adhesive bonding.

Similarly to the latter (Lees 1987), (Hart-Smith 1973b) proposed another joint design so that it limits bending effects due to the misalignment of the joint loading directions. This design is referred as the Double-Lap Joint (DLJ). The DLJ then suggests limiting the effect of the misalignment of the axial loading directions by offering two symmetrical paths for transferring the applied load. The main advantage of such design is then that, besides reducing by half the load transferred through both upper and lower adhesive layers, is to limit the bending effects by constraining the transverse displacements of the mid plan adherend.



**Figure 8.** Schematic representation of the Double-Lap Joint (DLJ). Idealized distributions of adhesive stresses. Adhesive joint geometries. Structural adhesive bonding.

However, although the DLJ is generally assumed as experiencing essentially adhesive shear loadings (Mittal 2002), peel loadings cannot be entirely neglected so that the applied load is still transferred through the adhesive to the adherends away for their neutral axes (see Fig.8). Then the internal bending moments that arise in the outer adherends cannot be entirely neglected and still affects the overall joint performances (structural integrity). Similarly, numbers of other joint geometries such as the Tapered Single-Lap Joint (TSLJ) and (or) the Tapered Double-Strap Joint (TDSJ) have been suggested for reducing the rise of peel stresses within the adhesive layer over the past decades.

1.5.

T

## The fracture of adhesive joints

Depending on the joint geometry and (or) loading conditions, adhesively bonded joints are expected to fail either in the adhesive layer or in the adherends. The fracture of the adhesive layer is governed by three main mechanisms (see Fig.9). The first one, the cohesive failure, happens when the adhesive fracture starts (and propagates) within the core of the adhesive layer. It refers to the classical degradation process as described within most of the theoretical analyses of the fracture of adhesively bonded joints. The cohesive failure is governed by the constitutive properties of the adhesive layer only and is generally reproducible. The second one, the interfacial or adhesive failure, happens when the adhesive starts to disbond at the adhesive-to-adherend upper (lower) interface. This mechanism generally happens for smaller loads than the cohesive failure and is typically due to poor surface preparation of the adherends before bonding. It then results in non-optimal adhesion properties between the adhesive and the upper (lower) adherend. The interfacial fracture is generally complicated to reproduce since the interfacial strength of the adhesive-to-adherend upper (lower) interface results from a complex interaction between both mechanical, process and environmental parameters. The last one, the mixed-mode failure, is a mix between cohesive and interfacial failures. It generally takes the form of a crack path that oscillates between one adhesive-to-adherend interface to another or between one adhesive-to-adherend interface to the core of the adhesive layer.

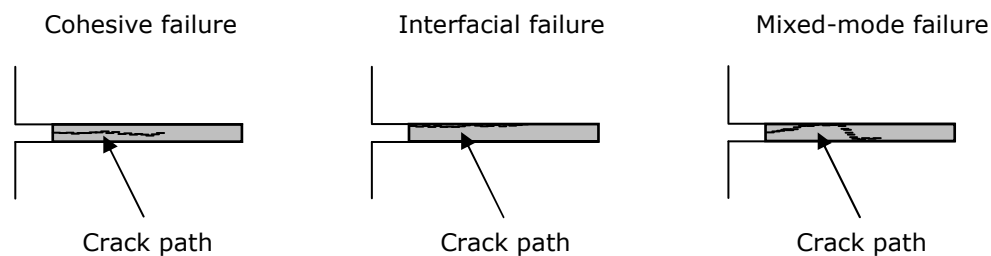


**Figure 9.** Schematic representation of fracture mechanisms of adhesive joints. Fracture of the adhesive layer. Cohesive failure. Interfacial failure. Mixed-mode failure.

Similarly, the fracture of the surrounding adherends is governed by two main mechanisms (see Fig.10) that generally depend on the nature of the adherends themselves. The cohesive failure of the adherend refers to the failure of the adherend due to the rise of important axial stresses nearby the overlap edges. This mechanism generally applies to metallic adherends. On another side, the adherend delamination (i.e. also referred to as the adherend interlaminar failure) refers to the failure of the adherend at the interface between plies, and is due to the rise of important peeling stresses between each ply of the laminate. This mechanism generally applies to fiber reinforced composite materials.

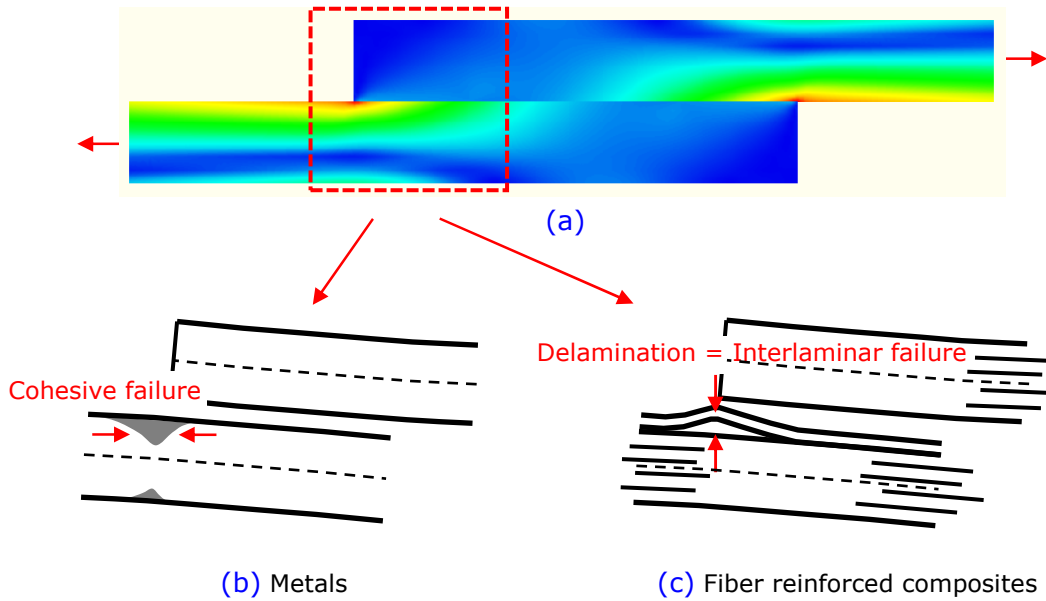


Figure 10. Schematic representation of fracture mechanisms of adhesive joints. Fracture of the surrounding adherends. Idealized Von Mises stress distribution developed in the Single-Lap Joint (SLJ) subjected to in-plane loading (a). Cohesive failure. Metals (b). Interlaminar failure. Fiber reinforced composites (c).

The present dissertation then takes interest in the cohesive failure of adhesive layers only (see Fig.11). The cohesive failure of the adhesive layers is ensured by using adequate surface preparations before bonding.

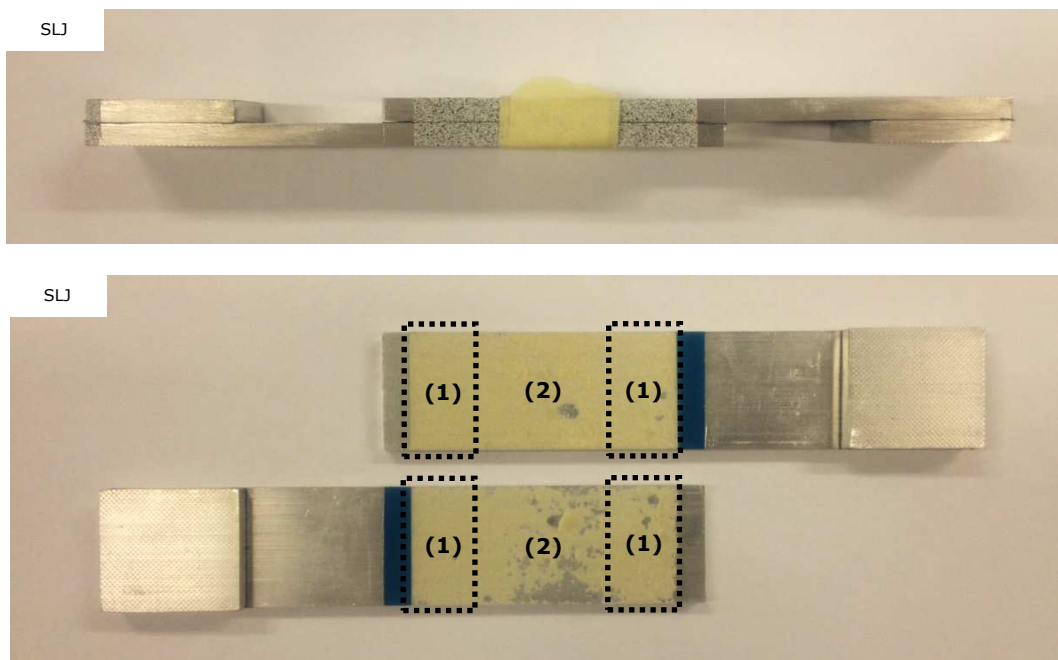


Figure 11. Fracture facies of an adhesive Single-Lap Joint (SLJ). (1): Apparent adhesive residue on both sides of the fracture facies = Propagation of the crack within the core of the adhesive layer. Cohesive failure of the adhesive. (2): Apparent surface of the adherend on the fracture facies.

lower fractured sample of the specimen. Mixed-mode failure of the adhesive. Due to the catastrophic (unstable) static load failure of the specimen.

1.6.

M

### mechanical analyses of adhesively bonded joints

Historically, the lack of suitable mechanical models and (or) failure criteria for the modeling of the fracture process of adhesively bonded joints has resulted in a tendency to overdesign adhesive joints. To allow for the design of adhesively bonded joints, numbers of engineers and researchers have thus worked on the extensive modeling of the mechanical response of such structures. Different approaches exist.

1.6.1.

C

### closed-form stress analyses of adhesively bonded joints

A large number of closed-form stress analyses of adhesively bonded joints exist in the open literature (Volkersen 1938, Goland & Reissner 1944, Adams and Peppiatt 1973, Hart-Smith 1973a, Hart-Smith 1973b, Williams 1975, Allman 1977, Bigwood & Crocombe 1991, Hogberg 2004, Weissgraeber 2014). Based on (van Ingen and Vlot 1993, Da Silva 2009), a non-exhaustive review of these simplified approaches is given in Appendix 1. In most of these approaches the joint kinematic is simplified so that the displacements field of each adherend is supposed relevant to the beam (or plate) theory while the adhesive displacement field is expressed in terms of that of adherends (i.e. then restricting the number of components of the adhesive stress tensor). A widespread modeling of the adhesive layer consists in a two dimensional elastic foundation, using a continuous distribution of peel and shear springs supporting both adherends interfaces (Volkersen 1938, Goland & Reissner 1944, Hart-Smith 1973a, Hart-Smith 1973b, Weissgraeber 2014). In these particular analyses, the adhesive stresses are then expressed as functions of the relative displacements of the surrounding adherends. The governing system of equilibrium equations of the joint is then derived and solved in view of its boundary conditions, so that the distribution of adhesive stresses along the overlap is given in the form of ready-for-use formulae.

A large amount of closed-form adhesive stress analyses consider solving the equilibrium equations of the joint along the overlap region only (see Fig.12), so that it allows for the analysis of various joint configurations (e.g. SLJ, L-Joint, T-Joint, etc). These analyses are classically separated in two distinct phases: (i) determining the loads acting onto the edges of the adhesive overlap and (ii) determining the distribution of joint stresses as functions of these applied loads. For convenience, these analyses will thereafter be referred as sandwich type analyses.

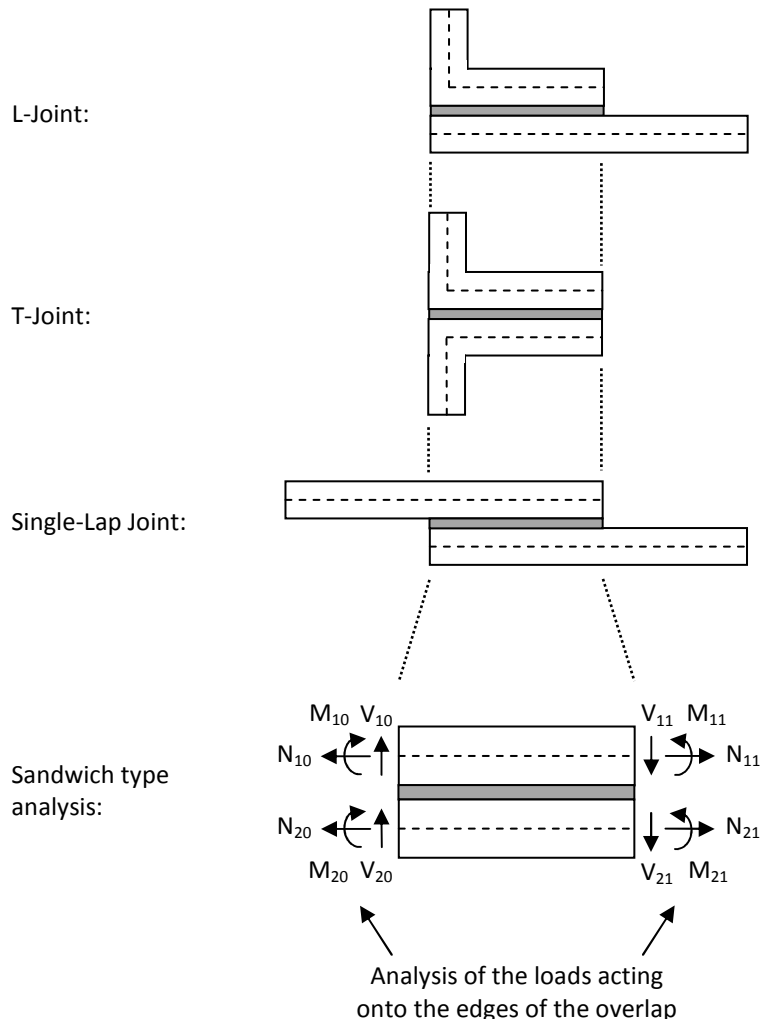


**Figure 12.** Adhesively bonded joint sandwich type analysis. Closed-form stress analyses of adhesively bonded joints. Mechanical analyses of adhesively bonded joints.

The accuracy of such approaches in predicting the distributions of stresses within the adhesive layer then lies on the validity of the simplifying hypotheses used to integrate the governing system of equilibrium equations only. However they are generally easy to implement and require few computational resources.

**Goland & Reissner's sandwich type analysis.** The Goland & Reissner's sandwich type analysis has been firstly introduced in (Goland & Reissner 1944) and has formed the theoretical foundations of most later investigations on the strength analysis of adhesive joints.

In (Goland & Reissner 1944), the authors suggest determining analytical expressions for the elastic shearing and peeling (normal) stresses in single-lap cemented joints (i.e. simply supported and in-plane loaded). The theory is then divided in two parts: (i) determining the loads acting onto the edges of the adhesive overlap and (ii) determining the joint stresses as functions of these applied loads. For simplification purpose, they suggest modeling the surrounding adherends as monolithic beams with symmetric geometry and material (i.e.

$E_1=E_2=E$ ,  $t_1=t_2=t$  and  $\nu_1=\nu_2=\nu$ , with  $E_j$ ,  $\nu_j$  and  $t_j$  respectively the Young's modulus, the Poisson's ratio and the thickness of adherend  $j$  ( $j=1,2$ ).

First assuming the whole joint (i.e. the bonded overlap + the outer adherends) as behaving as a cylindrical bent plate of variable cross section and neutral axis, the authors derive a relationship between the bending moment applied at the overlap edge and the applied axial load. The given relationship accounts for the equilibrium of the deformed geometry instead of the initial (undeformed) geometry. Then, the authors suggest defining the bending moment factor  $k_{GR}$  as the ratio between the resulting bending moment (i.e. applied at the overlap edge) and the axial load multiplied by the half thickness of the surrounding adherends, so that:

$$k_{GR}^{-1} = \frac{1}{2} Pt/M_0 = 1 + 2\sqrt{2} \tanh\left(\sqrt{\frac{P}{8D}} \frac{L}{2}\right) \quad (1)$$

where  $P$  is the applied axial load,  $M_0$  the bending moment acting at the overlap edge,  $L$  the length of the bonded overlap and  $D$  the adherends constitutive bending stiffness defined as:

$$D = \frac{Ebt^3}{12(1-\nu^2)} \quad (2)$$

In a second time, the authors suggests solving in view of its boundary conditions the set of governing differential equations (i.e. derived from a linear elastic analysis of the bonded overlap) that account for the effect of both shearing and normal (peeling) adhesive stresses onto the equilibrium of the surrounding adherends.

The authors finally suggest deriving two analytical expressions for the adhesive shear ( $T$ ) and peel ( $S$ ) distributions, so that:

$$T(x) = \frac{P}{bL} \left[ \frac{1+3k}{4} \beta \frac{\cosh(\beta(2x/L-1))}{\sinh(\beta)} + \frac{3}{4}(1-k_{GR}) \right] \quad (3)$$

$$S(x) = \frac{4Pt}{bL^2\Delta} \left[ \left( \frac{1}{2} R_2 \lambda^2 k_{GR} + \lambda k \cosh(\lambda) \cos(\lambda) \right) \cosh\left(\lambda \frac{2x}{L}\right) \cos\left(\lambda \frac{2x}{L}\right) \right. \\ \left. + \left( \frac{1}{2} R_1 \lambda^2 k_{GR} + \lambda k' \sinh(\lambda) \sin(\lambda) \right) \sinh\left(\lambda \frac{2x}{L}\right) \cos\left(\lambda \frac{2x}{L}\right) \right] \quad (4)$$

where:

$$k = \frac{L}{2} \sqrt{\frac{1}{4D}} k_{GR} \quad (5)$$

$$\beta = \frac{L}{2} \sqrt{\frac{8G}{Ete}} \quad \text{and} \quad \lambda = \frac{L}{2} \sqrt{\frac{6E}{Ete}} \quad (6)$$

$$R_1 = \cosh(\lambda)\sin(\lambda) + \sinh(\lambda)\cos(\lambda) \quad (7)$$

$$R_2 = \sinh(\lambda)\cos(\lambda) - \cosh(\lambda)\sin(\lambda) \quad (8)$$

$$\Delta = 1/2 (\sinh(2\lambda) - \sin(2\lambda)) \quad (9)$$

and where  $G$ ,  $E$  respectively refer to the shearing, peeling (normal) modulus of the adhesive layer and  $e$  to the thickness of the adhesive layer.

**Hart-Smith's sandwich type analysis.** In (Hart-Smith 1973a), the author suggests reworking the earlier Goland & Reissner's theory so that: (i) the expression of the bending moment factor is re-established using different simplifying hypotheses and (ii) the set of joint equilibrium equations is re-derived so that it accounts for the thickness of the adhesive layer onto the load path eccentricity.

Contrary to the Goland & Reissner's approach for deriving the bending moment applied at the overlap edge from the applied axial load, the author does not assume the entire joint (i.e. the bonded overlap + the outer adherends) as a unique structure of variable cross-section and neutral axis. Then, the author analyses the joint using the same set of governing differential equations as used for the following stress analysis of the bonded overlap.

By successive combinations and differentiations of the joint equilibrium equations, the author then derives a new expression of the bending moment factor as:

$$k_{HS}^{-1} = \frac{1}{2} P(t+e)/M_0 \approx 1 + \frac{L}{2} \sqrt{\frac{P}{D}} + \frac{L^2}{24} \frac{P}{D} \quad (10)$$

where  $P$  is the applied axial load (in N),  $M_0$  the bending moment acting at the overlap edge,  $L$  the length of the bonded overlap and  $D$  the adherends constitutive bending stiffness defined as:

$$D = \frac{k_B E b t^3}{12(1-\nu^2)} \quad (11)$$

and that account for possible laminated adherends through the parameter  $k_B$ .

The author finally derives new analytical expressions for the adhesive shear ( $T$ ) and peel ( $S$ ) distributions, so that:

$$T(x) = \frac{P}{bL} \left[ \frac{1 + 3(1 + e/t)k_{HS}}{1 + 3(1 + e/t)} \beta \frac{\cosh(\beta(2x/L - 1))}{\sinh(\beta)} + \left( 1 - \frac{1 + 3(1 + e/t)k_{HS}}{1 + 3(1 + e/t)} \right) \right] \quad (12)$$

$$S(x) = \frac{EM_0 L^2}{4De\lambda^2 \exp(\lambda)} \left[ (\cos(\lambda) - \sin(\lambda)) \cosh(\lambda(2x/L - 1)) \cos(\lambda(2x/L - 1)) \right. \\ \left. + (\sin(\lambda) + \cos(\lambda)) \sinh(\lambda(2x/L - 1)) \sin(\lambda(2x/L - 1)) \right] \quad (13)$$

where:

$$\beta = \frac{L}{2} \sqrt{\frac{2G}{Ete}} \sqrt{1 + 3\left(1 + \frac{e}{t}\right)} \quad \text{and} \quad \lambda = \frac{L}{2} \sqrt{\frac{E}{2De}} \quad (14)$$

and where  $G$ ,  $E$  respectively refer to the shearing, peeling (normal) modulus of the adhesive layer and  $e$  to the thickness of the adhesive layer.

### 1.6.2.

F

#### Finite Element (FE) analyses of adhesively bonded joints

The Finite Element (FE) method is a computational method which allows for the approximate solution of various engineering problems to be obtained. The stress analysis of adhesively bonded joints is one of these problems. Although this general resolution procedure is computationally expensive and can lead to numerical convergence issues, so that the mesh of adhesive layers has generally to be intensively refined to capture the local stress gradients at bondline edges, the FE method allows for the study of various joint configurations. Then, various adhesive and adherends geometries as well as various loading and boundary conditions are addressable using FE methods (see Fig.13).

Numbers of authors such as (Pickthall and Heller 1997, Lang and Mallick 1998, Broughton 1999, Broughton 2001b, Hansson 2002, Tsai and Morton 2010, Anyfantis 2012), have thus worked on the intensive modeling of adhesively bonded structures using FE techniques. However, converged FE analyses generally imply highly refined meshes and so time consuming computations.

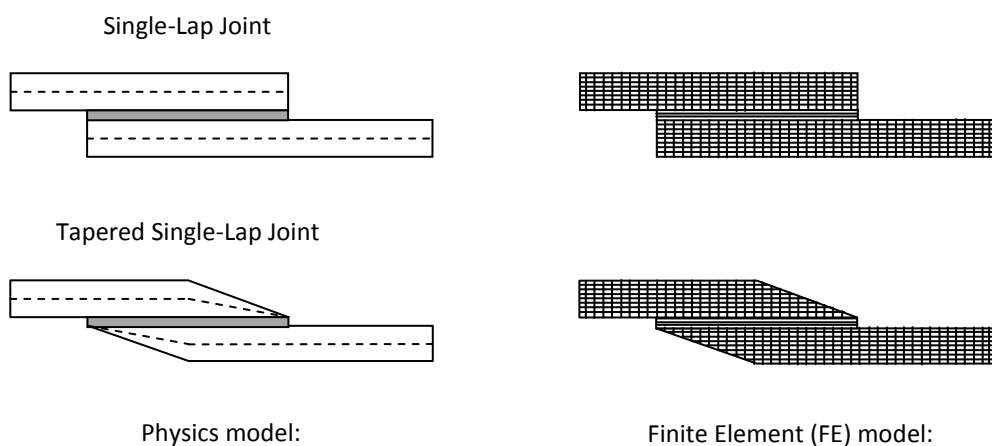


**Figure 13.** Schematic representation of Finite Element (FE) models of a Single-Lap Joint (SLJ) and a Tapered Single-Lap Joint (TSLJ). Finite Element (FE) analyses of adhesively bonded joints. Mechanical analyses of adhesively bonded joints.

### 1.6.3.

A

#### Analysis of adhesively bonded joints using macro-elements

Similarly to closed-form stress analyses, the macro-element approach is based on the resolution of the system of governing differential equations of the joint. However, since the simplifying assumptions are here voluntarily restricted a closed-form solution is not explicitly expressible. Different approaches that use alternative mathematical resolution procedures can be found in the open literature, such as the multi-segment integration technique (Mortensen 1997) or the macro-element technique (Paroissien 2006, Da Veiga 2009, Stapleton 2012, Paroissien *et al.* 2013).

In (Paroissien 2006, Da Veiga 2009, Paroissien *et al.* 2013), an original solution procedure inspired by the Finite Element (FE) method is developed by the authors. The authors then formulate what will be thereafter referred as the Bonded-Beam macro-element – denoted BBe. The method then consists in meshing the structure. The overlap is meshed using a unique 4-node macro-element specifically formulated to allow for the resolution of the governing system of differential equations of the joint at low computational costs. The outer adherends are meshed using specifically formulated outer beam elements (see Section 2.3.2 and Section 2.3.3 of Chapter 2).

According to the classical Finite Element (FE) method, the stiffness matrix of the entire structure – termed  $\mathbf{K}$  – is assembled from the both the BBe macro-element and the surrounding outer beam adherends.

As for the classical Finite Element method, the minimization of the potential energy is ensured by solving equation  $\mathbf{F}=\mathbf{K}\mathbf{U}$ , where  $\mathbf{F}$  is the vector of nodal forces,  $\mathbf{U}$  the vector of nodal displacements and  $\mathbf{K}$  the specifically formulated stiffness matrix of the entire structure. The whole distribution of the adhesive stresses along the overlap is then related to the nodal displacements the BBe macro-element through a coupling parameter matrix denoted  $\mathbf{M}$  (see Section 2.3.2 of Chapter 2).

According to (Paroissien *et al.* 2013), the macro-element approach offers the advantage of: (i) providing predictions of the adhesive stress distributions in extremely good agreement with equivalent FE analyses, (ii) being highly computational time saving compared to equivalent FE analyses and (iii) allowing for the modeling of more complex structures involving single-lap joints at low computational costs.

Recently, an original solution procedure based on the Finite Element method has been adapted to the BBe formulation to allow for the modeling of various adhesive material nonlinear behaviors (Gaubert 2011, Schwartz 2013, Gavaille 2014). However, the authors show that the aforementioned procedure is theoretically limited to the analysis of SLJ configurations only and do apply to sufficiently small material nonlinearities of the adhesive layer only.

1.7.

E

xperimental characterization of adhesively bonded joints

As presented in Section 1.1, in structural components design the choice of the joining technology is essential. In this context, adhesive bonding may appear as an attractive joining

process compared to conventional ones, such as bolting or riveting. Indeed, adhesive bonding offers the possibility of joining without damaging various combinations of materials, including plastics and metals. However, the interest of adhesive bonding remains while the integrity of the joint is ensured. To take advantage of adhesive bonding, accurate strength predictions are thus required.

The strength prediction of bonded joints requires the determination of computed criteria and experimentally characterized allowable. Several approaches are proposed in the open literature. These approaches could besides be used in the experimental characterization process of allowable.

The stress analysis approach, based on the Strength of Materials, is the classical approach. It aims at localizing the maximal values of stresses and strains (Igens 1993, Tsai 1994, Da Silva 2009, Da Silva 2012). A second approach is based on the Fracture Mechanics. Assuming the presence of an initial crack judiciously localized and sized by the user, it allows for the computation of the strain energy release rate (or J-integral) at crack tip as a function of applied loads (or adhesive stresses) (Fraise 1993, Tong 1994, Fernlund 2007, Da Silva 2012). In the coupled stress and energy criterion approach, the crack length at initiation is not assumed but derived from the analysis itself (Leguillon 2002, Weissgraeber 2013). Then, the computed crack length at initiation is not a material characteristic and depends both on geometrical parameters as well as on material critical stress and energy release rate. Finally, the Cohesive Zone Modeling – denoted CZM – enables a diagnostic of the current state of damage and an update of the strength prediction. According to the recent literature (Li *et al.* 2005, Crocombe 2009, De Moura 2009, Crocombe 2010, Crocombe 2011, Da Silva 2012, Gift *et al.* 2013), the CZM appears as one of the most suitable approach able to model both static strength as well as the fatigue degradation process of adhesive layers. In (Martin *et al.* 2016), the authors show good agreement comparing the coupled stress and energy criterion and the CZM in predicting the debonding initiation of a bimaterial specimen subjected to 4-points flexion loads.

#### 1.7.1. Cohesive Zone Modeling (CZM)

The CZM finds its root in the Continuum Damage Mechanics and the Fracture Mechanics. The basic idea of CZM is that structural damage during loading can be found in the form of micro-cracks forming and (or) voids coalescence over a finite distance from the initial damaged area (Da Silva 2012). Resulting in a locally reduced load bearing capability, the degradation process of the material is modeled as a drop of the transferred stresses after a given value of deformation. An idealized CZM bilinear traction separation law is presented in Fig.14. However CZM is not limited to this particular shape of traction separation law only (see Chapter 2 and Chapter 3).

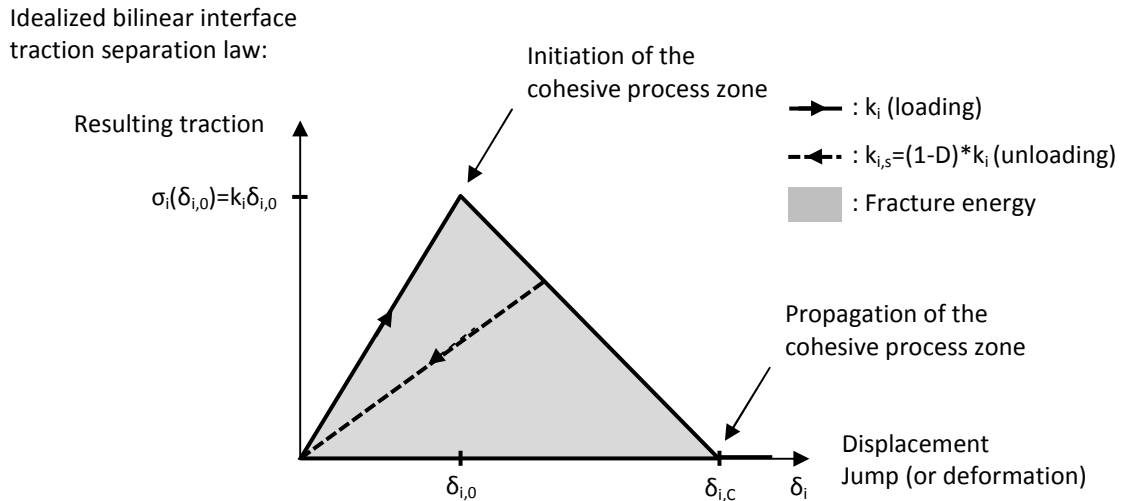


Figure 14. Representation of an idealized bilinear interface traction separation law. Cohesive Zone Modeling (CZM). Experimental characterization of adhesively bonded joints.

According to (Crocombe 2009) CZM has the advantage of: (i) indicating both damage initiation and propagation as direct outputs of the model, (ii) allowing for the prediction of undamaged materials without the need to introduce a pre-existing crack and (iii) advancing the crack front when locally reaching the critical value of the energy release rate without the need of complex moving mesh techniques.

#### 1.7.2. Determination of cohesive zone model parameters

To take full advantage of CZM, computed criteria as well as experimental allowable have to be determined from experimental testing. As a result, numbers of authors suggested developing experimental protocols for characterizing the traction separation laws of thin interfaces over the past few years (Anderson *et al.* 2003, Alfredsson 2003, Alfredsson *et al.* 2003, Alfredsson 2004, Leffler *et al.* 2006, Hogberg 2006, Hogberg *et al.* 2007, Cui *et al.* 2014, Cui 2014, Da Silva 2012).

For most, these protocols refer to the concept of the energetic balance associated to the computation of the path independent J-integral (Rice 1968) along a closed contour of specifically designed specimens. The main advantage of these protocols is that they offer the possibility of monitoring the evolution of the adhesive stresses (strains) at crack tip from the supervision of macroscopic quantities easily measurable from the experimental testing fixture, such as the applied load, the evolution of the adhesive strains at crack tip, etc. The lack of standardized testing for determining the cohesive zone model parameters of thin adhesive interfaces has then conducted numerous researchers and engineers to call for various test configurations. As a result, numbers of specimens has been explored for both pure mode I (II) and mixed-mode I/II characterization of adhesive layers. According to (Da Silva 2012), Double Cantilever Beam (DCB) and End-Notched Flexure (ENF) adhesive test specimens have respectively emerged as the specimens the most commonly used for quantifying the cohesive parameters of adhesive layers in pure mode I and pure mode II over the past few years.

On the contrary, (Reeder 1990, Kenane 1997, Hogberg 2006) established that most the proposed mixed-mode I/II test configurations present practical limitations: (i) complex loading fixtures, (ii) stable/unstable fracture process, (iii) complex manufacturing of the specimens, etc, although few of them present several advantages. The main advantage of the Mixed-mode Cantilever Beam (MCB) and the Mixed-Mode Bending (MMB) testing fixtures (see Fig.15 and Fig.16) is the possibility of working over a wide range of adhesive mode mixities without the need of modifying the geometry of the specimen. Then allowing for adhesive specimens with fully controlled dimensions to be more easily manufactured. It is seen from Fig.15 and Fig.16 that the MCB testing fixture allows for the complete spectrum of adhesive mode mixities to be fully addressed by simply varying the inclination of the antisymmetric loading directions, although the MMB testing fixture is limited by the adhesive itself so that it can difficulty address pure mode I adhesive solicitations. However, a significant advantage of the MMB testing fixture (compared to the MCB testing fixture) is that it can be easily designed in advance of the experiment so that it allows for specific adhesive mixed-mode ratios to be addressed (Boussarie 2013) (see Fig.16).

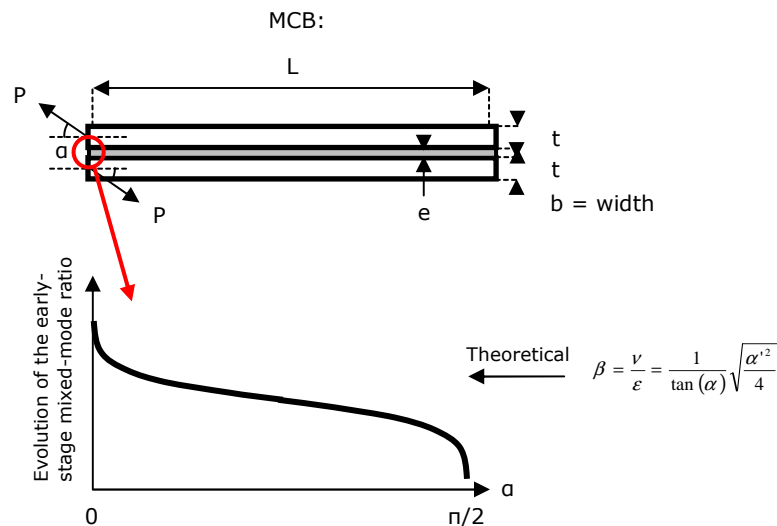
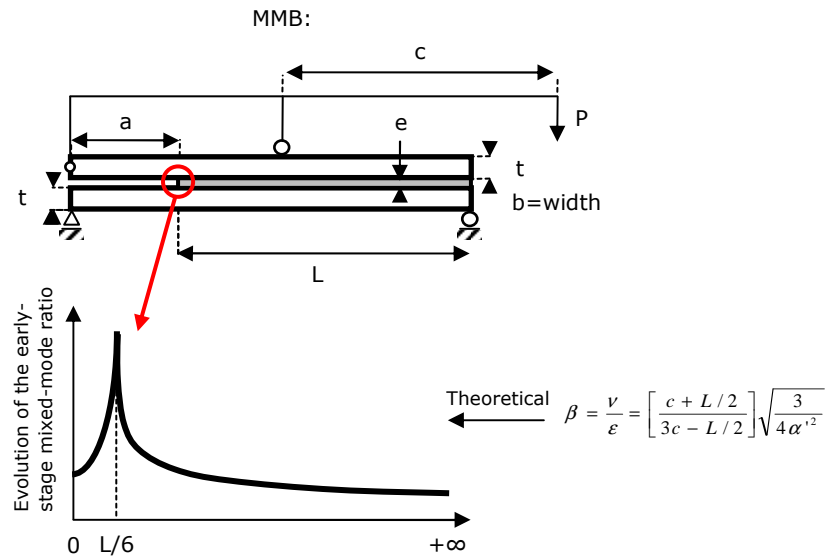


Figure 15. Evolution of the early stage mixed-mode ratio at crack tip ( $\beta = \nu/\varepsilon$ ) as a function of the inclination of the antisymmetric loading directions ( $\alpha$ ).  $\nu$ : Adhesive shearing deformation at crack tip.  $\varepsilon$ : Adhesive peeling deformation at crack tip. Mixed-mode Cantilever Beam (MCB). Determination of cohesive zone model parameters. Experimental characterization of adhesively bonded joints.



**Figure 16.** Evolution of the early stage mixed-mode ratio at crack tip ( $\beta=v/\varepsilon$ ) as a function of the length of the lever arm ( $c$ ).  $v$ : Adhesive shearing deformation at crack tip.  $\varepsilon$ : Adhesive peeling deformation at crack tip. Mixed-Mode Bending (MMB). Determination of cohesive zone model parameters. Experimental characterization of adhesively bonded joints.

1.8.

O

bjectives of the thesis

The following dissertation then falls into two parts. First, [Chapter 2](#) aims at presenting a method that extends the macro-element approach as originally described in (see [Section 1.6.3](#)) to possibly account for various adhesive as well as adherends nonlinear constitutive behaviors. The method is inspired by the Finite Element (FE) method and allows for various adhesive and (or) adherends material nonlinear behaviors to be simultaneously accounted with no restriction on the specimen geometry and (or) level of material nonlinearities. The main originality of the solution procedure presented lies in the use of the adhesive and (or) adherends secant stiffness properties to iteratively approach the solution of the nonlinear problem. The vector of imbalanced loads resulting from the projection of the nonlinear adhesive and (or) adherends stresses is then computed through the knowledge of the adhesive and (or) adherends secant stiffness properties only. The proposed nonlinear adhesive material models are formulated under a two dimensional mixed-mode model that account for the possible interaction between both pure mode I and pure mode II adhesive stress-strain evolutions laws while the proposed adherends material models are formulated under a pure axial model that account for the axial deformation of the surrounding adherends due to coupled tension/bending loadings.

Secondly, [Chapter 3](#) aims to present three different existing protocols for the measurement of the adhesive cohesive properties of thin interfaces ([Anderson et al. 2003](#), [Alfredsson 2004](#), [Hogberg et al. 2007](#)), to set out and to discuss their inherent limitations. Then, a new experimental protocol to evaluate the effective stress-strain relationships of thin adhesive layers subjected to mode I, mode II and (or) mixed-mode I/II adhesive deformations is presented and developed in view of its implementation. The new protocol aims at monitoring

the evolution of the adhesive stresses (strains) at crack tip by supervising the evolution of the adherend-to-adherend displacement field nearby the adhesive crack tip. Finally, the results of an experimental test campaign as well as their comparison with semi-analytical predictions are provided so that the new experimental protocol is validated in the case of metal-to-metal adhesive bonding subjected to pure mode I, pure mode II and mixed-mode I/II. Good agreement is shown.

## **Chapter 2. Extension and validation of the simplified 1D-beam adhesive stress analysis**

Chapter 2 aims at presenting the modeling of adhesively bonded joints facing in-plane adhesive loadings using macro-elements. First, the method originally described in (Paroissien 2006, Da Veiga 2009, Paroissien *et al.* 2013) is presented. Then, the method is extended and validated in the case of adhesive (adherends) material nonlinearities. The results obtained from the semi-analytical analyses are finally compared to those of both existing sandwich type analyses and 2D Finite Element (FE) predictions involving cohesive interface elements. Good agreement is shown.

### **Table of contents**

- 2.1. 2.1. Introduction
- 2.2. Organization of the chapter
- 2.3. Semi-analytical analysis of adhesively bonded joints using macro-elements
  - 2.3.1. The simplified 1D-beam adhesive stress analysis: Overview
  - 2.3.2. Formulation of the BBe macro-element
  - 2.3.3. Formulation of the outer beam element
  - 2.3.4. Resolution procedures
  - 2.3.5. Comparison with existing sandwich type analyses
  - 2.3.6. Comparison with Finite Element (FE) analyses
- 2.4. Introduction of adhesive material nonlinearities
  - 2.4.1. Description of the interface models
  - 2.4.2. Overview of the Newton-Raphson iteration procedure
  - 2.4.3. Local equilibrium of the bonded overlap
  - 2.4.4. Adaptation of the Newton-Raphson iteration procedure to the particular formulation of the BBe element
  - 2.4.5. Comparison with existing sandwich type analyses
  - 2.4.6. Comparison with Finite Element (FE) analyses
- 2.5. Introduction of adherend material nonlinearities
  - 2.5.1. Adaptation of the classical theory of beam plasticization to the particular formulation of the BBe element
  - 2.5.2. Comparison with Finite Element (FE) analyses
- 2.6. Conclusion and discussion

## 2.1.

I

## Introduction

A large number of simplified approaches for the stress analysis of bonded joints exist in the open literature (Volkersen 1938, Goland & Reissner 1944, Hart-Smith 1973a, Hart-Smith 1973b, Williams 1975, Bigwood & Crocombe 1991, Hogberg 2004, Weissgraeber 2014). A non-exhaustive review of these simplified approaches is given in Appendix 1. In most of these simplified approaches the joint kinematic is simplified so that the displacement field of adherends is supposed relevant to the beam or plate theory while the adhesive displacement field is expressed in terms of that of adherends (then restricting the number of components of the adhesive stress tensor). A widespread modeling of the adhesive layer consists in an elastic foundation, supporting both adherends interfaces (Volkersen 1938, Goland & Reissner 1944, Weissgraeber 2014). The adhesive stresses are then expressed as functions of the relative displacements of the facing adherends. Depending on additional simplifying hypotheses, a closed-form solution is not always expressible so that mathematical procedures are necessary to integrate the system of governing differential equations in view of its boundary conditions, such as the macro-element technique (Stapleton 2012, Paoissien 2006) or that the multi-segment integration scheme (Mortensen 1998).

The mathematical solution presented in (Paoissien 2006, DaVeiga 2009, Paoissien *et al.* 2013) applies to Single-Lap Joint (SLJ) configurations and considers the adherends as Euler-Bernoulli laminated beams supported by an infinite number of elastic shear (peel) springs. Besides, an original procedure allowing for non-linear adhesive behaviors to be accounted for is presented. However, the authors show that the aforementioned procedure is theoretically limited to the analysis of SLJ configurations only and do apply to sufficiently small material nonlinearities of the adhesive layer only (Schwartz 2013, Gavaille 2014).

In the present section, a reworked semi-analytical procedure enabling for various nonlinear adhesive (adherends) behaviors to be accounted for with no restriction on the specimen geometry is presented. The possible mixed mode I/II response of the adhesive layer is introduced through an extension of the classical CZM procedure (Valoroso 2004, De Moura 2008, Anyfantis 2012, Campilho 2013). A particular emphasis is given to bilinear adhesive and (or) elastic perfectly plastic adherend stress-strain evolution laws. However, the suggested procedure is not limited to these particular adhesive (adherends) behaviors only.

## 2.2.

O

## Organization of the chapter

First, for lecturer comfort, a short description of the simplified 1D-beam adhesive stress analysis in the case of a linear elastic adhesive layer is provided. However a more comprehensive description of the simplified 1D-beam adhesive stress analysis can be found in (Paoissien *et al.* 2013). The solution procedure is presented in the case of linear elastic solicitations of both the adhesive layer and the surrounding adherends only. The results obtained from the simplified 1D-beam adhesive stress analysis and those from the most recent

Weissgraeber's sandwich type analysis are then compared in terms of peel and shear adhesive stress distributions along the interface. The results obtained from the simplified 1D-beam adhesive stress analysis are also compared to those of 2D Finite Element (FE) predictions involving cohesive interface elements. Good agreement is shown with both sandwich type analysis and FE predictions.

Secondly an iterative solution procedure based on a modified Newton-Raphson iterative solution procedure, and allowing for various nonlinear adhesive stress-strain evolution laws to be accounted for, is presented and developed in view of its implementation. The main originality of the presented solution procedure lies in the use of the adhesive secant stiffness properties to address the nonlinear solution of the problem. The vector of imbalanced loads resulting from the projection of the non-linear adhesive stresses is then computed through the knowledge of the adhesive secant stiffness properties only. The presented procedure allows for various nonlinear adhesive stress-strain evolution laws to be accounted for (ie. softening, plastic, coupled, etc.) with no restriction on the specimen geometry. The proposed adhesive material models are formulated under a two dimensional mixed-mode model that account for the possible interaction (interdependency) between both pure mode I and pure mode II adhesive stress-strain evolutions laws. The presented two dimensional mixed-mode model is inspired from the classical Cohesive Zone Modeling (CZM) theory. The results obtained from the suggested solution procedure are then compared to those of two sandwich type analyses involving nonlinear adhesive stress-strain evolution laws. Finally, the results obtained from the so modified simplified 1D-beam adhesive stress analysis are compared to those of 2D FE predictions involving cohesive interface elements. Good agreement is shown with both nonlinear sandwich type analyses and FE predictions.

To conclude, the preceding iterative solution procedure is upgraded so that it can account for both adhesive and adherends material nonlinearities simultaneously. Then, an original way of accounting for the effect of the surrounding adherends plasticization based on an adaptation of the classical theory of beam plasticity (Oudin 2011) is presented and developed in view of its implementation. The results obtained from the so modified simplified 1D-beam adhesive stress analysis are compared to those of 2D FE predictions involving elastic perfectly plastic adherends stress-strain evolution laws. Good agreement is shown.

2.3.	emi-analytical stress analysis of adhesively bonded joints using macro-elements	S
2.3.1.	he simplified 1D-beam adhesive stress analysis: Overview	T

The simplified 1D-beam adhesive stress analysis is inspired by the Finite Element (FE) resolution procedure and allows for the resolution of the system of governing differential equations of the bonded overlap at low computational costs. The displacements (forces) of both adherends as well as the adhesive stresses (strains) are then obtained from solving the local equilibrium of the adherends. The method consists in meshing the structure. A fully bonded overlap is meshed using a unique 4-nodes macro-element (see Fig.17). This macro-element is specially formulated to allow for the resolution of the system of governing

differential equations of the bonded overlap at low computational costs. For convenience, the bonded overlap macro-element will be thereafter referred as the Bonded-Beam macro-element, and denoted BBe.

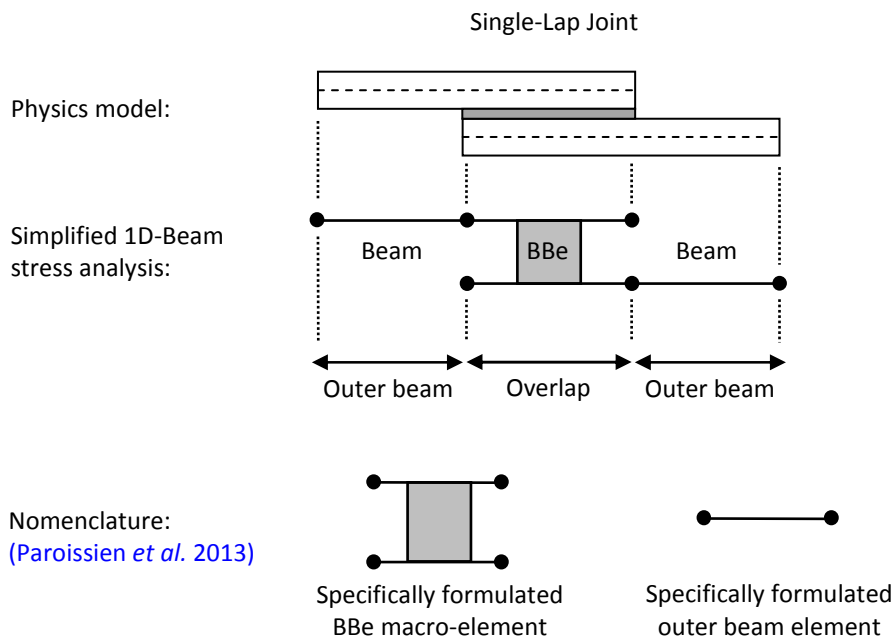


**Figure 17.** Assembly of the Single-Lap Joint (SLJ) configuration using both outer beam and BBe macro-elements. The simplified 1D-beam adhesive stress analysis. Overview.

The outer adherends are in turn meshed using specifically formulated Euler-Bernoulli beam elements. For convenience, the two Euler-Bernoulli beam elements will be thereafter referred as the outer beam elements, and denoted Beam. According to classical assembly FE rules, the stiffness matrix of the entire structure – termed  $\mathbf{K}$  – is assembled and the selected boundary conditions are applied. For convenience, the stiffness matrix of the entire structure ( $\mathbf{K}$ ) will thereafter be referred as the master stiffness matrix. The minimization of the total potential energy is then ensured by solving the equation  $\mathbf{F}=\mathbf{K}\mathbf{U}$ , where  $\mathbf{F}$  is the vector of nodal forces and  $\mathbf{U}$  the vector of nodal displacements. The suggested approach takes the advantage of the flexibility of FE techniques and the robustness of theoretical approaches. Using BBe macro-elements as elementary bricks of larger models then offers the possibility to simulate more complex structures involving single-lap bonded joints at low computational costs (see Fig.18).

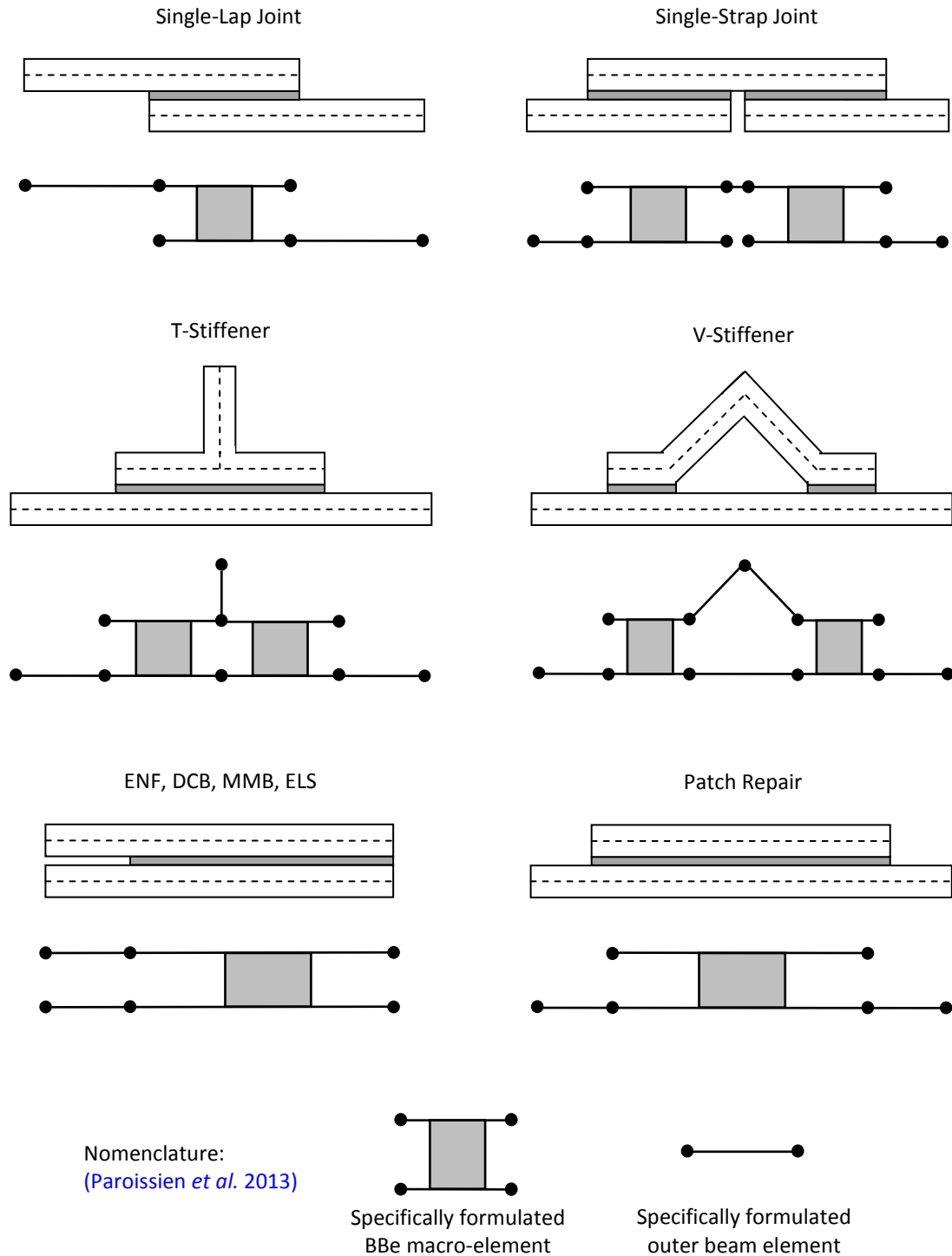


Figure 18. BBe macro-elements as bricks of larger models for linear and nonlinear adhesive stress analysis. The simplified 1D-beam adhesive stress analysis. Overview.

2.3.2.

F

ormulation of the BBe macro-element

**Hypotheses.** The linear elastic 1D-Beam model is based on the following hypotheses: (i) the thickness of the adhesive layer is constant along the overlap, (ii) both adherends are assumed

as behaving as linear elastic Euler-Bernoulli laminated beams in coupled tension/flexion, and (iii) the adhesive layer is simulated by an infinite number of elastic shear and peel springs supporting both upper (lower) adherends interfaces.

**Governing differential equations.** The local equilibrium of each adherend is expressed in the form of the following system of six differential equations (see Fig.19):

$$\begin{cases} \frac{dN_j}{bdx} = (-1)^j T \\ \frac{dV_j}{bdx} = (-1)^{j+1} S \\ \frac{dM_j}{dx} + V_j + \frac{1}{2}(e_j + e) b T = 0 \end{cases}, j = 1, 2 \quad (17)$$

where  $S$  is the adhesive peel stress,  $T$  the adhesive shear stress,  $N_1$  ( $N_2$ ) the normal force in adherend 1 (2),  $V_1$  ( $V_2$ ) the shearing force in adherend 1 (2) and  $M_1$  ( $M_2$ ) the bending moment in adherend 1 (2). Note that equation (17) refers to the local equilibrium derived and employed in (Hart-Smith 1973a, Hart-Smith 1973b).

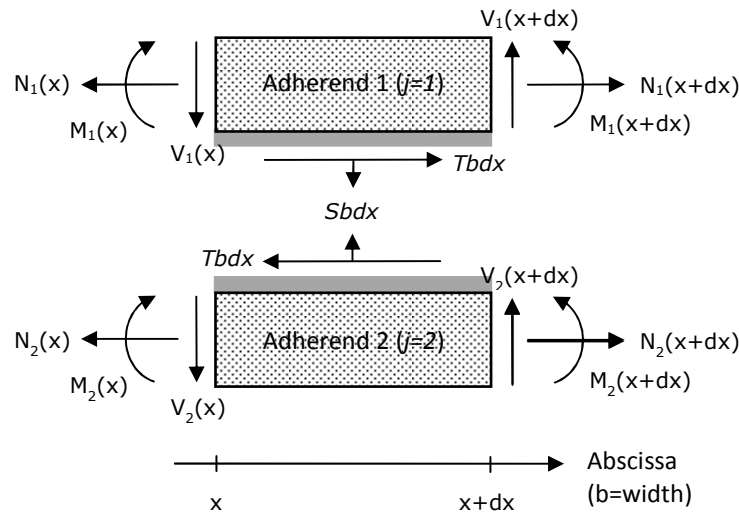


**Figure 19.** Schematic representation of the local equilibrium of the bonded adherends. The simplified 1D-beam adhesive stress analysis. Overview.  $N_j$ : Normal force of adherend (j) [N].  $V_j$ : Shear force of adherend (j) [N].  $M_j$ : Bending moment of adherend (j) [Nm].  $T$ : Adhesive shear stress [Mpa].  $S$ : Adhesive peel stress [Mpa].  $b$ : width [mm].

Considering the possible extensional, bending and coupling stiffnesses of each adherend gives the adherends constitutive relationships:

$$\begin{cases} N_j = A_j \frac{du_j}{dx} - B_j \frac{d\theta_j}{dx} \\ M_j = -B_j \frac{du_j}{dx} + D_j \frac{d\theta_j}{dx}, \quad j = 1, 2 \\ \theta_j = \frac{dw_j}{dx} \quad \leftarrow \text{Euler-Bernoulli} \end{cases} \quad (18)$$

with  $A_j$  the extensional stiffness,  $B_j$  the coupling stiffness, and  $D_j$  the bending stiffness of adherend  $j$  ( $j=1,2$ ). Further details on these adherends constitutive equations can be found in in [Appendix 2](#) or in standard textbooks on composite mechanics ([Jones 1998](#), [Berthelot 1999](#)). In the case of homogeneous isotropic adherends with rectangular cross sections the given relationships can be reduced to:

$$\begin{cases} A_j = bE_j e_j \\ B_j = 0 \\ D_j = bE_j e_j^3 / 12 \end{cases}, \quad j=1,2 \quad (19)$$

where  $E_j$  refers to the Young's modulus of adherend  $j$  ( $j=1,2$ ),  $e_j$  to the thickness of adherend  $j$  ( $j=1,2$ ) and  $b$  to the width of the adhesive test specimen. The afore-described theory has been here voluntarily restricted to the Kirchhoff-Love assumptions. However the adherend shear stress can possibly be assumed as varying linearly with the adherend thickness ([Tsai et al. 1998](#), [Da Veiga 2009](#), [Paroissien et al. 2013](#)).

Finally, and considering the adhesive layer as a linear elastic interface simulated by an infinite number of elastic shear (peel) springs, the adhesive shear (peel) stresses are expressed as:

$$\begin{cases} T = G\gamma = \frac{G}{e} \left( u_2 - u_1 - \frac{1}{2} e_1 \theta_1 - \frac{1}{2} e_2 \theta_2 \right) \\ S = E\varepsilon = \frac{E}{e} (w_1 - w_2) \end{cases} \quad (20)$$

where  $E$  refers to the *peel modulus* of the adhesive (see [Appendix 3](#)),  $G$  the shear modulus of the adhesive,  $\gamma$  to the shearing deformation of the adhesive,  $\varepsilon$  to the peeling deformation of the adhesive,  $u_1$  ( $u_2$ ) the normal displacement of adherend 1 (2),  $w_1$  ( $w_2$ ) the transverse displacement of adherend 1 (2),  $\theta_1$  ( $\theta_2$ ) the bending angle of adherend 1 (2) and  $e$  the thickness of the adhesive layer (see [Fig.20](#)).

For demonstration purpose it is assumed that  $\Delta_j = A_j D_j - B_j^2$  ( $j=1,2$ ) is not equal to zero.

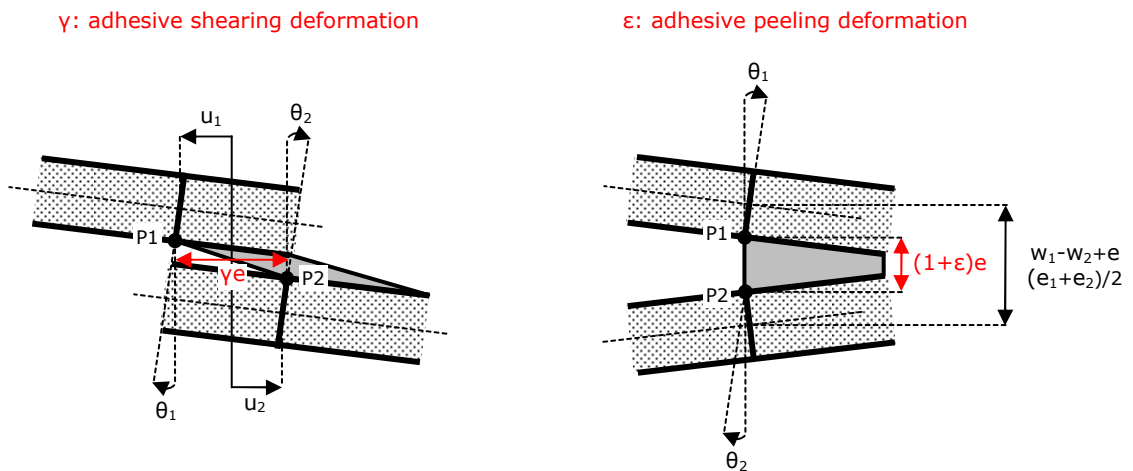


**Figure 20.** Schematic representation of the shearing and peeling adhesive deformations. The simplified 1D-beam adhesive stress analysis. Overview.  $u_j$ : Normal displacement of adherend

(j) [N].  $w_j$ : Transverse displacement of adherend (j) [N].  $\theta_j$ : Bending angle of adherend (j) [Nm].  $e_j$ : Thickness of adherend (j) [mm].  $e$ : Thickness of the adhesive layer [mm].

**Stiffness matrix of the BBe macro-element.** From equations (18) fall:

$$\begin{cases} \frac{du_j}{dx} = \frac{D_j N_j + B_j M_j}{\Delta_j} \\ \frac{d^2 w_j}{dx^2} = \frac{A_j M_j + B_j N_j}{\Delta_j} \end{cases}, j=1,2 \quad (21)$$

By combining equations (17) (18) (20) and (21), the following set of linear differential equations in terms of adhesive stresses is obtained:

$$\begin{cases} \frac{d^3 T}{dx^3} = k_1 \frac{dT}{dx} + k_2 S \\ \frac{d^4 S}{dx^4} = -k_4 S - k_3 \frac{dT}{dx} \end{cases} \quad (22)$$

where:

$$\begin{cases} k_1 = \frac{Gb}{e} \left[ \frac{D_1}{\Delta_1} \left( 1 + \frac{A_1 e_1 (e_1 + e)}{4D_1} \right) + \frac{D_2}{\Delta_2} \left( 1 + \frac{A_2 e_2 (e_2 + e)}{4D_2} \right) + \left( \frac{e_1 B_1}{\Delta_1} + \frac{e B_1}{2\Delta_1} - \frac{e_2 B_2}{\Delta_2} - \frac{e B_2}{2\Delta_2} \right) \right] \\ k_2 = \frac{Gb}{e} \left[ \frac{e_1 A_1}{2\Delta_1} - \frac{e_2 A_2}{2\Delta_2} + \left( \frac{B_1}{\Delta_1} + \frac{B_2}{\Delta_2} \right) \right] \\ k_3 = \frac{Eb}{e} \left[ \frac{(e_1 + e) A_1}{2\Delta_1} - \frac{(e_2 + e) A_2}{2\Delta_2} + \left( \frac{B_1}{\Delta_1} + \frac{B_2}{\Delta_2} \right) \right] \\ k_4 = \frac{Eb}{e} \left[ \frac{A_1}{\Delta_1} + \frac{A_2}{\Delta_2} \right] \end{cases} \quad (23)$$

By successive differentiations and linear combinations, the system of linear differential equations (22) can be uncoupled so that:

$$\begin{cases} \frac{d^6 S}{dx^6} - k_1 \frac{d^4 S}{dx^4} + k_4 \frac{d^2 S}{dx^2} + S(k_2 k_3 - k_1 k_4) = 0 \\ \frac{d}{dx} \left( \frac{d^6 T}{dx^6} - k_1 \frac{d^4 T}{dx^4} + k_4 \frac{d^2 T}{dx^2} + T(k_2 k_3 - k_1 k_4) \right) = 0 \end{cases} \quad (24)$$

So that equations (24) are solved with respect to the classical theory of homogeneous linear differential equations. The adhesive shear (peel) stresses are then expressed in the form of:

$$\begin{cases} S(x) = \left[ \begin{array}{l} \overline{K}_1 e^{sx} \sin(tx) + \overline{K}_2 e^{sx} \cos(tx) + \overline{K}_3 e^{-sx} \sin(tx) \\ + \overline{K}_4 e^{-sx} \cos(tx) + \overline{K}_5 e^{rx} + \overline{K}_6 e^{-rx} \end{array} \right] \\ T(x) = \left[ \begin{array}{l} K_1 e^{sx} \sin(tx) + K_2 e^{sx} \cos(tx) + K_3 e^{-sx} \sin(tx) \\ + K_4 e^{-sx} \cos(tx) + K_5 e^{rx} + K_6 e^{-rx} + K_7 \end{array} \right] \end{cases} \quad (25)$$

Where  $\overline{K_1} - \overline{K_6}$  and  $K_1 - K_7$  refer to integration constants that have to be determined from specified boundary conditions.

According to (Williams 1975), the given analytical expressions of the adhesive shear (peel) stress distribution(s) are unique and not depending on the material (geometrical) properties of the sandwich structure. However it appears that this statement is not entirely true, and can be completed by two additional expressions of the adhesive shear (peel) stress distribution(s) depending on the nature of the roots of the characteristic polynomial (25') (see Appendix 4).

$$P(R) = R^6 - k_1 R^4 + k_4 R^2 + (k_2 k_3 - k_1 k_4) = 0 \quad (25')$$

The determination of the stiffness matrix of BBe macro-element then requires the determination of both the nodal displacements and the nodal forces (see Fig.21). Following the resolution scheme introduced in (Hogberg 2004), the adherends displacements (forces) are finally expressed as functions of both the adhesive stresses and their respective derivatives. A comprehensive description of the adherends displacements (forces) computation is provided in (Paoissien *et al.* 2013). However it is shown that the entire problem is finally dependent on a total number of 12 integration constants only:

$${}^T \mathbf{C} = (K_1 \ K_2 \ K_3 \ K_4 \ K_5 \ K_6 \ K_7 \ J_1 \ J_2 \ J_3 \ J_5 \ J_7) \quad (26)$$

The nodal displacements (forces) are then derived from the values of each adherend displacement (force) at  $x=0$  and  $x=\Delta$  (see Fig.21). It is shown that the nodal displacement (force) are linearly dependent on the 12 integration constants, listed in  $\mathbf{C}$ , through a coupling parameter matrix  $\mathbf{M}$  ( $\mathbf{N}$ ) as:

$$\mathbf{U} = \begin{pmatrix} u_i \\ u_j \\ u_k \\ u_l \\ w_i \\ w_j \\ w_k \\ w_l \\ \theta_i \\ \theta_j \\ \theta_k \\ \theta_l \end{pmatrix} = \begin{pmatrix} u_1(0) \\ u_2(0) \\ u_1(\Delta) \\ u_2(\Delta) \\ w_1(0) \\ w_2(0) \\ w_1(\Delta) \\ w_2(\Delta) \\ \theta_1(0) \\ \theta_2(0) \\ \theta_1(\Delta) \\ \theta_2(\Delta) \end{pmatrix} = \mathbf{MC} \quad \text{and} \quad \mathbf{F} = \begin{pmatrix} Q_i \\ Q_j \\ Q_k \\ Q_l \\ R_i \\ R_j \\ R_k \\ R_l \\ S_i \\ S_j \\ S_k \\ S_l \end{pmatrix} = \begin{pmatrix} -N_1(0) \\ -N_2(0) \\ N_1(\Delta) \\ N_2(\Delta) \\ -V_1(0) \\ -V_2(0) \\ V_1(\Delta) \\ V_2(\Delta) \\ -M_1(0) \\ -M_2(0) \\ M_1(\Delta) \\ M_2(\Delta) \end{pmatrix} = \mathbf{NC} \quad (27)$$

where  $Q_m$ ,  $R_m$  and  $S_m$  ( $m=i,j,k,l$ ) respectively refer to the normal forces, shearing forces and bending moments acting onto the edges of the bonded overlap (i.e. at nodes  $i,j,k,l$ ), and where the coupling parameter matrix  $\mathbf{M}$  ( $\mathbf{N}$ ) depends on both material and geometrical properties of the overlap.

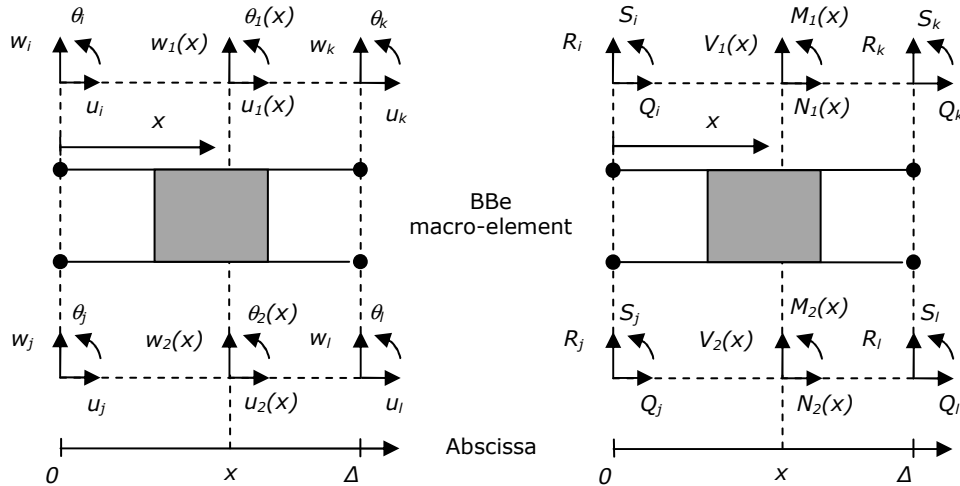


**Figure 21.** Definition of the nodal displacement (forces) acting onto the BBe macro-element. At nodes  $i, j, k$  and  $l$ . The simplified 1D-beam adhesive stress analysis. Overview.  $u_j$ : normal displacement of adherend ( $j$ ) [mm].  $w_j$ : transverse displacement of adherend ( $j$ ) [mm].  $\theta_j$ : bending angle of adherend ( $j$ ) [rad].  $N_j$ : Normal force of adherend ( $j$ ) [N].  $V_j$ : Shear force of adherend ( $j$ ).  $M_j$ : Bending moment of adherend ( $j$ ) [Nm].

In classical Finite Element (FE) theory, the coefficients of the stiffness matrix are then obtained by differentiating each component of the nodal forces by their corresponding nodal displacements:

$$\mathbf{K}_{\text{BBe}} = \begin{pmatrix} \left[ \frac{\partial Q_m}{\partial u_p} \right] & \left[ \frac{\partial Q_m}{\partial w_p} \right] & \left[ \frac{\partial Q_m}{\partial \theta_p} \right] \\ \left[ \frac{\partial R_m}{\partial u_p} \right] & \left[ \frac{\partial R_m}{\partial w_p} \right] & \left[ \frac{\partial R_m}{\partial \theta_p} \right] \\ \left[ \frac{\partial S_m}{\partial u_p} \right] & \left[ \frac{\partial S_m}{\partial w_p} \right] & \left[ \frac{\partial S_m}{\partial \theta_p} \right] \end{pmatrix}, (m, p) = (i, j, k, l) \times (i, j, k, l) \quad (28)$$

so that:

$$\mathbf{F} = \mathbf{K}_{\text{BBe}} \mathbf{U} \quad (29)$$

But, considering the expression for the vector of nodal forces ( $\mathbf{F}$ ) as a function of the vector of integration constants ( $\mathbf{C}$ ) as well as the vector  $\mathbf{C}$  as a function of the vector of nodal displacements ( $\mathbf{U}$ ), the stiffness matrix of the BBe macro-element can be computed as follows:

$$\mathbf{K}_{\text{BBe}} = \mathbf{N} \mathbf{M}^{-1} \quad (30)$$

### 2.3.3.

ormulation of the outer beam element

F

**Hypotheses.** The simplified 1D-beam adhesive stress analysis is based on the following hypotheses: (i) both adherends are assumed as behaving as linear elastic Euler-Bernoulli laminated beams in coupled tension/flexion.

**Governing differential equations.** Similarly to the bonded overlap, the local equilibrium of the outer adherends is expressed in the form of the following system of three differential equations (see Fig.22):

$$\begin{cases} \frac{dN}{dx} = 0 \\ \frac{dV}{dx} = 0 \\ \frac{dM}{dx} + V = 0 \end{cases} \quad (31)$$

where  $N$  is the normal force in adherend,  $V$  the shearing force in adherend,  $M$  the bending moment in adherend and where the adherends constitutive equations are given as:

$$\begin{cases} N = A \frac{du}{dx} - B \frac{d\theta}{dx} \\ M = -B \frac{du}{dx} + D \frac{d\theta}{dx} \\ \theta = \frac{dw}{dx} \end{cases} \quad (31') \quad \leftarrow \text{Euler-Bernoulli}$$

with  $A$  the extensional stiffness,  $B$  the coupling stiffness, and  $D$  the bending stiffness of the adherend (see Section 2.3.2).

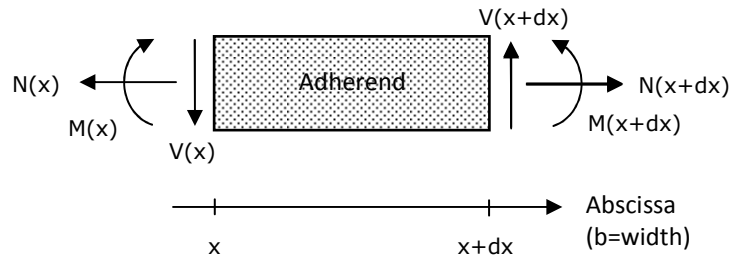


**Figure 22.** Schematic representation of the local equilibrium of the outer beam element. The simplified 1D-beam adhesive stress analysis. Overview.  $N$ : Normal force of adherend [N].  $V$ : Shear force of adherend [N].  $M$ : Bending moment of adherend [Nm].

**Stiffness matrix of the outer beam adherends.** Similarly to the solution procedure introduced in Section 2.3.2, the stiffness matrix of the outer beam adherends is derived from the resolution of the set of adherend governing differential equations (equations (31) and (31')).

Then, and by successively differentiating and combining equations (31) and (31'), it is shown that the problem is dependent on a number of 6 integration constants only:

$${}^T \mathbf{C}' = (C_1 \ C_2 \ C_3 \ C_4 \ C_6 \ C_7) \quad (32)$$

So that the solution of the problem can be expressed in the form of:

$$\begin{cases} u(x) = 3BC_1/A x^2 + C_6x + C_7 \\ w(x) = C_1x^3 + C_2x^2 + C_3x + C_4 \end{cases} \quad (33)$$

As for the BBe macro-element, the outer beam displacements (forces) are expressed as functions of both solutions presented in equation (33). The nodal displacements (forces) acting onto the edges of the outer beam element are then computed from the values of the displacements (forces) at  $x=0$  and  $x=\Delta$  (see Fig.23). As for the BBe macro-element, it can be shown that the outer adherend nodal displacements (forces) are linearly dependent on the 6 integration constants, through a new coupling parameter matrix  $\mathbf{M}'$  ( $\mathbf{N}'$ ):

$$\mathbf{U} = \begin{pmatrix} u_i \\ u_j \\ w_i \\ w_j \\ \theta_i \\ \theta_j \end{pmatrix} = \begin{pmatrix} u(0) \\ u(\Delta) \\ w(0) \\ w(\Delta) \\ \theta(0) \\ \theta(\Delta) \end{pmatrix} = \mathbf{M}'\mathbf{C}' \quad \text{and} \quad \mathbf{F} = \begin{pmatrix} Q_i \\ Q_j \\ R_i \\ R_j \\ S_i \\ S_j \end{pmatrix} = \begin{pmatrix} -N(0) \\ N(\Delta) \\ -V(0) \\ V(\Delta) \\ -M(0) \\ M(\Delta) \end{pmatrix} = \mathbf{N}'\mathbf{C}' \quad (34)$$

where  $Q_m$ ,  $R_m$  and  $S_m$  ( $m=i,j$ ) refer to the nodal normal forces, shearing forces and bending momenta acting onto the edges of the outer beam element (i.e. at nodes  $i,j$ ).

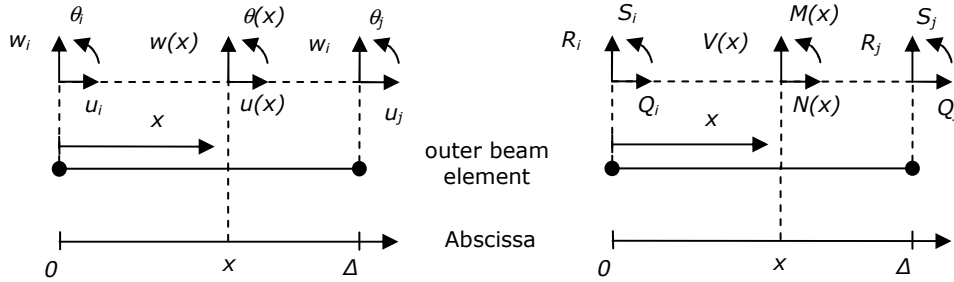


**Figure 23.** Definition of the nodal displacement (forces) acting onto the outer beam element. At nodes  $i,j$ . The simplified 1D-beam adhesive stress analysis. Overview.  $u$ : normal displacement of adherend [mm].  $w$ : transverse displacement of adherend [mm].  $\theta$ : bending angle of adherend [rad].  $N$ : Normal force of adherend [N].  $V$ : Shear force of adherend.  $M$ : Bending moment of adherend [Nm].

Finally, and considering the expression for the vector of nodal forces ( $\mathbf{F}$ ) as a function of the vector of integration constants ( $\mathbf{C}'$ ) as well as the vector  $\mathbf{C}'$  as a function of the vector of nodal displacements ( $\mathbf{U}$ ), the stiffness matrix of the outer beam element can be expressed in the form of:

$$\mathbf{K}_{\text{Beam}} = \mathbf{N}\mathbf{M}^{-1} \quad (35)$$

so that:

$$\mathbf{F} = \mathbf{K}_{\text{Beam}} \mathbf{U} \quad (36)$$

and:

$$\mathbf{K}_{\text{Beam}} = \begin{pmatrix} A_1/\Delta & -A_1/\Delta & 0 & 0 & -B_1/\Delta & B_1/\Delta \\ -A_1/\Delta & A_1/\Delta & 0 & 0 & B_1/\Delta & -B_1/\Delta \\ 0 & 0 & 12\Delta_1/A_1\Delta^3 & -12\Delta_1/A_1\Delta^3 & 6\Delta_1/A_1\Delta^2 & 6\Delta_1/A_1\Delta^2 \\ 0 & 0 & -12\Delta_1/A_1\Delta^3 & 12\Delta_1/A_1\Delta^3 & -6\Delta_1/A_1\Delta^2 & -6\Delta_1/A_1\Delta^2 \\ -B_1/\Delta & B_1/\Delta & 6\Delta_1/A_1\Delta^2 & -6\Delta_1/A_1\Delta^2 & (3\Delta_1/A_1 + D_1)/\Delta & (3\Delta_1/A_1 - D_1)/\Delta \\ B_1/\Delta & -B_1/\Delta & 6\Delta_1/A_1\Delta^2 & -6\Delta_1/A_1\Delta^2 & (3\Delta_1/A_1 - D_1)/\Delta & (3\Delta_1/A_1 + D_1)/\Delta \end{pmatrix} \quad (37)$$

2.3.4.

R

resolution procedures

**Load-based resolution procedure.** To address the distribution of adhesive stresses along the overlap, the loads are applied to the master structure in the form of defining the vector  $\mathbf{F}^{\text{pilot}}$  so that:

$$\mathbf{F}^{\text{pilot}} = \mathbf{K}\mathbf{U} \quad (38)$$

However it appears that both the stiffness matrices of the outer beam element and the BBe macro-elements are singular, so that the master stiffness matrix (i.e. assembled from both outer beam and BBe stiffness matrices) is singular too.

To override this singularity problem it is required to reduce the dimension of the mathematical problem by removing the rows and columns of the master stiffness matrix corresponding to prescribed zero displacement conditions. Where  $\mathbf{U}'$ ,  $\mathbf{K}'$  and  $\mathbf{F}'^{\text{pilot}}$  thereafter refer to the reduced form of the vector of nodal displacements, the master stiffness matrix and the vector of applied nodal forces.

Then, the linear problem is solved in the form of inverting the reduced master stiffness matrix, and computing the reduced vector of nodal displacement  $\mathbf{U}'$  as:

$$\mathbf{U}' = \mathbf{K}'^{-1} \mathbf{F}'^{\text{pilot}} \quad (39)$$

Finally, the complete vector of nodal displacements is reconstructed from the knowledge of the prescribed displacements so that we finally derive the vector of integration constants ( $\mathbf{C}$ ) from the reconstructed vector nodal displacement ( $\mathbf{U}$ ) as:

$$\mathbf{C} = \mathbf{M}^{-1} \mathbf{U} \quad (40)$$

where  $\mathbf{M}$  refers to the coupling parameter matrix defined in [Section 2.3.2](#), and  $\mathbf{U}$  to the vector resuming the 12 nodal displacements of the BBe element.

**Displacement-based resolution procedure.** In constrained mathematical optimization problems, the Lagrange's multipliers method is a technique to find the minimum (maximum) of a function whose variables are related by equality constraints.

Considering the constrained optimization problem:

$$P : \left\{ \min_{(x,y) \in V \subset \mathbb{R}^2} f(x,y), V = \{(x,y) \in \mathbb{R}^2 / g(x,y) = c, c \in \mathbb{R}\} \right\} \quad (41)$$

where both  $f$  and  $g$  have continuous first partial derivatives. The Lagrange multipliers method then suggests that if  $(x,y)$  is a minimum (maximum) of the constrained optimization problem ( $P$ ), it exists a variable  $\lambda$  such that  $(x,y,\lambda)$  is a stationary point of the Lagrange's function:

$$L(x,y,\lambda) = f(x,y) + \lambda(g(x,y) - c) \quad (42)$$

Classically, in structural mechanics, the function to minimize is the total potential energy, the variables the nodal Degrees of Freedom (DOFs) of the structure and the equality constraints expressed in the form of:

$$\mathbf{B}\mathbf{U} = \mathbf{U}^{\text{pilot}} \quad (43)$$

where  $\mathbf{U}$  is the vector of nodal DOFs of the structure,  $\mathbf{B}$  a  $n \times p$  coupling parameter matrix and  $\mathbf{U}^{\text{pilot}}$  the set of  $p$  constrained displacements (i.e. not necessarily equal to zero).

Due to its FE like formulation, the mathematical problem derived for the resolution of the joint equilibrium equations (see [Section 2.3.2](#)) take the form of finding the solution  $\mathbf{U}$  so that:

$$\mathbf{F} = \mathbf{K}\mathbf{U} \quad (44)$$

where  $\mathbf{F}$  is the vector of applied nodal forces,  $\mathbf{U}$  the vector of nodal displacements and  $\mathbf{K}$  the specifically formulated stiffness matrix of the entire structure (i.e. the master stiffness matrix).

Which appears to be the differential form of the minimization problem:

$$P : \left\{ \min_{\mathbf{U} \in V \subset \mathbb{R}^n} Q(\mathbf{U}) = \frac{1}{2} \mathbf{U} \mathbf{K} \mathbf{U}^{-\text{T}} \mathbf{U} \mathbf{F}, V = \{\mathbf{U} \in \mathbb{R}^n / \mathbf{B}\mathbf{U} = \mathbf{U}^{\text{pilot}}, \mathbf{U}^{\text{pilot}} \in \mathbb{R}^p\} \right\} \quad (45)$$

with  $n$  the number of nodal DOFs of the assembled structure,  $p$  the number of kinematic constraints and  $Q(\mathbf{U})$  the quadratic form associated to equation (44).  $Q(\mathbf{U})$  can remind the traditional expression associated to the total potential energy in structure mechanics. However it is important to keep in mind that the expression of the master stiffness matrix  $\mathbf{K}$  (see [Section 2.3.2](#)) does not fall from the minimization of the total potential energy, but from the direct resolution of the joint equilibrium equations. Indeed, the total potential energy associated to the structure is never defined or used within the formulation of both the BBe and the outer beam elements (see [Section 2.3.2](#)). The simplified 1D-beam adhesive stress analysis then simply takes advantage from its FE like formulation.

The basic idea of Lagrange's multipliers method then consists in introducing  $p$  new undetermined parameters  $\lambda_i$  ( $i=1\dots p$ ):

$${}^T\boldsymbol{\lambda} = (\lambda_1 \quad \lambda_2 \quad \dots \quad \lambda_p) \quad (46)$$

so that  $(\mathbf{U}, \boldsymbol{\lambda})$  the solution of the *augmented* minimization problem:

$$P : \left\{ \min_{\mathbf{U} \in \mathbb{R}^n, \boldsymbol{\lambda} \in \mathbb{R}^p} L(\mathbf{U}, \boldsymbol{\lambda}) = Q(\mathbf{U}) + {}^T(\mathbf{B}\mathbf{U} - \mathbf{U}^{\text{pilot}}) \boldsymbol{\lambda} \right\} \quad (47)$$

which can be rewritten as:

$$\frac{\partial L}{\partial \mathbf{U}} = \mathbf{K}\mathbf{U} - \mathbf{F} + {}^T\mathbf{B}\boldsymbol{\lambda} = \mathbf{0} \quad \frac{\partial L}{\partial \boldsymbol{\lambda}} = \mathbf{B}\mathbf{U} - \mathbf{U}^{\text{pilot}} = \mathbf{0} \quad (48)$$

Or:

$$\begin{cases} \mathbf{K}\mathbf{U} + {}^T\mathbf{B}\boldsymbol{\lambda} = \mathbf{F} \\ \mathbf{B}\mathbf{U} + \mathbf{0} = \mathbf{U}^{\text{pilot}} \end{cases} \quad (49)$$

So that the initial linear problem  $\mathbf{K}=\mathbf{K}\mathbf{U}$  with  $\mathbf{B}\mathbf{U}=\mathbf{U}^{\text{pilot}}$  can be rewritten in the form of the *augmented* linear problem:

$$\mathbf{F}^L = \mathbf{K}^L \mathbf{U}^L \quad (50)$$

$$\mathbf{U}^L = \mathbf{K}^{L,-1} \mathbf{F}^L \quad (51)$$

where:

$$\mathbf{K}^L = \begin{pmatrix} \mathbf{K} & {}^T\mathbf{B} \\ \mathbf{B} & \mathbf{0} \end{pmatrix} \quad (52)$$

$${}^T\mathbf{U}^L = ({}^T\mathbf{U} \quad {}^T\boldsymbol{\lambda}) \quad (53)$$

and:

$${}^T\mathbf{F}^L = ({}^T\mathbf{F} \quad {}^T\mathbf{U}^{\text{pilot}}) \quad (54)$$

Similarly to load-based resolution procedures, the vector of integration constants ( $\mathbf{C}$ ) is finally derived from the vector nodal displacement ( $\mathbf{U}$ ) as:

$$\mathbf{C} = \mathbf{M}^{-1} \mathbf{U} \quad (55)$$

where  $\mathbf{M}$  refers to the coupling parameter matrix defined in [Section 2.3.2](#), and  $\mathbf{U}$  to the vector resuming the nodal displacements of the BBe element.

### 2.3.5.

omparison with existing sandwich type analyses

C

As mentioned in [Section 2.1](#), a large number of simplified approaches for the stress analysis of adhesively bonded joints can be found in the open literature ([Volkersen 1938](#), [Goland & Reissner 1944](#), [Hart-Smith 1973](#), [Williams 1975](#), [Bigwood & Crocombe 1991](#), [Hogberg 2004](#), [Weissgraeber 2014](#)). Those analyses are generally referred as sandwich-type analyses, and allow for the resolution of the set of governing differential equations from the knowledge of both the forces acting onto the edges of the bonded overlap and the material (geometrical) properties of the joint. Most of these analyses apply to linear elastic solicitations of both the adherends and the adhesive layer only. Here is presented a comparison between the presented simplified 1D-beam adhesive stress analysis and the most recent Weissgraeber's sandwich type analysis. The comparison is performed on one of the most common adhesive joint configuration that can be found in practice, the SLJ. The SLJ has the advantage of involving both shear and peel of the adhesive layer in a simple geometrical configuration.

In [Fig.25](#) is presented a comparison between the simplified 1D-beam adhesive stress analysis and the most recent Weissgraeber's sandwich-type analysis. The comparison is made in terms of both adhesive shear stress (a) and peel stress (b) distributions along the overlap. The comparison is performed in the case of linear elastic adhesive (adherends) loadings. The geometry of the specimen is balanced (i.e. symmetric upper/lower adherends). The effect of the adhesive thickness on the load path eccentricity is accounted. The overlap is meshed using a unique 4-nodes BBe element. The loads acting onto the edges of the bonded overlap are computed in advance of the analysis and directly applied to the sandwich structure. The overall geometry as well as the adhesive (adherends) material properties are given in [Fig.24](#). To allow for the comparison of comparable results, the extensional and bending stiffnesses of the macro-element are computed from the plane-stress adherends Young's moduli as follows:

$$E_j^* = E_j / (1 - \nu_j^2) \quad (56)$$

where  $E_j$  and  $\nu_j$  respectively refer to the Young's modulus and the Poisson's ratio of adherends  $j$  ( $j=1,2$ ) determined from bulk material properties.

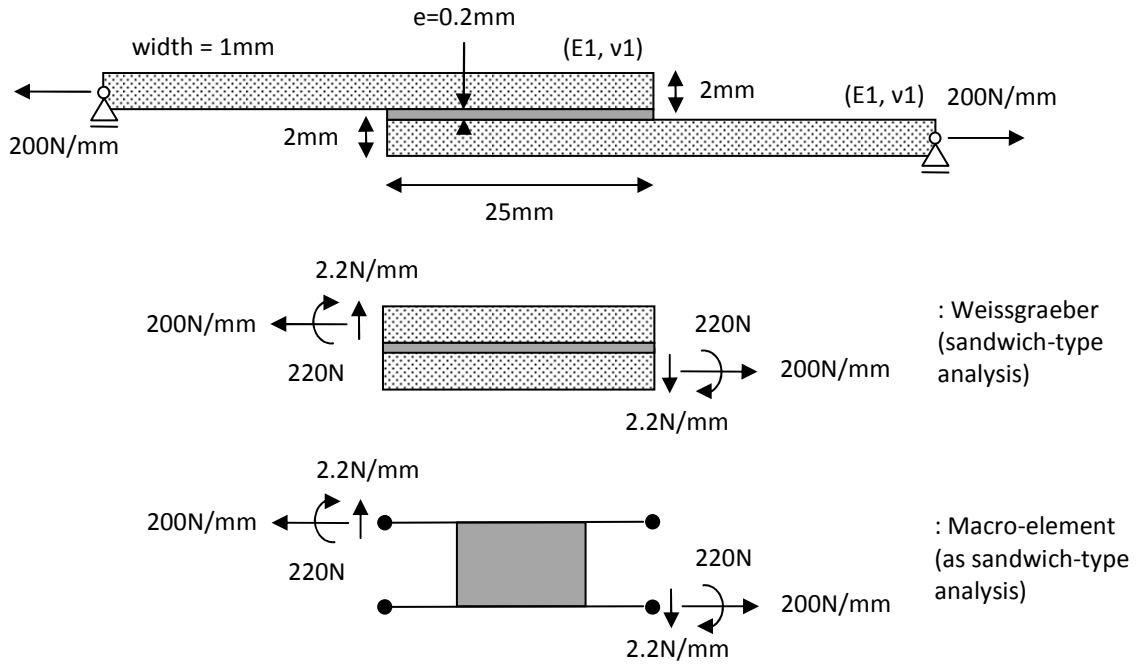
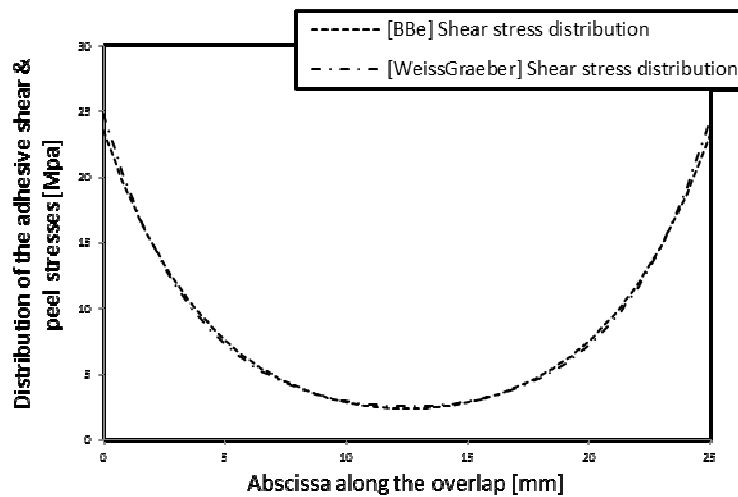


**Figure 24.** Schematic representation of the Single-Lap Joint (SLJ) test configuration. Loads acting onto the sandwich edges. Comparison with existing sandwich-type analyses. Simplified 1D-beam stress analysis versus Weissgraeber's sandwich type analysis.  $e_1$ : Thickness of the upper/lower adherend.  $P$ : applied load ( $=5000\text{N}/20\text{mm}$ ).  $E_1$ : Young's modulus of the upper/lower adherend ( $=72400\text{ MPa}$ ).  $\nu_1$ : Poisson's ratio of the upper/lower adherend ( $=0.33$ ).  $e$ : Thickness of the adhesive layer [mm].  $E$ : Peel modulus of the adhesive layer ( $=185\text{MPa}$ ).  $G$ : Shear modulus of the adhesive layer ( $=65\text{MPa}$ ).



(a)

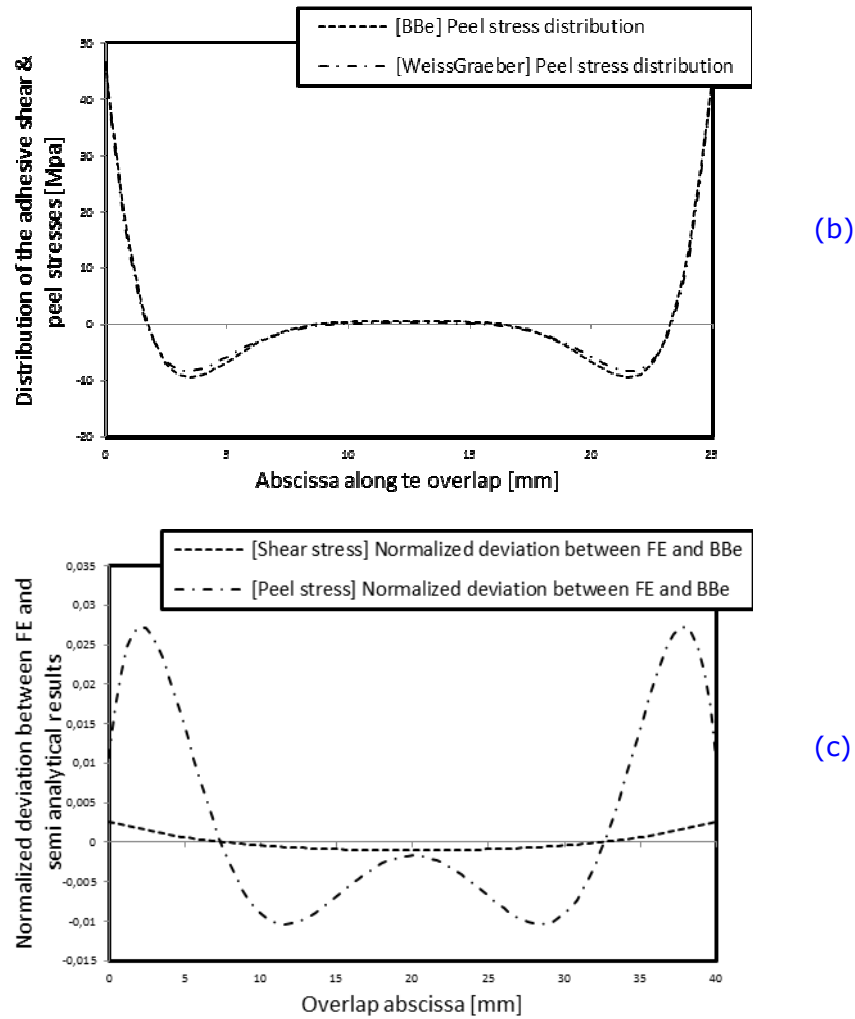


Figure 25. Comparison of the predicted adhesive shear (a) and peel (b) stress distributions along the overlap. Normalized deviation between FE and semi analytical results (c). Single-Lap Joint (SLJ) configuration. Comparison with existing sandwich type analyses. Simplified 1D-beam stress analysis versus Weissgraeber’s sandwich type analysis.

It is shown from Fig.25 that even if in close agreement, the results obtained from the simplified 1D-beam adhesive stress analysis and those obtained from the Weissgraeber’s sandwich type theory are not exactly equivalent. These differences between the two models come from the less restrictive hypotheses of the Weissgraeber’s theory. Indeed, in his original theory, Weissgraeber did not limited the behavior of the bonded adherends to the classical Kirchhoff-Love assumptions and included the effect of the possible rotation between the cross-section and the bending line (i.e. leading to the addition of a second order derivative of the adhesive peel stress in (6a) and (6b)).

However, due to its sandwich-type formulation, the Weissgraeber’s model is limited by the need to evaluate the forces acting onto the overlap edges in advance of the sandwich analysis. It then requires simplifying the overall joint behavior to allow for the a priori evaluation of the forces acting onto the edges of the sandwich structure. In the simplified 1D-Beam adhesive stress analysis, the outer adherends are presumed as behaving as classical Euler-Bernoulli beams (i.e. leading to the formulation of a specific outer beam element (see Section 2.3.3)).

The resolution of the governing differential equations is then ensured by solving equation  $F=KU$ , where  $F$  is the vector of nodal forces,  $U$  the vector of nodal displacements, and  $K$  the specifically formulated master stiffness matrix of the structure. The forces acting onto the edges of the overlap have then not to be evaluated in advance of the simplified 1D-beam adhesive stress analysis, but lie from the resolution procedure itself. It then allows for the modeling of various combinations of BBe and outer beam elements with great simplicity (see Fig.18). However, and since the less restrictive hypotheses of the Weissgraeber's theory simply lead to the addition of a second order derivative of the adhesive peel stress in (6a) and (6b), a dedicated BBe macro-element could be easily developed on the basis of Weissgraeber's equilibrium equations. However the guiding equations required for the development of this dedicated higher-order BBe macro-element are not provided within the present manuscript.

### 2.3.6.

C

#### omparison with Finite-Element (FE) analyses

As presented in Chapter 1, the FE method is a computational method which allows for the approximate solution of various engineering problems to be assessed. The stress analysis of adhesively bonded joints is one of these problems. Although this general procedure is computationally expensive and can lead to numerical convergence issues (i.e. the mesh of adhesive layers has to be intensively refined to capture the local stress gradient at bondline edges), the FE method allows for the study of various joint configurations (e.g. various adherends geometries, various adhesive geometries, various loading conditions, etc.).

In Fig.27 is presented a comparison in terms of adhesive peel stress (b) and shear stress (c) distributions between the results obtained from the simplified 1D-beam adhesive stress analysis and those of 2D Finite Element Analyses (FEA) involving cohesive interface elements. The comparison is performed in the case of linear elastic loadings of both the adhesive and the adherends and applies to SLJ configurations only. The adhesive bondline is modelled using cohesive interface elements and both adherends meshed using classical 2D plane-stress elements. The specimen geometry as well as the adhesive (adherends) material properties are given in Fig.26. Similarly to Section 2.3.5, and to account for the apparent stiffness of the 2D plane-stress elements, the extensional and bending stiffnesses of the macro-element are computed from the plane-stress adherends Young's moduli as provided in equation (56).

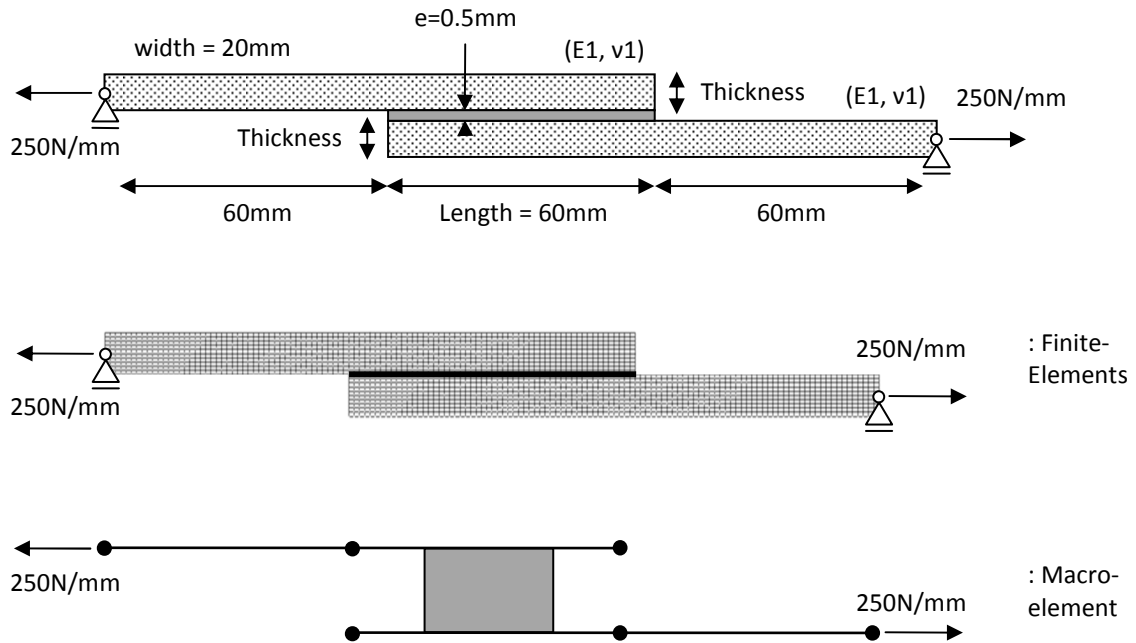
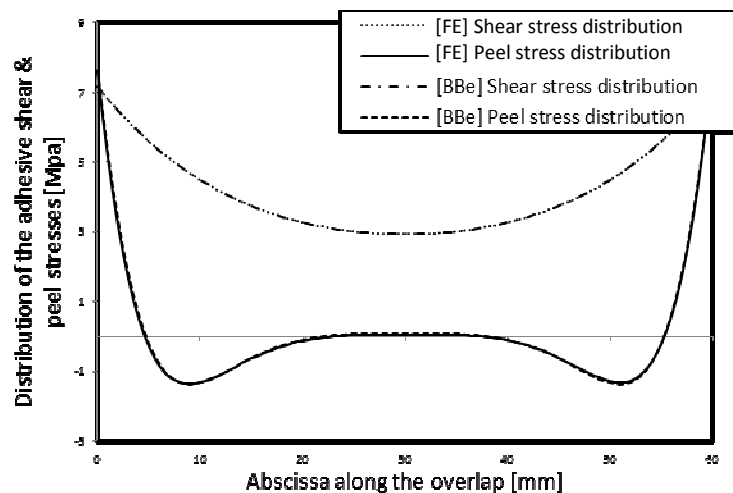


**Figure 26.** Schematic representation of the Single-Lap Joint (SLJ) test configuration. Comparison with Finite Element (FE) analyses. Simplified 1D-beam stress analysis versus Finite Element (FE) analyses.  $e_1$ : Thickness of the upper/lower adherend.  $P$ : applied load ( $=5000\text{N}/20\text{mm}$ ).  $E_1$ : Young's modulus of the upper/lower adherend ( $=72400\text{ MPa}$ ).  $\nu_1$ : Poisson's ratio of the upper/lower adherend ( $=0.33$ ).  $e$ : Thickness of the adhesive layer [mm].  $E$ : Peel modulus of the adhesive layer ( $=185\text{MPa}$ ).  $G$ : Shear modulus of the adhesive layer ( $=65\text{MPa}$ ).



(a)

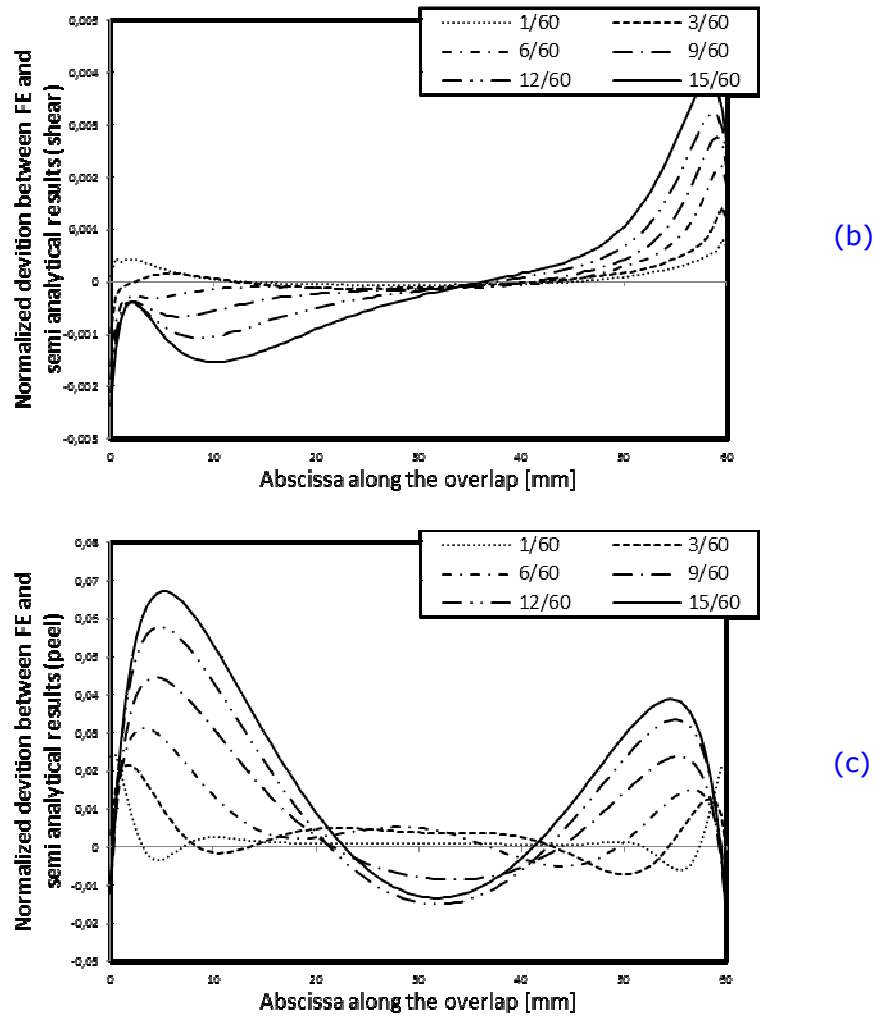


Figure 27. Comparison of the predicted adhesive shear and peel (a) stress distributions along the overlap. Adherends thickness = 3mm. Normalized deviation between Finite Element (FE) and semi-analytical shear (b) and peel (c) stress distributions for various adherends thickness/length ratios. Single-Lap Joint (SLJ) configuration. Comparison with Finite Element (FE) analyses. Simplified 1D-beam stress analysis versus Finite Element (FE) analyses.

It is seen from Fig.27 that the results of the simplified 1D-beam adhesive stress analysis are in close agreement with those of 2D FE analyses for various adherends thickness/length ratios (e.g. 1/60, 3/60, 6/60, 9/60, 12/60 and 15/60). However it is also seen that the normalized deviation between the simplified 1D-beam adhesive stress analysis and the 2D FE analyses increases for increasing adherends thickness/length ratios. This increasing deviation comes from two reasons. First, in the linear elastic 1D-beam analysis the adherends kinematics is simplified so that it is relevant to the classical Euler-Bernoulli beam theory. However, the classical Euler-Bernoulli beam theory applies to the mechanical response of beams that exhibit small enough thickness/length ratios (i.e. typically above 1/10). The increasing simulated adherends thickness/length ratios then progressively put into question the legitimacy of such simplified kinematics in the modelling of the overall joint response. A possible solution to overcome this limitation could be to consider higher-order beam theory.

## 2.4.

I

## Introduction of adhesive material nonlinearities

The effective adhesive stress-strain relationship has been shown as a critical parameter involved in the ruin of adhesively bonded joints ([Hart-Smith 1973a](#), [Hart-Smith 1973b](#), [Lachaud 2009](#), [Crocombe \*et al.\* 2009](#), [Paroissien \*et al.\* 2013](#)). Since simple linear elastic adhesive stress analyses are not able to address the complete behavior of such structures, an effort has been made on the introduction of nonlinear adhesive material behaviors to the simplified 1D-beam adhesive stress analysis.

This section is then dedicated to the development of a generic procedure that allow for various adhesive material nonlinearities to be introduced in the particular formulation of the simplified 1D-beam adhesive stress analysis. The suggested procedure is partly inspired by the CZM theory. A particular emphasis has been voluntarily given to the modeling of bilinear adhesive stress-strain evolution laws. However the given procedure is not limited to these particular behaviors only and has been successfully applied to various other shapes of adhesive stress-strain relationships (see [Chapter 3](#)). The proposed adhesive material models are formulated under a two dimensional mixed-mode model that account for the possible interaction (interdependency) between both pure mode I and pure mode II adhesive stress-strain relationships. For convenience, the adhesive stress-strain relationships will be thereafter referred as the adhesive traction separation laws. However it does not limit the following procedure to damaging behavior only.

## 2.4.1.

D

## Description of the interface models

**Description of the pure mode interface models.** As presented in [Chapter 1](#), in CZM the description of the damage along an interface results from the definition of the interface pure mode traction-separation laws. These pure mode traction-separation laws resume both the evolution of the interface traction load as a function of the corresponding interface displacement jump (or deformation) and the criterion met to propagate the cohesive process zone (see [Fig.28](#)).

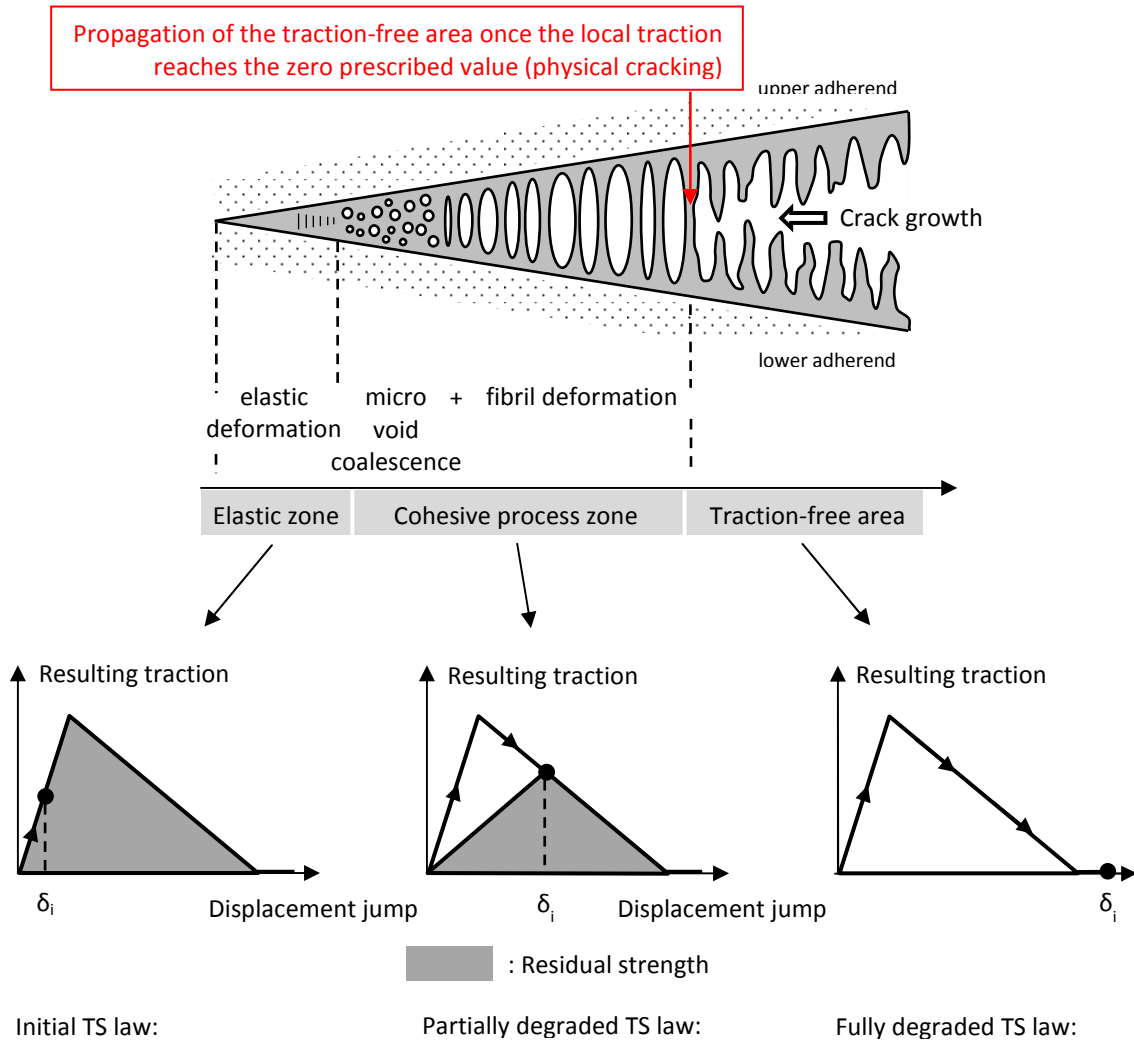
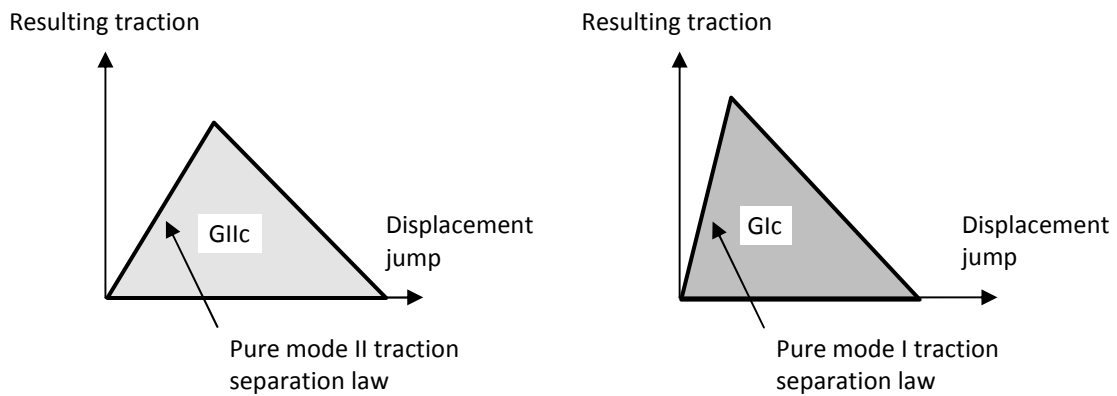


**Figure 28.** Schematic representation of the cohesive traction separation laws. Description of the cohesive process zone. Description of the pure mode interface models. Introduction of adhesive material nonlinearities.

In the case of pure mode solicitations, the local response of the interface results from the related pure mode traction-separation law only. However, in the case of mixed-mode loading (i.e. combining both shearing and through-thickness deformations of the adhesive layer) the local response of the interface results from the interaction (combination) of both the traction separation laws in pure mode I and pure mode II (see Fig.29).

Description of the interface pure mode TS laws:



Combination of the interface pure mode TS laws:

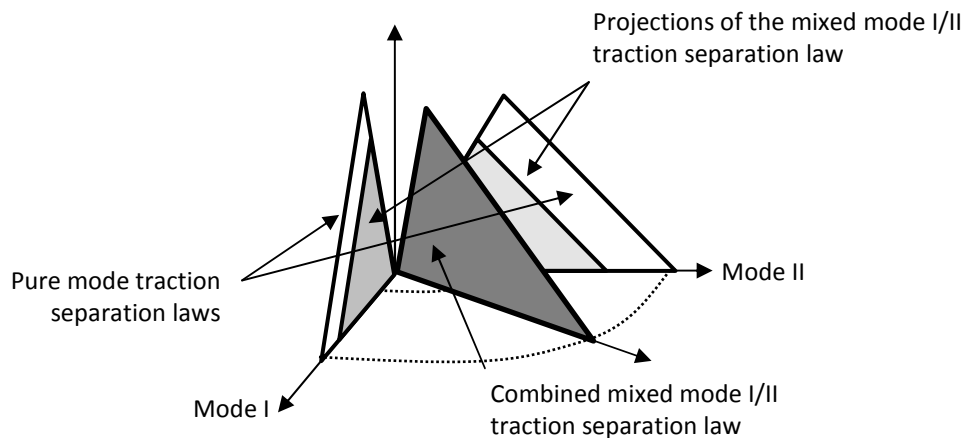


**Figure 29.** Schematic representation of the interaction between the pure mode cohesive traction separation laws in the case of mixed mode adhesive solicitations.  $G_{Ic}$  the fracture energy in pure mode I.  $G_{IIc}$  the fracture energy in pure mode II. Description of the mixed mode interface models. Introduction of adhesive material nonlinearities.

### Description of the mixed-mode I/II interface model.

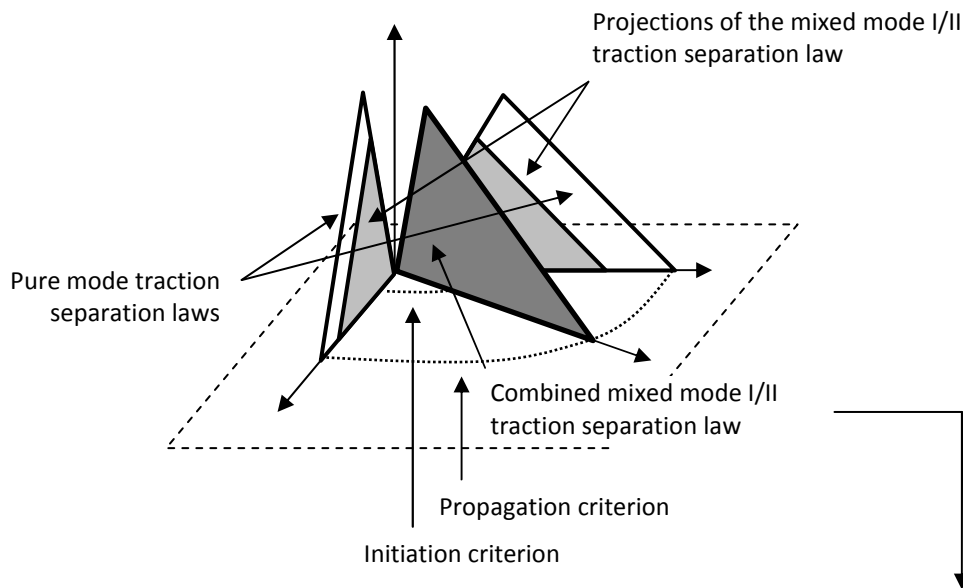
*Description of the mixed-mode I/II guidance parameters.* As presented in [Chapter 1](#), the description of the damage along an interface relies upon the definition of the related pure mode traction-separation laws. These pure mode traction-separation laws resume both the evolution of the adhesive surface traction load and the corresponding interface displacement (or deformation) and the criterion met to propagate the cohesive process zone (see [Fig.28](#)).

Because of the 1D-beam foundation of the linear elastic system of governing differential equations, it is necessary to account for the possible interaction of the two pure mode traction separation laws. To account for this possible interaction, two mixed-mode guidance parameters are defined:

$$\begin{cases} \beta = \frac{\delta_{II}}{\delta_I} \\ \delta_m = \sqrt{\delta_I^2 + \delta_{II}^2} \end{cases} \quad (57)$$

where  $\beta$ ,  $\delta_I$ ,  $\delta_{II}$ ,  $\delta_m$ , respectively refer to the mixed-mode ratio, the pure mode I (peel) deformation, the pure mode II (shear) deformation and the mixed-mode equivalent deformation of the interface. A schematic representation of those parameters is given in Fig.30.

Combination of the interface pure mode TS laws:



Evolution of the mixed-mode guidance parameters:

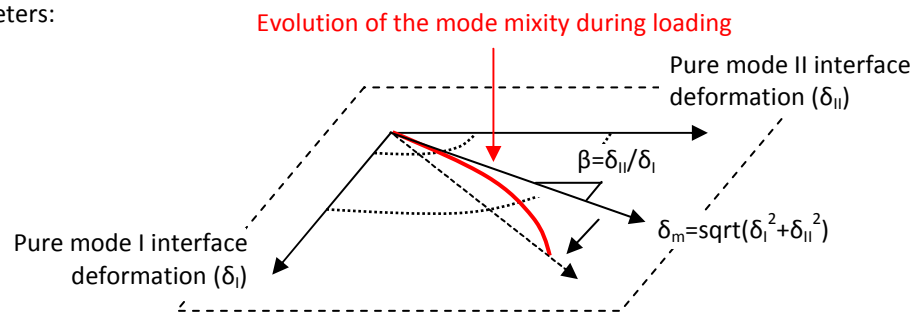


Figure 30. Schematic representation of the mixed-mode guidance parameters. Description of the mixed mode interface models. Introduction of adhesive material nonlinearities.

*Combination of the pure mode interface models.* The basic idea of mixed-mode modeling is then to combine the interface pure mode traction-separation laws through both initiation and propagation criteria (see Fig.29 and Fig.30). The effective properties of the adhesive layer (i.e. the projections of the mixed mode traction separation law) are then computed with respect to both the local mixed-mode ratio and the corresponding initiation (propagation)

criteria. Numbers of these initiation (propagation) criteria can be found in the open literature (see [Tab.1](#)).

**Tab 1.** Examples of initiation (propagation) mixed-mode criteria. Description of the mixed-mode interface model. Combination of the pure mode adhesive behaviors. Introduction of adhesive material nonlinearities.

Power law criterion (Reeder 1992, Anyfantis 2012)	Polynomial law criterion (Reeder 1992)
$\left(\frac{G_I^m}{G_I}\right)^k + \left(\frac{G_{II}^m}{G_{II}}\right)^n = 1$	$G_T - (G_I^m + G_{II}^m) + \rho \left(\frac{G_{II}^m}{G_I^m}\right) + \tau \left(\frac{G_{II}^m}{G_I^m}\right)^2 = 0$
Interaction criterion (Reeder 1992)	Benzeggagh-Kenane criterion (Reeder 1992, Kenane 1997)
$\left(\frac{G_I^m}{G_I} - 1\right) \left(\frac{G_{II}^m}{G_{II}} - 1\right) - \kappa \left(\frac{G_I^m}{G_I}\right) \left(\frac{G_{II}^m}{G_{II}}\right) = 0$	$G_T (G_{II} - G_I) \left(\frac{G_{II}^m}{G_I^m + G_{II}^m}\right)^\eta - (G_I^m + G_{II}^m) = 0$
Exponential $K_I/K_{II}$ criterion (Reeder 1992)	$G_T$ criterion (Reeder 1992)
$G_I^m + G_{II}^m = (G_{II} - G_I) e^{\eta \sqrt{G_I^m / G_{II}^m}} + G_I$	$G_I^m + G_{II}^m = G_I = G_{II} = G_T$

The list of criteria provided in [Tab.1](#) is not exhaustive. The first remark that can be made is that most of these initiation (propagation) criteria reveal the need of defining both initiation and propagation energies associated to the transition of a phase to another. For simplification purpose, the power law criterion ( $k=n$ ) will be thereafter considered only. However the following procedure is not limited to this particular criterion only.

*Analytical projection of the mixed-mode I/II interface model in the case of bilinear pure mode traction separation laws.* To allow for the combination of these pure mode traction separation laws, both initiation and propagation fracture energies are then required. The initiation and propagation energies are then defined as:

$$G_{i,0} = \int_0^{\delta_{i,0}} \sigma_i(\delta_i) d\delta_i, \quad i = I, II \quad (58)$$

$$G_{i,C} = \int_0^{\delta_{i,C}} \sigma_i(\delta_i) d\delta_i, \quad i = I, II \quad (59)$$

Where  $G_{i,0}$  and  $G_{i,C}$  respectively refer to the pure mode  $i$  ( $i=I,II$ ) energies accumulated at initiation and propagation of the cohesive process zone,  $\delta_i$  to the pure mode  $i$  ( $i=I,II$ ) interface deformation and  $\sigma_i(\delta_i)$  to the interface traction load resulting from  $\delta_i$ .

It is seen from equations (58) and (59) that the estimation of the pure mode initiation and propagation fracture energies then requires a mathematical description of the pure mode traction separation laws. The bilinear traction separation law is a well-established interface behavior that assumes first a linearly increasing relationship between the interface

displacement jump (or deformation) and the resulting interface traction load. Then, the damage initiation is described by a linear traction softening behavior. Finally, the propagation of the damage is modeled by virtually setting the resulting traction to zero, hence modeling the creation of two traction-free surfaces (physical cracking) (see Fig.31).

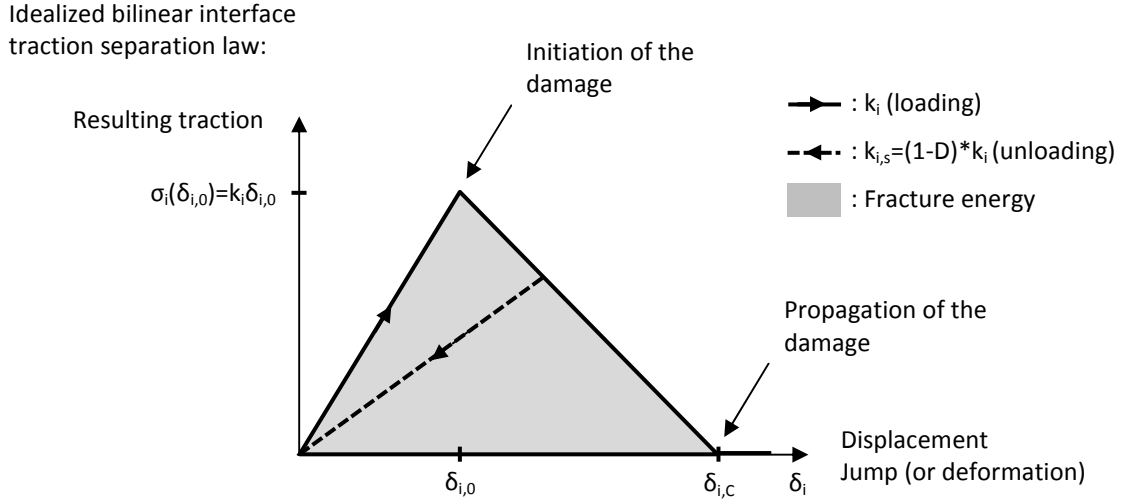


**Figure 31.** Representation of an idealized bilinear interface traction separation law. Description of the mixed-mode interface model. Analytical projection of the mixed-mode interface model in the case of bilinear pure mode traction separation laws. Introduction of adhesive material nonlinearities.

In the case of bilinear pure mode traction separation laws, the evolution of the interface traction load can then be described mathematically as (see Fig.31):

$$\sigma_i(\delta_i) = k_i \delta_i \text{ for } \delta_i \in [0, \delta_{i,0}], i = I, II \quad (60)$$

$$\sigma_i(\delta_i) = \frac{k_i \delta_{i,0} (\delta_{i,C} - \delta_i)}{\delta_{i,C} - \delta_{i,0}} \text{ for } \delta_i \in [\delta_{i,0}, \delta_{i,C}], i = I, II \quad (61)$$

$$\sigma_i(\delta_i) = 0 \text{ for } \delta_i \in [\delta_{i,C}, +\infty], i = I, II \quad (62)$$

With  $k_i$  the initial stiffness of the interface in pure mode  $i$  ( $i=I/II$ ), and where the evolution of the damage of the interface is characterized by the damage variable ( $D$ ) as follows (see Fig.31):

$$D(\delta_i) = 0 \text{ for } \delta_i \in [0, \delta_{i,0}], i = I, II \quad (63)$$

$$D(\delta_i) = \frac{\delta_{i,C} (\delta_i - \delta_{i,C})}{\delta_i (\delta_{i,C} - \delta_{i,0})} \text{ for } \delta_i \in [\delta_{i,0}, \delta_{i,C}], i = I, II \quad (64)$$

$$D(\delta_i) = 1 \text{ for } \delta_i \in [\delta_{i,C}, +\infty], i = I, II \quad (65)$$

Then, the total amount of energy consumed to initiate the damage in pure mode  $i$  ( $i=I/II$ ) can be expressed in the form of:

$$G_{i,0} = \int_0^{\delta_{i,0}} \sigma_i(\delta_i) d\delta_i = \int_0^{\delta_{i,0}} k_i \delta_i d\delta_i = \frac{1}{2} k_i \delta_{i,0}^2, \quad i = I, II \quad (66)$$

And the total amount of energy consumed to physically crack the interface in pure mode  $i$  ( $i=I/II$ ) in the form of:

$$G_{i,c} = \int_0^{\delta_{i,c}} \sigma_i(\delta_i) d\delta_i = \int_0^{\delta_{i,0}} \sigma_i(\delta_i) d\delta_i + \int_{\delta_{i,0}}^{\delta_{i,c}} \sigma_i(\delta_i) d\delta_i = \frac{1}{2} k_i \delta_{i,0} \delta_{i,c}, \quad i = I, II \quad (67)$$

Where  $\delta_{i,0}$  and  $\delta_{i,c}$  respectively refer to the initiation and propagation thresholds of the interface when subjected to pure mode  $i$  ( $i=I/II$ ) interface solicitations.

Assuming the shape of the projected traction separation laws as agreeing the initial pure mode traction separation laws, the expression of the mixed-mode I/II initiation and propagation fracture energies can be directly derived from equations (66) and (67) by adding the superscript  $m$ , so that:

$$G_{i,0}^m = \int_0^{\delta_{i,0}^m} \sigma_i(\delta_i) d\delta_i = \frac{1}{2} k_i \delta_{i,0}^{m2}, \quad i = I, II \quad (68)$$

$$G_{i,c}^m = \int_0^{\delta_{i,c}^m} \sigma_i(\delta_i) d\delta_i = \frac{1}{2} k_i \delta_{i,0}^m \delta_{i,c}^m, \quad i = I, II \quad (69)$$

Where  $\delta_{i,0}^m$  and  $\delta_{i,c}^m$  respectively refer to the projected initiation and propagation thresholds of the interface when subjected to mixed-mode I/II interface solicitations.

Then, assuming a damage initiation criterion taking the form of a power law criterion ( $k=n$ ) gives:

$$\left( \frac{G_{I,0}^m}{G_{I,0}} \right)^n + \left( \frac{G_{II,0}^m}{G_{II,0}} \right)^n = 1 \quad (70)$$

Which can be expressed in terms of the interface initiation thresholds, as follows:

$$\left( \frac{\delta_{I,0}^{m2}}{\delta_{I,0}^2} \right)^n + \left( \frac{\delta_{II,0}^{m2}}{\delta_{II,0}^2} \right)^n = 1 \quad (71)$$

$$\left( \frac{\delta_{I,0}^{m2}}{\delta_{I,0}^2} \right)^n + \left( \frac{\beta^2 \delta_{I,0}^{m2}}{\delta_{II,0}^2} \right)^n = 1 \quad (72)$$

$$\left( \frac{1}{\delta_{I,0}^{2n}} + \frac{\beta^{2n}}{\delta_{II,0}^{2n}} \right) \delta_{I,0}^{m2n} = 1 \quad (73)$$

where:

$$\delta_{I,0}^m = \frac{\delta_{I,0} \delta_{II,0}}{\sqrt[2n]{\delta_{II,0}^{2n} + \beta^{2n} \delta_{I,0}^{2n}}} \quad (74)$$

$$\delta_{II,0}^m = \beta \delta_{I,0}^m = \frac{\beta \delta_{I,0} \delta_{II,0}}{\sqrt[2n]{\delta_{II,0}^{2n} + \beta^{2n} \delta_{I,0}^{2n}}} \quad (75)$$

$$\delta_{m,0} = \sqrt{\delta_{I,0}^{m^2} + \delta_{II,0}^{m^2}} = \frac{\delta_{I,0} \delta_{II,0} \sqrt{1 + \beta^2}}{\sqrt[2n]{\delta_{II,0}^{2n} + \beta^{2n} \delta_{I,0}^{2n}}} \quad (76)$$

Finally, assuming a damage propagation criterion taking the form of a power law criterion (k=n) gives:

$$\left( \frac{G_{I,C}^m}{G_{I,C}} \right)^n + \left( \frac{G_{II,C}^m}{G_{II,C}} \right)^n = 1 \quad (77)$$

Which can be expressed in terms of both the interface initiation and propagation thresholds so that:

$$\left( \frac{\delta_{I,0}^m \delta_{I,C}^m}{\delta_{I,0} \delta_{I,C}} \right)^n + \left( \frac{\delta_{II,0}^m \delta_{II,C}^m}{\delta_{II,0} \delta_{II,C}} \right)^n = 1 \quad (78)$$

$$\left( \frac{\delta_{I,0}^m \delta_{I,C}^m}{\delta_{I,0} \delta_{I,C}} \right)^n + \left( \frac{\delta_{II,0}^m \beta \delta_{I,C}^m}{\delta_{II,0} \delta_{II,C}} \right)^n = 1 \quad (79)$$

$$\left( \frac{\delta_{I,0}^{m^n} \delta_{I,C}^{m^n}}{\delta_{I,0}^n \delta_{I,C}^n} + \frac{\beta^n \delta_{II,0}^{m^n} \delta_{II,C}^{m^n}}{\delta_{II,0}^n \delta_{II,C}^n} \right) \delta_{I,C}^{m^n} = 1 \quad (80)$$

where:

$$\delta_{I,C}^m = \frac{\delta_{I,0} \delta_{I,C} \delta_{II,0} \delta_{II,C}}{\sqrt[n]{\delta_{I,0}^{m^n} \delta_{II,0}^n \delta_{II,C}^n + \beta^n \delta_{II,0}^{m^n} \delta_{I,0}^n \delta_{I,C}^n}} \quad (81)$$

$$\delta_{II,C}^m = \beta \delta_{I,C}^m = \frac{\beta \delta_{I,0} \delta_{I,C} \delta_{II,0} \delta_{II,C}}{\sqrt[n]{\delta_{I,0}^{m^n} \delta_{II,0}^n \delta_{II,C}^n + \beta^n \delta_{II,0}^{m^n} \delta_{I,0}^n \delta_{I,C}^n}} \quad (82)$$

$$\delta_{m,C} = \sqrt{\delta_{I,C}^{m^2} + \delta_{II,C}^{m^2}} = \frac{\delta_{I,0} \delta_{I,C} \delta_{II,0} \delta_{II,C} \sqrt{1 + \beta^2}}{\sqrt[n]{\delta_{I,0}^{m^n} \delta_{II,0}^n \delta_{II,C}^n + \beta^n \delta_{II,0}^{m^n} \delta_{I,0}^n \delta_{I,C}^n}} \quad (83)$$

*Projection of the mixed-mode I/II interface model using numerical procedures.* As presented in the previous subsection, and considering the projected elastic and fracture energies ( $G_{i,0}$ ,  $G_{i,C}$ ) as functions of the effective pure mode traction separation thresholds ( $\delta_{i,0}$ ,  $\delta_{i,C}$ ), both initiation and propagation criteria can be expressed in the form of:

$$F(\delta_{i,0}^m, \delta_{i,C}^m, \delta_{i,0}, \delta_{i,C}, \beta) = 0 \quad , i = I, II \quad (84)$$

where  $F(\delta_{i,0}^m, \delta_{i,C}^m, \delta_{i,0}, \delta_{i,C}, \beta)$  refers to a function of the effective initiation and propagation thresholds ( $\delta_{i,0}^m$ ,  $\delta_{i,C}^m$ ), the mixed-mode ratio ( $\beta$ ), and the initial pure mode traction separation properties ( $\delta_{i,0}$ ,  $\delta_{i,C}$ ).

However, since simple algebraic expressions of the effective initiation (propagation) thresholds cannot be always written (e.g. power law criterion with  $k \neq n$ , initiation criterion  $\kappa \neq 0$ , Benzeggagh-Kenane criterion  $\eta \neq 0$ , etc.) an iterative resolution procedure based on the false position method is derived. It results in the pure mode projections of the mixed-mode traction separation law to be easily computable for various nonlinear adhesive stress-strain evolution laws and (or) initiation (propagation) criteria. Assuming two initial sets of physically acceptable test values ( $\mathbf{a}$ ,  $\mathbf{b}$ ), the solution of the problem  $F_k(\delta_{i,0}^m, \delta_{i,C}^m, \delta_{i,0}, \delta_{i,C}, \beta) = 0$  is iteratively approached using the root of the secant line between ( $\mathbf{a}$ ,  $F(\mathbf{a})$ ) and ( $\mathbf{b}$ ,  $F(\mathbf{b})$ ) so that ( $\mathbf{a}$ ,  $\mathbf{b}$ ) will naturally converged (by construction) toward the root of equation (84) (see Fig.32).

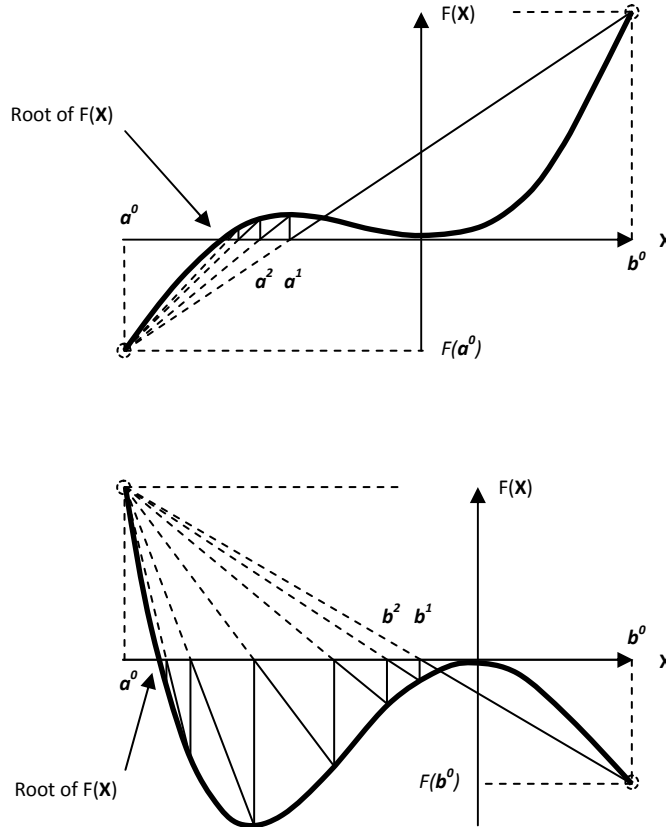


**Figure 32.** Schematic representation of the false position method. Estimation of the effective initiation (propagation) thresholds for various initiation (propagation) criteria. Description of the mixed-mode interface model. Projection of the mixed-mode interface model using iterative numerical procedures. Introduction of adhesive material nonlinearities.

The given procedure then allows for the effective properties ( $\delta_{i,0}^m$ ,  $\delta_{i,C}^m$ ) of the interface facing mixed-mode loadings to be computed from both the mixed-mode ratio ( $\beta$ ) and the initial pure mode traction separation properties ( $\delta_{i,0}$ ,  $\delta_{i,C}$ ) for various nonlinear adhesive stress-strain evolution laws and (or) initiation (propagation) criteria (Gavoille 2014).

#### 2.4.2.

O

overview of the Newton-Raphson iteration procedure

As for the false position method the Newton-Raphson procedure is a numerical procedure which allows for the root of non-linear equations to be iteratively approached. However the Newton-Raphson procedure is particularly well-suited for approaches that use FE like formulations. The method then consists in building a vector series  $\mathbf{X}^n$  converging towards the solution  $\mathbf{X}$  of a non-linear problem  $F(\mathbf{X})=0$ . To allow for the next iteration  $\mathbf{X}^{n+1}$  to be computed from the knowledge of  $\mathbf{X}^n$ , the function  $F(\mathbf{X})$  is approached by its first order Taylor expansion around  $\mathbf{X}^n$  such that:

$$0 \approx F(\mathbf{X}^{n+1}) = F(\mathbf{X}^n) + F'(\mathbf{X}^n)(\mathbf{X}^{n+1} - \mathbf{X}^n) \quad (85)$$

Assuming  $\mathbf{X}^{n+1}$  as satisfying  $F(\mathbf{X}^{n+1}) \approx 0$ , the next iteration  $\mathbf{X}^{n+1}$  can be computed as follows:

$$\mathbf{X}^{n+1} = \mathbf{X}^n - [F'(\mathbf{X}^n)]^{-1} F(\mathbf{X}^n) \quad (86)$$

Where  $F'(\mathbf{X})$  refers to the tangent linear application associated with the function  $F(\mathbf{X})$ . Then, the exact value of  $F(\mathbf{X}^{n+1})$  is recomputed and the function  $F(\mathbf{X})$  re-linearized using its first order Taylor expansion around  $\mathbf{X}^{n+1}$ . The given procedure is then repeated until the difference between two following iterations falls below a given convergence criterion. The re-computation of  $F(\mathbf{X}^{n+1})$  is generally referred as the projection step. In the case of linear applications, the derivative  $F'(\mathbf{X})$  is referred as the Jacobian matrix of  $F(\mathbf{X})$  at point  $\mathbf{X}$ .

One of the greatest advantages of the Newton-Raphson procedure is that the convergence rate near to the solution  $\mathbf{X}$  is quadratic. However, the use of this procedure requires the computation of the tangent linear application at each convergence step, implying time-consuming calculations, possible divergence of the algorithm and (or) numerical issues.

Since the computation of the Newton-Raphson iteration  $\mathbf{X}^{n+1}$  has not necessarily to be approached using the first order Taylor expansion of  $F(\mathbf{X})$ , numbers of latter authors suggested the use of other linear applications (Raydan 2011). These modified procedures are referred as quasi Newton-Raphson procedures. The false position method can be seen as a modified Newton-Raphson procedure.

### 2.4.3. Local equilibrium of the bonded overlap

As presented in Section 2.3.4, and because of the FE like formulation of the simplified 1D-beam adhesive stress analysis, the equilibrium of the adhesive joint specimen is ensured by:

$$\mathbf{F}^{pilot} = \mathbf{K}\mathbf{U} \quad (87)$$

Which is equivalent to the minimization problem of the quadratic form:

$$Q(\mathbf{U}) = \frac{1}{2} \mathbf{U}^T \mathbf{K} \mathbf{U} - \mathbf{U}^T \mathbf{F}^{pilot} \quad (88)$$

where  $\mathbf{K}$  refers to the master stiffness matrix (i.e. the stiffness matrix of the entire structure),  $\mathbf{U}$  to the vector of nodal displacements and  $\mathbf{F}_{ext}$  to the vector of applied nodal loads as defined in Section 2.3.4.

However, it is seen from Fig.31 that in the case of nonlinear adhesive stress-strain evolution laws the solution of  $\mathbf{F}=\mathbf{K}\mathbf{U}$  is by construction equivalent to the solution of:

$$\mathbf{F}^{pilot} = \mathbf{K}^{(s)} \mathbf{U}$$

Which is equivalent to the minimization problem of the quadratic form:

$$Q(\mathbf{U}) = \frac{1}{2} \mathbf{U}^T \mathbf{K}^{(s)} \mathbf{U} - \mathbf{U}^T \mathbf{F}^{pilot} \quad (89)$$

where  $\mathbf{K}^{(s)}$  refers here to the secant master stiffness matrix, stiffness matrix that depends on the secant stiffness properties of the adhesive layer,  $\mathbf{U}$  to the vector of nodal displacements and  $\mathbf{F}^{pilot}$  to the applied nodal forces.

### 2.4.4.

A

daptation of the Newton-Raphson iteration procedure to the particular formulation of the BBe element

**Adaptation of the general Newton-Raphson procedure.** For simplification purpose, the following demonstration will now refer to the equilibrium of a unique BBe macro-element. However it can be easily extended to the entire structure using the classical FE assembly rules. As a result, the vector  $\mathbf{U}$  as well as  $\mathbf{F}^{pilot}$  will now refer to the vectors of nodal displacements and nodal forces applying/acting onto a unique BBe macro-element.

Assuming  $\delta\mathbf{U}^T$  as kinematically acceptable, the aforementioned equilibrium can be expressed as:

$$\mathbf{L}^{int}(\mathbf{U}) = \mathbf{L}^{ext}(\mathbf{U}) \quad (90)$$

where  $\mathbf{L}^{int} = \mathbf{K}^{(s)}\mathbf{U}$  and  $\mathbf{L}^{ext} = \mathbf{F}^{pilot}$  respectively refer to the internal reactions and the external forces acting on the BBe element. It is indicated that in the general case, both  $\mathbf{L}^{int}$  and  $\mathbf{L}^{ext}$  depend on the vector of nodal displacements  $\mathbf{U}$ . Considering that no following forces, such as

load pressure or centrifugal forces, are applied to the joint,  $L^{ext}$  does not depend on the vector of nodal displacements  $U$ .

The expression of the element equilibrium can then be simplified as:

$$\mathbf{L}^{\text{int}}(\mathbf{U}) = \mathbf{L}^{\text{ext}} \quad (91)$$

Defining the linear application  $R$  as the difference between  $\mathbf{L}^{\text{int}}$  and  $\mathbf{L}^{\text{ext}}$ , the research of the solution of the element equilibrium can be reduced to the research of the root of  $R(\mathbf{U})=0$ . For convenience, the linear application  $R(\mathbf{U})$  will be thereafter referred as the vector of imbalanced loads.

$$R(\mathbf{U}) = 0 = \mathbf{L}^{\text{int}}(\mathbf{U}) - \mathbf{L}^{\text{ext}} \quad (92)$$

The research of the solution of the non-linear problem  $R(\mathbf{U})=0$  can thus be seen as a direct application of the Newton-Raphson procedure. Considering  $\mathbf{U}^n$  as an increasingly better estimation of the equilibrium solution  $\mathbf{U}$ , the next iteration  $\mathbf{U}^{n+1}$  can be computed as follows:

$$\mathbf{U}^{n+1} = \mathbf{U}^n - [R'(\mathbf{U}^n)]^{-1} R(\mathbf{U}^n) \quad (93)$$

Within the original Newton-Raphson procedure, the tangent linear application  $F'(X)$  has to be computed at each convergence iteration. In equation (93),  $R'(\mathbf{U})$  refers to the tangent linear application associated with  $R(\mathbf{U})$ . In the absence of *following forces*, the tangent linear application  $R'(\mathbf{U})$  can be expressed as:

$$R'(\mathbf{U}^n) = \left. \frac{\partial \mathbf{L}^{\text{int}}}{\partial \mathbf{U}} \right|_{\mathbf{U}^n} - \left. \frac{\partial \mathbf{L}^{\text{ext}}}{\partial \mathbf{U}} \right|_{\mathbf{U}^n} = \left. \frac{\partial \mathbf{L}^{\text{int}}}{\partial \mathbf{U}} \right|_{\mathbf{U}^n} \quad (94)$$

where the derivative of  $\mathbf{L}^{\text{int}}$  refers to the Jacobian matrix of the linear application  $\mathbf{L}^{\text{int}} = \mathbf{K}_S \mathbf{U}$  (see equation (95)). It is indicated that if *following forces* are applied to the structure, the tangent linear application  $R'(\mathbf{U})$  cannot be reduced to the single derivative of  $\mathbf{L}^{\text{int}}$ .

$$\left. \frac{\partial \mathbf{L}^{\text{int}}}{\partial \mathbf{U}} \right|_{\mathbf{U}^n} = \frac{\partial}{\partial \mathbf{U}} \mathbf{K}^{(s)} \mathbf{U} \Big|_{\mathbf{U}^n} = \begin{bmatrix} \left. \frac{\partial L_1^{\text{int}}}{\partial U_1} \right|_{\mathbf{U}^n} & \dots & \left. \frac{\partial L_1^{\text{int}}}{\partial U_k} \right|_{\mathbf{U}^n} \\ & \ddots & \\ \left. \frac{\partial L_k^{\text{int}}}{\partial U_1} \right|_{\mathbf{U}^n} & \dots & \left. \frac{\partial L_k^{\text{int}}}{\partial U_k} \right|_{\mathbf{U}^n} \end{bmatrix} \quad (95)$$

However, as the secant stiffness matrix  $\mathbf{K}^{(s)}$  depends by construction on the BBe element vector of nodal displacement  $\mathbf{U}$ , the exact computation of the tangent linear application is extremely complicated and results in non-necessary extra computation time. It is then decided to focus on quasi Newton-Raphson procedures, so that the computation of the tangent linear application  $R'(\mathbf{U})$  is no longer required.

**Computation of the vector of imbalanced loads.** Since the exact computation of the imbalance load vector highly determines the convergence of the series  $\mathbf{U}^n$  toward the equilibrium solution  $\mathbf{U}$ , a particular attention has to be given to its correct estimation. As previously presented, the imbalance load vector is defined as the difference between the vectors of internal reactions  $\mathbf{L}^{int}$  and applied forces  $\mathbf{L}^{ext}$  acting on the BBe element (see equation (90)).

The vector of internal reactions  $\mathbf{L}^{int} = \mathbf{K}^{(s)} \mathbf{U}$  can then be computed from both the secant stiffness matrix  $\mathbf{K}^{(s)}$  of the BBe element and the vector of nodal displacements  $\mathbf{U}$ . However, the secant stiffness matrix is defined on a set of constant adhesive peel and shear moduli (see Section 2.3.2). Since the projection of the adhesive stresses can lead to dissimilar left side and right side adhesive secant stiffnesses (see Fig.33), it is decided to update the secant stiffness matrix using the averaged peel and shear moduli along the element.

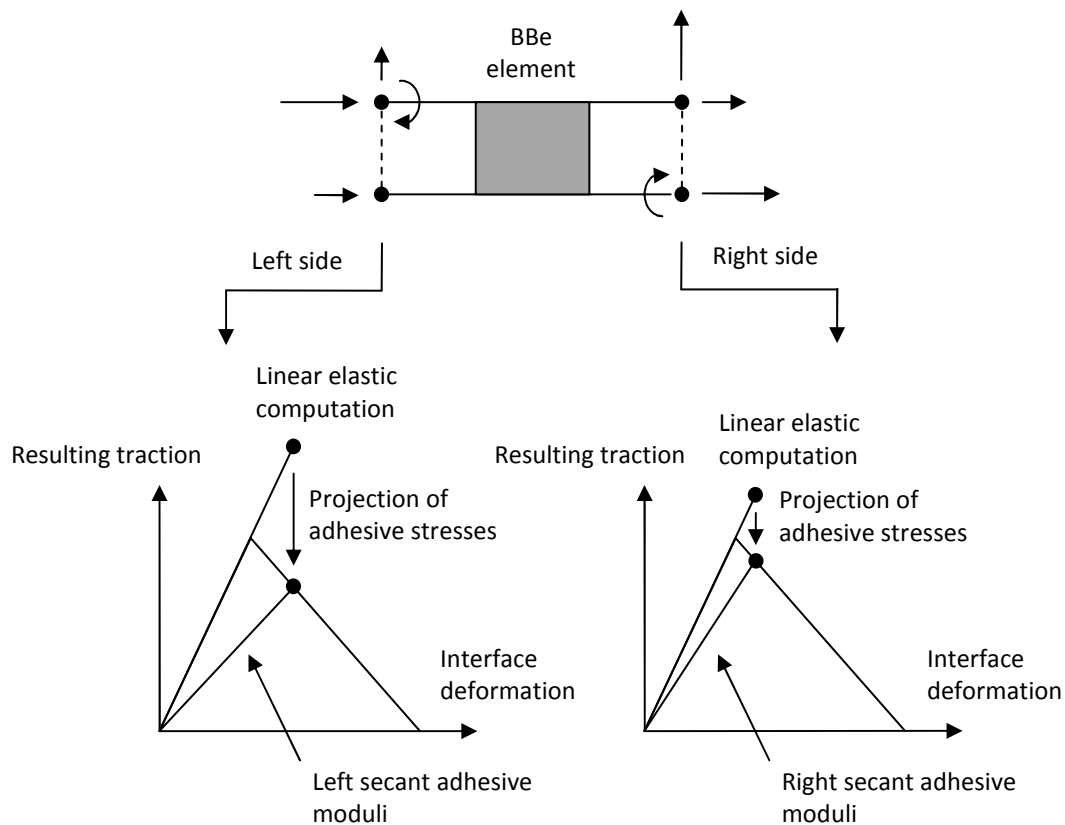


**Figure 33.** Dissimilar left side and right side adhesive secant moduli. Computation of the secant stiffness matrix  $\mathbf{K}^{(s)}$ . Adaptation of the Newton-Raphson iterative procedure. Computation of the vector of imbalanced loads. Introduction of adhesive material nonlinearities.

The vector  $\mathbf{L}^{ext} = \mathbf{F}^{pilot}$  can in turn be computed from the external forces applied to the BBe element. Using the definition of the secant stiffness matrix  $\mathbf{K}^{(s)}$ ,  $\mathbf{L}^{ext}$  can be expressed from the secant stiffness matrix at iteration  $\mathbf{U}^{n-1}$  and the vector of the BBe element nodal displacements at iteration  $\mathbf{U}^n$ .

Finally, the vector of imbalanced loads  $R(\mathbf{U})$  can be expressed in the form of:

$$R(\mathbf{U}) = \mathbf{K}^{(S)} (\mathbf{U}^{n-1}) \mathbf{U}^n - \mathbf{K}^{(S)} (\mathbf{U}^n) \mathbf{U}^n \quad (96)$$

where  $n$  refers to the current iteration of the Newton-Raphson algorithm.

**Implementation of the modified Newton-Raphson procedure.** Finally, by meshing the adhesive overlap with an adequate number of BBe macro-element (only one when facing linear elastic deformations), it is then possible to address the nonlinear response of the adhesive layer so that:

1. Initialization of the first iteration of the vector of nodal displacements ( $\mathbf{U}=\mathbf{0}$ )
2. Computation of the initial elastic stiffness matrix of each element ( $\mathbf{K}_{BBe}$ )
3. Assembly of the initial master stiffness matrix ( $\mathbf{K}$ )
4. Assembly of the vector of applied loads ( $\mathbf{F}$ )
5. Initialization of the vector of imbalanced loads ( $\mathbf{R}=-\mathbf{F}$ )
6. Computation of the first (next) iteration of vector  $\mathbf{U}$  ( $\mathbf{U}^{n+1}=\mathbf{U}^n-\mathbf{K}^{-1}\mathbf{R}$ )
7. Computation of the mixed-mode traction-separation parameters
8. Projection of the adhesive stresses (T, S) with respect to the computed effective traction-separation properties.
9. Computation of the updated secant stiffness matrix of each element ( $\mathbf{K}_{BBe}$ )
10. Assembly of the updated secant master stiffness matrix ( $\mathbf{K}$ )
11. Computation of the updated vector of imbalanced loads ( $\mathbf{R}$ )

*(Repeat steps 6 to 11 until a specified convergence criterion is satisfied)*

#### 2.4.5.

C

#### omparison with existing sandwich type analyses

A large amount of existing closed form stress analyses applies to linear elastic adhesive solicitations only. However realistic adhesive stress-strain evolution laws are generally not purely elastic so that simple linear elastic strength analyses are unable to address the complete behavior of such structures. In (Hart-Smith 1973a), the author developed a method for accounting for the plasticity of the adhesive layer in classical closed form stress analyses.

In (Hart-Smith 1973a), the author suggests introducing a new parameter – termed  $d$  – to separate the adhesive layer in two distinct parts (see Fig.34). This new parameter being referred to as the size of the elastic process zone. In the first part, the adhesive layer is presumed as facing linear elastic deformations only. In the second part, the adhesive layer is presumed as facing perfectly plastic deformations only. This separation of the adhesive layer then results in writing a set of two governing linear differential equations. Each one valid in either the linear elastic part of the adhesive layer or the perfectly plastic part of the adhesive layer. Finally, by solving independently each linear differential equations plus ensuring the continuity of both solutions at the interface ( $x=\pm d/2$ ), the author comes to derive an additional set of equations allowing for the computation of the new parameter  $d$ .

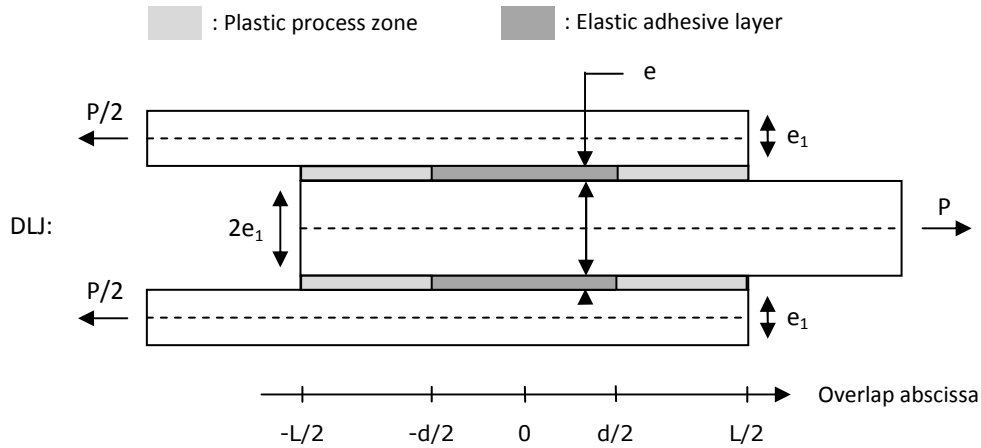


Figure 34. Comparison with existing sandwich type analyses. Hart-Smith’s nonlinear sandwich type analysis. Introduction of adhesive material nonlinearities.

**Hart-Smith’s sandwich type analysis in pure mode II.** In (Alfredson 2004), the author suggests using the solution procedure introduced and described in (Hart-Smith 1973a) in the particular case of the End-Notched Flexure test specimen (see Fig.35).

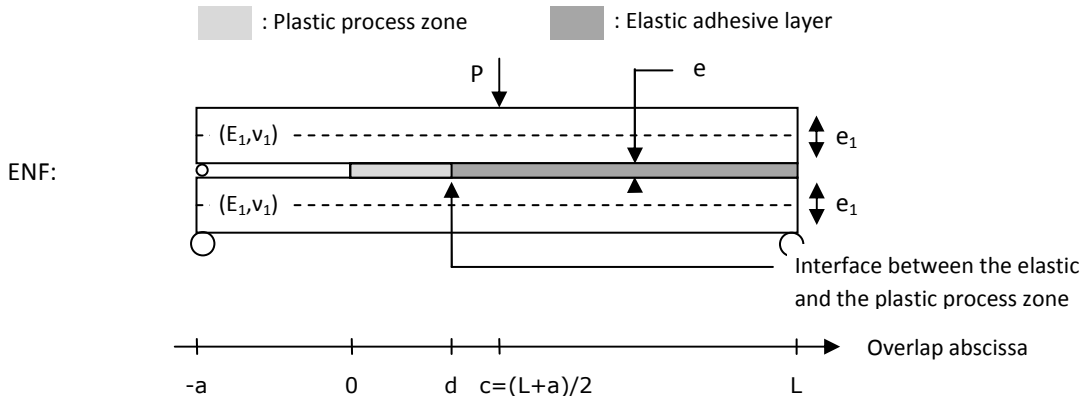


Figure 35. Comparison with existing sandwich type analyses. Hart-Smith’s sandwich type analysis in mode II. End-Notched Flexure test specimen. Introduction of adhesive material nonlinearities.

By developing and simplifying the adhesive equilibrium equations in the case of an idealized perfectly plastic adhesive behavior (see Fig.36), the author derives a set of three linear differential equations, so that:

$$\begin{cases} \frac{dN}{dx} = bT \\ \frac{dV}{dx} = 0 \\ V = \frac{dM}{dx} + \frac{1}{2}btT \end{cases} \quad \begin{cases} N = Ebt \frac{du}{dx} \\ M = -\frac{Ebt^3}{12} \frac{d^2w}{dx^2} \end{cases} \quad \begin{cases} N(0) = 0 & N(L) = 0 \\ M(0) = Pa/4 & M(L) = 0 \\ V(0) = P/4 & V(L) = -P/4 \end{cases}$$

$$\begin{cases} T(v) = kv & \text{for } x \in [d, L] \\ T(v) = kv_b = T_p & \text{for } x \in [0, d] \end{cases} \quad \left\{ \begin{array}{l} v = 2u + t \frac{dw}{dx} \end{array} \right. \quad (97)$$

Leading to:

$$\begin{cases} \frac{d^2 v}{dx^2} = \kappa^2/k(T_p - \bar{T}) & \text{for } x \in [0, d] \\ \frac{d^2 v}{dx^2} - \kappa^2 v = -\bar{T}\kappa^2/k & \text{for } x \in [d, c] \\ \frac{d^2 v}{dx^2} - \kappa^2 v = \bar{T}\kappa^2/k & \text{for } x \in [c, L] \end{cases} \quad (98)$$

where  $\kappa^2 = 8k/Et$ ,  $\bar{T} = 3/8 * P/bt$ ,  $k$  the initial adhesive stiffness in pure mode II and  $v$  the evolution of the adhesive mode II (shear) deformation along the overlap, and where  $N$ ,  $V$  and  $M$  respectively refer to the normal force, shearing force and bending moment in both upper and lower adherends.

Then, the respective solutions of equations (98) are given by:

$$\begin{cases} v(x) = \frac{C_1}{L}x + C_2 + \frac{(T_p - \bar{T})}{2k} \kappa^2 x^2 & \text{for } x \in [0, d] \\ v(x) = C_3 e^{\kappa x} + C_4 e^{-\kappa x} + \frac{\bar{T}}{k} & \text{for } x \in [d, c] \\ v(x) = C_5 e^{\kappa x} + C_6 e^{-\kappa x} - \frac{\bar{T}}{k} & \text{for } x \in [c, L] \end{cases} \quad (99)$$

Idealized perfectly plastic interface traction separation law:

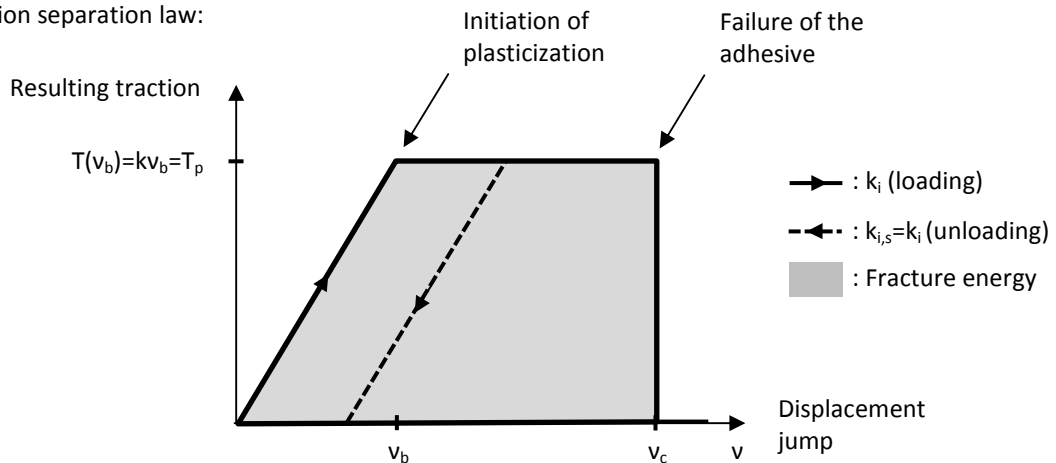


**Figure 36.** Representation of an idealized elastic perfectly plastic interface traction separation law. Comparison with existing sandwich type analyses. Hart-Smith's sandwich type analysis in pure mode II. End-Notched Flexure test specimen. Introduction of adhesive material nonlinearities.

By ensuring the continuity of the solutions (and their first derivatives) at point  $x=d$  and  $x=c$ , the author comes to derive a system of four additional equations so that:

$$\begin{cases} C_1 \frac{d}{L} + C_2 + \frac{1}{2} \frac{T_p - \bar{T}}{k} \kappa^2 d^2 = C_3 e^{\kappa d} + C_4 e^{-\kappa d} + \frac{\bar{T}}{k} \\ C_1 + \frac{T_p - \bar{T}}{k} \kappa^2 d = C_3 \kappa e^{\kappa d} - C_4 \kappa e^{-\kappa d} \\ C_3 e^{\kappa c} + C_4 e^{-\kappa c} = C_5 e^{\kappa c} + C_6 e^{-\kappa c} - \frac{2\bar{T}}{k} \\ C_3 \kappa e^{\kappa c} - C_4 \kappa e^{-\kappa c} = C_5 \kappa e^{\kappa c} - C_6 \kappa e^{-\kappa c} \end{cases} \quad (100)$$

And the boundary conditions:

$$\begin{cases} \frac{C_1}{L} = -\frac{8\bar{T}a}{EH} = v'(0) \\ C_5 \kappa e^{\kappa L} - C_6 \kappa e^{-\kappa L} = 0 = v'(L) \end{cases} \quad (101)$$

To determine the six integration constants  $C_1$ ,  $C_2$ ,  $C_3$ ,  $C_4$ ,  $C_5$  and  $C_6$ , the author finally suggests considering the length of the plastic process zone  $d$  as an independent variable (i.e. variable that can be determined independently from equations (100) and (101)). To determine this length of the plastic process zone  $d$ , the author then uses the equation provided by the knowledge of the level of deformation at point  $x=d$  ( $v(d)=v_b$ ), so that:

$$C_1 \frac{d}{L} + C_2 + \frac{1}{2} \frac{T_p - \bar{T}}{k} \kappa^2 d^2 = v_b = C_3 e^{\kappa d} + C_4 e^{-\kappa d} + \frac{\bar{T}}{k} \quad (102)$$

By combining equation (100) with equations (101) and (102), the author then derives the guiding equation:

$$\begin{aligned} & \frac{1}{2e^{\kappa d}} \left[ -\frac{8\bar{T}a}{EH} \left( d + \frac{1}{\kappa} \right) + v_b - \left( \frac{1}{2} \frac{T_b - \bar{T}}{k} \kappa^2 d^2 - \frac{8\bar{T}a}{EH} d \right) + \frac{T_b - \bar{T}}{k} \left( \kappa d + \frac{1}{2} \kappa^2 d^2 \right) - \frac{\bar{T}}{k} \right] + \frac{\bar{T}}{k e^{\kappa c}} \\ & = e^{-2\kappa d} \left[ \frac{1}{2e^{-\kappa d}} \left[ -\frac{8\bar{T}a}{EH} \left( d + \frac{1}{\kappa} \right) + v_b - \left( \frac{1}{2} \frac{T_b - \bar{T}}{k} \kappa^2 d^2 - \frac{8\bar{T}a}{EH} d \right) + \frac{T_b - \bar{T}}{k} \left( \kappa d + \frac{1}{2} \kappa^2 d^2 \right) - \frac{\bar{T}}{k} \right] + \frac{\bar{T}}{k e^{-\kappa c}} \right] \end{aligned} \quad (103)$$

where the length of the plastic process zone  $d$  is obtained as the root of equation (103). No simple algebraic expression of  $d$  can be written so that it might be estimated using numerical iterative procedures (e.g. the false position method, etc).

Finally, considering  $d$  as fully determined by equation (103), it may be observed that the set of linear equations formed by equations (100) and (101) can be expressed in the form of a simple matrix system, so that:

$$\mathbf{AC} = \mathbf{B} \quad (104)$$

where:

$$\mathbf{A} = \begin{pmatrix} 1/L & 0 & 0 & 0 & 0 & 0 \\ d/L & 1 & -e^{\kappa l} & -e^{-\kappa l} & 0 & 0 \\ 1/L & 0 & -\kappa e^{\kappa l} & \kappa e^{-\kappa l} & 0 & 0 \\ 0 & 0 & e^{\kappa c} & e^{-\kappa c} & -e^{\kappa c} & -e^{-\kappa c} \\ 0 & 0 & \kappa e^{\kappa c} & -\kappa e^{-\kappa c} & -\kappa e^{\kappa c} & \kappa e^{-\kappa c} \\ 0 & 0 & 0 & 0 & \kappa e^{\kappa L} & -\kappa e^{-\kappa L} \end{pmatrix} \quad (105)$$

$${}^T\mathbf{C} = (C_1 \ C_2 \ C_3 \ C_4 \ C_5 \ C_6) \quad (106)$$

$${}^T\mathbf{B} = \left( -\frac{8\bar{T}a}{EH} \quad \frac{\bar{T}}{k} - \frac{1}{2} \frac{(T_b - \bar{T})}{k} \kappa^2 d^2 \quad -\frac{(T_b - \bar{T})}{k} \kappa^2 d \quad -\frac{2\bar{T}}{k} \quad 0 \quad 0 \right) \quad (107)$$

The integration constants  $C_1, C_2, C_3, C_4, C_5$  and  $C_6$  being finally determined as:

$$\mathbf{C} = \mathbf{A}^{-1}\mathbf{B} \quad (108)$$

**Hart-Smith's sandwich type analysis in pure mode I.** The solution procedure presented in Section 2.4.5.1. applies to pure mode II solicitations of the adhesive layer only. However it can be easily extended to the case of pure mode I solicitations (see Fig.37).

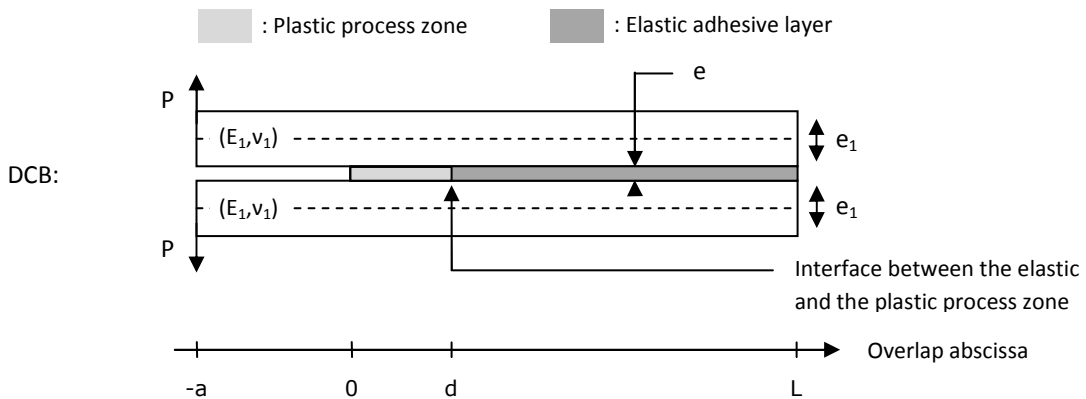


Figure 37. Comparison with existing sandwich type analyses. Hart-Smith's sandwich type analysis in mode I. Double Cantilever Beam test specimen. Introduction of adhesive material nonlinearities.

Modifying the equilibrium and constitutive equations gives:

$$\left\{ \begin{array}{l} \frac{dN}{dx} = 0 \\ \frac{dV}{dx} = -bS \\ \frac{dM}{dx} = V \end{array} \right. \left\{ \begin{array}{l} N = Ebt \frac{du}{dx} \\ M = \frac{Ebt^3}{12} \frac{d^2w}{dx^2} \end{array} \right. \left\{ \begin{array}{l} N(0) = 0 \quad N(L) = 0 \\ M(0) = Pa \quad M(L) = 0 \\ V(0) = P \quad V(L) = 0 \end{array} \right.$$

$$\left\{ \begin{array}{l} S(\varepsilon) = k\varepsilon \quad \text{for } \varepsilon \in [0, \varepsilon_b] \\ S(\varepsilon) = k\varepsilon_b = S_p \quad \text{for } \varepsilon \in [\varepsilon_b, \varepsilon_c] \end{array} \right. \quad \{\varepsilon = 2w\} \quad (109)$$

Leading to the following set of two linear differential equations:

$$\left\{ \begin{array}{l} \frac{d^4\varepsilon}{dx^4} = -\kappa^4/k S_p \quad \text{for } x \in [0, d] \\ \frac{d^4\varepsilon}{dx^4} + \kappa^4\varepsilon = 0 \quad \text{for } x \in [d, L] \end{array} \right. \quad (110)$$

where  $\kappa^4 = 24k/Et^3$ ,  $\kappa' = \kappa/\sqrt{2}$ ,  $k$  the new initial adhesive stiffness in pure mode I and  $\varepsilon$  the evolution of the adhesive mode I (peel) deformation along the overlap, and where  $N$ ,  $V$  and  $M$  respectively refer to the normal force, shearing force and bending moment in both upper and lower adherends.

Then, the respective solutions of equations (110) are given by:

$$\left\{ \begin{array}{l} \varepsilon(x) = \frac{C_1}{6}x^3 + \frac{C_2}{2}x^2 + C_3x + C_4 - \frac{S_p}{24k}\kappa^4x^4 \quad \text{for } x \in [0, d] \\ \varepsilon(x) = C_5e^{\kappa x} \sin(\kappa x) + C_6e^{\kappa x} \cos(\kappa x) + C_7e^{-\kappa x} \sin(\kappa x) + C_8e^{-\kappa x} \cos(\kappa x) \quad \text{for } x \in [d, L] \end{array} \right. \quad (111)$$

Idealized perfectly plastic interface traction separation law:

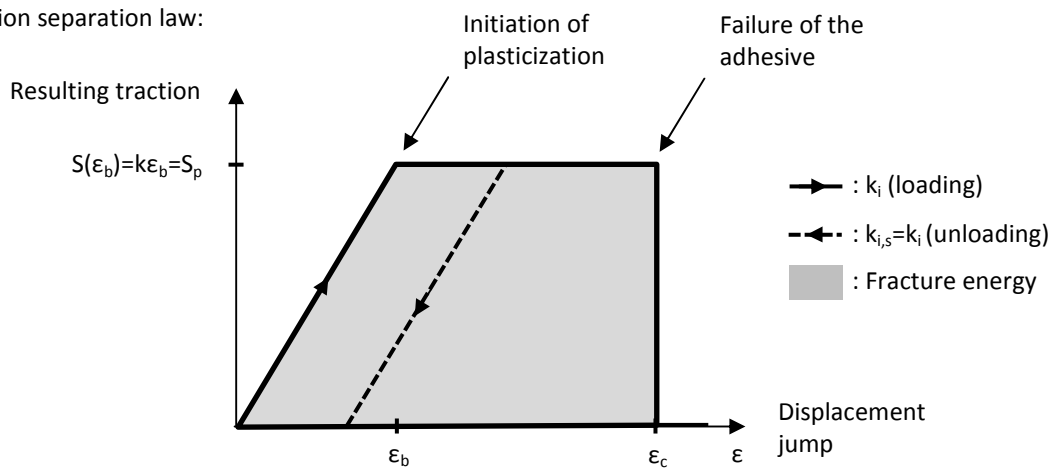


Figure 38. Representation of an idealized elastic perfectly plastic interface traction separation law. Comparison with existing sandwich type analyses. Hart-Smith's sandwich type analysis

in pure mode I. Double Cantilever Beam test specimen. Introduction of adhesive material nonlinearities.

Ensuring the continuity of the solutions (and their first derivatives) at point  $x=d$  gives:

$$\left\{ \begin{array}{l} C_1 \frac{d^3}{6} + C_2 \frac{d^2}{2} + C_3 d + C_4 - \frac{S_p}{24k} \kappa^4 d^4 = C_5 e^{\kappa d} \sin(\kappa d) + C_6 e^{\kappa d} \cos(\kappa d) + C_7 e^{-\kappa d} \sin(\kappa d) + C_8 e^{-\kappa d} \cos(\kappa d) \\ C_1 \frac{d^2}{2} + C_2 d + C_3 - \frac{S_p}{6k} \kappa^4 d^3 = C_5 \kappa e^{\kappa d} \text{trig}(\kappa d) + C_6 \kappa e^{\kappa d} \text{trig}(-\kappa d) + C_7 \kappa e^{-\kappa d} \text{trig}(-\kappa d) - C_8 \kappa e^{-\kappa d} \text{trig}(\kappa d) \\ C_1 d + C_2 - \frac{S_p}{2k} \kappa^4 d^2 = 2C_5 \kappa^2 e^{\kappa d} \sin(\kappa d) - 2C_6 \kappa^2 e^{\kappa d} \cos(\kappa d) - 2C_7 \kappa^2 e^{-\kappa d} \sin(\kappa d) + 2C_8 \kappa^2 e^{-\kappa d} \cos(\kappa d) \\ C_1 - \frac{S_p}{k} \kappa^4 d = 2C_5 \kappa^3 e^{\kappa d} \text{trig}(-\kappa d) - 2C_6 \kappa^3 e^{\kappa d} \text{trig}(\kappa d) + 2C_7 \kappa^3 e^{-\kappa d} \text{trig}(\kappa d) + 2C_8 \kappa^3 e^{-\kappa d} \text{trig}(-\kappa d) \end{array} \right. \quad (112)$$

And the boundary conditions:

$$\left\{ \begin{array}{l} C_2 = \frac{24Pa}{EWH^3} = \varepsilon''(0) \\ C_1 = \frac{24P}{EWH^3} = \varepsilon'''(0) \\ 2C_5 \kappa^2 e^{\kappa L} \cos(\kappa L) - 2C_6 \kappa^2 e^{\kappa L} \sin(\kappa L) - 2C_7 \kappa^2 e^{-\kappa L} \cos(\kappa L) + 2C_8 \kappa^2 e^{-\kappa L} \sin(\kappa L) = 0 = \varepsilon''(L) \\ 2C_5 \kappa^3 e^{\kappa L} \text{trig}(-\kappa L) - 2C_6 \kappa^3 e^{\kappa L} \text{trig}(\kappa L) + 2C_7 \kappa^3 e^{-\kappa L} \text{trig}(\kappa L) + 2C_8 \kappa^3 e^{-\kappa L} \text{trig}(-\kappa L) = 0 = \varepsilon'''(L) \end{array} \right. \quad (113)$$

where  $\text{trig}(x) = \cos(x) + \sin(x)$ .

To determine the eight integration constants  $C_1, C_2, C_3, C_4, C_5, C_6, C_7$  and  $C_8$ , the length of the plastic process zone  $d$  is again considered as an independent variable (i.e. variable that can be determined independently from equations (112) and (113)). The last equation required is provided by the knowledge of the level of deformation at  $x=d$  ( $\varepsilon(d) = \varepsilon_b$ ), so that:

$$\begin{aligned} \frac{C_1}{6} d^3 + \frac{C_2}{2} d^2 + C_3 d + C_4 - \frac{S_p}{24k} \kappa^4 d^4 &= \varepsilon_b \\ &= C_5 e^{\kappa d} \sin(\kappa d) + C_6 e^{\kappa d} \cos(\kappa d) + C_7 e^{-\kappa d} \sin(\kappa d) + C_8 e^{-\kappa d} \cos(\kappa d) \end{aligned} \quad (114)$$

The combination of equations (112) (113) and (114) finally providing the guiding equation that allows for the computation of the length of the plastic process zone ( $d$ ).

Finally, considering  $d$  as fully determined by the guiding equation resulting from the combination of equations (112) (113) and (114), it may be observed that the set of linear equations formed by equations (112) and (113) can be expressed in the form of a simple matrix system, so that:

$$\mathbf{AC} = \mathbf{B} \quad (115)$$

where:

$$\mathbf{A} = \begin{pmatrix} 0 & 1 & 0 & 0 & 0 & 0 & 0 & 0 \\ 1 & 0 & 0 & 0 & 0 & 0 & 0 & 0 \\ d^3/6 & d^2/2 & d & 1 & -e^{\kappa l} \sin(\kappa l) & -e^{\kappa l} \cos(\kappa l) & -e^{-\kappa l} \sin(\kappa l) & -e^{-\kappa l} \cos(\kappa l) \\ d^2/2 & d & 1 & 0 & -\kappa e^{\kappa l} \text{trig}(\kappa l) & -\kappa e^{\kappa l} \text{trig}(-\kappa l) & -\kappa e^{-\kappa l} \text{trig}(-\kappa l) & \kappa e^{-\kappa l} \text{trig}(\kappa l) \\ d & 1 & 0 & 0 & -2\kappa^2 e^{\kappa l} \cos(\kappa l) & 2\kappa^2 e^{\kappa l} \sin(\kappa l) & 2\kappa^2 e^{-\kappa l} \cos(\kappa l) & -2\kappa^2 e^{-\kappa l} \sin(\kappa l) \\ 1 & 0 & 0 & 0 & -2\kappa^3 e^{\kappa l} \text{trig}(-\kappa l) & 2\kappa^3 e^{\kappa l} \text{trig}(\kappa l) & -2\kappa^3 e^{-\kappa l} \text{trig}(\kappa l) & -2\kappa^3 e^{-\kappa l} \text{trig}(-\kappa l) \\ 0 & 0 & 0 & 0 & 2\kappa^2 e^{\kappa L} \cos(\kappa L) & -2\kappa^2 e^{\kappa L} \sin(\kappa L) & -2\kappa^2 e^{-\kappa L} \cos(\kappa L) & 2\kappa^2 e^{-\kappa L} \sin(\kappa L) \\ 0 & 0 & 0 & 0 & 2\kappa^3 e^{\kappa L} \text{trig}(-\kappa L) & -2\kappa^3 e^{\kappa L} \text{trig}(\kappa L) & 2\kappa^3 e^{-\kappa L} \text{trig}(\kappa L) & 2\kappa^3 e^{-\kappa L} \text{trig}(-\kappa L) \end{pmatrix} \quad (115)$$

$${}^T \mathbf{C} = (C_1 \ C_2 \ C_3 \ C_4 \ C_5 \ C_6 \ C_7 \ C_8) \quad (116)$$

$${}^T \mathbf{B} = \left( \frac{24Pa}{EWH^3} \ \frac{24P}{EWH^3} \ \frac{S_p}{24k} \kappa^4 d^4 \ \frac{S_p}{6k} \kappa^4 d^3 \ \frac{S_p}{2k} \kappa^4 d^2 \ \frac{S_p}{k} \kappa^4 d \ 0 \ 0 \right) \quad (117)$$

The integration constants  $C_1, C_2, C_3, C_4, C_5, C_6, C_7$  and  $C_8$  being finally determined as:

$$\mathbf{C} = \mathbf{A}^{-1} \mathbf{B} \quad (118)$$

### Comparison with the simplified 1D-beam adhesive stress analysis.

*Description of the simplified 1D-beam adhesive stress analyses.* Here is investigated the mechanical response of two adhesive joint specimens (e.g. *ENF, DCB*). Those specimens are characteristic of pure mode I and pure mode II adhesive solicitations and have been widely shown as consistent with the experimental characterization of adhesive joint interfaces (Kenane 1997, Reeder 1992). A schematic representation of each simplified 1D-beam adhesive stress analysis is presented in Fig.39.

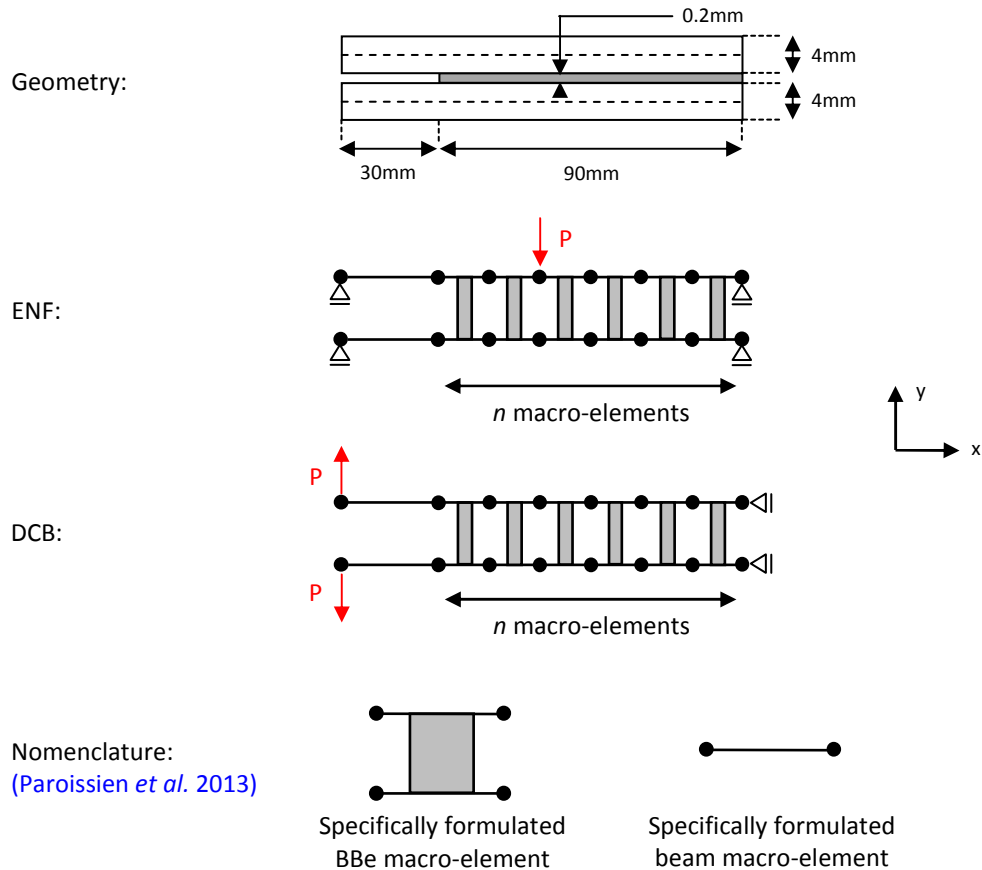


**Figure 39.** Schematic representation of End-Notched Flexure (ENF), Double Cantilever Beam (DCB). Description of the simplified 1D-beam adhesive stress analyses. Comparison with the simplified 1D-beam adhesive stress analysis.

The adhesive overlap is meshed using  $n$  uniformly distributed BBe elements. Each outer adherend is meshed using a unique outer beam element. Both adherends are modeled as monolithic beams. The adhesive layer is modeled using an elastic perfectly plastic traction-separation law. Both the material and geometrical properties of the studied specimens are given in [Tab.2](#).

**Tab 2.** Comparison with existing sandwich type analyses. Set of material and geometrical properties. End Notched Flexure + Double Cantilever Beam test specimens. Introduction of adhesive material nonlinearities.

Geometry		Material properties	
L	90	E	74200
H	4	k	250/e
W	20	$\nu_b$ ( $\epsilon_b$ )	0.00966
a	30	$\nu_c$ ( $\epsilon_c$ )	0.167
e	0.2		

: Adhesive     : Adherends

*Convergence of the simplified 1D-beam adhesive stress analyses.* As presented in [Section 2.3.2](#), when facing purely linear elastic deformations, the adhesive overlap can be modeled using a unique 4-nodes BBe element. However, when facing nonlinear adhesive deformations, the suggested solution procedure needs the adhesive overlap to be meshed with an adequate number of BBe elements to address the correct behavior of the adhesive layer. Since the adhesive overlap has to be meshed, the results obtained can depend on its refinement. To allow for the comparison of converged results, the mesh of the overlap using BBe macro-elements was optimized so that the solutions obtained were independent on its refinement (see [Appendix 5](#)).

*Comparison with Hart-Smith's sandwich type analyses.* In [Fig.40](#) and [Fig.41](#) is presented a direct comparison between the adhesive shear and peel stress distributions obtained from the reworked Hart-Smith's sandwich type analyses and the simplified 1D-beam adhesive stress analysis in the case of perfectly plastic adhesive traction separation evolution laws for both ENF and DCB adhesive test samples. Both material and geometrical properties of the studied specimens are given in [Tab.2](#).

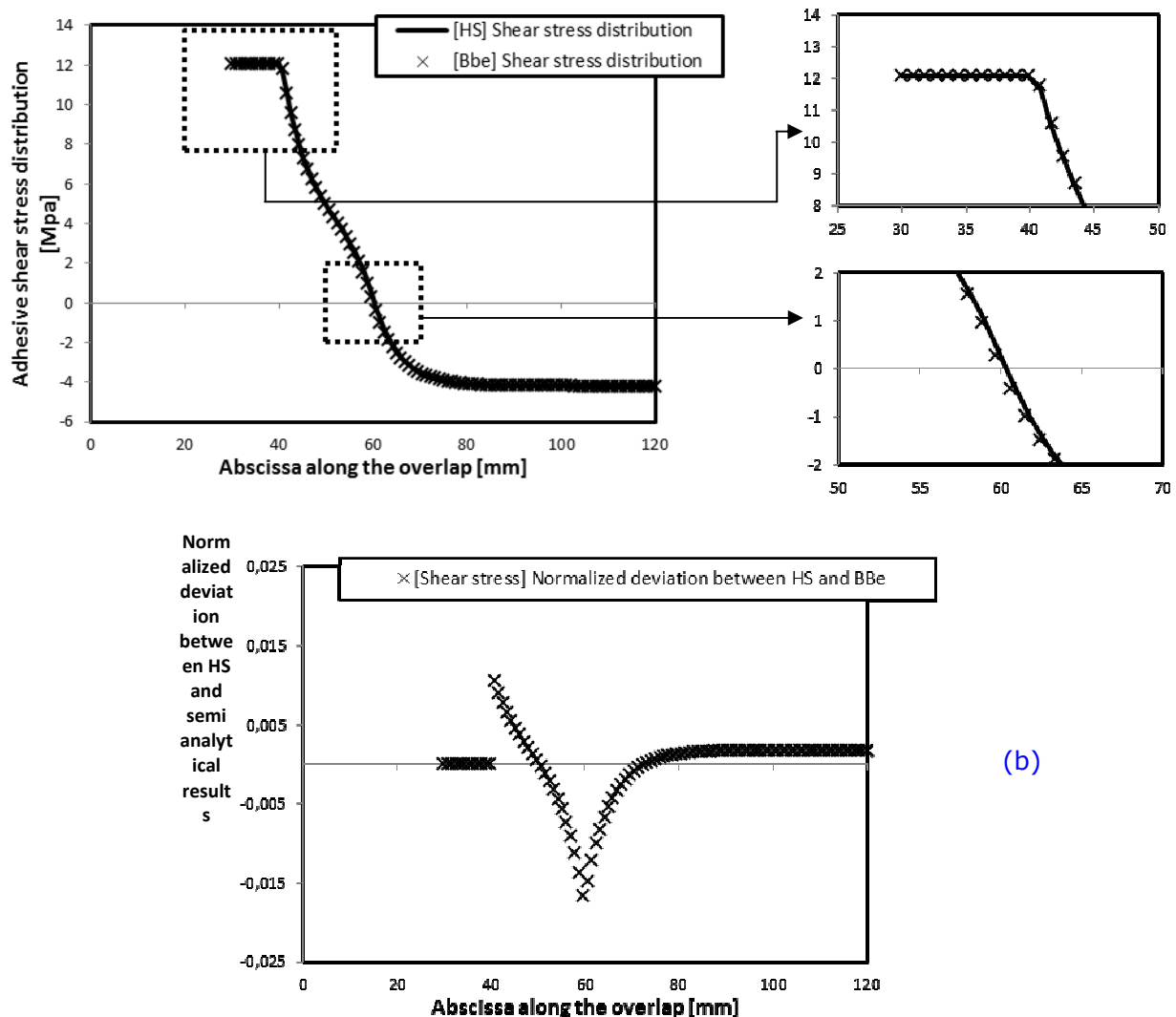


**Figure 40.** Comparison between semi analytical and sandwich type results in terms of adhesive shear stress distribution. Comparison with existing sandwich type analyses. Hart-

Smith's sandwich type analysis in pure mode II. End-Notched Flexure test specimen. Introduction of adhesive material nonlinearities.

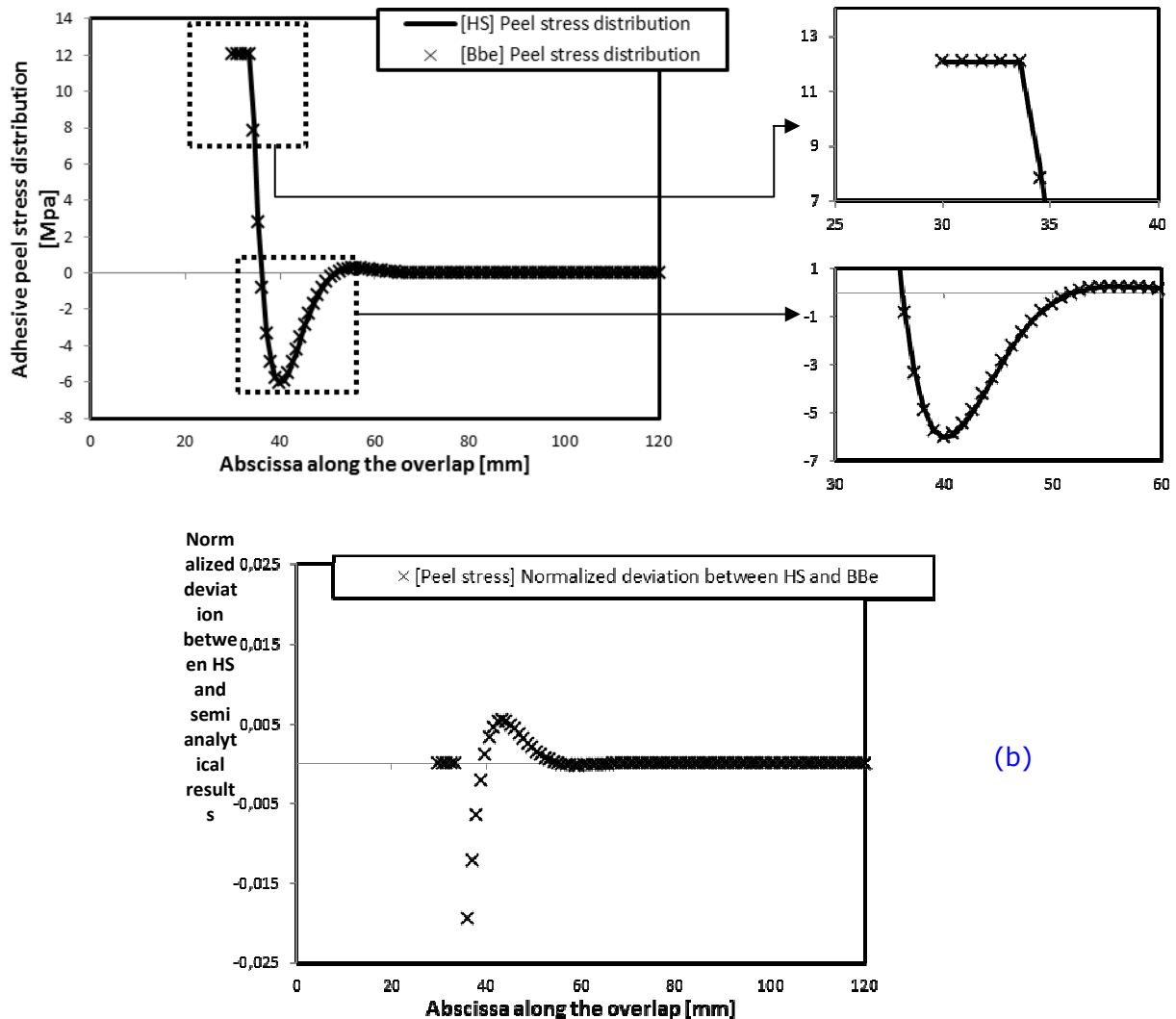


Figure 41. Comparison between semi analytical and sandwich type results in terms of adhesive peel stress distribution. Comparison with existing sandwich type analyses. Hart-Smith's sandwich type analysis in pure mode I. Double Cantilever Beam test specimen. Introduction of adhesive material nonlinearities.

It is seen from Fig.40 and Fig.41 that the results obtain from the simplified 1D-beam adhesive stress analysis and the reworked Hart-Smith's sandwich type analyses are in close agreement (in both pure mode I and pure mode II). However, peaks of normalized deviations can be observed where the adhesive layer experiences the highest values of shearing (peeling) adhesive stress gradients. These peaks of normalized deviation can be explained by the fact that the updated secant stiffness matrix (i.e. simplified 1D-beam adhesive stress analysis) is computed through the averaged adhesive secant moduli along each BBe element. Which leads to an increasing deviation with theoretical analyses at locations where the adhesive layer experiences the most important stress gradients.

It is also seen from [Section 2.4.5](#) that the reworked Hart-Smith's sandwich type analyses is highly dependent on the type of adhesive specimen and (or) loading/boundary conditions that are applied to the structure. Indeed, both equilibrium equations and boundary conditions have to be reworked for each new test configurations and can lead to increasingly complex algebraic expressions for the final solution. The advantage of the suggested simplified 1D-beam adhesive stress analysis then lies in the adequate use of the FE methodologies. Thus taking advantage of the flexibility of FE techniques (e.g. wide application range, simple assembly procedure, etc.) and the simplicity (robustness) of closed form stress analyses (e.g. limited number of macro-elements, results independent on the mesh refinement when facing linear-elastic adhesive deformations, etc).

2.4.6.

C

Comparison with Finite Element (FE) analyses

**Description of the Finite-Element (FE) models.** Here is investigated the mechanical response of three adhesive joint specimens (i.e. ENF, DCB & MMB). Those specimens are characteristic of pure mode I, pure mode II and mixed-mode I/II adhesive solicitations, and have been widely shown as consistent with the experimental characterization of adhesive interfaces ([Kenane 1997](#), [Reeder 1992](#)). A schematic representation of each specimen is presented in [Fig.42](#).

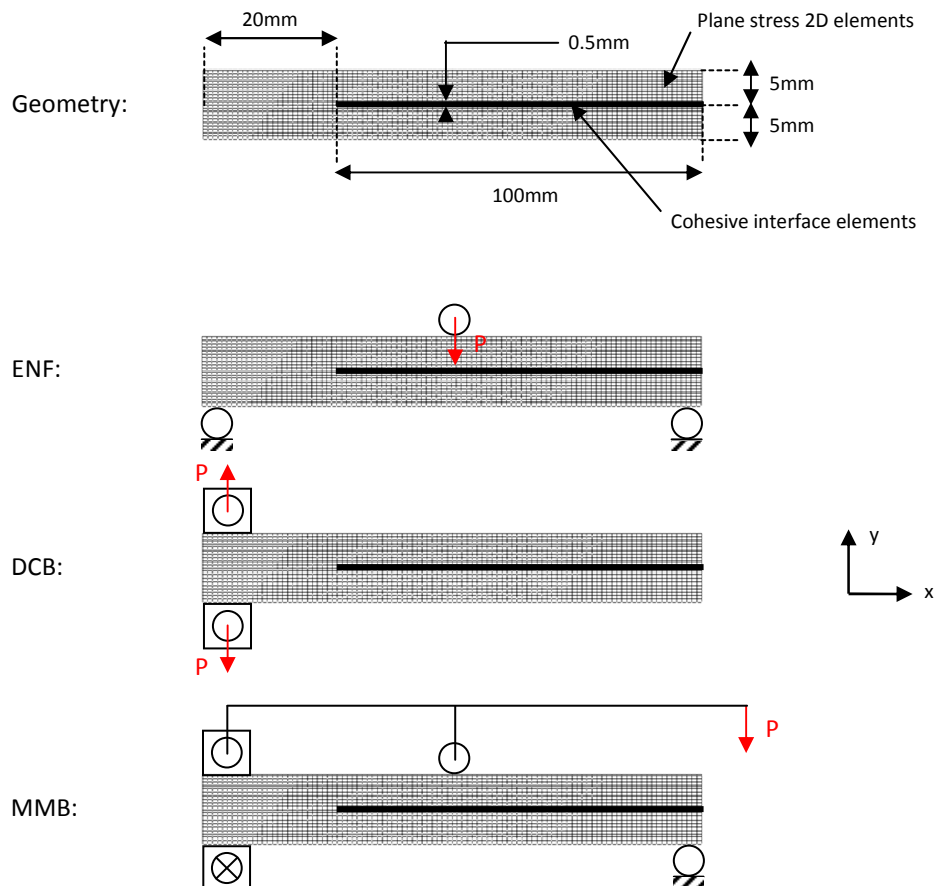


**Figure 42.** Schematic representation of End-Notched Flexure (ENF), Double Cantilever Beam (DCB). Description of the Finite Element (FE) models. Comparison with Finite Element (FE) analyses.

The geometry of each specimen is balanced. The simulations are performed using SAMCEF FE Code v14-1.02. Both adherends are modeled as facing purely linear elastic deformations only (see [Tab.3](#)). The adhesive layer is modeled using a bi-linear cohesive traction-separation law. Both linear energetic initiation and propagation criteria are assumed (see [Tab.4](#)).

**Tab 3.** Comparison with existing Finite Element (FE) analyses. Adherends elastic properties. Introduction of adhesive material nonlinearities.

Adherends elastic properties.			
E	74200 MPa	$\nu$	0.34
G	27900 MPa		-

**Tab 4.** Comparison with existing Finite Element (FE) analyses. Adhesive cohesive properties. Introduction of adhesive material nonlinearities.

Adhesive properties.			
$k_I$	185 MPa	$k_{II}$	65 MPa
$G_{I,0}$	2 J/mm <sup>2</sup>	$G_{II,0}$	2 J/mm <sup>2</sup>
$G_{I,C}$	4 J/mm <sup>2</sup>	$G_{II,C}$	5 J/mm <sup>2</sup>
Initiation criteria	Linear energetic	Propagation criteria	Linear energetic

The adherends are meshed using 2D SAMCEF type T015 elements. SAMCEF type T015 elements have linear interpolation functions and 4 internal modes (ie. 4 nodes and 12 degrees of freedom). The normal integration scheme is chosen. The adhesive interface is meshed using 2D cohesive interface SAMCEF type T146 elements. SAMCEF type T146 elements have linear interpolation functions and no internal modes (ie. 4 nodes and 8 degrees of freedom). Because of numerical convergence issues, the Gauss-Lobatto integration scheme is chosen ([Samcef 2013](#)). In purpose of comparing comparable analyses, loads and boundary conditions are applied to the mesh so that it fits at best the as conditions described in the simplified 1D-beam adhesive stress analysis (see [Fig.43](#)).

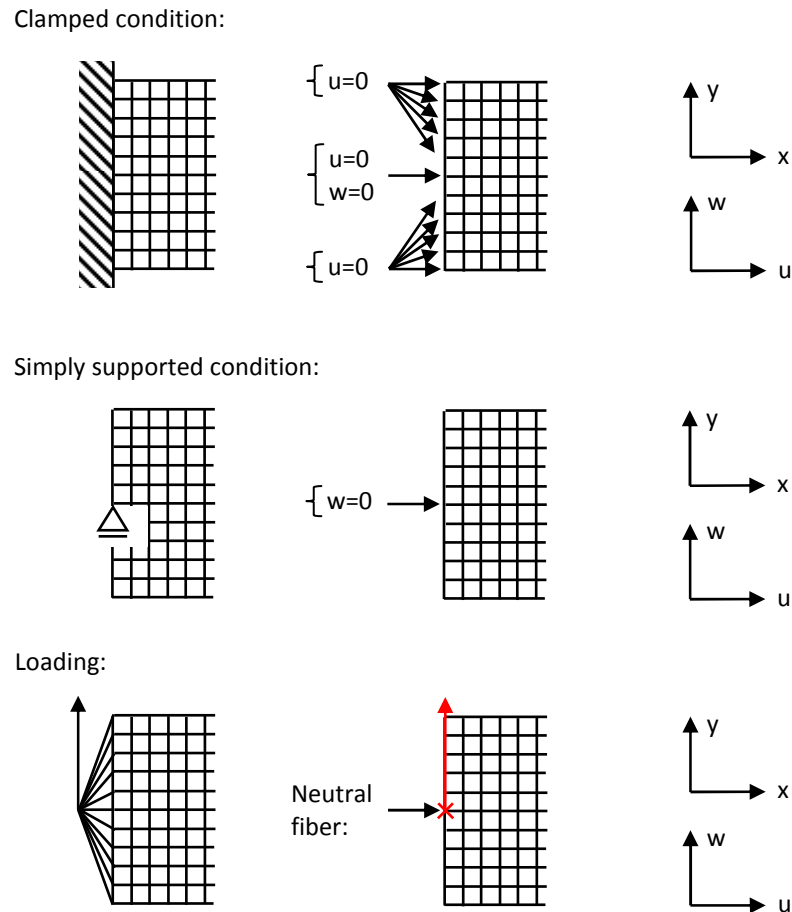


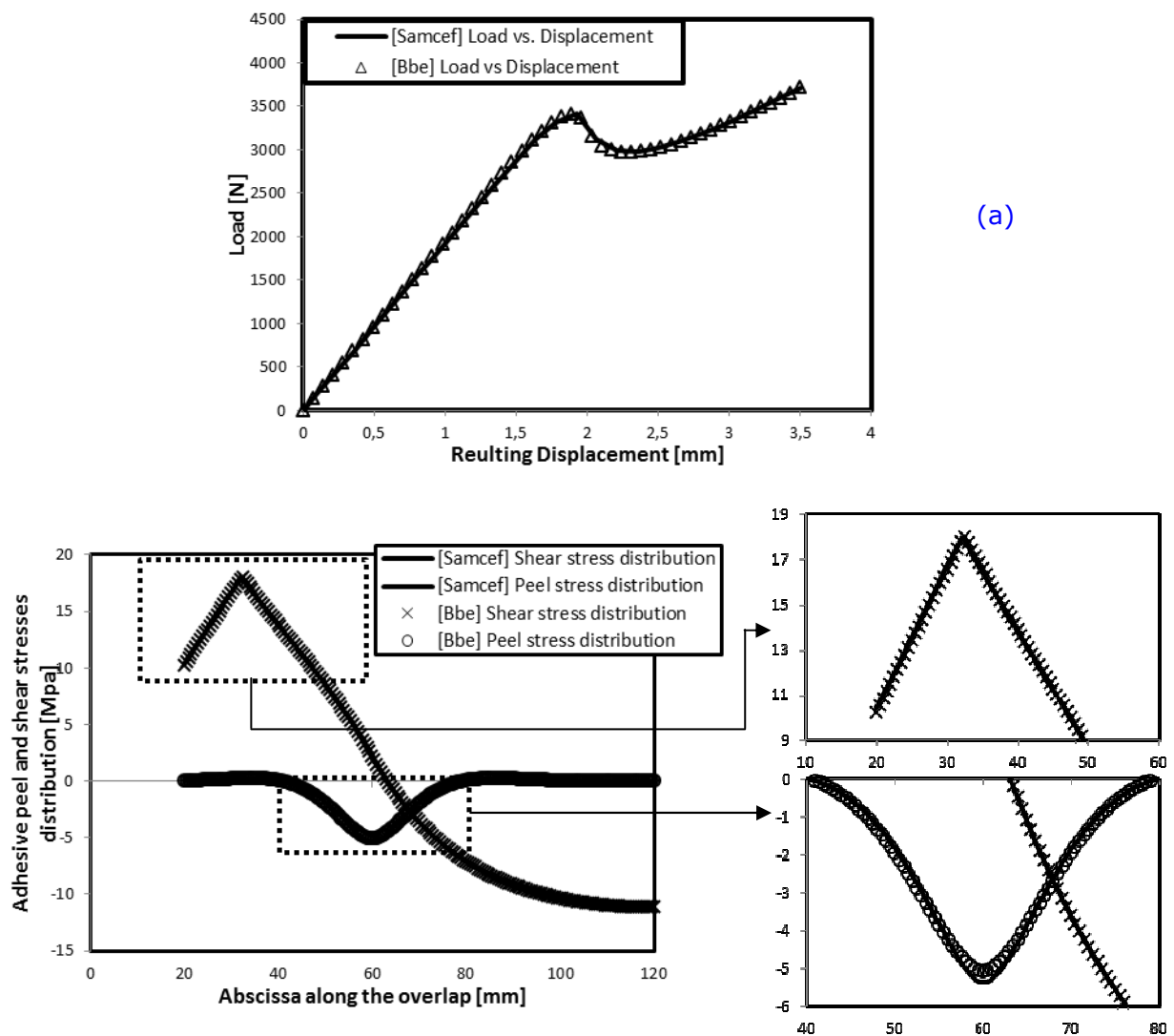
**Figure 43.** Schematic representation of the applied boundary conditions. Clamped boundary condition and simply supported boundary condition. Description of the Finite Element (FE) models. Comparison with Finite Element (FE) analyses.

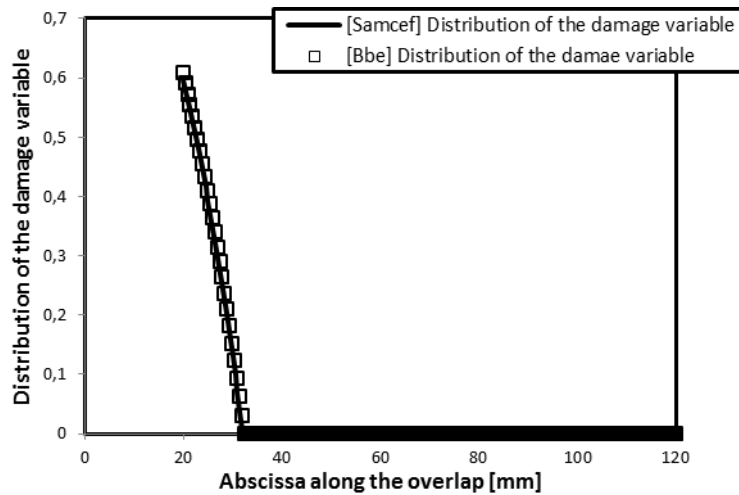
Finally, to address the complete nonlinear response of the adhesive specimen when subjected to steadily increasing loads, it is firstly decided to focus on what will be thereafter referred as the load/displacement instability point. This point refers to the instant  $t$  when the structure faces the maximum level of the applied load that can be transferred (i.e. very top of the applied load vs resulting displacement curve). This choice is made since the distributions of the adhesive shear and peel stresses at this particular moment are characteristic of the structure itself and refers to the maximum level of material nonlinearities that faces the adhesive layer during the initiation phase. To address this particular point during the specimen load history, a load based Newton-Raphson resolution procedure is employed in both FE and semi-analytical analyses (i.e. resolution procedure that stops as early as the maximum level of applicable load is reached). However the precision in reaching this particular point is directly determined by the arbitrary fixed convergence threshold. It then results in significant numerical differences due to the varying maximum load reached by the Newton-Raphson procedure. It is then decided to evaluate the adhesive peel stress and adhesive shear stress distribution at a slightly decreased maximum load (i.e. 95% of the specimen maximum load bearing capability).

**Convergence of the Finite Element (FE) models.** To allow for the comparison of converged results, the mesh of each FE models was optimized so that the solution obtained is independent on its refinement. The optimization of the mesh is based on the following hypotheses: (i) the mesh of the specimen is uniformly distributed over the length, the width and the thickness of the adherends, (ii) the mesh of the upper adherend, the adhesive interface, and the lower adherend are corresponding, (iii) the aspect ratio of each element of the structure is equal to 1. It is shown from hypotheses (i) to (iii) that the mesh of the entire specimen is then dependent on the number of elements within the length of the adhesively bonded overlap only (see [Appendix 5](#)).

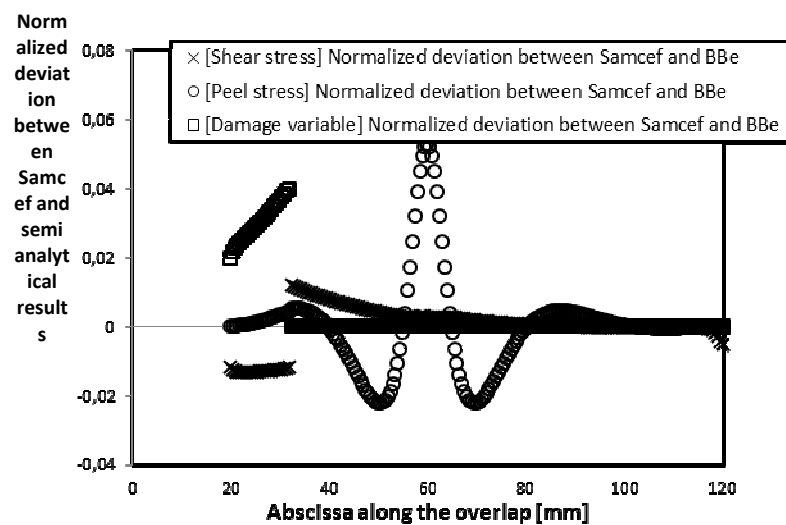
**Comparison with the simplified 1D-Beam adhesive stress analysis.**

*End Notched Flexure test specimen (ENF).* Fig.44 presents the comparison between semi-analytical results and Finite Element predictions in terms of Load versus Resulting Displacement curve (a), distribution of adhesive stresses (b) and distribution of the damage variable (c) along the overlap. Fig.44-(d) then presents the *normalized deviation* between semi-analytical and Finite Element predictions. Good agreement is shown.





(c)

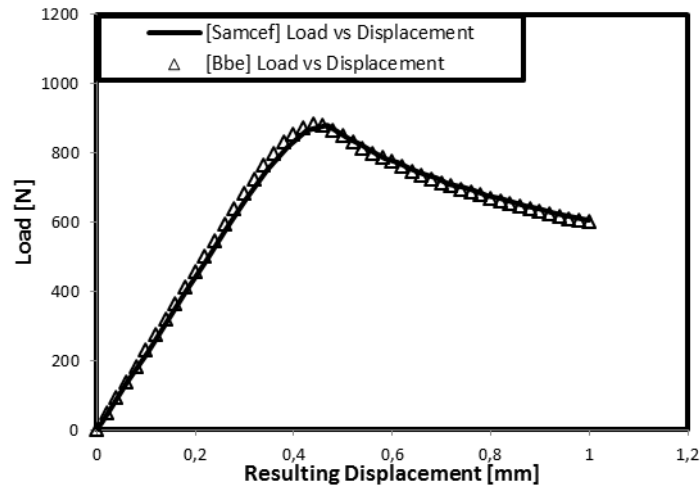


(d)

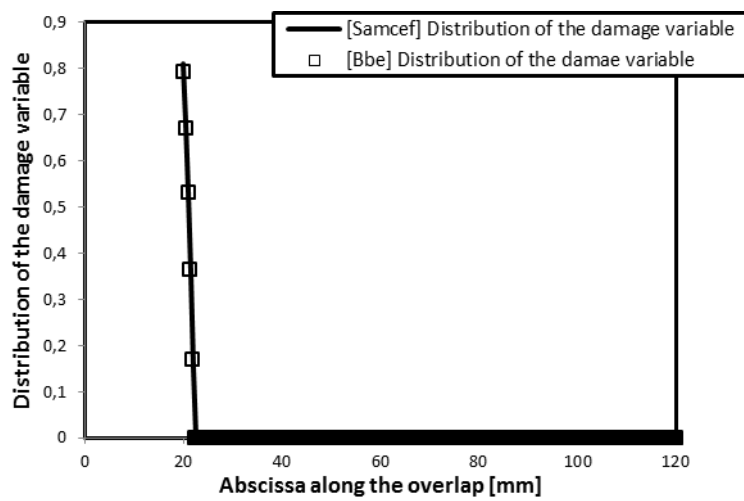
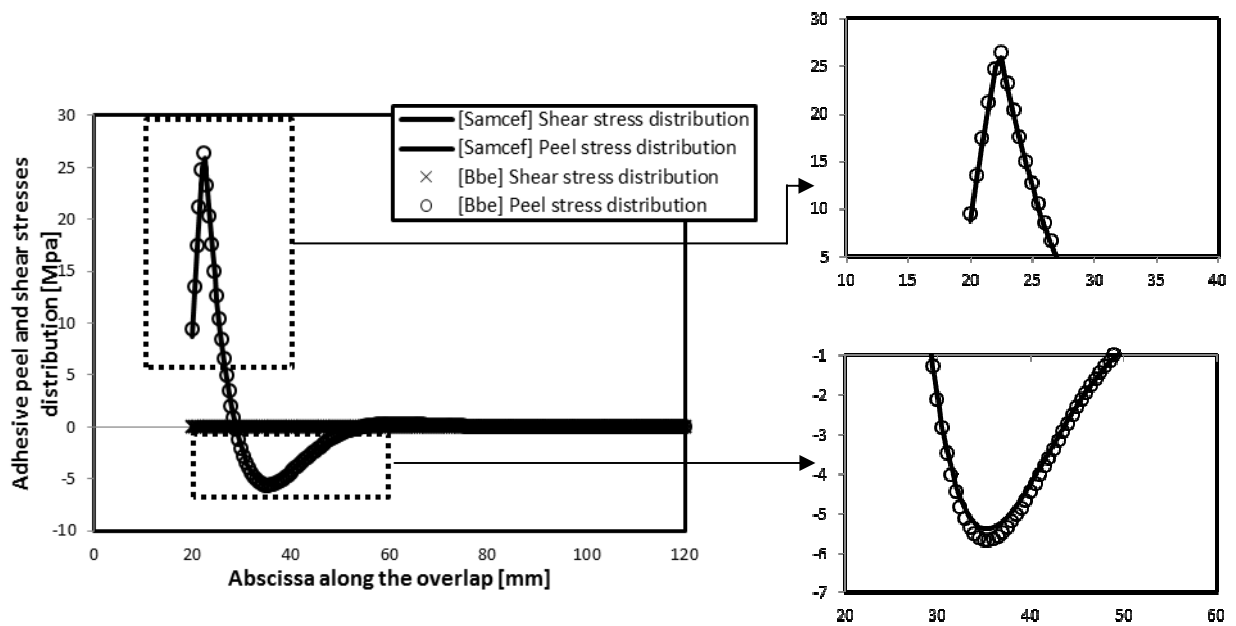
Figure 44. Comparison with Finite-Element (FE) analyses in pure mode II. End Notched Flexure test specimen (ENF). Description of the Finite-Element (FE) models. Introduction of adhesive material nonlinearities.

*Double Cantilever Beam test specimen (DCB).* Fig.45 presents the comparison between semi-analytical results and Finite Element predictions in terms of Load versus Resulting Displacement curve (a), distribution of adhesive stresses (b) and distribution of the damage variable (c) along the overlap. Fig.45-(d) then presents the *normalized deviation* between semi-analytical and Finite Element predictions. Good agreement is shown.

Chapter 2. Extension and validation of the simplified 1D-beam adhesive stress analysis



(a)



(c)

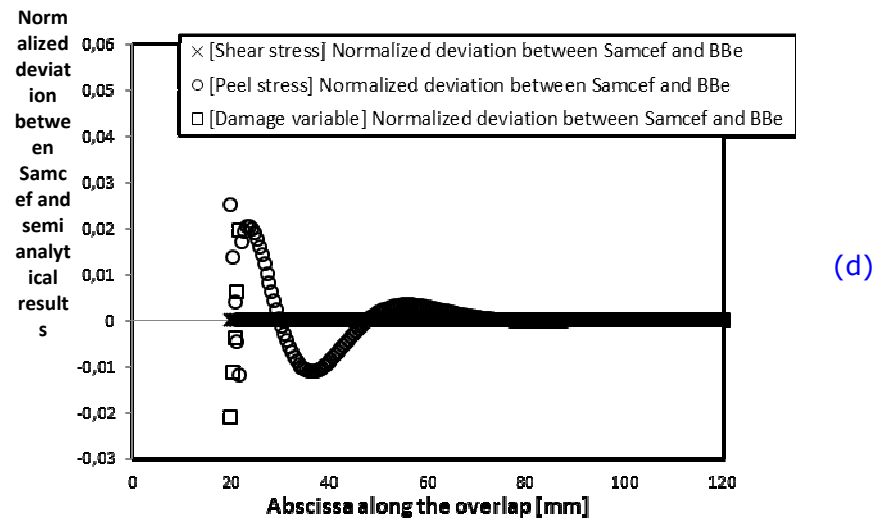
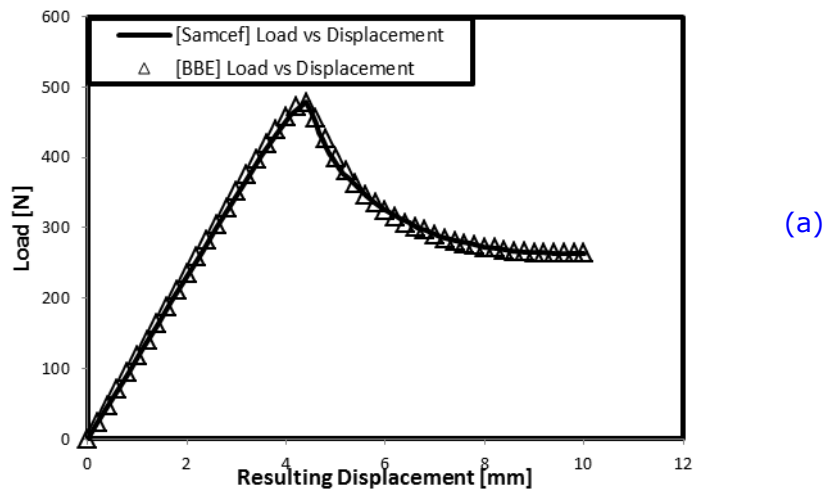
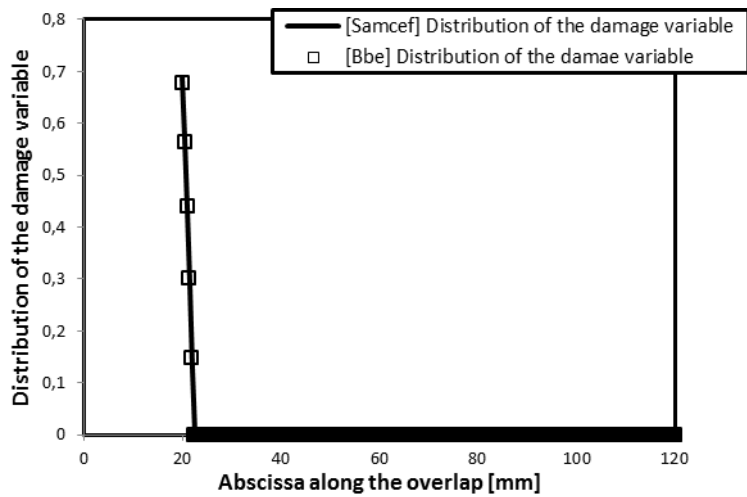
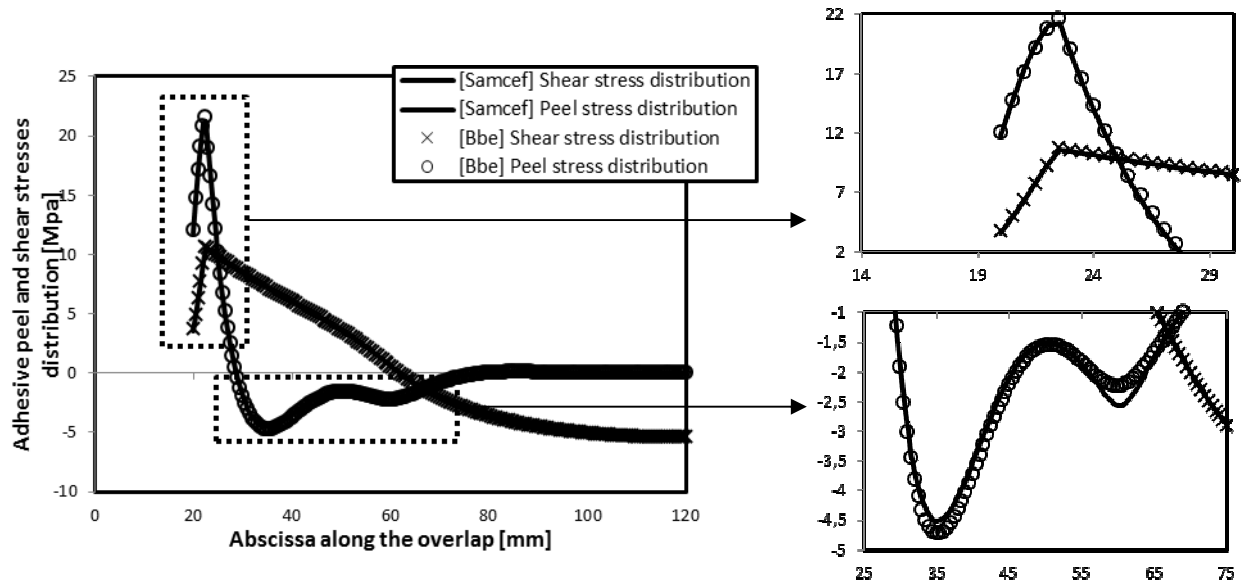


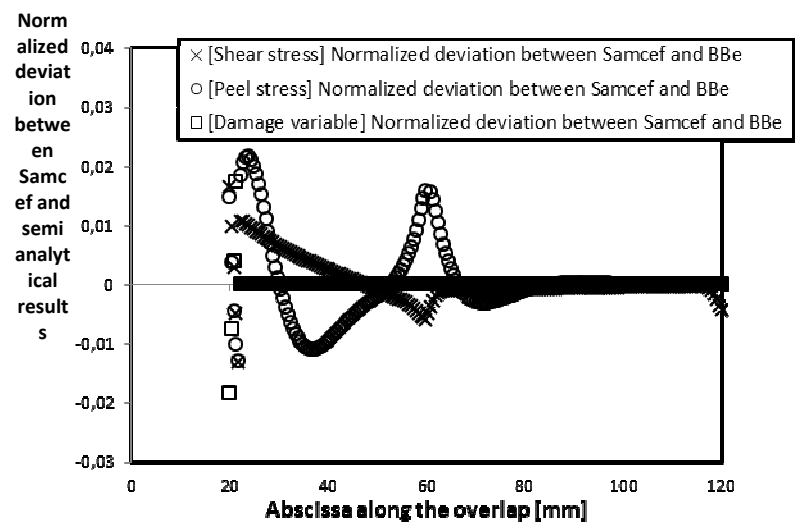
Figure 45. Comparison with Finite-Element (FE) analyses in pure mode I. Double-Cantilever Beam test specimen (DCB). Description of the Finite-Element (FE) models. Introduction of adhesive material nonlinearities.

*Mixed-Mode Bending test specimen (MMB)*. Fig.46 presents the comparison between semi-analytical results and Finite Element predictions in terms of Load versus Resulting Displacement curve (a), distribution of adhesive stresses (b) and distribution of the damage variable (c) along the overlap. Fig.46-(d) then presents the *normalized deviation* between semi-analytical and Finite Element predictions. Good agreement is shown.





(c)



(d)

**Figure 46.** Comparison with Finite-Element (FE) analyses in mixed-mode I/II. Mixed-Mode Bending test specimen (MMB). Description of the Finite-Element (FE) models. Introduction of adhesive material nonlinearities.

- 2.5. I  
Introduction of adherend material nonlinearities
- 2.5.1. A  
Adaptation of the classical theory of beam plasticization to the particular formulation of the BBe element

**Adaptation of the classical theory of beam plasticity.** For simplification purpose each adherend is thereafter considered as an isotropic homogeneous material exhibiting elastic perfectly plastic stress-strain evolution law (see Fig.47). Additionally, the adhesive layer is considered as experiencing linear elastic deformations only. However the following procedure is not limited to these particular behaviors only, and can be easily be extended to more general anisotropic laminated materials by considering independently each ply of the material, and coupled to nonlinear adhesive stress-strain evolution laws.

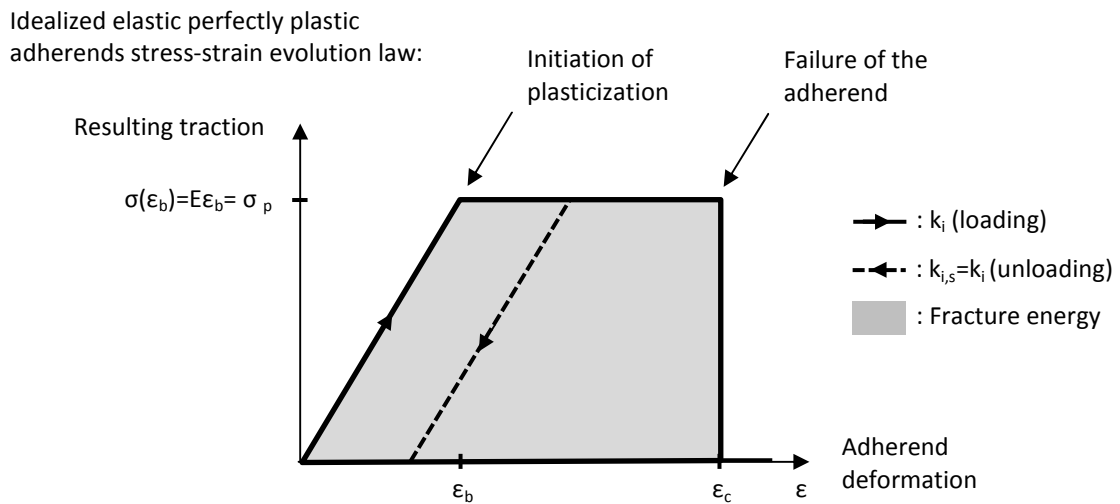


**Figure 47.** Representation of an idealized elastic perfectly plastic adherend stress-strain evolution law. Adaptation of the classical theory of beam plasticization to the particular formulation of the BBe element. Introduction of adherend material nonlinearities.

As presented in Sections 2.3.2 and 2.3.3, and according to the form of the Euler-Bernoulli beam kinematic it is possible to express the displacement field of both adherends in the form of (see Fig.48):

$$\begin{cases} u^j(x, y) = u_j(x, y = 0) - yw_{j,x}(x, y = 0) \\ w^j(x, y) = w_j(x, y = 0) \end{cases}, j = 1, 2 \quad (119)$$

where  $u^j(x, y)$  and  $w^j(x, y)$  respectively refer to the longitudinal and transverse displacement fields of adherend  $j$  ( $j=1, 2$ ), and  $u_j(x, y=0)$ ,  $w_j(x, y=0)$  and  $\theta_j(x, y=0)$  to the longitudinal, transverse and rotational displacements of the neutral fiber of adherend  $j$  ( $j=1, 2$ ).

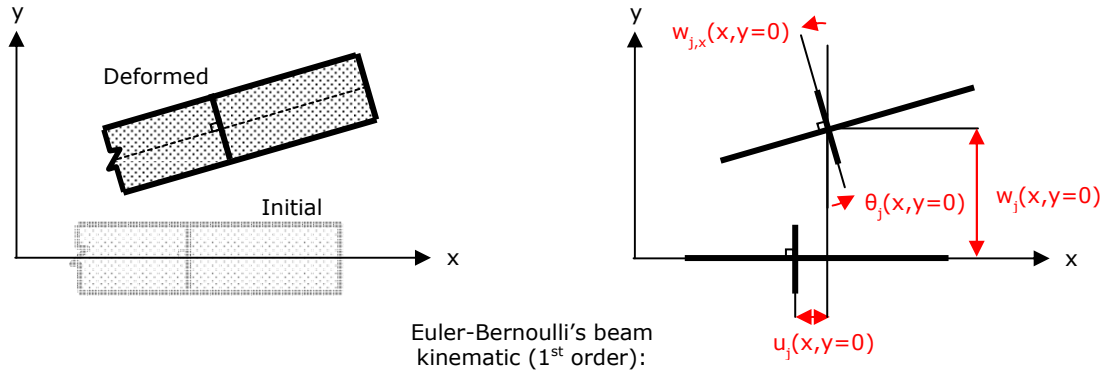


**Figure 48.** Schematic representation of the adherends displacement field. Adaptation of the classical theory of beam plasticization to the particular formulation of the BBe element. Introduction of adherend material nonlinearities.

Thanks to equation (119) the cross-section axial deformation of adherend  $j$  ( $j=1,2$ ) can be expressed in the form of:

$$\varepsilon_{xx}^j(x, y) = u_{,x}^j(x, y) = u_{j,x}(x, y=0) - yw_{j,xx}(x, y=0) \quad (120)$$

And the resulting axial stress as:

$$\sigma_{xx}^j(x, y) = E_j \varepsilon_{xx}^j(x, y) \quad (121)$$

Where  $E_j$  refers to the extensional modulus, also referred as Young's modulus, of adherend  $j$  ( $j=1,2$ ).

As initially introduced for the adhesive layer in [Section 2.4](#), the basic idea of introducing nonlinear adhesive (adherend) stress-strain evolution laws in the particular formulation of the simplified 1D-beam adhesive stress analysis is to transform the initial problem  $\mathbf{F}=\mathbf{K}\mathbf{U}$  in finding the correct set of adherends secant properties that satisfies the original equilibrium equations and boundary conditions.

As presented in [Section 2.4.3](#), the solution of the initial problem:

$$\mathbf{F}^{pilot} = \mathbf{K}\mathbf{U} \quad (122)$$

Which in the case of nonlinear materials properties, is by construction equivalent to the solution of the secant equivalent problem:

$$\mathbf{F}^{pilot} = \mathbf{K}^{(s)}\mathbf{U} \quad (123)$$

where  $\mathbf{K}^{(s)}$  refers to the secant master stiffness matrix that depends on both mode I and mode II secant adhesive moduli resulting from the projection of the adhesive stresses onto the specified adhesive stress-strain evolution laws (see [Section 2.4](#)),  $\mathbf{U}$  to the vector of nodal displacements and  $\mathbf{F}^{pilot}$  to the applied nodal forces. As in [Section 2.4](#), equation (123) refers to

the equilibrium of a unique BBe element. However it can be easily extended to the entire structure by applying classical FE assembly rules.

Similarly to the adhesive layer, the projection of the adherend stresses then results in a modification of the through-thickness secant properties of both adherends (i.e. modification of the local adherend extentional secant moduli). This modification of the local secant properties results in a modification of the integrated adherend secant extensional, bending and coupling stiffnesses, so that:

$$\begin{cases} A_j^{(s)} = b \int_{-e_j/2}^{e_j/2} E_j^{(s)}(y) dy \\ B_j^{(s)} = b \int_{-e_j/2}^{e_j/2} E_j^{(s)}(y) y dy \\ D_j^{(s)} = b \int_{-e_j/2}^{e_j/2} E_j^{(s)}(y) y^2 dy \end{cases}, j = 1, 2 \quad (124)$$

where  $A_j^{(s)}$ ,  $D_j^{(s)}$  and  $B_j^{(s)}$  respectively refers to the secant extensional, bending and coupling stiffnesses of adherend  $j$  ( $j=1,2$ ), and  $E_j^{(s)}$  to the through-thickness distribution of the adherend secant moduli resulting from the projection of the adherends stresses onto the specified stress-strain evolution law (see [Fig.49](#)).

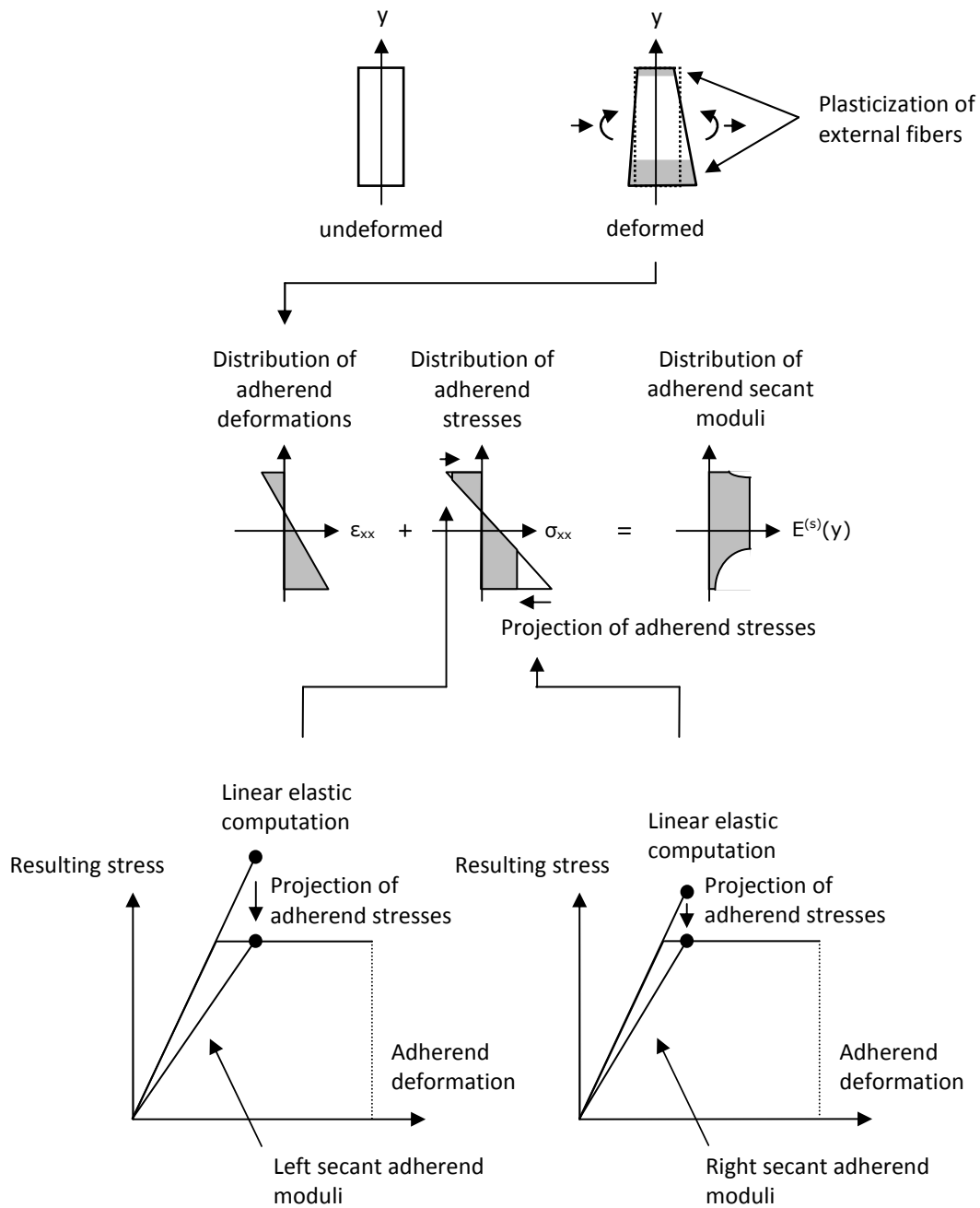
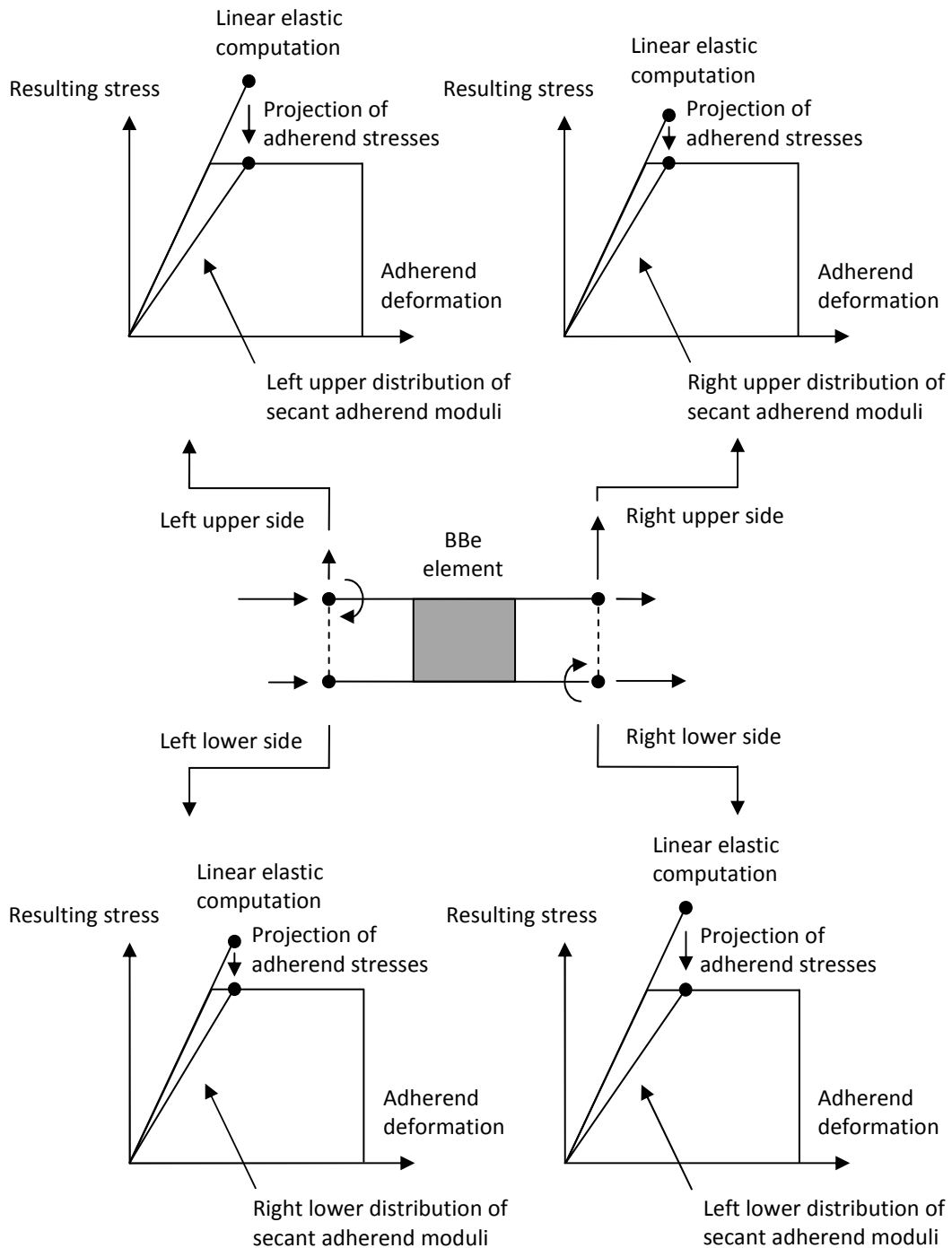


Figure 49. Computation of the through-thickness adherend secant properties. Adaptation of the classical theory of beam plasticization to the particular formulation of the BBe element. Introduction of adherend material nonlinearities.

At this stage, since the general projection of the adherend stresses can result in complex through-thickness distributions of adherend secant properties (see Fig.49), the integration of the secant extensional, bending and coupling stiffnesses can be done either by analytical integration or numerical integration (e.g. Gauss, Newton-Cotes, etc). For the sake of clarity and robustness, here is chosen to integrate the adherend secant stiffnesses using the trapezoid Newton-Cotes integration scheme.

**Computation of the vector of imbalanced loads.** The basic idea of introducing adherend material nonlinearities within the particular formulation of the simplified 1D-beam adhesive stress analysis then lies in allowing for the computation of the updated secant stiffness matrix of the element due to the projection of the adherend stresses onto the specified stress-strain evolution law (see Fig.50).



**Figure 50.** Computation of the through-thickness adherend secant properties. Adaptation of the classical theory of beam plasticization to the particular formulation of the BBe element. Introduction of adherend material nonlinearities.

Then, and similarly to the introduction of adhesive material nonlinearities, the vector of internal reactions  $L^{int} = K^{(s)}U$  can be computed from both the secant stiffness matrix  $K^{(s)}$  at iteration  $n$  and the vector of nodal displacements  $U$  while  $L^{ext}$  can be expressed from the secant stiffness matrix  $K^{(s)}$  at iteration  $n-1$  and the vector of nodal displacements  $U$ .

The vector of imbalanced loads  $R(U)$  can then be expressed in the form of:

$$R(U) = K^{(s)}(U^{n-1})U^n - K^{(s)}(U^n)U^n \quad (125)$$

where  $R(U)$  refers here to the vector of imbalanced loads resulting from the projection of the adherends stresses onto the specified stress-strain evolution law.

A great advantage of introducing adherend material nonlinearities using the same modified Newton-Raphson procedure as for the adhesive layer lies in the fact that both adhesive and adherend material nonlinearities are simultaneously addressable using the exact same iteration convergence procedure. Then not requiring for nested iterative convergence procedures to address first the effect of the adhesive stress-strain nonlinear evolution law and in a second time the effect of the adherend stress-strain nonlinear evolution law.

### 2.5.2.

C

omparison with Finite Element (FE) analyses

**Description of the Finite Element (FE) models.** For simplification purpose, here is investigated the mechanical response of a cantilever beam in pure flexion only (see Fig.51). However the afore described procedure is not limited to the introduction of adherends material plasticity within the outer beam elements only, and is capable of addressing simultaneously the effect of adherends plasticization in both outer beam and BBe elements (see Chapter 3). The simulation is performed using SAMCEF FE Code v14-1.02. The specimen is considered as a monolithic beam facing elastic perfectly plastic axial stress-strain evolution law (see Fig.47). The specimen is meshed using 2D SAMCEF type T015 elements. SAMCEF type T015 elements have linear interpolation functions and 4 internal modes (ie. 4 nodes and 12 degrees of freedom). The normal integration scheme is chosen.

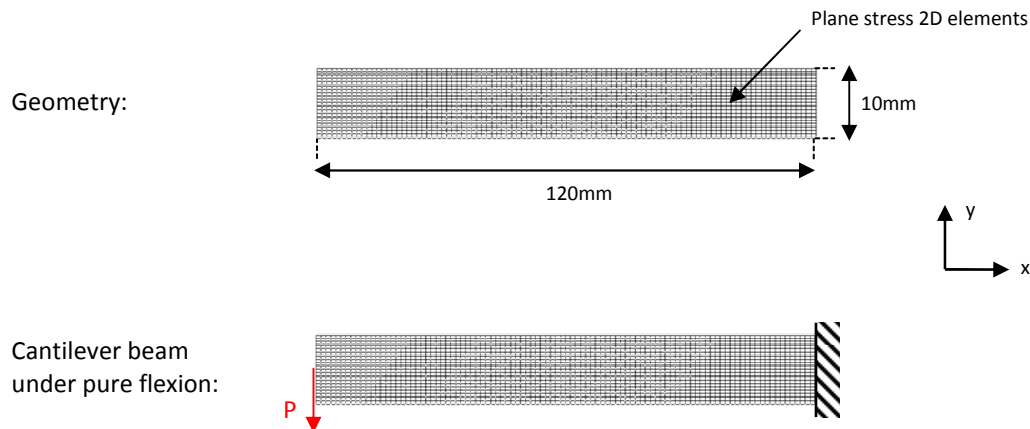


**Figure 51.** Schematic representation of the cantilever beam in pure flexion. Description of the Finite Element (FE) models. Comparison with Finite Element (FE) analyses.

Similarly to [Section 2.4.6](#), the right end clamped boundary condition is modeled by constraining separately the neutral fiber and the surrounding cross-section so that it fits as best the boundary conditions as described in the simplified 1D-beam adhesive stress analysis. The projection of through-thickness axial stresses only is then ensured by modifying the implemented Hill's yield criterion as:

$$\sigma_{Hill} = \sqrt{\frac{1}{B+C} \left( A(\sigma_{yy} - \sigma_{zz})^2 + B(\sigma_{zz} - \sigma_{xx})^2 + C(\sigma_{xx} - \sigma_{yy})^2 + 6(L\tau_{xy}^2 + M\tau_{yz}^2 + N\tau_{zx}^2) \right)} \geq \sigma_p \quad (126)$$

where:

$$\begin{pmatrix} A \\ B \\ C \\ L \\ M \\ N \end{pmatrix} = \begin{pmatrix} -1/2 & 1/2 & 1/2 & 0 & 0 & 0 \\ 1/2 & -1/2 & 1/2 & 0 & 0 & 0 \\ 1/2 & 1/2 & -1/2 & 0 & 0 & 0 \\ 0 & 0 & 0 & 1/6 & 0 & 0 \\ 0 & 0 & 0 & 0 & 1/6 & 0 \\ 0 & 0 & 0 & 0 & 0 & 1/6 \end{pmatrix} \begin{pmatrix} 1/X_0^2 \\ 1/Y_0^2 \\ 1/Z_0^2 \\ 1/R_0^2 \\ 1/S_0^2 \\ 1/T_0^2 \end{pmatrix} \quad (127)$$

where  $X_0$ ,  $Y_0$ ,  $Z_0$ ,  $R_0$ ,  $S_0$  and  $T_0$  respectively refer to initial set of tensile and shear yield stresses of the material ([Samcef 2013](#)).

Then assuming  $B=1$  and  $A=C=L=M=N=0$  falls:

$$\begin{pmatrix} 1/X_0^2 \\ 1/Y_0^2 \\ 1/Z_0^2 \\ 1/R_0^2 \\ 1/S_0^2 \\ 1/T_0^2 \end{pmatrix} = \begin{pmatrix} -1/2 & 1/2 & 1/2 & 0 & 0 & 0 \\ 1/2 & -1/2 & 1/2 & 0 & 0 & 0 \\ 1/2 & 1/2 & -1/2 & 0 & 0 & 0 \\ 0 & 0 & 0 & 1/6 & 0 & 0 \\ 0 & 0 & 0 & 0 & 1/6 & 0 \\ 0 & 0 & 0 & 0 & 0 & 1/6 \end{pmatrix}^{-1} \begin{pmatrix} 0 \\ 1 \\ 0 \\ 0 \\ 0 \\ 0 \end{pmatrix} = \begin{pmatrix} 1 \\ 0 \\ 1 \\ 0 \\ 0 \\ 0 \end{pmatrix} \quad (128)$$

So that the modified Hill's yield criterion finally ends in ( $\sigma_{zz}=0$  due to plane-stress):

$$\sigma_{Hill} = \sqrt{B(\sigma_{zz} - \sigma_{xx})^2} = \sigma_{xx} \geq \sigma_p \quad (129)$$

**Convergence of the Finite Element (FE) models.** Similarly to [Section 2.4.6](#), the mesh of each FE models is optimized so that the solution obtained is independent on its refinement. The optimization of the mesh is based on the following hypotheses: (i) the mesh of the specimen is uniformly distributed over the length, the width and the thickness of the adherends and (ii) the aspect ratio of each element of the structure is equal to 1. It is shown from hypotheses (i) to (ii) that the mesh of the entire specimen then depends on the number of elements within the length of the specimen only (see [Appendix 5](#)).

**Comparison with the simplified 1D-Beam adhesive stress analysis.**

*Description of the simplified 1D-beam adhesive stress analyses.* Here is investigated the mechanical response of a cantilever beam in pure flexion. A schematic representation of the corresponding simplified 1D-Beam adhesive stress analysis is presented in Fig.52.

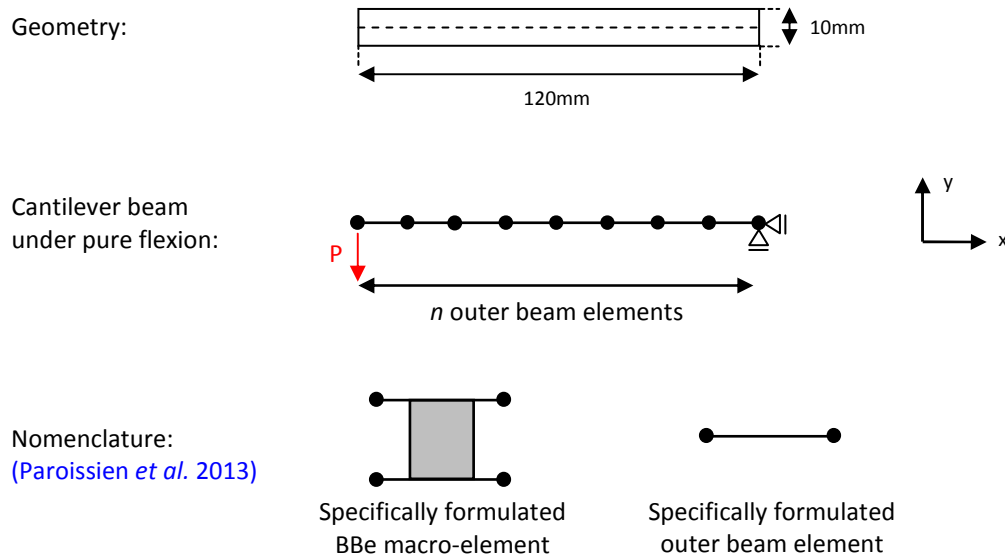
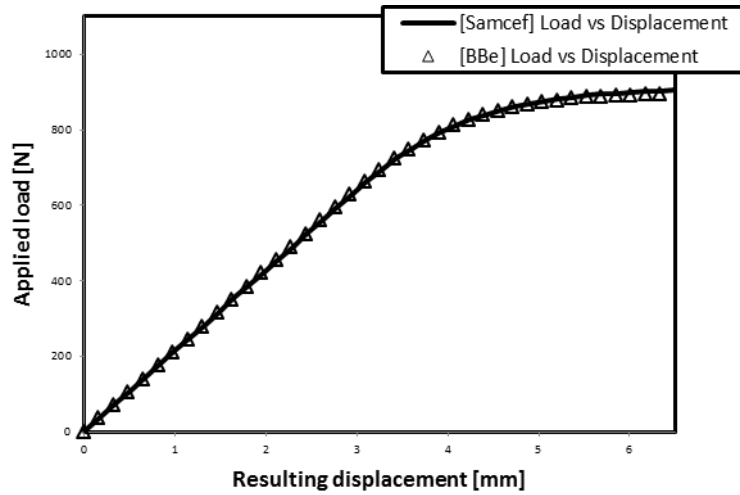


**Figure 52.** Schematic representation of the cantilever beam in pure flexion. Description of the simplified 1D-beam adhesive stress analyses. Comparison with the simplified 1D-beam adhesive stress analysis.

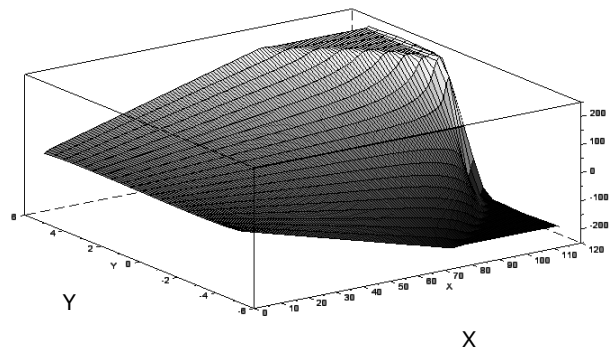
*Convergence of the simplified 1D-beam adhesive stress analyses.* As presented in Section 2.4, the introduction of adhesive material nonlinearities in the particular formulation of the simplified 1D-beam adhesive stress analysis resulted in the need of meshing the adhesive overlap within an adequate number of BBe macro-elements to reconstitute the true behavior of the adhesive layer. Similarly, the introduction of material nonlinearities within the constitutive behavior of the adherends results in the need of meshing each adherend with an adequate number of outer beam elements. To allow for the comparison of converged results, the number of outer beam elements is then optimized so that the solution obtained is independent on its refinement (see Appendix 5).

*Comparison with Finite Element (FE) analyses.* Fig.53 presents the comparison between semi-analytical results and FE predictions in terms of Load versus Resulting Displacement curve (a) and axial stress distribution along the specimen (b). Fig.53-(c) finally presents the *normalized deviation* between semi-analytical and FE adherend stress distributions due to bending loadings. Good agreement is shown.



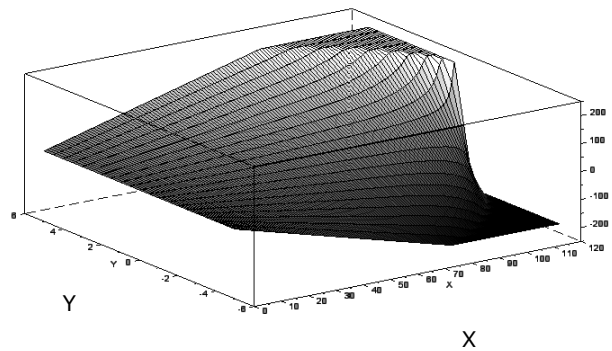
(a)

Finite Element:

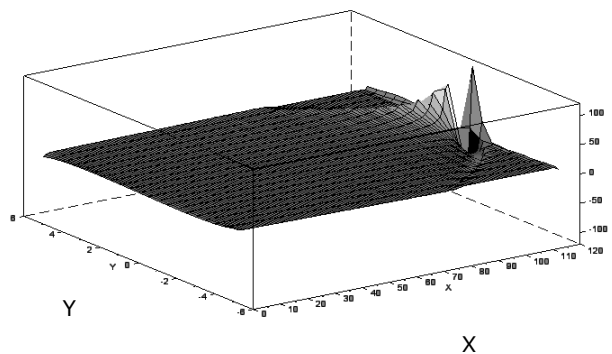


Axial stress distribution

Simplified 1D-Beam analysis:



Axial stress distribution



Normalized deviation

(b)

(c)

Figure 53. Comparison with Finite Element (FE) analyses in pure flexion. Cantilever beam in pure flexion. Description of the Finite-Element (FE) models. Introduction of adherend material nonlinearities.

## 2.6.

C

## Conclusion and discussion

Within the present chapter, an original procedure derived from the classical FE method is adapted to the particular formulation of the BBe element. Since the original approach developed in (Paroissien 2066, Da Veiga 2009, Paroissien *et al.* 2013) does not use the concept of shape matrix, so that the nodal displacements are not approximated but lies from the exact resolution of the set of joint governing differential equations (see Sections 2.2 and 2.3), specific calculations have to be performed to account for the possible non-linear behavior of the adhesive layer. Then an original procedure allowing for the nonlinear behavior of the adhesive layer to be accounted for (i.e. derived from the classical FE method) is adapted to the particular formulation of the BBe element. The main originality of the presented Newton-Raphson iteration procedure lies in the use of the secant stiffness properties to define the nonlinear problem. The vector of imbalanced loads (i.e. resulting from the projection of the non-linear adhesive stresses) is thus computed through the knowledge of the adhesive secant stiffness properties only. The suggested procedure then allows for various non-linear adhesive behaviors to be accounted for (ie. softening, plastic, coupled, etc) with no restriction on the specimen geometry. The proposed adhesive material models are formulated under a two dimensional mixed-mode model that account for the possible interaction (interdependency) between both pure mode I and pure mode II adhesive stress-strain evolutions laws. The two dimensional mixed-mode model is inspired from the classical Cohesive Zone Modeling (CZM) theory. The results obtained from the suggested solution procedure are then compared to those of two sandwich type analyses involving nonlinear adhesive stress-strain evolution laws. Finally, the results obtained from the so modified simplified 1D-beam adhesive stress analysis are compared to those of 2D FE predictions involving cohesive interface elements. Good agreement is shown with both nonlinear sandwich type analyses and FE predictions.

To conclude, the preceding iterative solution procedure is upgraded so that it can account for both adhesive and adherends material nonlinearities simultaneously (i.e. with no need of nested iterative convergence schemes). Then, an original way of accounting for the effect of the surrounding adherends plasticization based on an adaptation of the classical theory of beam plasticity (Oudin 2011) is presented and developed in view of its implementation. The results obtained from the so modified simplified 1D-beam adhesive stress analysis are compared to those of 2D FE predictions involving elastic perfectly plastic adherends stress-strain evolution laws. For simplification purpose, the comparison is made in terms of a cantilever beam in pure flexion only. Good agreement is shown.

By the use of the presented simplified joint kinematic, it is shown that the mechanical response of a large range of bonded overlaps can be simulated using a restricted number of specifically formulated BBe elements (i.e. only one when facing linear elastic perturbations only). Those models based on the use of BBe elements thus takes the advantage of the flexibility of FE methods: (i) wide application range, (ii) open assembly procedure, (iii)

specified boundary conditions, etc, and the robustness of theoretical approaches: (i) analytical resolution of the set of governing differential equations, (ii) results independent on the mesh refinement when facing linear elastic adhesive deformations, (iii) results shown as rapidly converging toward an asymptote when facing non-linear adhesive deformations, etc.

Since classical 2D FE analyses approximates the solutions in terms of both adhesive and adherends kinematics, converged FE results generally imply highly refined meshes and so time-consuming computations. The suggested simplified 1D-beam adhesive stress analysis thus finds it interest in many extensive parametric studies. It is shown from Fig.54 that the gain in terms of total number of degrees of freedom can vary from a factor 50 to 500 depending on the specimen geometry (i.e. ENF, DCB and MMB) and can easily be increased by a factor 3 or 4 since non-linear effects are generally limited to the close vicinity of the overlap edges (see Fig.44, Fig.45 and Fig.46). Moreover the given procedure has been shown as 50 to 100 times quicker than equivalent 2D/3D FE predictions (Paroissien *et al.* 2013).

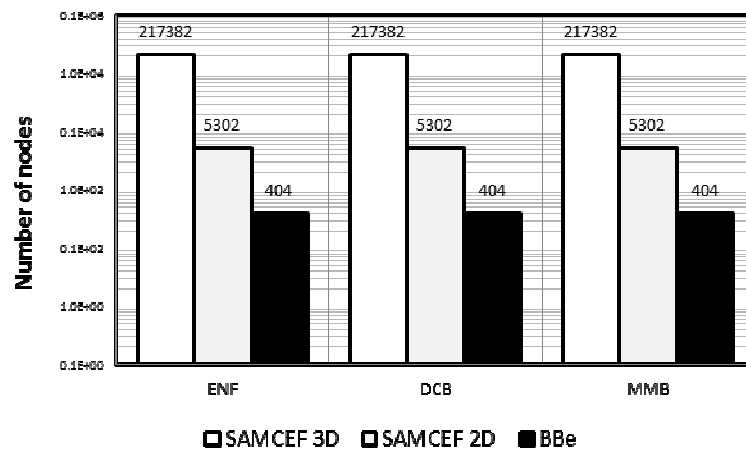


Figure 54. Comparison between semi-analytical and Finite Element (FE) analyses. Converged results. Comparison of the total number of nodes.

For convenience, all of the later numerical analyses will then be performed using the simplified 1D-beam adhesive stress analysis exclusively, so that it allows for extensive parametric studies to be performed at low computation costs.

## **Chapter 3. On the experimental characterization of thin adhesive layers**

Chapter 3 aims at presenting experimental protocols for the characterization of thin adhesive interfaces. First, three characterization protocols based on the energetic balance associated to the computation of the path independent J-integral (Rice 1968) are presented. Several deviations/limitations are set out and discussed. Then, a new characterization technique based on the monitoring of the adherend-to-adherend displacement field is presented and developed in view of its implementation. The new characterization protocol is then compared to semi analytical predictions and experimental testing. Good agreement is shown with both semi analytical predictions and experimental testing in the case of metal-to-metal adhesive bonding.

### **Table of contents**

- 3.1. 3.1 Introduction
- 3.2. Organization of the chapter
- 3.3. Bulk material properties
  - 3.3.1. Adherends
  - 3.3.2. Adhesive
- 3.4. On the experimental characterization of CZM: Energetic methods
  - 3.4.1. Overview
  - 3.4.2. On the constitutive relationship of a thin adhesive layer loaded in pure shear (mode II)
  - 3.4.3. On the constitutive relationship of a thin adhesive layer loaded in pure peel (mode I)
  - 3.4.4. On the constitutive relationship of a thin adhesive layer loaded in mixed-mode I/II
  - 3.4.5. Confrontation with semi-analytical predictions
- 3.5. On the experimental characterization of CZM: The direct method
  - 3.5.1. Overview
  - 3.5.2. On the constitutive relationship of a thin adhesive layer loaded in pure shear (mode II)
  - 3.5.3. On the constitutive relationship of a thin adhesive layer loaded in pure peel (mode I)
  - 3.5.4. On the constitutive relationship of a thin adhesive layer loaded in mixed-mode I/II
  - 3.5.5. Confrontation with semi-analytical predictions
- 3.6. Experimental investigations on metal-to-metal adhesive joints
  - 3.6.1. Experimental data processing
  - 3.6.2. Experimental setup, preparation of the specimens and instrumentations
  - 3.6.3. Material description
  - 3.6.4. Quasi-static experiments
- 3.7. Conclusion and discussion

## 3.1.

I

## Introduction

According to (Crocombe 2009), the CZM have the advantage of: (i) considering finite strains and stresses at the adhesive crack tip, (ii) indicating both damage initiation and propagation as direct outputs, (iii) advancing the crack tip as soon as the local energy release rate reaches its critical value with no need of complex moving mesh techniques.

The Finite Element (FE) method is one of the first simulation techniques that have taken advantage of the CZM by developing specific elements allowing for the modeling of the fracture process of thin interfaces. However, accurate FE strength analyses of bonded assemblies are generally computationally expensive and can lead to the rise of numerical artifacts.

In (Paroissien 2006, Da Veiga 2009, Paroissien *et al.* 2013) and in Chapter 1, a semi-analytical procedure allowing for the modeling of various adhesive joint configurations facing in-plane adhesive loadings has been developed and validated in the case of both adhesive and adherends material nonlinearities. For convenience, the aforementioned procedure will be thereafter referred as the simplified 1D-beam adhesive stress analysis. The simplified 1D-beam adhesive stress analysis allows for the resolution of the (Hart-Smith 1973a, Hart-Smith 1973b) set of governing differential equations of the joint in the case of linear (non-linear) adhesive (adherend) stress-strain evolution laws. The method is inspired by the FE method. However it allows for the semi-analytical resolution of the simplified system of governing differential equations of the joint at low computational costs. Good agreement is shown with both sandwich type analyses and classical 2D FE analyses involving cohesive interface elements during both damage initiation and propagation phases (see Chapter 2).

However, both FE and simplified 1D-beam adhesive stress analyses are based on the modeling of the adhesive interfacial strength through a set of adhesive cohesive properties (e.g. in pure mode I, pure mode II and mixed-mode I/II). Accurate experimental protocols for the measurement of the effective adhesive cohesive properties are then essential for the strength prediction of adhesively bonded joints.

The present section then aims to present different existing experimental protocols for the experimental characterization of the mechanical properties of thin adhesive layers and to discuss their inherent limitations. Then, a brand new experimental protocol to evaluate the effective stress-strain relationship of thin adhesive layers in mode I, mode II and mixed-mode I/II is presented and developed in view of its implementation. For convenience, the adhesive stress-strain relationships will be thereafter referred as the adhesive traction separation laws.

## 3.2.

O

## Organization of the chapter

First, the response of classical adhesive (adherend) Tensile Test (TT) specimens under pure axial loading conditions is investigated. The results are presented in terms of axial stress

versus axial deformation and Poisson's ratio versus axial deformation evolution laws. Then, the linear elastic properties of both the adherends and the adhesive materials are derived and compared to conventional values found in the open literature. Finally, the limitations of such classical approaches are set out and discussed.

Secondly, three existing characterization protocols based on the energetic balance of three adhesive Fracture Mechanics test specimens are presented (e.g. ENF, DCB and MCB). For convenience, these experimental characterization protocols will be thereafter referred as the energetic methods. For lecturer comfort, a short description of the mathematical foundations of each experimental protocol is presented. However a more comprehensive description of each protocol can be found in ([Anderson \*et al.\* 2003](#), [Alfredsson 2004](#), [Hogberg \*et al.\* 2007](#)). The underlined simplifications as well as the direct limitations of those approaches are set out and discussed. The results obtained are finally compared to those of semi-analytical analyses. Significant deviations with semi-analytical predictions are pointed out and different explanations are presented.

Thirdly, a new and original characterization protocol based on the experimental monitoring of the adherend-to-adherend displacement field nearby the adhesive crack tip is presented and developed in view of its implementation. For convenience, the suggested experimental characterization protocol will be thereafter referred as the direct method. The underlined simplifications and limitations are then set out and discussed and the results obtained compared to those of semi-analytical analyses. Good agreement is shown for various adhesive joint test configurations and adhesive (adherends) set of material properties.

Finally, the results of an experimental test campaign are provided so that the new characterization protocol is validated in the case of metal-to-metal adhesive bonding in pure mode I, pure mode II and mixed-mode I/II solicitations. Good agreement is shown.

3.3.		B
	ulk material properties	
3.3.1.		A
	dherends	

First, the mechanical response of 4 aluminum Tensile Test (TT) bulk specimens under pure axial loading conditions is here investigated. Each TT specimen is manufactured from a laminated aluminum-magnesium-silicon aluminum alloy (6060 series). The geometry of each specimen is controlled after fabrication. The controlled dimensions are listed in [Fig.55](#).

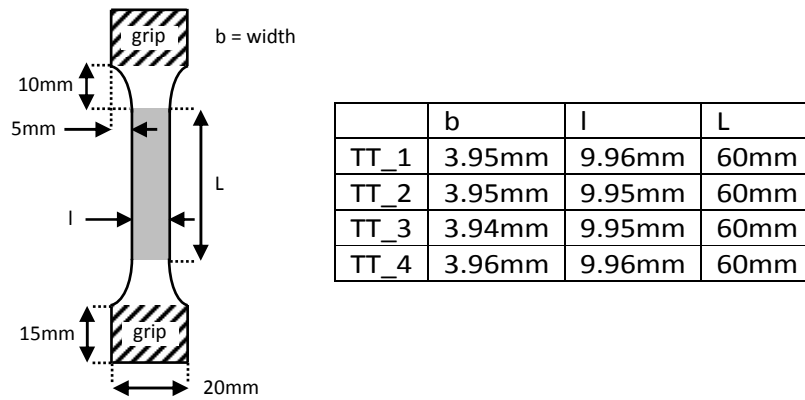


Figure 55. Geometry of the aluminum Tensile Test (TT) bulk specimens. Aluminum= 6060 series. Bulk material properties.

All the tests are performed on an electro-mechanical test machine (Ref: Instron AI735-1325). Both the applied load, the resulting displacement and the specimen displacement field are measured during the tests. The evolution of both the applied load and the resulting displacement are measured using the build in machine load and displacement cells. The evolution of the specimen displacement field is measured using the Digital Image Correlation (DIC) technique (see Fig.56). The axial deformation as well as the Poisson's ratio of the specimen are computed from the evolution of the specimen displacement field. The specimens are displacement loaded using the build in machine displacement command instruction. The loading speed is arbitrary fixed at 0.5mm/min.

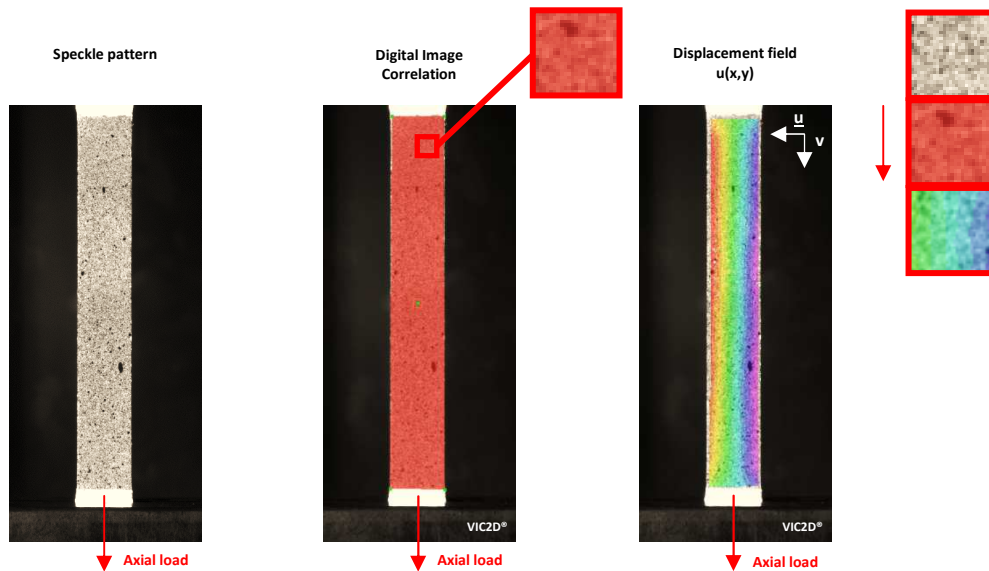


Figure 56. Geometry of the aluminum Tensile Test (TT) bulk specimens. Aluminum= 6060 series. Bulk material properties.

Fig.57 then presents the results obtained in terms of both the axial stress-strain evolution law (a) and the evolution of the measured Poisson's ratio (b) along the experiment. It is seen from Fig.57-(a) that the aluminum bulk material exhibits two distinct phases. The first one, the linear elastic phase, appears as extremely limited compared to the whole deforming

capability of the aluminum alloy (e.g. ~3% of the whole deforming capability). The second phase, the plastic phase, appears on another side as extremely important (e.g. ~97% of the whole deforming capability). It then suggests that the plasticization of the surrounding adherends could possibly play a significant role in the degradation process of adhesive sandwich structures. This statement will be discussed later on in Sections 3.5 and 3.6. Both the linear elastic Young's tensile modulus and the Poisson's coefficient ratio (Nu) of the studied aluminum alloy are extracted from the obtained results (see Tab.6).

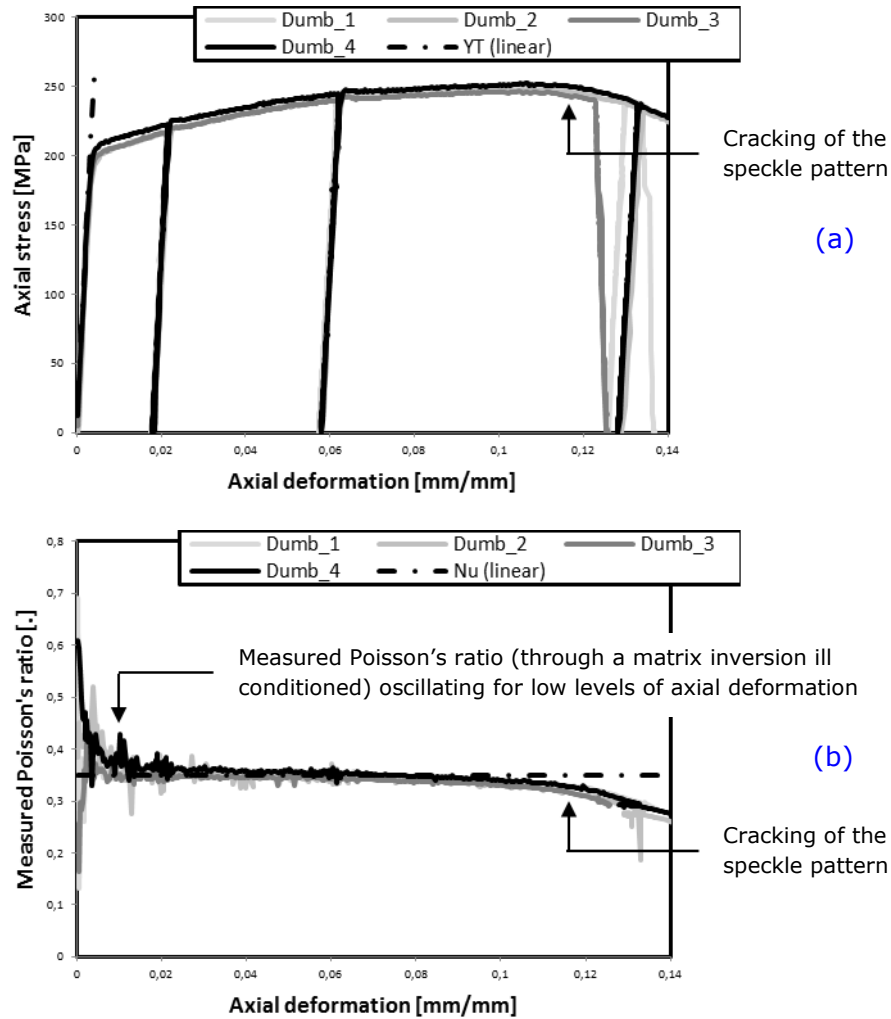


Figure 57. Experimental characterization of aluminum Tensile Test (TT) bulk specimens in terms of axial stress-strain evolution law (a) and evolution of the measured Poisson's ratio (b). Aluminum= 6060 series. Bulk material properties.

Tab 6. Experimental characterization of aluminum Tensile Test (TT) bulk specimens. Elastic material properties. Young's Tensile (YT) modulus. Poisson's ratio (Nu). Aluminum= 6060 series. Bulk material properties.

Young's Tensile modulus (YT)	Poisson's ratio (Nu)
66000 MPa	0.35

3.3.2.

A

adhesive

Secondly, the mechanical response of 4 adhesive TT bulk specimens under pure axial loading conditions is here investigated. Each adhesive TT specimen is manufactured using the SAF-30MIB adhesive paste from AEC-Polymers. The SAF-30MIB adhesive paste is a room-temperature cured highly flexible methacrylate adhesive used in the outboard manufacturing/repairing industry. The geometry of each specimen is controlled after fabrication. The controlled dimensions are listed in Fig.58.

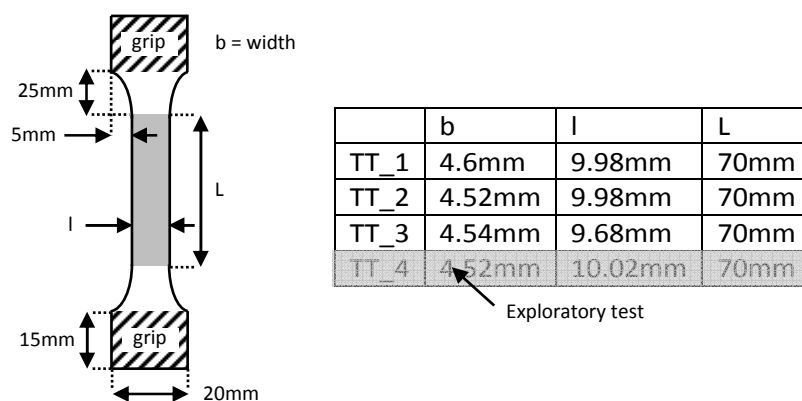
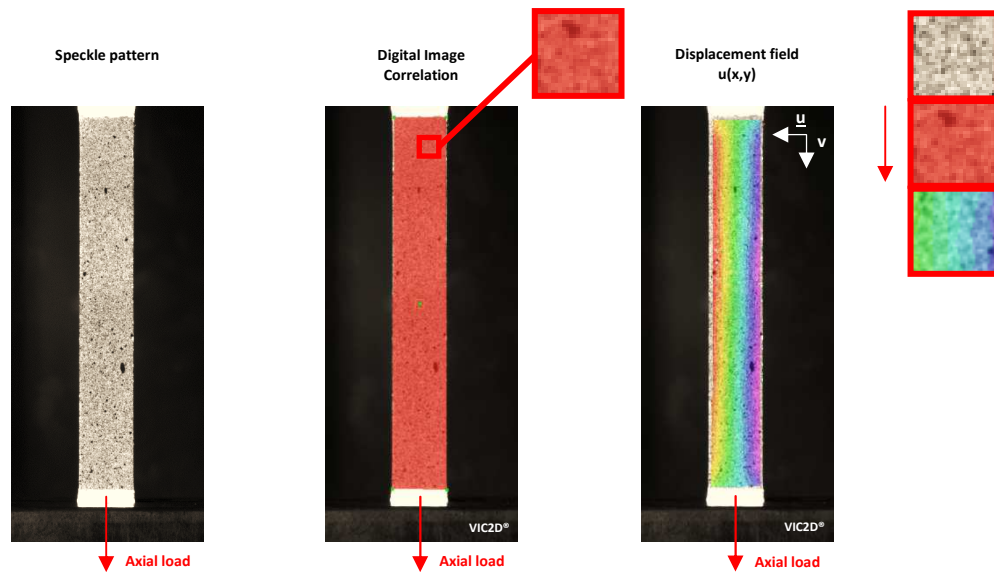


Figure 58. Geometry of the adhesive Tensile Test (TT) bulk specimens. Adhesive= SAF-30MIB. Bulk material properties.

Similarly to Section 3.3.1, all the tests are performed on an electro-mechanical test machine (Ref: Instron AI735-1325). Both the applied load, the resulting displacement and the specimen displacement field are measured during the tests. The evolution of both the applied load and the resulting displacement are measured using the build in machine load and displacement cells. The evolution of the specimen displacement field is measured using the Digital Image Correlation (DIC) technique (see Fig.59). The axial deformation as well as the Poisson's ratio of the specimen are computed from the evolution of the specimen displacement field. Similarly to Section 3.3.1, the adhesive specimens are displacement loaded using the build in machine displacement command instruction. However various loading speeds are applied to each specimen (e.g. TT\_1= 0.25mm/min, TT\_2= 0.5mm/min and TT\_3= 0.75mm/min).



**Figure 59.** Geometry of the adhesive Tensile Test (TT) bulk specimens. Adhesive= SAF-30MIB. Bulk material properties.

**Fig.60** then presents the results obtained in terms of both the axial stress-strain evolution law **(a)** and the evolution of the measured Poisson's ratio **(b)** along the experiment. Similarly to the aluminum bulk material, it is seen from **Fig.60-(a)** that the adhesive bulk material exhibits two distinct phases. The linear elastic phase appears again as extremely limited compared to the entire deforming capability of the adhesive bulk material (e.g.  $\sim 5\%$  of the whole deforming capability). On another side, the plastic phase appears as extremely important (e.g.  $\sim 95\%$  of the whole deforming capability). It is also seen from **Fig.60-(a)** that significant hysteresis effects appears during unloading phases. It then suggests that a significant amount of energy is probably dissipated during unloading phases. However it appears that this hysteresis effect does not clearly depend on the loading speed (i.e. TT\_1= 0.25mm/min, TT\_2= 0.5mm/min and TT\_3= 0.75mm/min). Then making think that instead of being due to viscous dissipative effects, this hysteresis effect could possibly be the result of a nonlinear elastic behavior of the adhesive material (i.e. Mullins effect). Additionally, **Fig.60-(b)** shows the measured Poisson's ratio as linearly depending on the axial deformation of the bulk specimen. This linear dependency of the measured Poisson's ratio can be due to several reasons. First, it is extremely complicated to entirely control the manufacturing process of adhesive TT bulk specimens. Indeed, the manufacturing process of TT bulk specimen using adhesive pastes is highly dependent on various environmental factors such as the ambient temperature, the atmosphere, or factors related to the manufacturing process itself such as the open/curing cycle, the mixing or the holding pressure. However, the geometry of each specimen has been controlled after fabrication. Which would have theoretically limited the effects linked to possibly poor manufactured specimens. Secondly, expecting a Poisson's ratio that does not depend on the deformation of the material itself is an idea that is taken from the classical mechanics of metallic materials. However, an adhesive can be at best considered as a semi-crystalline polymer material. Indeed, while the physical mechanisms hidden behind the plasticity of metallic materials is generally caused by two main modes of deformation in the crystal lattice, slip and twinning, the plastic deformation process of semi-

crystalline polymers generally involves a complete molecular rearrangement of the chain-folded lamellar morphology into a more or less chain-unfolded fibrillary microstructure (Bartczak 2010). In metallic plasticization, slip is a shear deformation which locally moves the atoms through several interatomic distances relative to their initial positions. Twinning is the plastic deformation which takes place along two planes due to a set of forces applied to a given metal piece. Then, it is not senseless to think that the molecular rearrangement of the adhesive material due to its plasticization can significantly modify the measured Poisson's ratio along the experiment. Nevertheless, for simplification purpose, the effective adhesive Poisson's ratio will be thereafter averaged along the experiment (see Fig.60 and Tab.7).

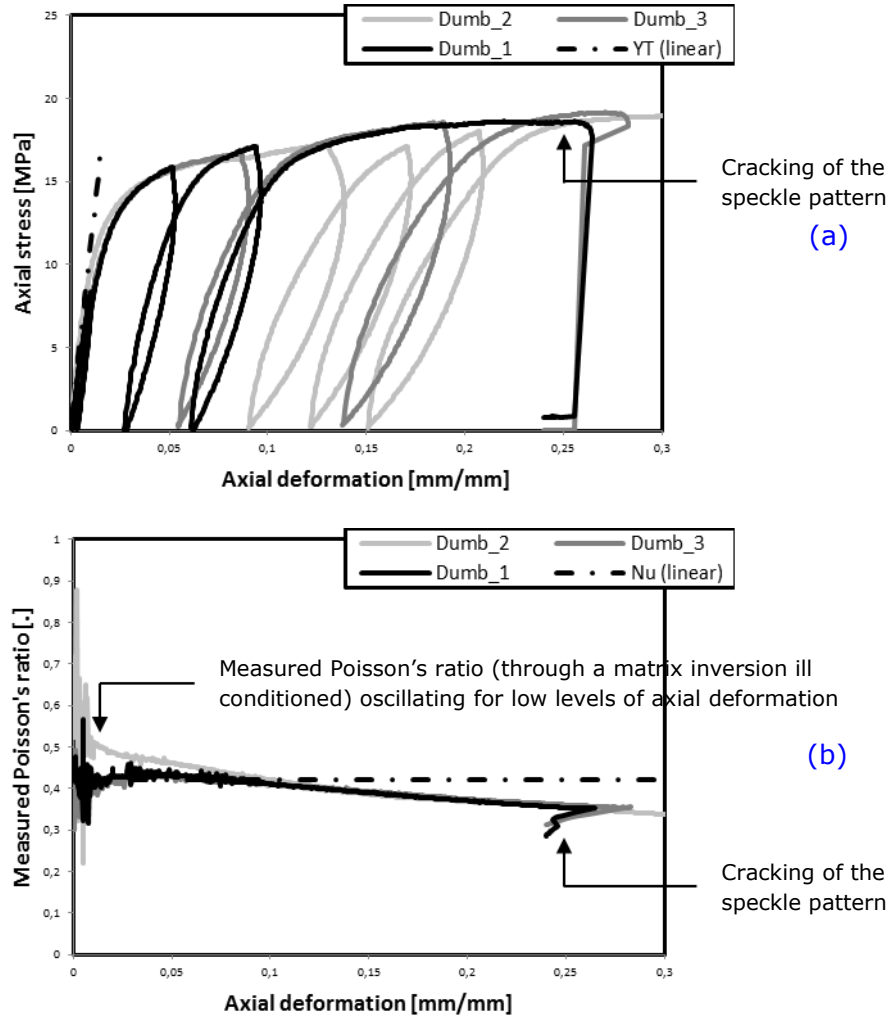


Figure 60. Experimental characterization of adhesive Tensile Test (TT) bulk specimens in terms of axial stress-strain evolution law (a) and evolution of the measured Poisson's ratio (b). Adhesive= SAF-30MIB. Bulk material properties.

Tab 7. Experimental characterization of adhesive Tensile Test (TT) bulk specimens. Elastic material properties. Young's Tensile (YT) modulus. Poisson's ratio (Nu). Adhesive= SAF 30MIB. Bulk material properties.

Young's Tensile modulus (YT)	Poisson's ratio (Nu)
1100 MPa	0.42

## 3.4. On the experimental characterization of CZM: Energetic methods

## 3.4.1. Overview

All of the experimental protocols presented in this section reclaim the concept of the adhesive specimen energetic balance associated with the computation of the path independent J-integral (Rice 1968) onto specifically formulated integration paths:

$$J = \int_{\Gamma} W dy - \bar{T} \frac{d\bar{u}}{dx} ds \quad (131)$$

where  $W$  refers to the strain energy density,  $\bar{T}=n\sigma$  to the traction vector,  $\sigma$  to the stress tensor,  $\bar{u}$  to the displacement vector,  $n$  to the normal unit vector directed outward to the counter-clock wise integration path  $\Gamma$ , and  $(x,y)$  to the specified two-dimensional coordinate system.

However the aim of the following section is not to cover all of the existing protocols for the experimental characterization of CZM using energetic balance, but to highlight three of them which are according to the author of the present dissertation representative of the characterization of adhesive interfaces in both mode I, mode II and mixed-mode I/II. For convenience, these characterization protocols will be thereafter referred as the energetic methods.

## 3.4.2. On the constitutive relationship of a thin adhesive layer loaded in pure shear (mode II)

In this section is presented an experimental protocol to determine the constitutive stress-strain relationship of a thin adhesive layer loaded in pure shear (mode II). This experimental protocol has been firstly introduced in (Alfredsson *et al.* 2003) and taken up in (Alfredsson *et al.* 2003, Alfredsson 2004, Leffler *et al.* 2006, Biel *et al.* 2011). This protocol applies to End-Notched Flexure (ENF) adhesive specimens. The ENF adhesive specimen consists in two adherends partially joined by a thin adhesive layer. The antisymmetric geometry and loading conditions of the specimen provide essentially pure mode II solicitations of the adhesive layer. However, significant mode I adhesive stresses appear nearby center of the specimen (see Fig.61). For convenience, the unbonded area of the specimen will be thereafter referred as the adhesive crack tip.

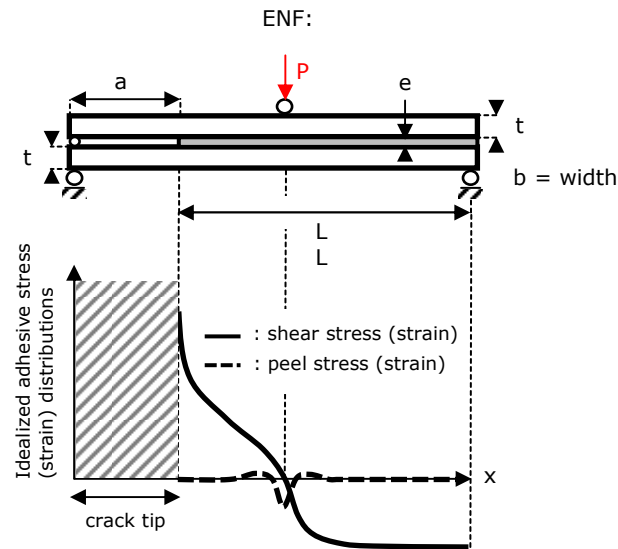


Figure 61. Schematic representation the End-Notched Flexure (ENF) adhesive joint specimen. Idealized adhesive stress (strain) distributions. On the constitutive relationship of a thin adhesive layer loaded in pure shear (mode II). On the experimental characterization of CZM. Energetic methods.

In (Alfredsson *et al.* 2003) the authors then suggest determining the complete mode II adhesive traction-separation law by simultaneously monitoring both the adhesive instantaneous energy release rate and the adhesive shearing deformation at crack tip. By handling the computation of the path independent J-integral (Rice 1968) onto a specific contour of the adhesive test specimen (see Fig.62), the author then derives an approximate solution to the inverse problem “given the ENF joint specimen behavior, what is the constitutive relationship of the adhesive layer?”.

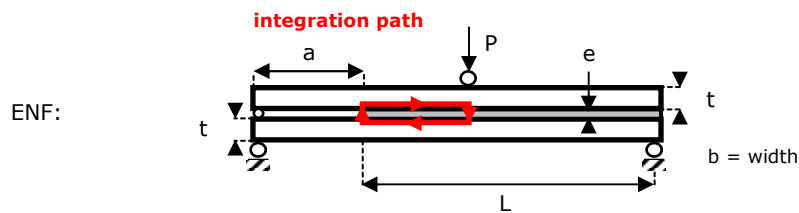


Figure 62. Schematic representation the End-Notched Flexure (ENF) adhesive joint specimen. Computation of the path independent J-integral. Representation of the integration path. On the constitutive relationship of a thin adhesive layer loaded in mixed-mode I/II. On the experimental characterization of CZM. Energetic methods.

Then leading to an expression of the instantaneous energy release rate at crack tip which requires no a priori knowledge on the constitutive stress-strain relationship of the adhesive layer  $\tau(v)$  (132).

$$J(v) = \int_0^v \tau(v) dv \approx \frac{9}{16} \frac{P^2 a^2}{Eb^2 t^3} + \frac{3}{8} \frac{Pv}{bt} - \frac{9}{128} \frac{P^2}{k_s b^2 t^2} \quad (132)$$

where  $J(v)$  here refers to the adhesive mode II instantaneous energy release rate at crack tip,  $v$  to the adhesive shearing deformation at crack tip and  $P$  to the applied load.

To legitimate the use of the different simplifying hypotheses leading to equation (132) the authors suggest using a specifically designed specimen geometry so that:

$$\kappa_s(L/2 - a/2) \geq 5 \quad (133)$$

where  $\kappa_s = \sqrt{8k_s/Et}$ ,  $E$  the adherends Young's tensile modulus,  $k_s$  the initial shearing stiffness of the adhesive layer,  $L$  the total length of the bonded overlap and  $a$  the length of the adhesive crack tip.

However, it is shown from equation (132) that the given relationship is also dependent on the initial shearing stiffness of the adhesive layer  $k_s$ , and not known a priori. To override this initial adhesive stiffness dependence of the relationship, the authors suggest determining  $k_s$  from the early stage data of the experiment.

To this end, the authors show (asymptotically) that:

$$\frac{P}{\nu} = \frac{8}{3} \frac{k_s b t}{\kappa_s a + 1} \rightarrow \left. \frac{dP}{d\nu} \right|_0 = c \quad \text{when } \nu \rightarrow 0 \quad (134)$$

By adjusting a polynomial series to the initial part of the  $P(\nu)$  experimental curve its initial slope  $c$  is determined. Solving equation (134) with respect to  $k_s$ , the authors then suggest determining the initial stiffness of the adhesive layer so that:

$$k_s = \frac{9}{32} \frac{a^2}{Et^3} \left( \frac{c}{b} \right)^2 \left( 1 + \sqrt{1 + \frac{4}{3} \frac{Et^2}{a^2} \frac{c}{b}} \right)^2 \quad (135)$$

Although equation (135) is demonstrated as experimentally suitable in the case of specifically optimized specimen geometries, so that  $\kappa_s(L/2 - a/2) \geq 5$ , an alternative resolution procedure can be used to evaluate the initial stiffness of the adhesive layer. This particular procedure has not been introduced in (Alfredsson *et al.* 2003).

Assuming that the adhesive layer faces purely linear-elastic solicitations at early stage of the experiment, equation (132) can be written as follows:

$$J(\nu) = \int_0^\nu \tau(\nu) d\nu = \frac{1}{2} k_s \nu^2 \approx \frac{9}{16} \frac{P^2 a^2}{Eb^2 t^3} + \frac{3}{8} \frac{P\nu}{bt} - \frac{9}{128} \frac{P^2}{k_s b^2 t^2} \quad \text{when } \nu \rightarrow 0 \quad (136)$$

Then solving equation (136) with respect to  $k_s$ , the initial stiffness of the adhesive layer can be computed as:

$$k_s = \frac{1}{2} \left[ \left( \frac{9}{8} c^2 \frac{a^2}{Eb^2 t^2} + \frac{3}{8} \frac{c}{bt} \right) + \sqrt{\left( \frac{9}{8} c^2 \frac{a^2}{Eb^2 t^2} + \frac{3}{8} \frac{c}{bt} \right)^2 + \frac{9}{16} \frac{c^2}{b^2 t^2}} \right] \quad (137)$$

Finally, the authors suggest deriving the mode II adhesive stress-strain constitutive relationship differentiating the so computed mode II instantaneous energy release rate with respect to the measured adhesive shearing deformation at crack tip, so that:

$$\tau(\nu) = \frac{\partial J}{\partial \nu} \quad (138)$$

### 3.4.3. On the constitutive relationship of a thin adhesive layer loaded in pure peel (mode I)

In this section is presented an experimental protocol to determine the constitutive stress-strain relationship of an adhesive layer loaded in pure peel (mode I). This experimental protocol, derived from the original protocol described in Section 3.4.2, has been firstly introduced in (Anderson *et al.* 2003) and applies to Double Cantilever Beam (DCB) adhesive specimens. The DCB adhesive specimen consists in two adherends partially joined by a thin adhesive

layer. The modified loading (boundary) conditions provide exclusively pure mode I solicitations of the adhesive layer (see Fig.63). For convenience, the unbonded area of the specimen will be thereafter referred as the adhesive crack tip.

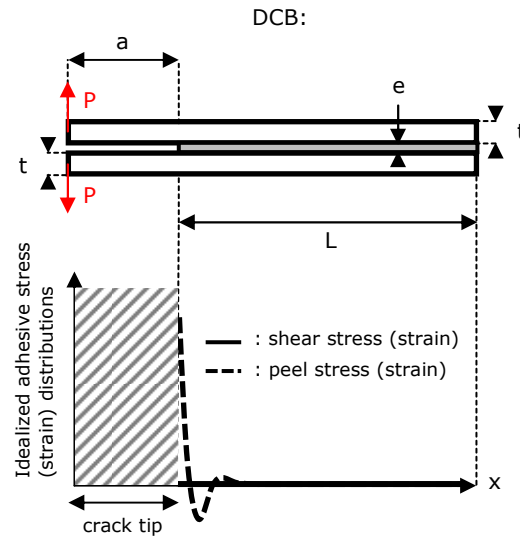
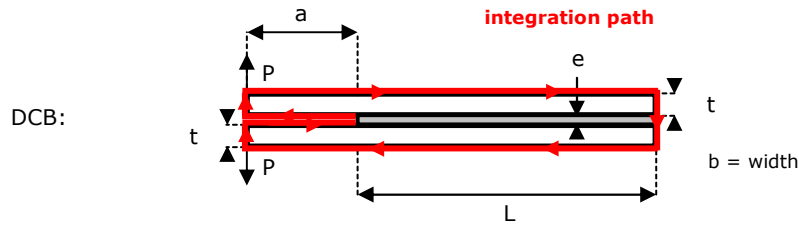


Figure 63. Schematic representation the Double Cantilever Beam (DCB) adhesive joint specimen. Idealized adhesive stress (strain) distributions. On the constitutive relationship of a thin adhesive layer loaded in pure peel (mode I). On the experimental characterization of CZM. Energetic methods.

In (Anderson *et al.* 2003) the authors suggest determining the complete mode I adhesive traction-separation law by simultaneously monitoring both the adhesive instantaneous energy release rate and the adhesive peeling deformation at crack tip. By handling the computation of the path independent J-integral (Rice 1968) onto a different contour of adhesive test specimen (see Fig.64), the authors come to derive a new formula of the instantaneous energy release rate at crack tip which requires no a priori knowledge on the constitutive stress-strain relationship of the adhesive layer  $\sigma(\varepsilon)$  (139).

$$J(\varepsilon) = \int_0^{\varepsilon} \sigma(\varepsilon) d\varepsilon \approx 2 \frac{P\theta(-a)}{b} \quad (139)$$

where  $J(\varepsilon)$  here refers to the adhesive mode I instantaneous energy release rate at crack tip,  $\varepsilon$  to the peeling deformation of the adhesive layer at crack tip,  $P$  to the applied load and  $\theta(-a)$  to the rotation angle of the bending line of adherend 1 (2) at load application point.



**Figure 64.** Schematic representation the Double Cantilever Beam (DCB) adhesive joint specimen. Computation of the path independent J-integral. Representation of the integration path. On the constitutive relationship of a thin adhesive layer loaded in mixed-mode I/II. On the experimental characterization of CZM. Energetic methods.

Finally, the authors suggest deriving the mode I adhesive stress-strain constitutive relationship differentiating the so computed mode I instantaneous energy release rate with respect to the measured adhesive peeling deformation at crack tip, so that:

$$\sigma(\varepsilon) = \frac{\partial J}{\partial \varepsilon} \tag{140}$$

Although not explicitly indicated in the original paper, the afore described theory lies on the assumption that no adhesive peel stresses rises at the free-loaded edge of the adhesive test specimen. As in Section 3.4.2, this condition may be formulated in the form of using a specifically designed specimen geometry, so that:

$$\kappa_p L \geq 5 \tag{141}$$

where  $\kappa_p = \sqrt[4]{24k_p/Et^3}$ ,  $E$  the adherends Young's tensile modulus,  $k_p$  the initial peeling stiffness of the adhesive layer and  $L$  the total length of the bonded overlap.

#### 3.4.4. On the constitutive relationship of a thin adhesive layer loaded in mixed-mode I/II

Although the characterization of the adhesive pure modes is essential for adhesive strength predictions, in-service adhesive bonds are more often expected to serve under mixed-mode I/II than under pure mode I (II) loading conditions. It is then essential to develop techniques that allow for the effective mixed-mode I/II behavior of adhesive interfaces to be addressed/determined.

Based on the approaches developed in Sections 3.4.2 and 3.4.3, this section aims to present an experimental protocol to determine the mixed-mode I/II cohesive properties of a thin adhesive interface. This procedure reclaims once again the concept of the specimen energetic balance associated with the computation of the path independent J-integral (Rice 1968). This experimental protocol has been firstly introduced in (Hogberg 2006) and applies to Mixed-mode Cantilever Beam (MCB) adhesive specimens (see Fig.65).

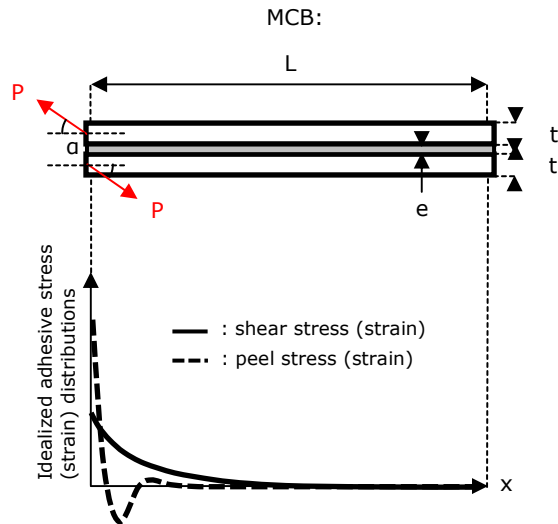


**Figure 65.** Schematic representation the Mixed-mode Cantilever Beam (MCB) adhesive joint specimen. Idealized adhesive stress (strain) distributions. On the constitutive relationship of a thin adhesive layer loaded in mixed-mode I/II. On the experimental characterization of CZM. Energetic methods.

As for the procedures described in Sections 3.4.2 and 3.4.3, the author suggests handling the computation of the path independent J-integral (Rice 1968) onto a specifically formulated contour of the adhesive test specimen (see Fig.66). From this analysis derives a new formula of the instantaneous energy release rate accounting for both the peel and shear adhesive stresses at crack tip (142).

$$J(v, \varepsilon) = \int_0^v \tau(v, \varepsilon) dv + \int_0^\varepsilon \sigma(v, \varepsilon) d\varepsilon \approx \frac{4}{Et} \left( \frac{P \cos(\alpha)}{b} \right)^2 + \frac{P \sin(\alpha)}{b} (w_1' - w_2') \quad (142)$$

where  $J(v, \varepsilon)$  here refers to the mixed-mode I/II instantaneous energy release rate at crack tip,  $\alpha$  to the angle between the antisymmetric loading directions and the neutral fiber of the upper (lower) adherends,  $w_1'$  ( $w_2'$ ) to the first order derivative of the upper (lower) adherend deflection at crack tip and  $P$  to the applied load.

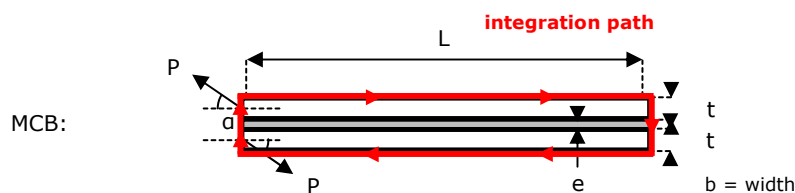


**Figure 66.** Schematic representation the Mixed-mode Cantilever Beam (MCB) adhesive joint specimen. Computation of the path independent J-integral. Representation of the integration path. On the constitutive relationship of a thin adhesive layer loaded in mixed-mode I/II. On the experimental characterization of CZM. Energetic methods.

To legitimate the use of the different simplifying hypotheses leading to equation (142) the author suggests using a specifically designed specimen geometry so that:

$$\min(\kappa_p L, \kappa_s L) \geq 3 \quad (143)$$

Where  $\kappa_p$  and  $\kappa_s$  refer to the two constants previously defined in Sections 3.4.2 and 3.4.3, and  $L$  to the total length of the bonded overlap.

The author finally suggests deriving both the pure mode projections of the adhesive constitutive stress-strain relationship differentiating the so computed mixed-mode I/II instantaneous energy release rate with respect to the measured adhesive peeling and adhesive shearing deformations at crack tip, so that:

$$\sigma(\varepsilon, \nu) = \frac{\partial J}{\partial \varepsilon} \quad \text{and} \quad \tau(\varepsilon, \nu) = \frac{\partial J}{\partial \nu} \quad (144)$$

### 3.4.5. Confrontation with semi-analytical predictions

**Description of the simplified 1D-beam adhesive stress analyses.** To check for the workability/sustainability of the so described theories three semi-analytical models are constructed (e.g. ENF, DCB and MCB). A schematic representation of each semi-analytical model is presented in Fig.67. The adhesive overlap is meshed using  $n$  uniformly distributed BBe elements. Each outer adherend is meshed using a unique and specifically formulated beam element. Both adherends are modeled as linear elastic monolithic beams. The adhesive layer is modeled as a cohesive interface resuming two arbitrary trapezoidal traction separation laws. The set of mechanical properties of both the adhesive layer and the surrounding adherends are given in Tab.8. It is indicated that the adhesive and adherends properties as well as the specimen dimensions have been voluntarily suited to fit the early-design criterion given in equations (133) (141) and (143).

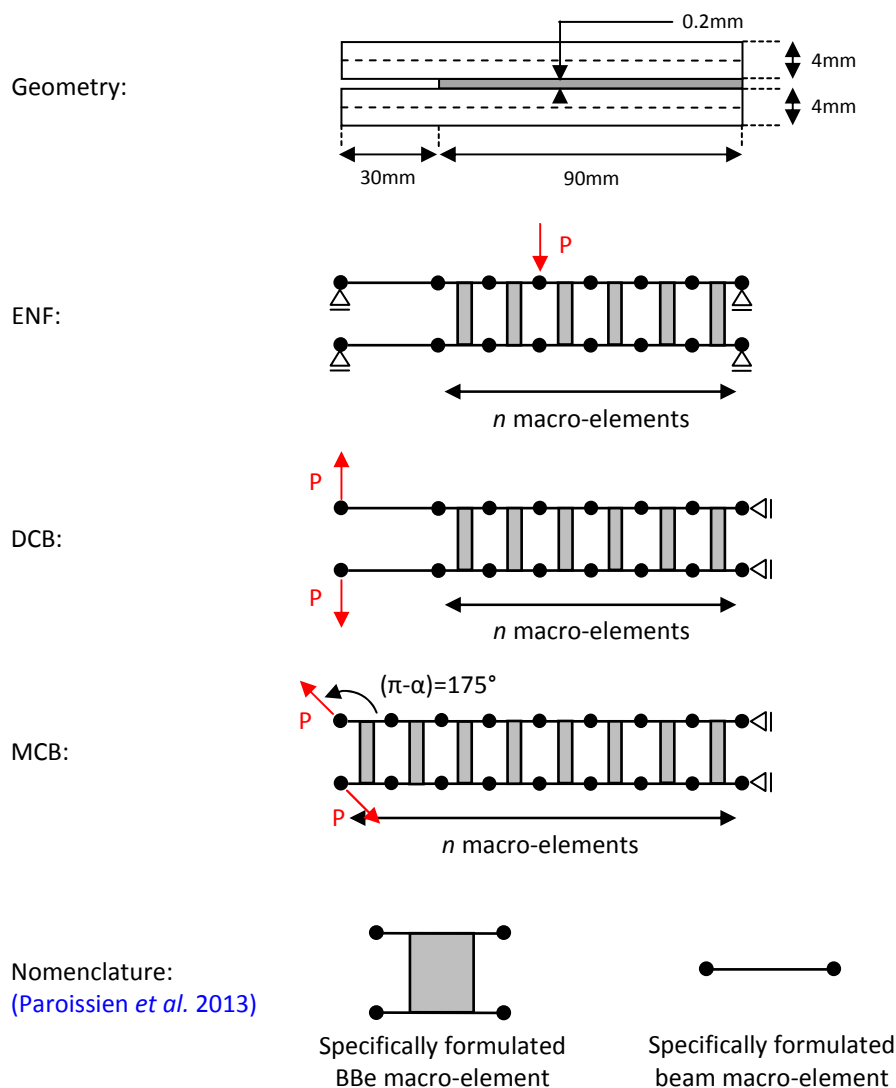


Figure 67. Schematic representation of End-Notched Flexure (ENF), the Double Cantilever Beam (DCB) and the Mixed-mode Cantilever Beam (MCB). Description of the simplified 1D-beam adhesive stress analyses. Confrontation with semi-analytical predictions. On the experimental characterization of CZM. Energetic methods.

Tab 8. Set of mechanical adhesive and adherends properties used in for the confrontation with semi-analytical predictions. Description of the simplified 1D-beam adhesive stress analyses. On the experimental characterization of CZM. Energetic methods.

	Elastic	Plastic	Softening
Model (CZM)	$T(\gamma) = k_T \gamma$	$T(\gamma) = T_1 + k_{T,1}(\gamma - \gamma_1)$	$T(\gamma) = T_2 \frac{\gamma_3 - \gamma}{\gamma_3 - \gamma_2}$
Parameters	$k_T = 145 \text{ MPa}$	$k_{T,1} = 4 \text{ MPa}$ $T_1 = 9.5 \text{ MPa}$ $\gamma_1 = 0.065$	$T_2 = 11.25 \text{ MPa}$ $\gamma_2 = 0.5$ $\gamma_3 = 0.7$
Validity	$0 \leq \gamma \leq \gamma_1$	$\gamma_1 \leq \gamma \leq \gamma_2$	$\gamma_2 \leq \gamma \leq \gamma_3$

	Elastic	Plastic	Softening
Model (CZM)	$S(\varepsilon) = k_s \varepsilon$	$S(\varepsilon) = S_1 + k_{s,1}(\varepsilon - \varepsilon_1)$	$S(\varepsilon) = S_2 \frac{\varepsilon_3 - \varepsilon}{\varepsilon_3 - \varepsilon_2}$
Parameters	$k_s = 310 \text{MPa}$	$k_{s,1} = 9.8 \text{MPa}$ $S_1 = 14 \text{MPa}$ $\varepsilon_1 = 0.045$	$S_2 = 17 \text{MPa}$ $\varepsilon_2 = 0.35$ $\varepsilon_3 = 0.5$
Validity	$0 \leq \varepsilon \leq \varepsilon_1$	$\varepsilon_1 \leq \varepsilon \leq \varepsilon_2$	$\varepsilon_2 \leq \varepsilon \leq \varepsilon_3$

Since the different parameters involved in the computation of the instantaneous energy release rates  $J(v)$ ,  $J(\varepsilon)$  and  $J(v,\varepsilon)$  can be set as direct outputs of the simplified 1D-beam adhesive stress analyses, those are directly taken as they were coming from experimental records. The evolution of each instantaneous energy release rate is then computed with respect to equations (132) (139) and (142) at each step of the simulated load versus displacement history. Finally, the adhesive constitutive relationships  $\sigma(\varepsilon)$  and  $\tau(v)$  are obtained differentiating the so computed instantaneous energy release rates  $J(v)$ ,  $J(\varepsilon)$  and  $J(v,\varepsilon)$  with respect to the associated adhesive crack tip deformations (see equations (138) (140) and (144)) using secant line approximations.

**Confrontation with semi-analytical predictions.** First, a direct comparison between the so predicted stress-strain relationships (energetic method) and the stress-strain evolution laws effectively experienced by both ENF and DCB adhesive joint specimens at crack tip (semi-analytical) is given in Fig.68 and Fig.69.

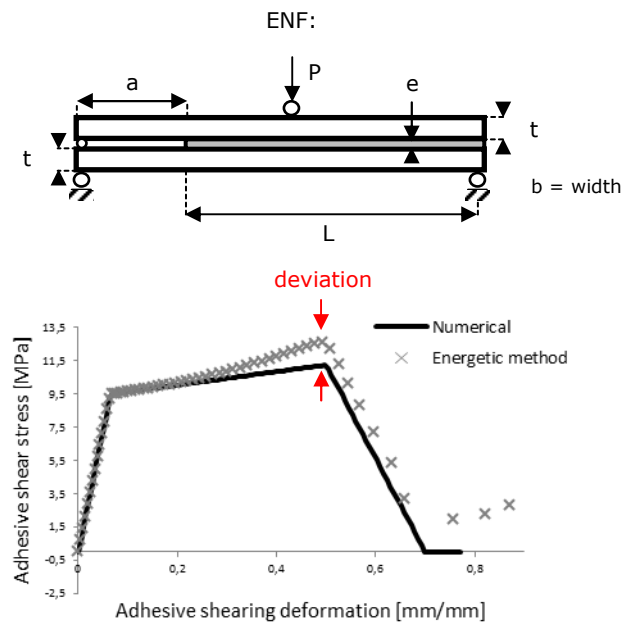
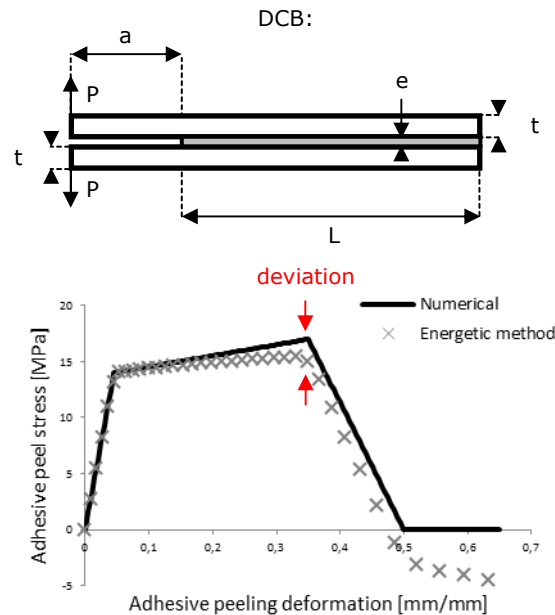


Figure 68. Schematic representation the End-Notched Flexure (ENF) adhesive joint specimen. Comparison of the predicted adhesive stress-strain relationships (energetic methods) and the stress-strain evolution laws effectively experienced (semi-analytical) by the specimen at crack tip. On the constitutive relationship of a thin adhesive layer loaded in pure

shear (mode II). Confrontation with semi-analytical predictions. On the experimental characterization of CZM. Energetic methods.



**Figure 69.** Schematic representation the Double Cantilever Beam (DCB) adhesive joint specimen. Comparison of the predicted adhesive stress-strain relationships (energetic methods) and the stress-strain evolution laws effectively experienced (semi-analytical) by the specimen at crack tip. On the constitutive relationship of a thin adhesive layer loaded in pure peel (mode I). Confrontation with semi-analytical predictions. On the experimental characterization of CZM. Energetic methods.

It is seen from Fig.68 and Fig.69 that the so predicted adhesive constitutive stress-strain relationships are in close agreement with the shear (peel) stress (strain) effectively experienced by the simulated ENF and DCB adhesive joint specimens at early stage of the experiment. However it is seen that the so predicted shear (peel) stress (strain) significantly deviate from the original adhesive constitutive stress-strain relationships for increasing levels of applied load.

These deviations owe to two reasons. First, the initial stiffnesses of the adhesive interface are not known a priori of the experiment. Indeed, since the design criteria provided in equations (133) and (141) are defined through these initial adhesive stiffnesses, it is essentially impossible to early-design the test specimens so that the validity of equations (132) and (139) is ensured a priori of the experiment. Secondly, even if fortuitously fulfilled, the design criteria provided in equations (133) and (141) simply derive from the integration of the bonded overlap equilibrium equations in the case of linear elastic solicitations of both the adhesive layer and the surrounding adherends. The validity of such design criteria then remains while the whole specimens experience linear elastic deformations only, or at least experiencing sufficiently small nonlinear deformations so that it affects negligibly the shear and peel stress distributions away from the crack tip. Then, depending on the nonlinear deforming capability of the adhesive layer itself, this hypothesis can rapidly become

insufficient to legitimate the use of the suggested theoretical relationships. Finally, an additional limitation of such approaches is that it is basically impossible to monitor the evolution of the adhesive stresses during unloading phases. This limitation is due to the mathematical description of the J-integral given in (Rice 1968) and cannot be a priori overridden. It then limits the use of energetic methods to monotonously increasing load histories only, so that the behavior of the adhesive layer during unloading phases cannot be addressed by such approaches.

Then, a direct comparison between the so predicted stress-strain relationships (energetic method) and the stress-strain evolution laws effectively experienced by the MCB adhesive joint specimen (semi-analytical) is given in Fig.70. For simplification purpose, here was considered an interface cohesive model resuming both bilinear pure mode adhesive constitutive stress-strain relationships related by both linear energetic initiation and propagation mixed-mode criteria.

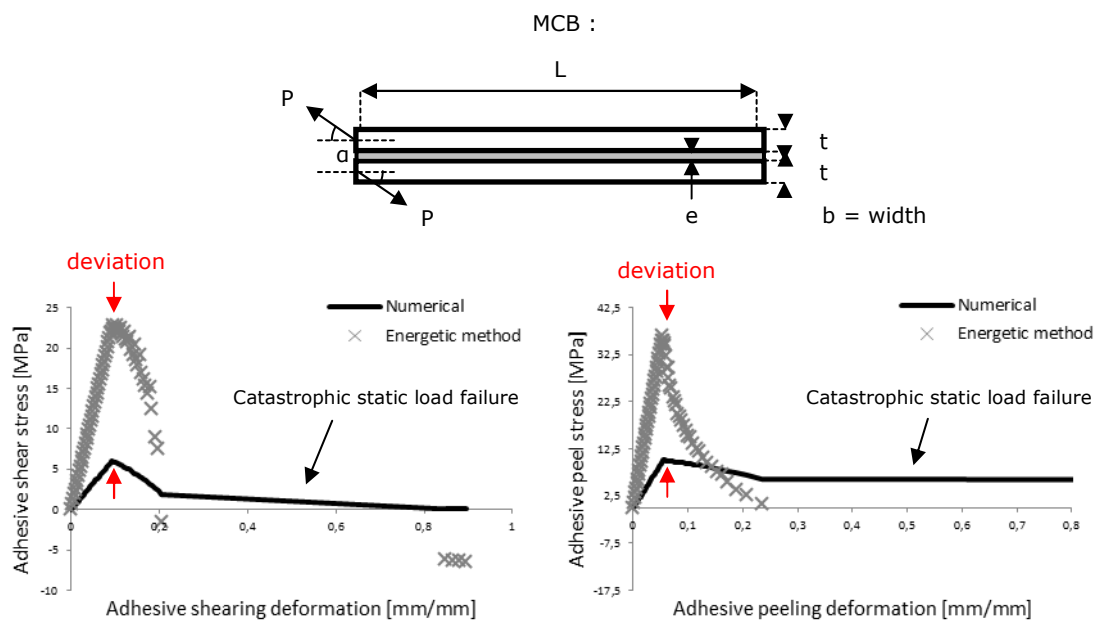


Figure 70. Schematic representation the Mixed-mode Cantilever Beam (MCB) adhesive joint specimen. Comparison of the predicted adhesive stress-strain relationships (energetic methods) and the stress-strain evolution laws effectively experienced (semi-analytical) by the specimen at crack tip. On the constitutive relationship of a thin adhesive layer loaded in mixed-mode I/II. Confrontation with semi-analytical predictions. On the experimental characterization of CZM. Energetic methods.

It is seen from Fig.70 that the so predicted adhesive constitutive stress-strain relationships (i.e. in the case of mixed-mode I/II adhesive solicitations) highly differ from the adhesive stresses (strains) effectively experienced by the simulated MCB adhesive joint specimen (with no distinction between the early or later stage of the experiment).

This deviation owe to two reasons. First, the afore described theory (i.e. mixed mode I/II adhesive loadings) lies on a mathematical inconsistency in the derivation of the mixed-mode I/II adhesive stresses at crack tip. Indeed, since  $\tau(\nu, \varepsilon)$  and  $\sigma(\nu, \varepsilon)$  are both functions of the two variables  $\nu$  and  $\varepsilon$  when subjected to mixed-mode I/II adhesive loads:

$$J = \int_0^{\nu} \alpha d\nu + \int_0^{\varepsilon} \sigma d\varepsilon \text{ does not imply that } \begin{cases} \tau(\varepsilon, \nu) = \partial J / \partial \nu \\ \sigma(\varepsilon, \nu) = \partial J / \partial \varepsilon \end{cases} \quad (145)$$

This assumption then applies to a simplistic vision of the joint equilibrium assuming that the mixed-mode ratio  $\beta = \nu / \varepsilon = I$  will not vary during loading. However this simplification appears to be false in most cases and will be discussed later on in [Sections 3.7](#) and [3.8](#). Then, the adhesive mixed-mode I/II constitutive stress-strain relationships cannot be simply derived from the differentiation the mixed-mode I/II instantaneous energy release rate with respect to their associated shear and peel adhesive deformations.

Secondly, the computation of the J-integral ([Rice 1968](#)) presented in ([Hogberg 2006](#)) lies on the assumption that the right edge of the MCB joint specimen is free of any load. However the misalignment of the antisymmetric loading directions results in the introduction of a left side bending moment of magnitude  $M = 0.5PH / \sqrt{1 + \tan^2 \alpha}$  so that the right side of the MCB joint specimen has to be clamped to avoid any rigid rotation of the joint specimen. This clamped condition then results in the introduction of complex load reactions that are not taken into account in the computation of the J-integral ([Rice 1968](#)) as presented in ([Hogberg 2006](#)).

### 3.5. On the experimental characterization of CZM: The direct method

#### 3.5.1. Overview

In response to [Section 3.4](#), the following section aims to present a new and original method for the characterization the cohesive properties of thin adhesive interfaces. This approach is derived in the case of pure mode I, pure mode II and mixed-mode I/II adhesive solicitations so that three different characterization protocols are presented (e.g. ENF, DCB and MCB). Each of these protocols is based on the monitoring of the adherend-to-adherend displacement field nearby the adhesive crack tip of Classical Fracture Mechanics (CFM) adhesive joint specimens and does not require any spatial integration of the joint equilibrium equations. Then limiting the number of simplifying hypotheses required to derive a closed-form solution to the problem “given the adhesive joint specimen behavior, what is the constitutive relationship of the adhesive layer?”.

For simplification purpose, the complete set of governing differential equations of the joint (i.e. described in [Chapter 2](#)) is voluntarily restricted to the equilibrium of the upper adherend only (see [Fig.71](#)). However the same relationships could be obtained, to the sign, using the equilibrium equations of the lower adherends.

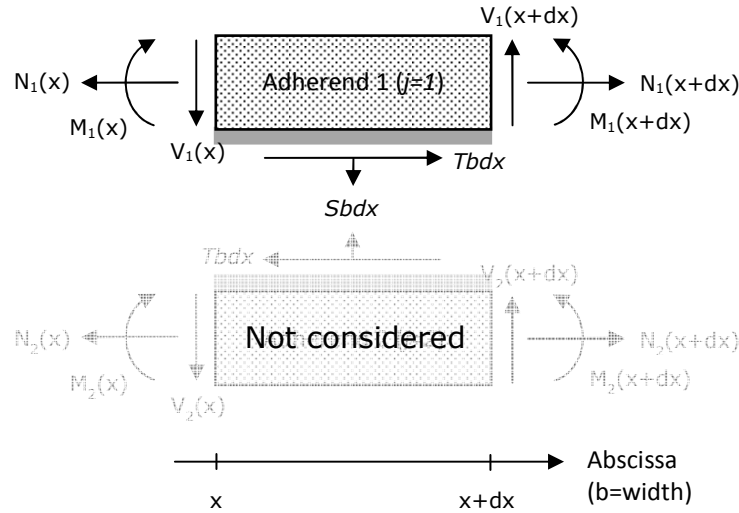


Figure 71. Schematic representation of the equilibrium of the bonded adherends relative to the End-Notched Flexure (ENF) adhesive joint specimen. On the constitutive relationship of a thin adhesive layer loaded in pure shear (mode II). On the characterization of CZM. The direct method.

### 3.5.2. On the constitutive relationship of a thin adhesive layer loaded in pure shear (mode II)

This section aims at presenting an original experimental protocol to determine the complete stress-strain relationship of a thin adhesive layer loaded in shear (mode II). The presented demonstration applies to the ENF adhesive test specimen despite the following data reduction scheme is not limited to this particular specimen only.

In the case of pure shear (mode II) adhesive solicitations, the local equilibrium of the upper adherend can be reduced in the form of the following set of differential equations (see Fig.71):

$$\begin{cases} \frac{dN_1}{bdx} = -T \\ \frac{dV_1}{bdx} = 0 \\ \frac{dM_1}{dx} + V_1 + \frac{1}{2}(e_1 + e)bT = 0 \end{cases} \quad (146)$$

where  $T$  refers to the adhesive shear stress,  $N_1$  to the normal force in adherend 1,  $V_1$  to the shearing force in adherend 1 and  $M_1$  to the bending momentum in adherend 1, while the constitutive beam equations of the upper adherend are given by:

$$\begin{cases} N_1 = A_1 \frac{du_1}{dx} - B_1 \frac{d\theta_1}{dx} \\ M_1 = -B_1 \frac{du_1}{dx} + D_1 \frac{d\theta_1}{dx} \end{cases} \quad (147)$$

with  $A_I$  the extensional stiffness,  $D_I$  the bending stiffness and  $B_I$  the coupling stiffness of adherend 1,  $u_I$  the normal displacement of adherend 1,  $w_I$  the transverse deflection of adherend 1 and  $\theta_I$  the cross-section rotation of adherend 1 derived from the Classical Laminates Theory (CLT) (Jones 1998, Berthelot 1999). For demonstration purpose, it is assumed that  $\Delta_I = A_I D_I - B_I^2$  is not equal to zero.

Then, from equation (147) falls:

$$\frac{d\theta_1}{dx} = \frac{A_1 M_1 + B_1 N_1}{\Delta_1} \quad (148)$$

Then differentiating equation (148) with respect to  $x$  gives:

$$\frac{d^2\theta_1}{dx^2} = \frac{A_1}{\Delta_1} \frac{dM_1}{dx} + \frac{B_1}{\Delta_1} \frac{dN_1}{dx} \quad (149)$$

Finally inserting equation (146) into equation (149) it is possible to express the shear stress  $T$  as a function of both the upper shearing force acting at point  $x$  and the second order derivative of the upper adherends cross-section rotation, so that:

$$T = \frac{-2}{b(e_1 + e)A_1 + 2B_1} \left( A_1 V_1 + \Delta_1 \frac{d^2\theta_1}{dx^2} \right) \quad (150)$$

which can be reduced in the case of symmetric (or monolithic) adherends to:

$$T = \frac{-2}{b(e_1 + e)} \left( V_1 + D_1 \frac{d^2\theta_1}{dx^2} \right) \quad (151)$$

Equation (151) then suggests it is possible to monitor the distribution of the adhesive shear stresses along the overlap by simultaneously monitoring both the distributions of the upper shearing force and the second order derivative of the upper adherends cross-section rotation. Nevertheless, the distribution of the shearing force along the overlap is a variable that is particularly difficult to measure experimentally. To overcome this problem, it is decided to focus on the close vicinity of the adhesive crack tip ( $x=0$ ).

From a simple linear equilibrium of the loads (reactions) acting onto the edges of the overlap (specimen), it is possible to demonstrate the shearing force acting onto the upper (lower) adherend at crack tip as equal to (see Fig.72):

$$V_1(x=0) = -P/4 \quad (152)$$

Leading to the modified relationship:

$$T(x=0) = \frac{2}{b(e_1 + e)} \left( P/4 - D_1 \frac{d^2\theta_1}{dx^2} \right) \quad (153)$$

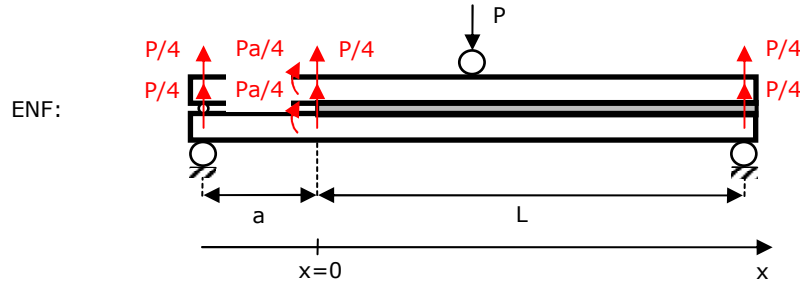


Figure 72. Schematic representation of the reaction loads acting onto the edges of the bonded overlap of the End-Notched Flexure (ENF) adhesive joint specimen. On the constitutive relationship of a thin adhesive layer loaded in pure shear (mode II). On the characterization of CZM. The direct method.

Finally, It appears from equation (153) that the evolution of the adhesive shear stress at crack tip ( $x=0$ ) can be determined by simultaneously monitoring the applied load and the second order derivative of the upper adherends cross-section rotation at crack tip ( $x=0$ ) making no more assumption than simply considering the joint equilibrium originally described in (Hart-Smith 1973a, Hart-Smith 1973b) as valid nearby the adhesive crack tip ( $x=0$ ).

### 3.5.3. On the constitutive relationship of a thin adhesive layer loaded in pure peel (mode I)

This section aims at presenting an original experimental protocol to determine the complete stress-strain relationship of an adhesive layer loaded in peel (mode I). The presented demonstration applies to the DCB adhesive test specimen despite the following data reduction scheme is not limited to this particular specimen only.

In the case of pure peel (mode I) adhesive solicitations, the local equilibrium of the upper adherend can be reduced in the form of the following set of differential equations (see Fig.71):

$$\left\{ \begin{array}{l} \frac{dN_1}{bdx} = 0 \\ \frac{dV_1}{bdx} = S \\ \frac{dM_1}{dx} + V_1 + 0 = 0 \end{array} \right. \quad (154)$$

where  $S$  refers to the adhesive peel stress,  $N_1$  to the normal force in adherend 1,  $V_1$  to the shearing force in adherend 1 and  $M_1$  to the bending momentum in adherend 1, while the constitutive beam equations of the upper adherend are unchanged from equation (147).

Similarly to Section 3.5.2, from equation (147) falls:

$$\frac{d\theta_1}{dx} = \frac{A_1 M_1 + B_1 N_1}{\Delta_1} \quad (155)$$

Then differentiating two times equation (155) with respect to  $x$  gives:

$$\frac{d^3\theta_1}{dx^3} = \frac{A_1}{\Delta_1} \frac{d^2M_1}{dx^2} + \frac{B_1}{\Delta_1} \frac{d^2N_1}{dx^2} \quad (156)$$

Finally inserting equation (154) into equation (156) it is possible to express the peel stress  $S$  as a function of the third order derivative of the upper adherends cross-section rotation only, so that:

$$S = -\frac{\Delta_1}{bA_1} \frac{d^3\theta_1}{dx^3} \quad (157)$$

which can be reduced in the case of symmetric (or monolithic) adherends to:

$$S = -\frac{D_1}{b} \frac{d^3\theta_1}{dx^3} \quad (158)$$

Equation (158) then suggests it is possible to monitor the whole overlap distribution of the adhesive peel stress, and a fortiori at crack tip ( $x=0$ ), by simply monitoring the third order derivative of the upper adherends cross-section rotation making no more assumption than simply considering the joint equilibrium originally described in (Hart-Smith 1973a, Hart-Smith 1973b) as valid nearby the adhesive crack tip ( $x=0$ ). It is indicated that in the case of pure peel adhesive solicitations the afore described theory requires no a priori evaluation of the reaction loads acting onto the edges of the bonded overlap.

#### 3.5.4. On the constitutive relationship of a thin adhesive layer loaded in mixed-mode I/II

Based on the approaches developed in Sections 3.5.2 and 3.5.3, this section aims at presenting an original experimental protocol to determine the complete stress-strain relationships of a thin adhesive layer facing mixed-mode I/II adhesive solicitations. The presented demonstration applies to both MCB and MMB adhesive test specimens despite the following data reduction scheme is not limited to these particular specimens only.

In the case of mixed-mode I/II adhesive solicitations, the local equilibrium of the upper adherend can be reduced in the form of the following set of differential equations (see Fig.71):

$$\begin{cases} \frac{dN_1}{bdx} = -T \\ \frac{dV_1}{bdx} = S \\ \frac{dM_1}{dx} + V_1 + \frac{1}{2}(e_1 + e)bT = 0 \end{cases} \quad (159)$$

where  $S$  refers to the adhesive peel stress,  $T$  to the adhesive shear stress,  $N_I$  to the normal force in adherend 1,  $V_I$  to the shearing force in adherend 1 and  $M_I$  to the bending momentum in adherend 1, while the constitutive beam equations are given in equation (147).

Finally inserting equation (147) in equation (159), it is finally possible to express both the shear stress  $T$  and the peel stress  $S$  as functions of the successive derivatives of the adherends cross-section rotation and longitudinal displacement, so that:

$$\begin{cases} T = -\frac{1}{b} \left[ A_1 \frac{d^2 u_1}{dx^2} - B_1 \frac{d^2 \theta_1}{dx^2} \right] \\ S = \frac{1}{b} \left[ -B_1 \frac{d^3 u_1}{dx^3} + D_1 \frac{d^3 \theta_1}{dx^3} + \frac{e_1 + e}{2} \left[ A_1 \frac{d^2 u_1}{dx^2} - B_1 \frac{d^2 \theta_1}{dx^2} \right] \right] \end{cases} \quad (160)$$

which can be reduced in the case of symmetric (or monolithic) adherends to:

$$\begin{cases} T = \frac{A_1}{b} \frac{d^2 u_1}{dx^2} \\ S = \frac{D_1}{b} \frac{d^3 \theta_1}{dx^3} + \frac{e_1 + e}{2} \frac{A_1}{b} \frac{d^2 u_1}{dx^2} \end{cases} \quad (161)$$

Equation (161) then suggests it is possible to monitor the overlap distribution as well as the evolution of both the adhesive shear and peel stresses at crack tip ( $x=0$ ) by monitoring the successive derivatives of both the cross-section rotation and longitudinal displacement of the upper adherend.

### 3.5.5. Confrontation with semi-analytical predictions

**Description of the simplified 1D-beam adhesive stress analyses.** As in Section 3.4.5, the workability/sustainability of the afore described theory (i.e. the direct method) was investigated. Three semi-analytical models are then constructed (e.g. ENF, DCB and MCB). Each model refers to one of those presented in Section 3.4.5, so that a schematic representation of each model is presented in Fig.67. Similarly, the mechanical properties of both the adhesive layer and the surrounding adherends are given in Tab.8. The adherend-to-adherend displacement field nearby the adhesive crack tip is set as a direct output of the simplified 1D-beam adhesive stress analyses and taken as it was coming from experimental records. The successive derivatives of the adherend-to-adherend displacement field are then obtained directly from the resolution procedure presented and described in Chapter 1. The evolution of both pure modes and mixed-mode adhesive shear and peel stress-strain evolution laws are finally obtained thanks to equations (153) (158) and (161).

**Confrontation with semi-analytical predictions.** A direct comparison between the so predicted stress-strain relationships (the direct method) and the stress-strain evolutions effectively experienced at crack tip by both ENF, DCB and MCB joint specimens (semi-analytical) is given in Fig.73, Fig.74 and Fig.75.

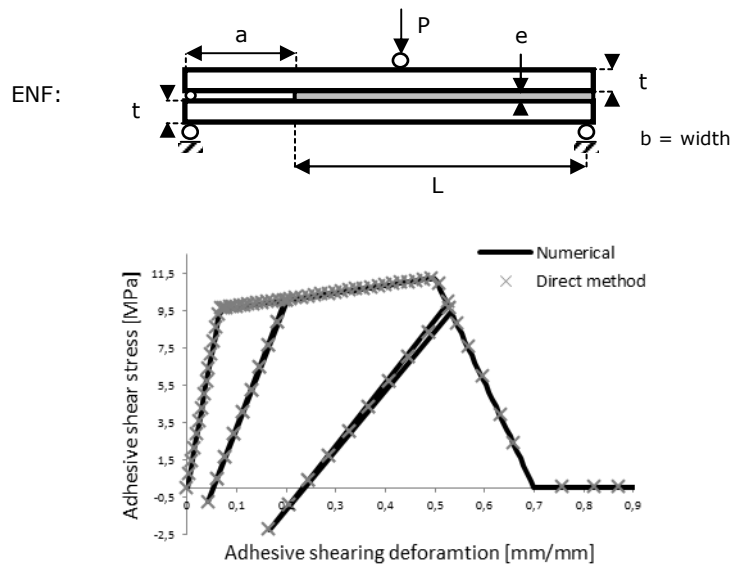


Figure 73. Schematic representation the End-Notched Flexure (ENF) adhesive joint specimen. Comparison of the predicted adhesive stress-strain relationships (the direct method) and the stress-strain evolution laws effectively experienced (semi-analytical) by the specimen at crack tip. On the constitutive relationship of a thin adhesive layer loaded in pure shear (mode II). Confrontation with semi-analytical predictions. On the experimental characterization of CZM. The direct method.

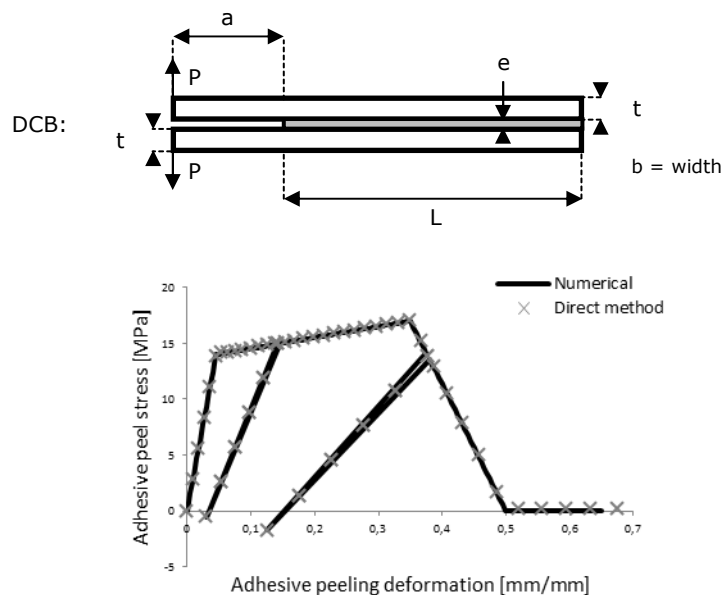
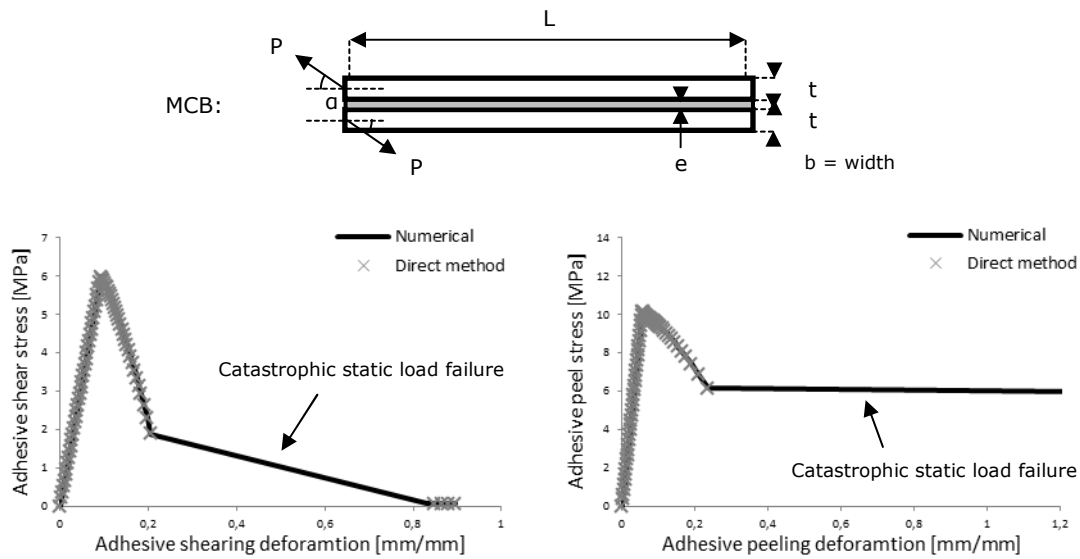


Figure 74. Schematic representation the Double Cantilever Beam (DCB) adhesive joint specimen. Comparison of the predicted adhesive stress-strain relationships (the direct method) and the stress-strain evolution laws effectively experienced (semi-analytical) by the specimen at crack tip. On the constitutive relationship of a thin adhesive layer loaded in pure

peel (mode I). Confrontation with semi-analytical predictions. On the experimental characterization of CZM. The direct method.



**Figure 75.** Schematic representation the Mixed-mode Cantilever Beam (MCB) adhesive joint specimen. Comparison of the predicted adhesive stress-strain relationships (the direct method) and the stress-strain evolution laws effectively experienced (semi-analytical) by the specimen at crack tip. On the constitutive relationship of a thin adhesive layer loaded in mixed-mode I/II. Confrontation with semi-analytical predictions. On the experimental characterization of CZM. The direct method.

It is seen from Fig.73, Fig.74 and Fig.75 that the so predicted adhesive constitutive stress-strain relationships are here in close agreement with both shear and peel adhesive stress-strain evolution laws effectively experienced by the simulated ENF, DCB and MCB joint specimens with no distinction between early stage and later stage of the experiment. It is also seen from Fig.73, Fig.74 and Fig.75 that the so predicted adhesive constitutive stress-strain relationships are able to address the constitutive behavior of the adhesive layer during unloading phases, which was basically impossible using energetic methods due to the inability of the J-integral as described in (Rice 1968) to account for possibly non-monotonous load histories. Thus resulting in allowing for the monitoring of the true degradation process in the case of coupled yielding and pure damage degradation of the adhesive interface stiffnesses during loading.

### 3.6. Experimental investigations on metal-to-metal adhesive joints

#### 3.6.1. Data processing

**Presentation of the data pre-processing algorithm.** It is shown from Sections 3.5.2 to 3.5.4 that the evolution of adhesive stresses at crack tip ( $x=0$ ) can be theoretically monitored by supervising the successive derivatives of the adherend-to-adherend displacement field nearby the adhesive crack tip ( $x=0$ ). However, since the numerical differentiation of raw (noised) experimental results can lead to the rise of important numerical artifacts/singularities, a particular attention has to be given to the correct evaluation of the successive derivatives of

the adherend-to-adherend displacement field nearby the adhesive crack tip ( $x=0$ ). Data pre-processing is then highly recommended to reduce experimental noises.

The data pre-processing algorithm used to reduce experimental noises from the measured adherend-to-adherend displacement fields then lies on the optimal sub rank approximation based on the Singular Value Decomposition (SVD), and is related to signal processing techniques that are commonly referred to as *SVD signal enhancement methods*, *reduced-rank signal processing methods* or simply *subspace methods* (Andrews & Patterson 1973, Orfanandis 2007). According to (Sadek 2012), optimal sub rank approximation based on the SVD of digital images finds its roots in the field of digital image compression. The optimal sub rank approximation method then states that a digital image  $\mathbf{X}$  of size  $M*N$ , with  $M \geq N$ , can be represented by its SVD as:

$$[\mathbf{X}]_M^N = [\mathbf{U}]_M^M [\mathbf{S}]_M^N [\mathbf{V}]_N^T \quad (162)$$

where  $\mathbf{U}=[\mathbf{u}^{(1)}, \mathbf{u}^{(2)}, \dots, \mathbf{u}^{(M)}]$ , a  $M*M$  real or complex unitary matrix (i.e. whose columns are referred as the left singular vectors),  $\mathbf{S}$  a  $M*N$  rectangular diagonal matrix with non-negative diagonal entries (i.e. referred to as the singular values and ranked in a strictly decreasing order), and  $\mathbf{V}^T$  the conjugate transpose of  $\mathbf{V}=[\mathbf{v}^{(1)}, \mathbf{v}^{(2)}, \dots, \mathbf{v}^{(N)}]$  a  $N*N$  real or complex unitary matrix (i.e. whose columns are referred as the right singular vectors). Among other significant advantages, the SVD is commonly recognized as the optimal matrix decomposition in the sense of the least squares method that packs most of the signal energy (information) into as few coefficients as possible (Moonen *et al.* 1992). This property of the SVD is generally referred to as the *maximum energy packing property*.

Then defining the rank- $R$  approximation of  $\mathbf{X}$  as:

$$[\mathbf{X}]_M^N (R) = \sum_{i=1}^R s_i \mathbf{u}^{(i)} \mathbf{v}^{(i),T} = [\mathbf{U}]_M^R [\mathbf{S}]_R^R [\mathbf{V}]_N^R \quad (163)$$

where  $\mathbf{U}=[\mathbf{u}^{(1)}, \mathbf{u}^{(2)}, \dots, \mathbf{u}^{(R)}]$ , the  $M*R$  matrix resuming the firsts  $R$  left singular vectors of  $\mathbf{X}$ ,  $\mathbf{S}$  a  $R*R$  the rectangular diagonal matrix resuming the first  $R$  singular values of  $\mathbf{X}$ , and  $\mathbf{V}^T$  the conjugate transpose of  $\mathbf{V}=[\mathbf{v}^{(1)}, \mathbf{v}^{(2)}, \dots, \mathbf{v}^{(R)}]$  the  $N*R$  matrix resuming the first  $R$  right singular vectors of  $\mathbf{X}$ . In Digital Image Processing (DIP), the singular value  $s_i$  is generally referred to as the energy (or luminance) of the  $i^{th}$  image layer while the rank-1 matrix deriving from the outer product  $\mathbf{u}^{(i)} \mathbf{v}^{(i),T}$  is generally referred to as the  $i^{th}$  image layer (or eigenimage) of  $\mathbf{X}$ .

The optimal sub rank approximation then suggests that the original image  $\mathbf{X}$  can be legitimately approximated by its lower rank approximation  $\mathbf{X}$ , so that  $R \leq \min(M, N)$  is chosen to minimize the difference between the *energy* (i.e. associated to the Frobenius-norm of the matrix  $\mathbf{X}$ ) of the initial image  $\mathbf{X}$  and the reconstructed image  $\mathbf{X}$ . Then, the storage of the rank- $R$  truncated SVD requires  $(N+M+1)*R$  numbers only versus  $M*N$  for the original image. Fig.76 presents an example of SVD truncation using the rank- $R$  approximation technique.

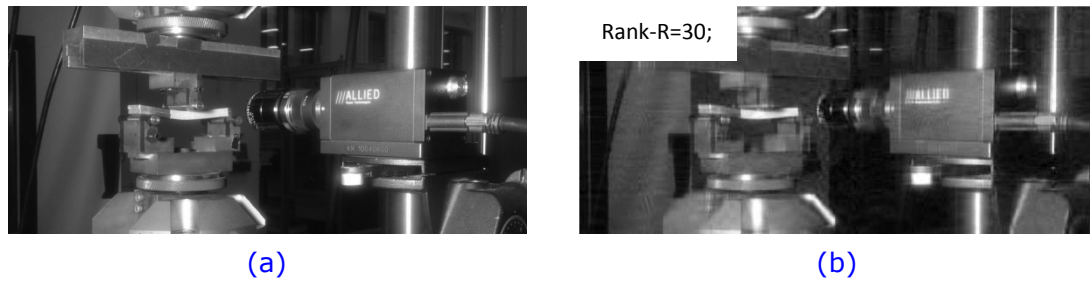


**Figure 76.** Illustration of SVD truncation techniques for the storage reduction of digital images. Original image (a), rank- $R=30$  SVD approximation (b).  $N=225$ .  $M=514$ .  $N*M=115650$ .  $(N+M+1)*R=22200$ . Presentation of the data pre-processing algorithm. Data pre-processing. On the experimental characterization of CZM. Experimental test campaign.

In (Konstantinides *et al.* 1997, Kamm 1998), the authors suggested using the optimal sub rank approximation for data (image) denoising purposes. The authors then stated that the SVD offers the possibility of splitting the image space into two distinct subspaces, the signal (i.e. referred as the dominant subspace) and the noise (i.e. referred as the subdominant subspace). So that the dominant and the subdominant subspaces are by construction orthogonal. Then, iteratively reconstructing the dominant subspace using an increasing number of singular values, starting from the most energetic, allows for the original signal (denoised) to be estimated from the SVD of the degraded (noised) signal (see Fig.77).

The key parameter of digital image denoising using SVD techniques then lies in finding the correct truncation  $R$  that separates the dominant subspace (i.e. the signal) from the subdominant subspace (i.e. the noise). Numbers of truncation strategies have been suggested over the past few years so that it allows for finding the best compromise in terms of capturing most of the energy (information) of the original signal (image) while reducing experimental noises (Orfanidis 2007).

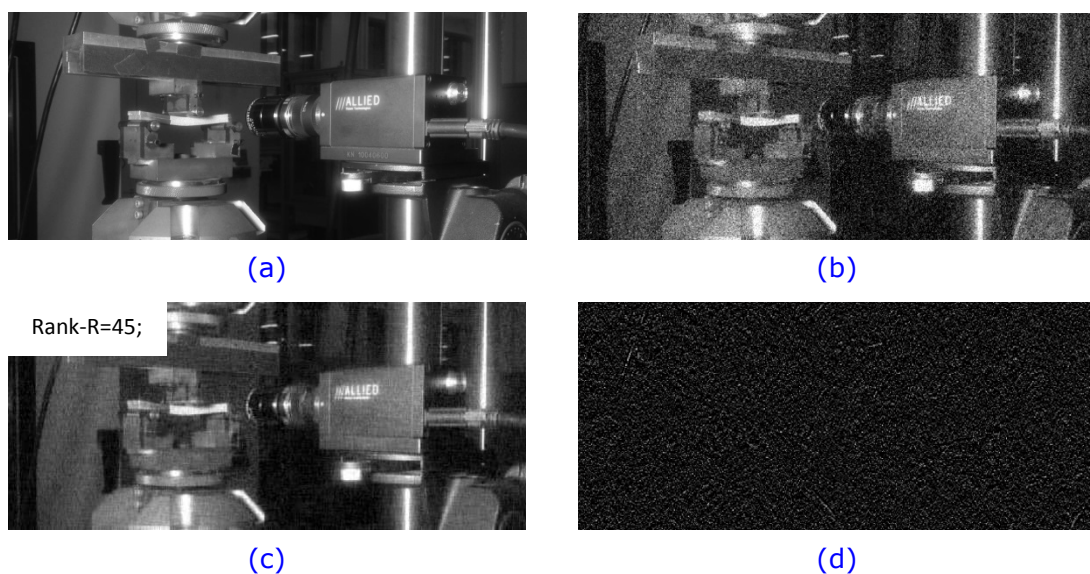


**Figure 77.** Illustration of the SVD truncation technique for data (image) denoising processing. Original image (a), noised image (b), unnoised image (dominant subspace) (c), reconstructed noise (subdominant subspace) (d). Presentation of the data pre-processing algorithm. Data pre-processing. On the experimental characterization of CZM. Experimental test campaign.

The data pre-processing algorithm used to reduce experimental noises from the measured adherend-to-adherend displacement fields then lies on the digital mapping of the adherend-to-adherend axial (transverse) displacement fields as a set of 2D matrices (see Fig.78). First, the evolution of the axial (transverse) displacement field of each adherend is mapped as 3D tensors resuming both the distributions of the adherend axial (transverse) displacements nearby the adhesive crack tip as well as their respective evolutions. Then, the so constructed 3D tensors of dimensions  $x$ ,  $y$  and  $t$  are rearranged in the form of simpler 2D matrices so that their new dimensions are respectively  $y$  and  $x*t$  (see Fig.78).

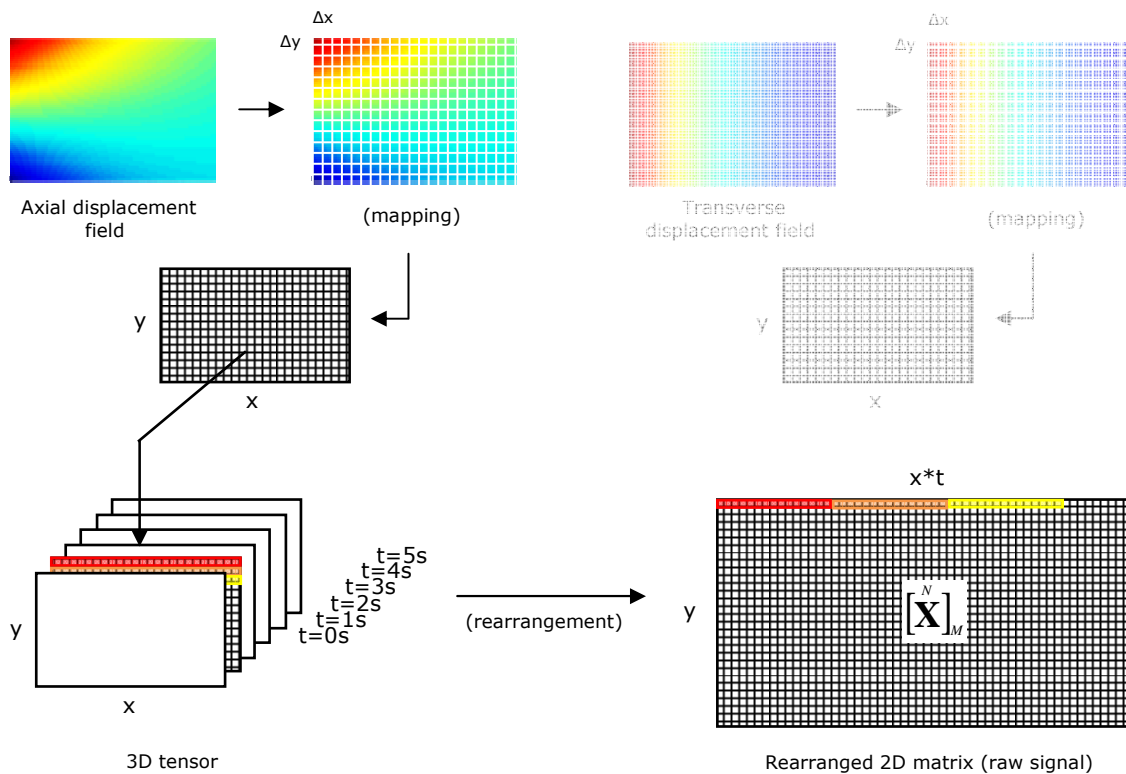


**Figure 78.** Data pre-processing algorithm. Digital mapping of the adherend-to-adherend axial and transverse displacement fields. Presentation of the data pre-processing algorithm. Data pre-processing. On the experimental characterization of CZM. Experimental test campaign.

The so constructed 2D matrices are then filtered using the rank- $R$  reduction approximation based on the Singular Value Decomposition (SVD) of the raw experimental results, so that  $R$  is chosen to capture 95% of the original data energy in the sense of the Frobenius-norm (see Fig.79).

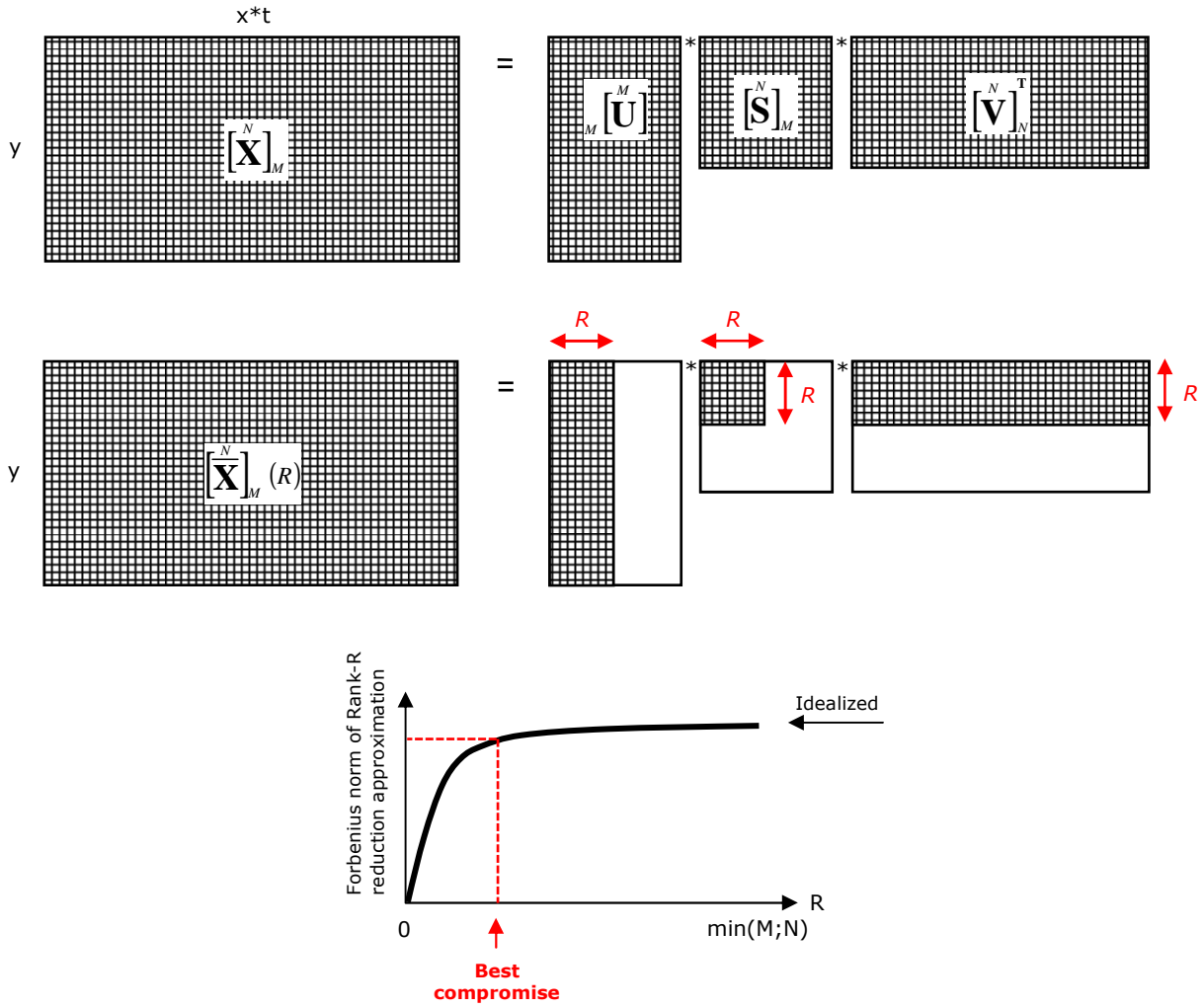


Figure 79. Data pre-processing algorithm. Filtering of the experimental results using the rank- $R$  reduction approximation based on Singular Value Decomposition (SVD). Presentation of the data pre-processing algorithm. Data pre-processing. On the experimental characterization of CZM. Experimental test campaign.

Then, the evolution of each adherend axial and transverse displacement fields are reconstructed from their respective decompositions and rearranged in the form of 3D tensors, so that the displacements of the upper (lower) neutral fiber are finally extracted from the reconstructed axial and transverse displacement fields and formatted into the relevant beam or plate theory (see Fig.80)

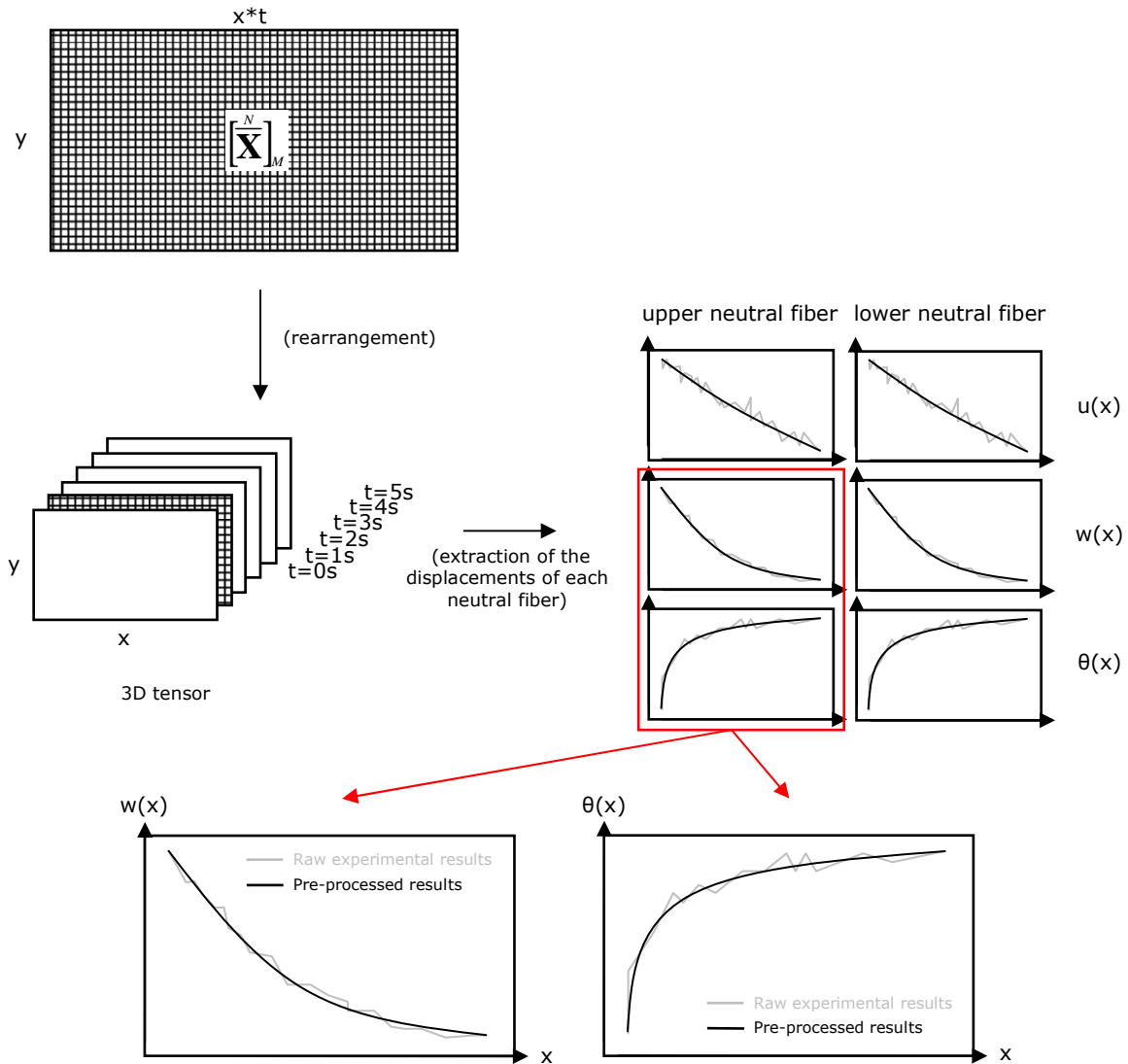
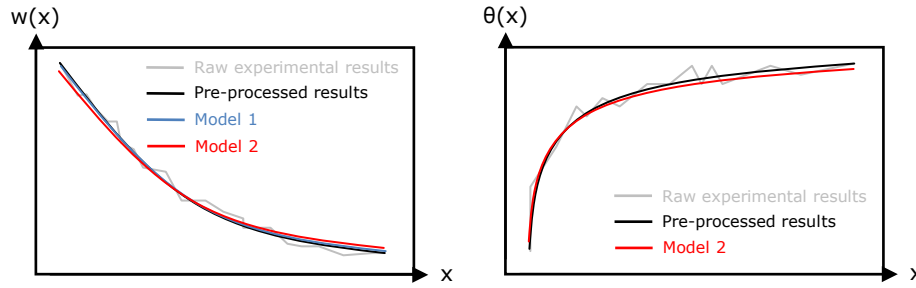


Figure 80. Data pre-processing. Extraction of the displacements of each adherend neutral fiber. Presentation of the data pre-processing algorithm. Data pre-processing. On the experimental characterization of CZM. Experimental test campaign.

Finally, the differentiation of the adherends cross-section rotation is ensured by fitting a polynomial series so that the vertical deviation with experimental data is minimized in the sense of the least squares method by using the Moore-Penrose pseudo inverse technique (see Appendix 6). Two models are used (see Fig.81). The first model takes interest in fitting  $w(x)$  only. The second model takes interest in fitting simultaneously  $w(x)$  and  $\theta(x)=dw(x)/dx$ . So that model 1 is by construction concatenated in model 2. The successive derivatives of the adherend-to-adherend displacement field are finally computed directly from differentiating the fitted polynomial series.



**Figure 81.** Data pre-processing. Fitting of the polynomial series using the Moore-Penrose pseudo inverse technique. Presentation of the data pre-processing algorithm. Data pre-processing. On the experimental characterization of CZM. Experimental test campaign.

**Presentation of the supervised experiment.** To characterize the ability of the suggested data pre-processing and differentiation algorithm to determine the successive derivatives of the adherend-to-adherend displacement field with sufficient accuracy, here is presented a supervised experiment.

This supervised experiment refers to the data pre-processing and data differentiation of a displacement field that is virtually generated so that the evolution of its successive derivatives is known in advance of the experiment. For simplification purpose, the comparison between the supervised data and those obtained from the data processing will be made in terms of the 3<sup>rd</sup> and 4<sup>th</sup> order derivatives of the transverse displacement of the adherend neutral fiber only. However the results are similar with other derivatives.

The virtual displacement field is generated using Matlab® R2012b and resumes the kinematic of a classical Euler-Bernoulli's beam in coupled in-plane tension/flexion, so that:

$$\begin{cases} u(x, y, t) = u(x, y = 0, t) - yw_{,x}(x, y = 0, t) \\ w(x, y, t) = w(x, y = 0, t) \end{cases} \quad (164)$$

where the evolutions of  $u(x, y=0, t)$  and  $w(x, y=0, t)$  are arbitrary fixed as:

$$\begin{cases} u(x, y = 0, t) = e^{-0.005tx} \\ w(x, y = 0, t) = e^{-0.15tx} \end{cases} \quad (165)$$

So that the simulated kinematics  $u(x, y)$  and  $w(x, y)$  at  $t=1s$  are finally presented in [Fig.82](#).

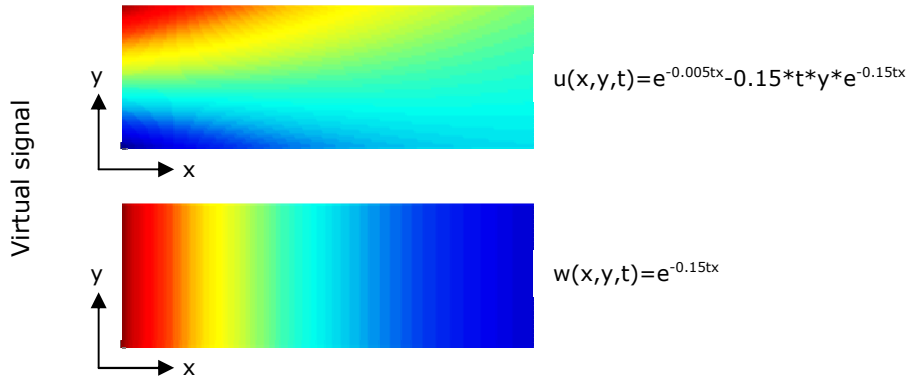


Figure 82. Representation of the virtual displacement fields  $u(x,y)$  and  $w(x,y)$  at  $t=1s$ . Data pre-processing. Presentation of the supervised data. On the experimental characterization of CZM. Experimental test campaign.

To model the effect of experimental noises, the virtual displacement field described in equations (164) and (165) is then degraded by adding a normal (Gaussian) noise using the  $normrnd(0,\sigma)$  Matlab® function. Where  $0$  refers to the prescribed zero mean value and  $\sigma$  to the configurable standard deviation of the normal (Gaussian) noise distribution (Matlab 2014). So that the simulated kinematics  $u_n(x,y)$  and  $w_n(x,y)$  are finally presented in Fig.83.

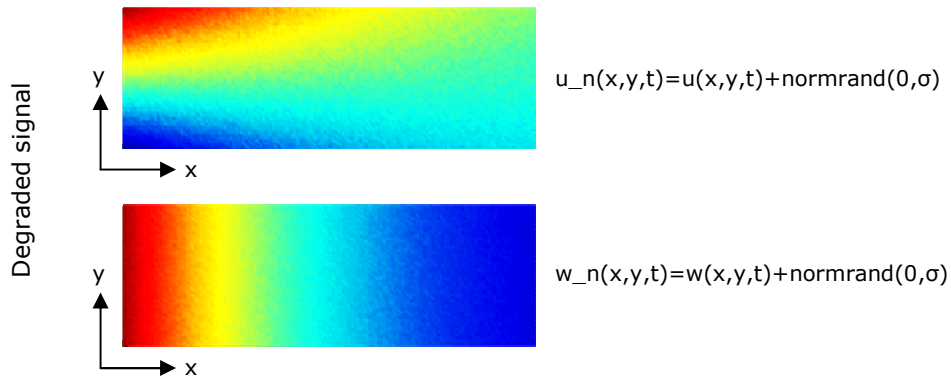


Figure 83. Representation of the degraded displacement fields  $u_n(x,y)$  and  $w_n(x,y)$  at  $t=1s$ . Data pre-processing. Presentation of the supervised data. On the experimental characterization of CZM. Experimental test campaign.

Finally, and to test for the linear dependency between the successive derivatives of the supervised data and those obtained from the fitted polynomial series, both the Pearson product-moment correlation coefficient, that is:

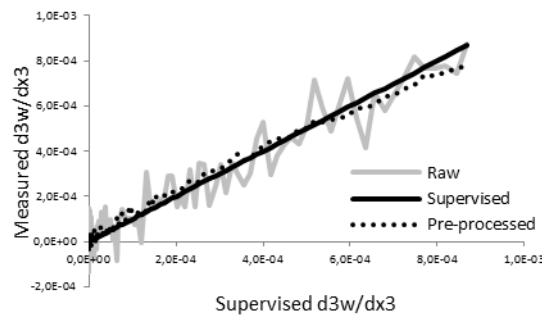
$$r = \frac{n(\sum xy) - (\sum x)(\sum y)}{\sqrt{[n\sum x^2 - (\sum x)^2][n\sum y^2 - (\sum y)^2]}} \quad (166)$$

And the Nash-Sutcliffe efficiency coefficient, that is:

$$nsc = 1 - \frac{\sum (y - x)^2}{\sum (x - \bar{x})^2} \quad (167)$$

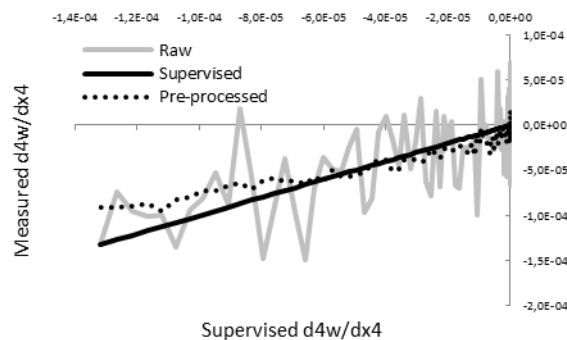
where  $x$  refers to the set of supervised data,  $y$  to the set of simulated data,  $n$  to the total number of data pairs and  $\bar{x}$  to the mean value of  $x$  are respectively estimated.

So that the correlation between the measured 3<sup>rd</sup> and 4<sup>th</sup> order derivatives of the transverse displacement of each adherend and its supervised evolution is presented in Fig.84 and Fig.85.



	Raw vs. Supervised	Pre-processed vs. Supervised
$r^2$	0.9160	0.9893
nsc	0.9121	0.9826
$1-\text{sqrt}(1-r^2)$	0.7102	0.8966

Figure 84. Comparison of the 3<sup>rd</sup> order derivative of the transverse displacement of the adherend neutral fiber obtained by fitting a 6<sup>th</sup> order polynomial series on both raw and pre-processed results. Comparison with the supervised data.



	Raw vs. Supervised	Pre-processed vs. Supervised
$r^2$	0.4110	0.9107
nsc	0.3758	0.7525
$1-\text{sqrt}(1-r^2)$	0.2325	0.7012

Figure 85. Comparison of the 4<sup>th</sup> order derivative of the transverse displacement of the adherend neutral fiber obtained by fitting a 6<sup>th</sup> order polynomial series on both raw and pre-processed results. Comparison with the supervised data.

For convenience the results presented will now refer to the measurement of the 3<sup>rd</sup> order derivative of the transverse displacement of the upper adherend neutral fiber only. Additionally, the squared Pearson product-moment correlation coefficient  $r^2$  will be now considered only. However the following conclusions are not limited to this particular derivative and (or) to the squared Pearson product-moment correlation coefficient only.

**Influence of the experimental (algorithmic) parameters on the accuracy of the experimental measures: DoE.** A full factorial Design of Experiments (DoE) consists in the following: (i) vary one factor at a time, (ii) perform experiments for all levels and combination of levels for all factors, (iii) hence perform a large number of experiments ( $N$ ), (iv) so that all effects and interactions are captured. Let  $k$  be the number of factor,  $n_i$  the number of levels of the  $i^{th}$  factor and  $p$  the number of replications to determine the impact of the measurement dispersion. The total number of experiments  $N$  of a full factorial DoE is then:

$$N = p \left( \prod_{i=1}^k n_i \right) \tag{168}$$

Here is considered a full factorial DoE of five factors with respectively 3x3x3x3x2 levels, so that the linear Taguchi's graph of effects and interactions can be represented in the form of Fig.86.

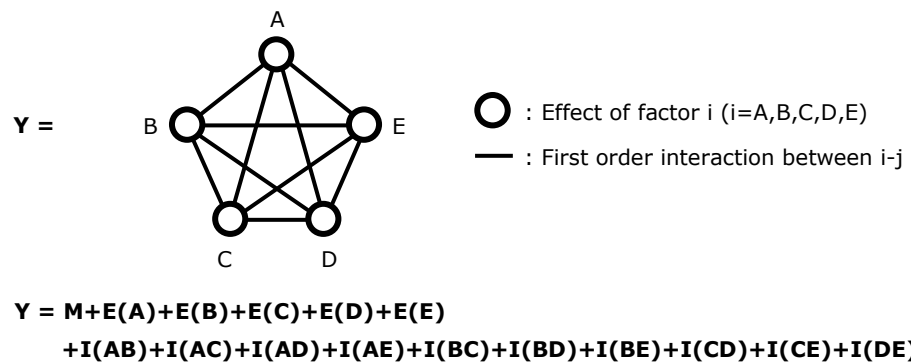


Figure 86. Linear Taguchi's graph of main effects and interactions. Full factorial Design of Experiments (DoE). Data pre-processing. On the experimental characterization of CZM. Experimental test campaign.

So that in Fig.86 are represented the main effects and interactions – respectively denoted  $E(i)$  and  $I(ij)$  – of factors  $i, j = A, B, C, D$  and  $E$  onto the objective function that is  $r^2$ .

Each experiment is replicated 15 times to capture the impact of the measurement dispersion, so that the total number of experiments is  $(3 \times 3 \times 3 \times 3 \times 2) \times 15 = 2430$ . The different factor levels are given in Tab.9.

**Tab 9.** Factor versus levels matrix. Full factorial Design of Experiments (DoE). Data pre-processing. On the experimental characterization of CZM. Experimental test campaign.

	$SNR^{-1}$ (A)	$x=y$ (B)	$t$ (C)	Degree (D)	Model (E)
Low (-1)	0.00175	201	51	4	1
Medium (0)	0.00350	401	101	6	N.A
High (+1)	0.00700	801	201	8	2

where  $SNR$  refers to the simulated Signal-to-Noise ratio,  $x=y$  to the spatial resolution of each displacement field instantaneous image,  $t$  to the number of instantaneous images taken during the experiment (i.e. thereafter referred as the temporal resolution),  $Degree$  to the degree of the polynomial series used to fit/differentiate the neutral fiber transverse displacement and  $Model$  to the model used for minimizing the vertical deviation with experimental data in the sense of the least squares method (see [Appendix 6](#)).

The results obtained from the full factorial DoE are then presented from [Fig.87](#) to [Fig.89](#).

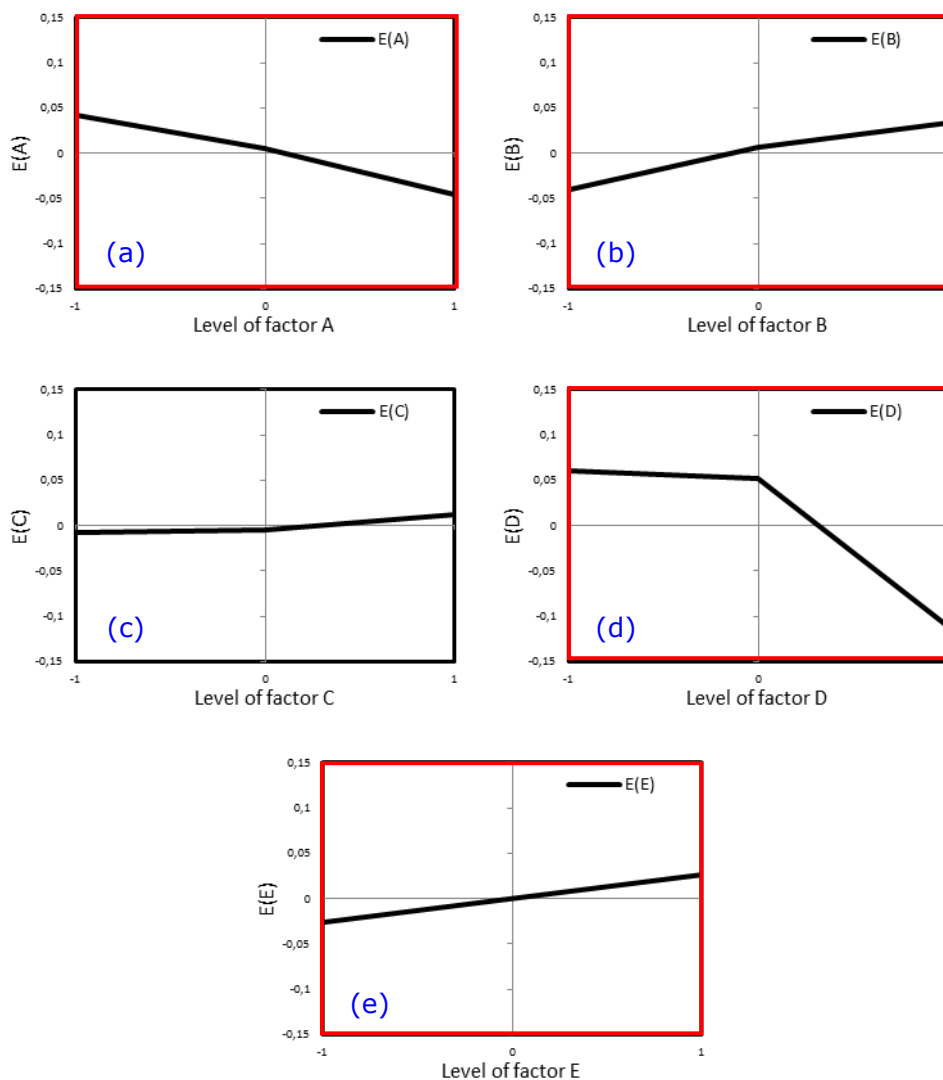
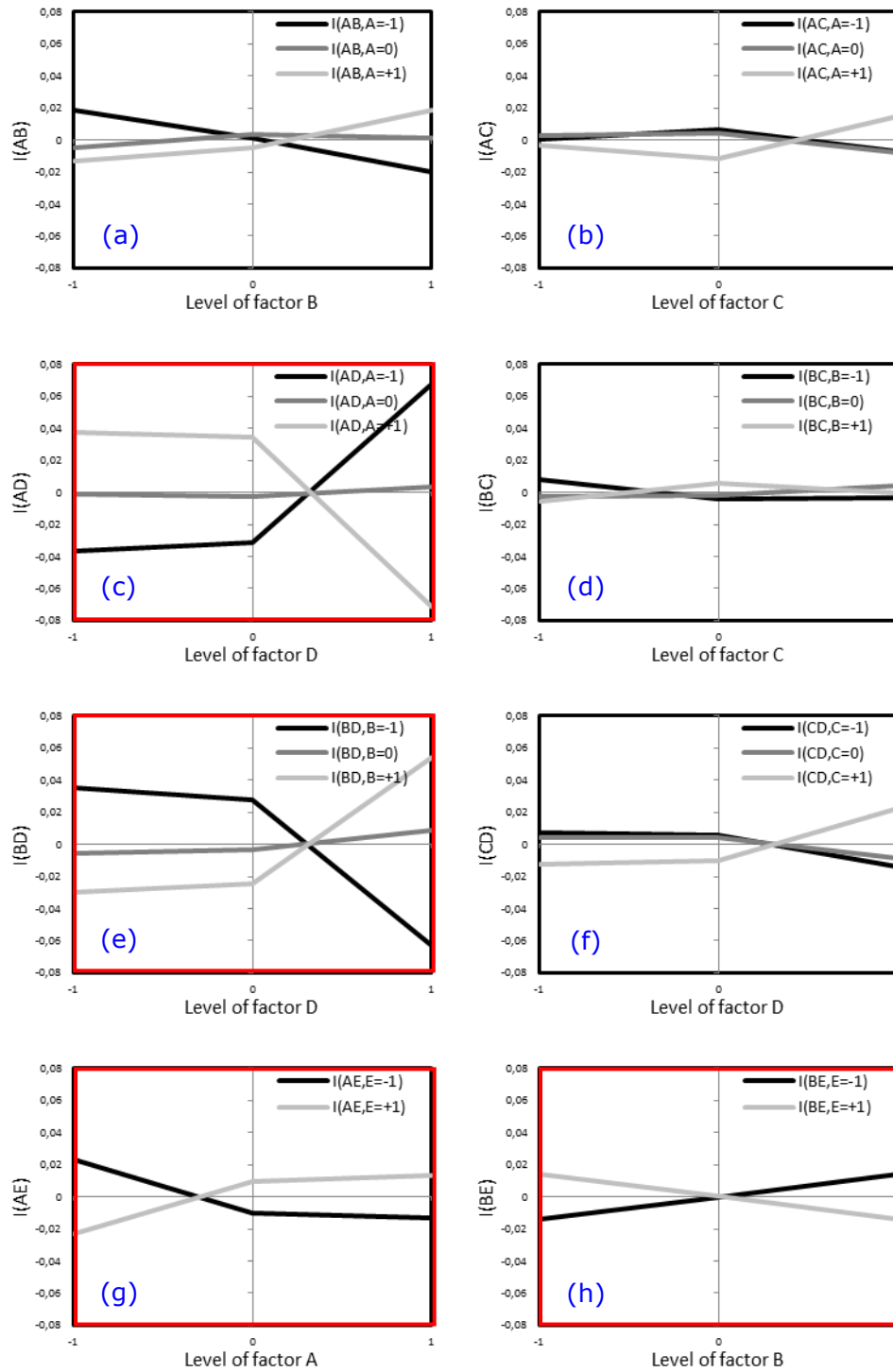


Figure 87. Effect of factor  $i$  ( $i=A,B,C,D,E$ ) on the correlation coefficient  $r^2$ . Influence of the experimental (algorithmic) parameters on the accuracy of the experimental measures. DoE.  $M=0.9307$ . Red= Significant effects. Black= Negligible effects. Validation of the data pre-processing algorithm. On the experimental characterization of CZM. Experimental test campaign.



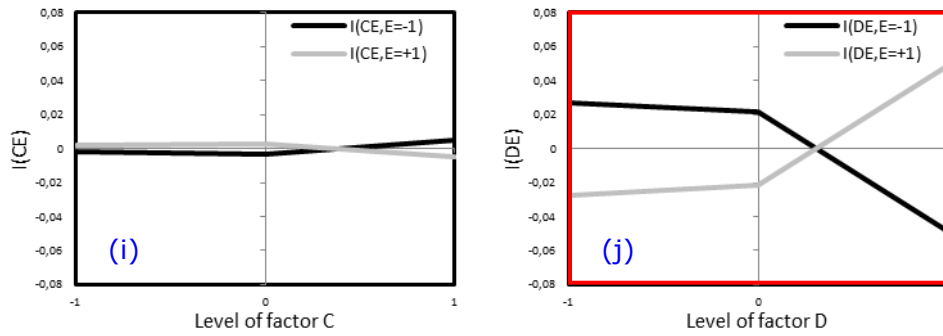


Figure 88. First order interaction between factors i-j (i,j=A,B,C,D,E) on the correlation coefficient  $r^2$ . Influence of the experimental (algorithmic) parameters on the accuracy of the experimental measures. DoE. Red= Significant interactions. Black= Negligible interactions.  $M=0.9307$ . Validation of the data pre-processing algorithm. On the experimental characterization of CZM. Experimental test campaign.

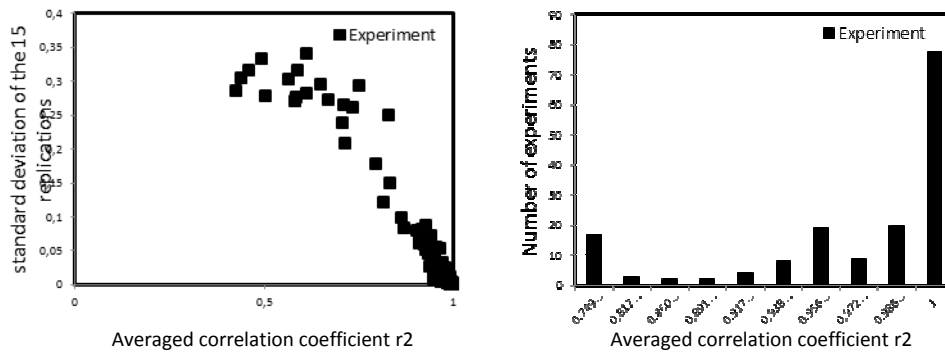


Figure 89. Evolution of the standard deviation (dispersion) of the 15 replications as a function of the averaged correlation coefficient  $r^2$ . Influence of the experimental (algorithmic) parameters on the accuracy of the experimental measures. DoE.  $M=0.9307$ . Validation of the data pre-processing algorithm. On the experimental characterization of CZM. Experimental test campaign.

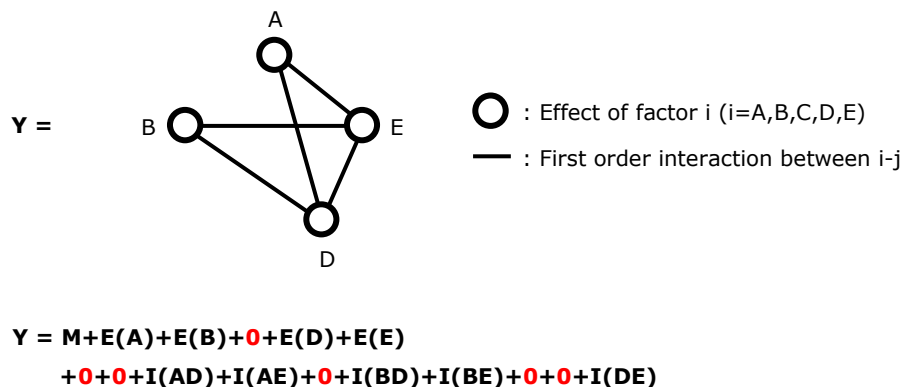


Figure 90. Reduced linear Taguchi's graph of main effects and interactions. Full factorial Design of Experiments (DoE). Black= Significant effects, interactions. Red= Negligible effects, interactions. Data pre-processing. On the experimental characterization of CZM. Experimental test campaign.

The results presented from Fig.87 to Fig.89 then suggest:

(i) The initial SNR appears as a key parameter in increasing the accuracy of measuring the successive derivatives of the upper adherend displacement field (see Fig.87-(a)), then suggesting that a significant attention has to be given into reducing the noise of the measured signal before any pre-processing of the data. This can be achieved in various ways so that it results in improving the overall quality of the displacement measures (DIC).

(ii) The spatial resolution of the instantaneous images of the upper adherend displacement field also appears as a key parameter in increasing the accuracy of the estimation of the successive derivatives of the upper adherend displacements (see Fig.87-(b), Fig.88-(e) and Fig.88-(h)). A particular attention has then to be given to measuring the displacements of the upper adherend with an sufficient enough spatial resolution.

(iii) On another side, the time resolution (i.e. number of images of the upper adherend displacement field taken during the experiment) appears as negligibly influencing the accuracy of the estimation of the successive derivatives of the upper adherend displacements (see Fig.87-(c), Fig.88-(b), Fig.88-(d), Fig.88-(f) and Fig.88-(i)). So that its own effect as well as its respective interactions with other factors can be legitimately neglected at first sight (see Fig.38).

(iv) Similarly to the initial SNR or the spatial resolution of the displacement images, the degree of the polynomial series used for fitting/differentiating the pre-processed displacements also appears as a parameter that has to be chosen with extreme caution. Indeed, although increasing the degree of the polynomial series from 4 to 6 appears as negligibly influencing the overall accuracy of the measure, increasing it from 6 to 8 results in a serious degradation of the accuracy of the measure (see Fig.87-(d)). This degradation of the accuracy of the measurement using high order polynomials is a well-known issue, and is due to the oscillation of the polynomial series around the experimental set of data points for increasing degrees (i.e. Runge's phenomenon). A particular attention has then to be given in choosing the best compromise between fitting the experimental data points using high order polynomials functions and preserving the overall accuracy of the measurement of its successive derivatives.

(v) Finally, the choice of the Moore-Penrose pseudo inverse model for minimizing in the sense of the least squares method the vertical deviation between the polynomial function (i.e. used for fitting/differentiating the set of experimental data points) and the experimental data points themselves appears as a worthwhile way of influencing the accuracy of the measured displacement derivatives (see Fig.87-(e)). It is then suggested that simultaneously accounting for both  $w(x)$  and  $\theta(x)=dw(x)/dx$  when fitting/differentiating the experimental set of data points significantly increases the accuracy of the measurement.

### 3.6.2. Experimental setup, preparation of the specimens and instrumentations

To check for the experimental workability/sustainability of the newly suggested characterization method (i.e. the direct method) the mechanical response of four adhesive

joint specimens is here investigated (e.g. ENF, DCB, MMB and SLJ). The ENF, DCB, MMB and SLJ adhesive test specimens are representative of either pure mode I, pure mode I and (or) mixed-mode I/II adhesive solicitations. The test specimens are bonded using the SAF-30MIB adhesive paste from AEC-Polymers. The SAF-30MIB adhesive paste is a room-temperature cured highly flexible methacrylate adhesive used in the outboard manufacturing/repairing industry. The adherends are made of a laminated aluminum-magnesium-silicon aluminum alloy (6060 series). The bulk material properties of the aluminum alloy are characterized from dumb tensile test specimens in advance of the present experimental test campaign (see Section 3.3.1). The adherends elastic properties are reminded in Tab.10. To enhance the adhesion properties of the adhesive layer before bonding, each adherend is cleaned using the AEC-Polymers T700 dry cleaning spray. To ensure a constant adhesive thickness along the overlap, two calibrated anti-adhesive tapes are stuck at each side of the bonded overlap (see Fig.91). The small cracks induced by the use of calibrated anti-adhesive tapes will be accounted in each of the latter on analyses. The dimensions of each specimen are controlled after bonding. The averaged dimensions are given in Tab.11.

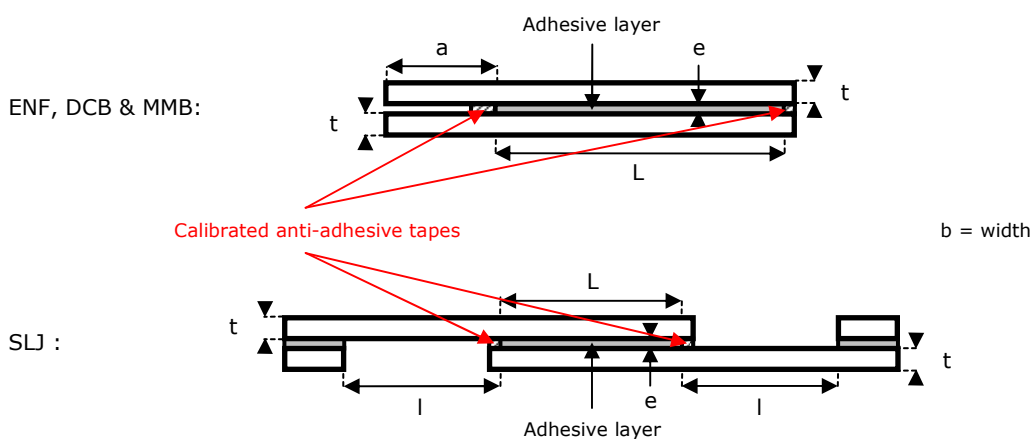


Figure 91. Schematic representation the manufacturing process of the ENF, DCB, MMB and SLJ adhesive joint specimens. Experimental setup, preparation of the specimens and semi-analytical analyses. On the experimental characterization of CZM. Experimental test campaign.

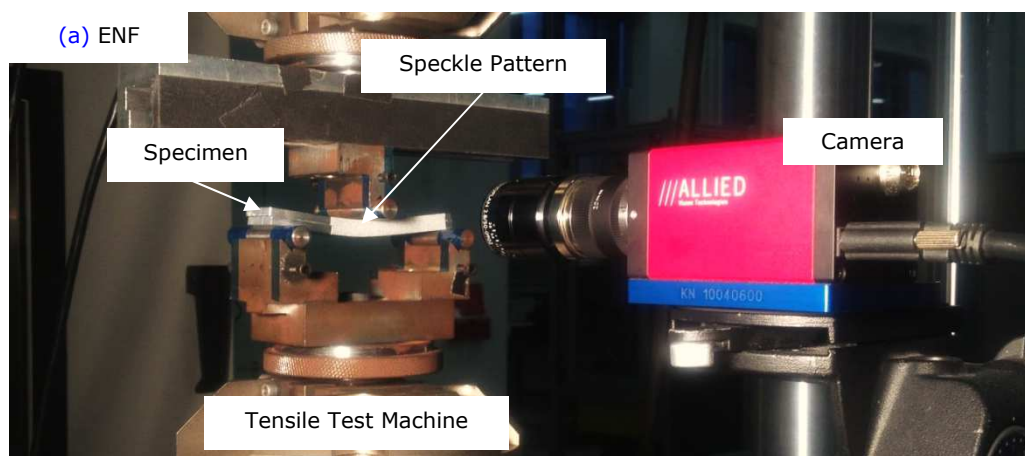
Tab 10. Experimental characterization of aluminum Tensile Test (TT) bulk specimens. Elastic material properties. Young's Tensile (YT) modulus. Poisson's ratio (Nu). Aluminum= 6060 series. Bulk material properties.

Young's Tensile modulus (YT)	Poisson's ratio (Nu)
66000 MPa	0.35

Tab 11. Controlled geometries of the ENF, DBC, MMB and SLJ adhesive joint specimens. Aluminum= 6060 series. Adhesive= SAF-30MIB. Experimental setup, preparation of the specimens and semi-analytical analyses. On the experimental characterization of CZM. Experimental test campaign.

	a	L	l	t	e	b
ENF	29.82mm	71.43mm	N.A.	3.96mm	0.230mm	22.0mm
DCB	30.69mm	70.0mm	N.A.	3.96mm	0.180mm	22.0mm
MMB	30.21mm	70.89mm	N.A.	3.96mm	0.180mm	22.0mm
SLJ	N.A.	51.4mm	29.35mm	3.96mm	0.120mm	22.0mm

Similarly to [Sections 3.3.1 and 3.3.2](#), the entire test campaign is performed on an electro-mechanical test machine (Ref: Instron AI735-1325). Except for the mixed-mode I/II characterization experiments that are performed on an electro-mechanical test machine (Ref: Kilo-Newton AI264-FT). Both the applied load, the resulting displacement and the adherend-to-adherend displacement field at crack tip are measured during the tests. The evolution of both the applied load and the resulting displacement are measured using the build in machine load and displacement cells. The evolution of the adherend-to-adherend displacement field is measured using the Digital Image Correlation (DIC) technique (see [Fig.92](#) and [Fig.93](#)). The pure mode deformations of the adhesive layer are computed from the relative displacement of the adherends neutral fibers (see [Fig.94](#)). Both DIC and build in machine measures are synchronized using an analogical-to-numerical National Instrument (NI) acquisition card so that it facilitates the processing of the adhesive constitutive CZM relationships. The mechanical stiffness of the Tensile Test Machine (TTM) is characterized so that the resulting displacement measured by the build in machine displacement cell is corrected to fit the true displacement of the adhesive test specimens. Four specimens of each configuration are tested (e.g. ENF, DCB, MMB and SLJ). The SLJ specimens are tested for validation purposes only. Correlations between experimental and numerical Force versus Resulting Displacement curves are used to evaluate the ability of the newly suggested approaches (i.e. the direct method) to characterize and reconstitute the mechanical response of the tested adhesive specimens. A particular emphasis is given to the ability of the suggested approaches to reconstitute both the experimental stiffness and the maximum load bearing capability of each adhesive specimen. The numerical analyses are performed using the procedure presented and described in ([Parioussien et al. 2013](#)) and in [Chapter 1](#). Both adhesive and adherends nonlinear stress-strain evolution laws are accounted for.



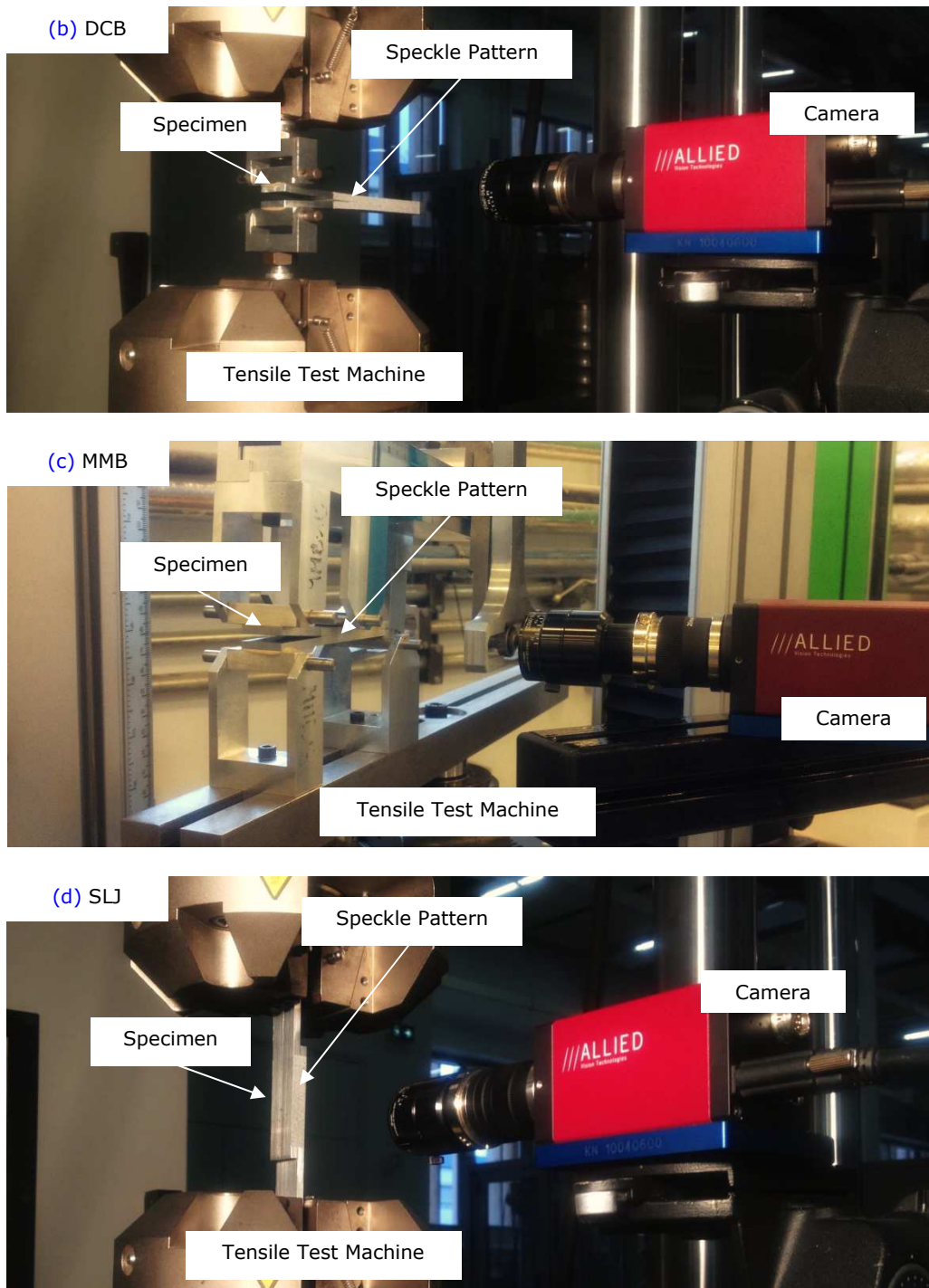


Figure 92. Experimental monitoring the of the adherend-to-adherend displacement field using Digital Image Correlation (DIC) techniques. Experimental setup, preparation of the specimens and semi-analytical analyses. On the experimental characterization of CZM. Experimental test campaign.

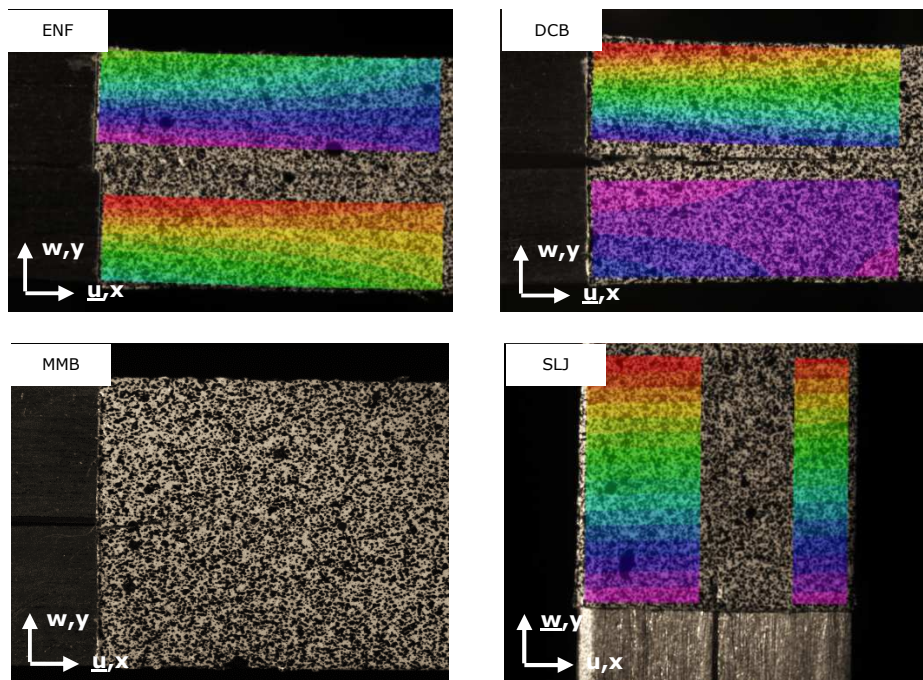


Figure 93. Experimental monitoring the of the adherend-to-adherend displacement field using Digital Image Correlation (DIC) techniques. Experimental setup, preparation of the specimens and semi-analytical analyses. On the experimental characterization of CZM. Experimental test campaign.

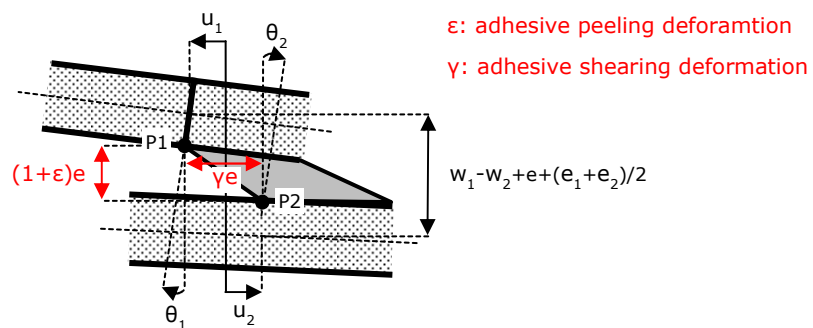
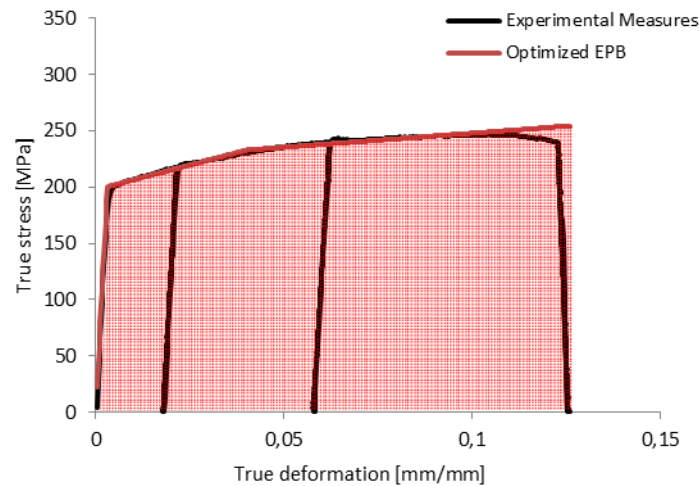


Figure 94. Schematic representation of the shearing and peeling adhesive deformations. Experimental setup, preparation of the specimens and semi-analytical analyses. On the experimental characterization of CZM. Experimental test campaign.

### 3.6.3. Material description

As presented in Section 3.6.2, the bulk material properties of each adherend are characterized from tensile test specimens in advance of the adhesive test campaign (see Section 3.3.1). The adherends constitutive stress-strain relationship is approximated using a trilinear elastic-plastic material behavior. The model is optimized so that it fits at best the measured stress-strain relationship in pure traction (see Fig.95).

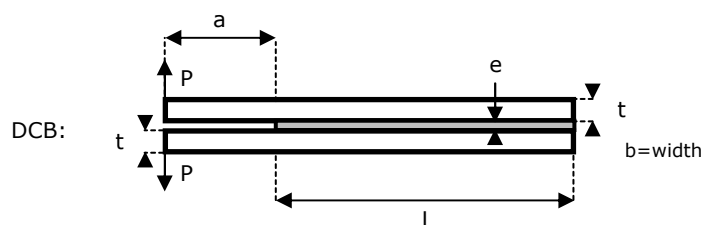


	Elastic	Plastic 1	Plastic 2
Model (EPB)	$\sigma(\varepsilon) = E\varepsilon$	$\sigma(\varepsilon) = \sigma_1 + E_{T,1}(\varepsilon - \varepsilon_1)$	$\sigma(\varepsilon) = \sigma_2 + E_{T,2}(\varepsilon - \varepsilon_2)$
Parameters	$E = 66000 MPa$	$E_{T,1} = 8800 MPa$ $\sigma_1 = 200.31 MPa$ $\varepsilon_1 = 0.003035$	$E_{T,2} = 250 MPa$ $\sigma_2 = 232.84 MPa$ $\varepsilon_2 = 0.04$
Validity	$0 \leq \varepsilon \leq \varepsilon_1$	$\varepsilon_1 \leq \varepsilon \leq \varepsilon_2$	$\varepsilon_2 \leq \varepsilon$

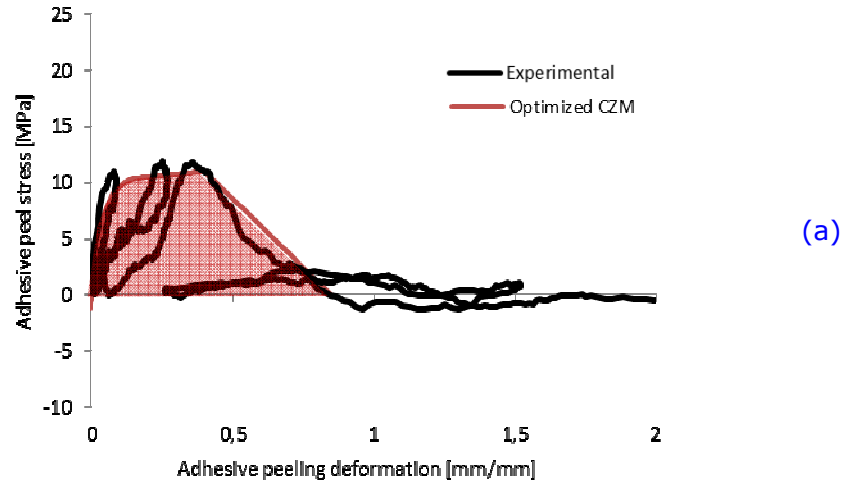
Figure 95. Experimental characterization of aluminum Tensile Test (TT) bulk specimens elastic-plastic properties. Aluminum= 6060 series.  $\sigma$ = True stress.  $\varepsilon$ = True deformation. Bulk material properties.

### 3.6.4. Quasi-static experiments

**Mode I: DCB.** Fig.96-(a) presents the obtained adhesive traction-separation laws in the case of pure mode I adhesive solicitations. Fig.96-(b) presents the comparison between experimental measures and semi-analytical predictions in terms of Applied Load versus Resulting Displacement evolution law. Three models are used for the comparison (see Section 3.7). The irregularities observed in the measured traction-separation law are due to residual noises when measuring the successive derivative of the adherend-to-adherend displacement field. However good agreement is shown in terms of both predicted stiffness and maximum load bearing capability of the DCB joint specimen.



	a	L	t	e	b
Dimensions	30.69mm	70.0mm	3.96mm	0.180mm	22.0mm



	Elastic	Plastic	Softening
Model (CZM)	$S(\varepsilon) = \frac{k_s \varepsilon_1}{\ln(e_s)} \left( 1 - \exp\left(\frac{\ln(e_s)}{\varepsilon_1} \varepsilon\right) \right)$	$S(\varepsilon) = S_1 + k_{s,1}(\varepsilon - \varepsilon_1)$	$S(\varepsilon) = S_2 \frac{\varepsilon_3 - \varepsilon}{\varepsilon_3 - \varepsilon_2}$
Parameters	$k_s = 250 \text{ MPa}$ $e_s = 0.030$ $\varepsilon_1 = 0.15$	$k_{s,1} = 2.5 \text{ MPa}$ $S_1 = 10.37 \text{ MPa}$ $\varepsilon_1 = 0.15$	$S_2 = 10.99 \text{ MPa}$ $\varepsilon_2 = 0.4$ $\varepsilon_3 = 0.75$
Validity	$0 \leq \varepsilon \leq \varepsilon_1$	$\varepsilon_1 \leq \varepsilon \leq \varepsilon_2$	$\varepsilon_2 \leq \varepsilon \leq \varepsilon_3$

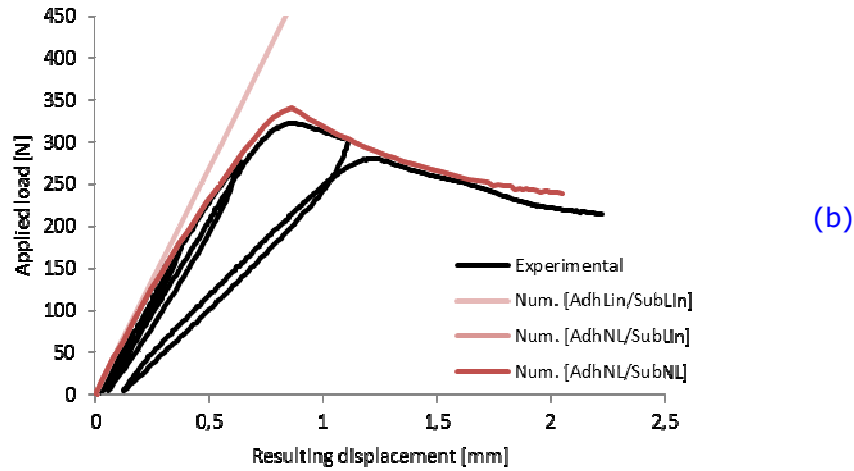
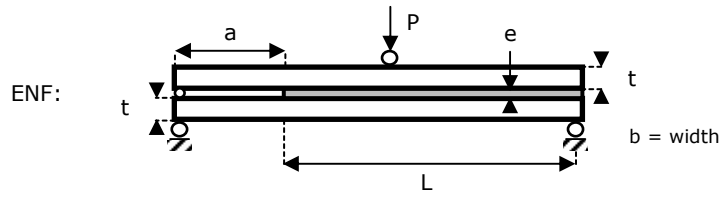


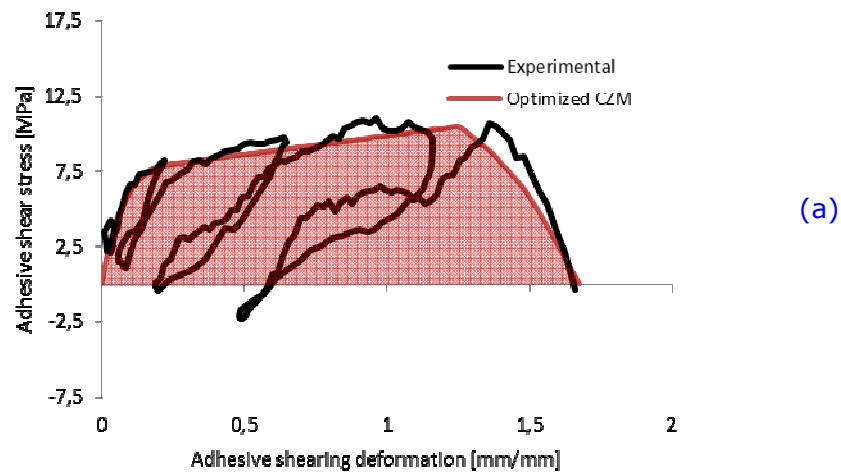
Figure 96. (a) Experimental adhesive traction separation law in pure mode I. (b) Comparison between experimental results and semi analytical predictions in terms of Applied versus Resulting Displacement evolution laws. Experimental investigation on metal-to-metal adhesive joints. Quasi-static experiment. Mode I. DCB.

**Mode II: ENF.** Fig.97-(a) presents the obtained adhesive traction-separation laws in the case of pure mode II adhesive solicitations. Fig.97-(b) presents the comparison between experimental measures and semi-analytical predictions in terms of Applied Load versus Resulting Displacement evolution law. Three models are used for the comparison (see Section 3.7). The irregularities observed in the measured traction-separation law are due to residual noises when measuring the successive derivative of the adherend-to-adherend displacement

field. However good agreement is shown in terms of both predicted stiffness and maximum load bearing capability of the ENF joint specimen.



	a	L	t	e	b
Dimensions	29.82mm	71.43mm	3.96mm	0.230mm	22.0mm



	Elastic	Plastic	Softening
Model (CZM)	$T(\gamma) = \frac{k_T \gamma_1}{\ln(e_T)} \left( 1 - \exp\left(\frac{\ln(e_T)}{\gamma_1} \gamma\right) \right)$	$T(\gamma) = T_1 + k_{T,1}(\gamma - \gamma_1)$	$T(\gamma) = T_2 \frac{\gamma_3^3 - \gamma^3}{\gamma_3^3 - \gamma_2^3}$
Parameters	$k_T = 110 \text{ MPa}$ $e_T = 0.075$ $\gamma_1 = 0.2$	$k_{T,1} = 2.5 \text{ MPa}$ $T_1 = 7.85 \text{ MPa}$ $\gamma_1 = 0.2$	$T_2 = 10.48 \text{ MPa}$ $\gamma_2 = 1.25$ $\gamma_3 = 1.675$
Validity	$0 \leq \gamma \leq \gamma_1$	$\gamma_1 \leq \gamma \leq \gamma_2$	$\gamma_2 \leq \gamma \leq \gamma_3$

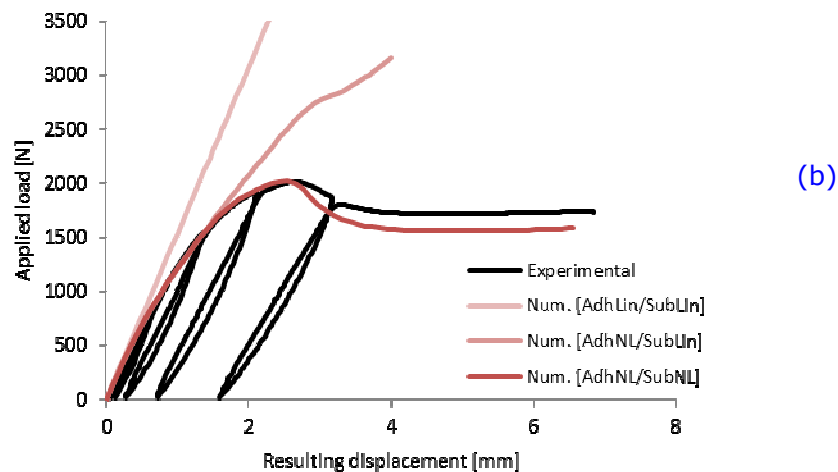


**Figure 97.** (a) Experimental adhesive traction separation law in pure mode II. (b) Comparison between experimental results and semi analytical predictions in terms of Applied versus Resulting Displacement evolution laws. Experimental investigation on metal-to-metal adhesive joints. Quasi-static experiment. Mode II. ENF.

### **Mixed-mode I/II: MMB.**

*The direct method.* Similarly to the previous subsections, the constitutive behavior of the adhesive layer facing mixed-mode I/II solicitations was investigated using the afore described direct method. However the results obtained were shown as practically unexploitable due to the extremely small levels of longitudinal displacements measured by the camera, compared to the transversal ones. It then resulted in extremely badly conditioned measures (i.e. high SNRs) in the axial direction, so that the longitudinal displacement of the upper neutral fiber was not differentiated with sufficient accuracy for the direct method to allow for the restitution of the adhesive constitutive relationships. An alternative characterization method was then developed for characterizing the effective mixed-mode I/II properties of the adhesive layer.

*Alternative characterization method: The inverse method.* Since the direct method is shown as unable to address with sufficient accuracy the effective evolution of the adhesive stresses (strains) at crack tip when facing mixed-mode I/II solicitations (see [Section 3.6.4](#)), an alternative characterization method has to be developed for characterizing the effective mixed-mode I/II properties of the adhesive layer. Here is suggested to use an inverse characterization method. Then, a complete semi-analytical model of the Mixed-Mode Bending (MMB) joint specimen is constructed. The model account for both the pure mode I and pure mode II adhesive traction separation laws characterized from [Fig.96-\(a\)](#) and [Fig.97-\(a\)](#). Since both adherends material nonlinearities are likely to appear, both adherend are modeled as monolithic beams exhibiting nonlinear axial stress-strain evolution law (see [Fig.95](#)). For simplification purpose, both initiation and propagation mixed-mode criteria are presumed as following a power law energetic relationship with the additional condition  $n=m$  (see [Fig.98](#)).

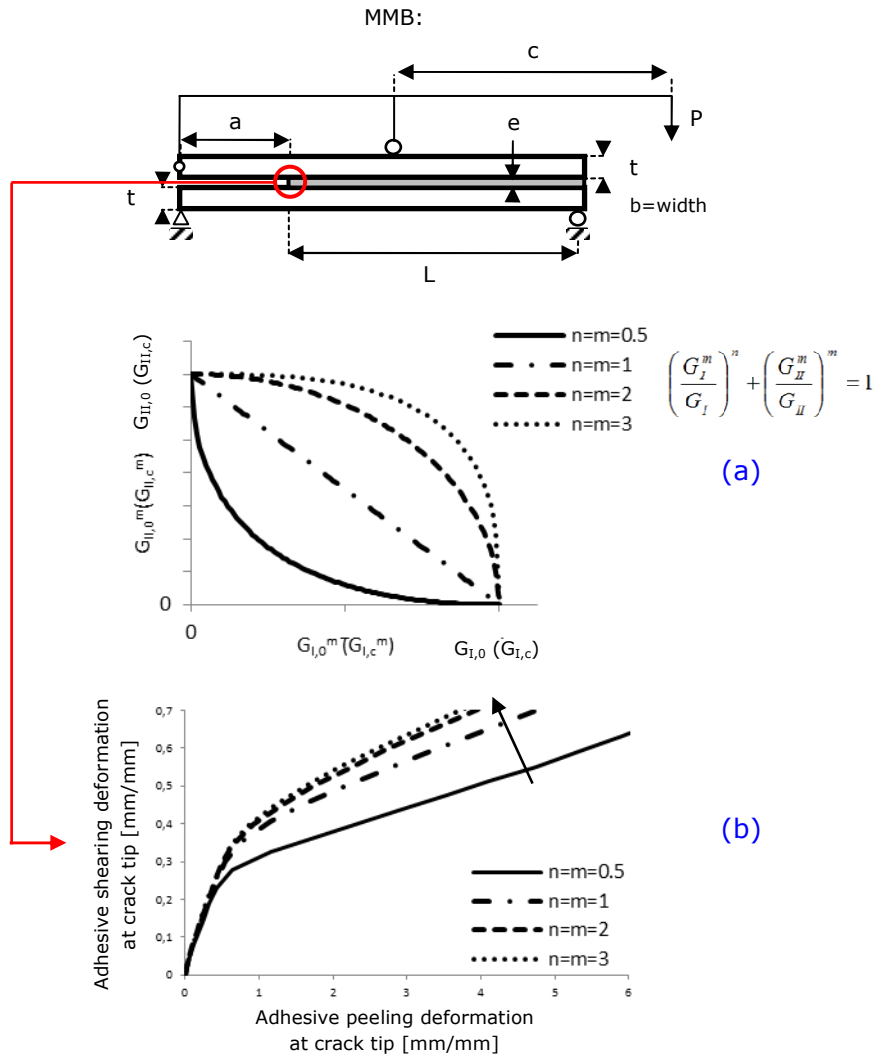


Figure 98. (a) Representation of the power law energetic relationship for  $n=m= 0.5, 1, 2,$  and  $3$ . (b) Influence of the mixed-mode criterion on the evolution of the adhesive mode mixity at crack tip. Experimental investigation on metal-to-metal adhesive joints. Quasi-static experiment. Mixed-mode I/II. MMB. Alternative characterization method. The inverse method.

Fig.99-(a) then presents the comparison between the measured and the predicted adhesive mixed-mode load path at crack tip for the best fit  $n=m=1$ . Fig.99-(b) presents the comparison between experimental measures and semi-analytical predictions in terms of Applied Load versus Resulting Displacement evolution law. Three models are used for the comparison (see Section 3.7). Good agreement is shown in terms of both stiffness and maximum load bearing capability of the MMB joint specimen (i.e. for both  $c=85.25\text{mm}$  and  $c=152.25\text{mm}$ ).

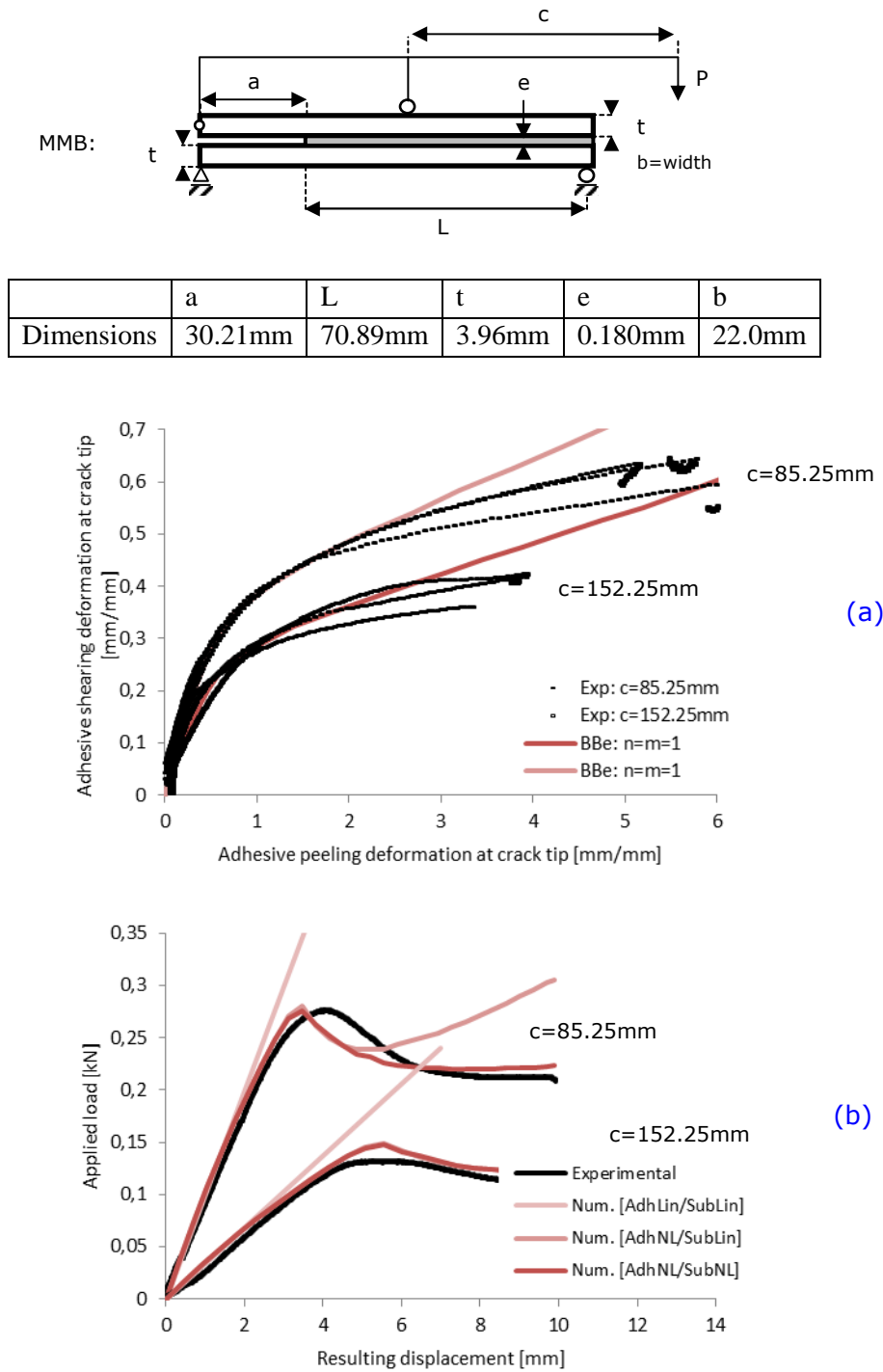


Figure 99. (a) Comparison between experimental and semi-analytical predictions of the adhesive mixed-mode load path at crack tip. Characterization of the effective adhesive mixed-mode properties using inverse method. (b) Comparison between experimental results and semi-analytical predictions in terms of Applied versus Resulting Displacement evolution laws. Experimental investigation on metal-to-metal adhesive joints. Quasi-static experiment. Mixed-mode I/II. MMB.

**Validation: SLJ.** Fig.100 presents the comparison between experimental measures and semi-analytical predictions in terms of Applied Load versus Resulting Displacement evolution law.

Three models are used for the comparison (see Section 3.7). Good agreement is shown in terms of both stiffness and maximum load bearing capability of the SLJ joint specimen.

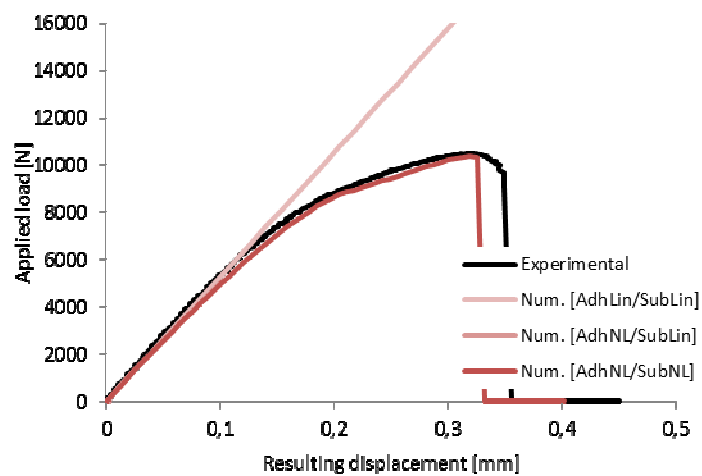
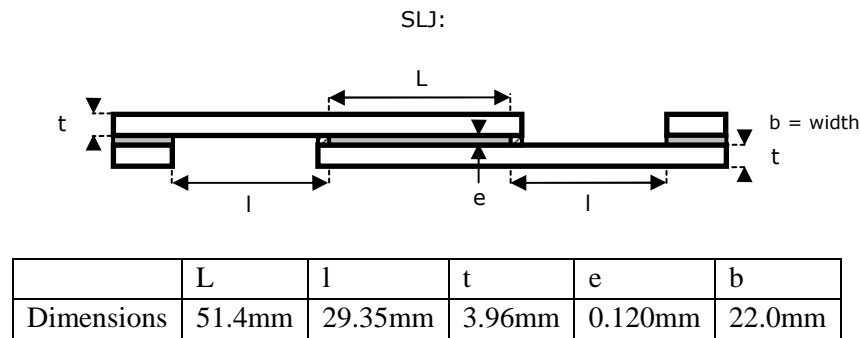


Figure 100. Comparison between experimental results and semi analytical predictions in terms of Applied versus Resulting Displacement evolution laws. Experimental investigation on metal-to-metal adhesive joints. Quasi-static experiment. Validation. SLJ.

### 3.7. Conclusion and discussion

Numbers of experimental protocols for the characterization of the cohesive properties of thin adhesive layers based on classical Fracture Mechanics tests have been suggested over the past few years (Anderson *et al.* 2003, Alfredsson 2003, Alfredsson *et al.* 2003, Alfredsson 2004, Leffler *et al.* 2006, Hogberg 2006, Hogberg *et al.* 2007, Cui *et al.* 2014, Cui 2014, Da Silva 2012). A large amount of them are based on the concept of the specimen energetic balance associated to the computation of the path independent J-integral. Three of them are presented in Sections 3.4.2 to 3.4.4. However the aim of the present thesis is not to cover all the existing protocols for the characterization of thin adhesive interfaces. The underlined simplifications as well as the direct limitations of those approaches are set out and discussed. It is seen from Sections 3.4.2 to 3.4.4 that most of those characterization procedures lie on assumptions that can appear as limiting for the true characterization of the cohesive properties of thin adhesive interfaces (i.e. validity of the early-design criteria, impossibility of early-designing the adhesive joint specimen without knowing in advance the adhesive peel (shear) modulus, inability of monitoring the evolution of adhesive stresses during unloading phases, etc).

Due to the necessity of developing techniques that allow for the characterization of cohesive interface properties, three new and original protocols for the characterization of the effective cohesive properties of thin adhesive interfaces are then presented and developed in view of their implementation. Those protocols are based on the monitoring of the successive derivatives of the adherend-to-adherend displacement field nearby the adhesive crack tip and have the advantage of not requiring any path integration of the joint equilibrium equations. It is seen from Fig.73 to Fig.75 that the obtained adhesive stress-strain evolution laws are in close agreement with those predicted by semi-analytical analyses (i.e. during both loading and unloading phases).

Finally, the first results of an experimental test campaign are provided so that it validates the new protocols in the case of metal-to-metal adhesive bonding. The mechanical response of three adhesive test specimens is investigated (e.g. ENF, DCB and SLJ). Those test specimens are representative of either pure mode I, pure mode II and/or mixed-mode I/II. The adhesive traction-separation laws are computed from both the measured adhesive stress and deformations at crack tip (see Sections 3.2 to 3.4). In pure mode II, it is shown that the adhesive layer experiences three distinct phases (see Fig.97). The first one, the linear-elastic phase, appears as extremely limited compared to the entire deforming capability of the adhesive layer (i.e. the plastic + softening phases representing up to 85% of the entire deforming capability of the adhesive layer). As a result, it then legitimately questions the legitimacy of using simplistic linear-elastic adhesive stress analyses, even for early-design purposes (see Sections 3.4.2 to 3.4.4). It is also seen from Fig.97 that the adhesive unloading behavior reveals a significant coupling between pure yielding and pure adhesive stiffness degradation. It then questions the ability of classical CZM approaches, that generally assume a pure degradation of the adhesive stiffness, to model the behavior of adhesive specimens subjected to varying loading amplitudes (e.g. static, fatigue, etc). The conclusions are similar in pure mode I.

To demonstrate the ability of such approaches to reconstitute the mechanical behavior of the studied adhesive specimens, three numerical models of each specimen are constructed. In the first one, the adhesive layer is presumed as acting as a linear-elastic interface resuming both the initial stiffnesses of the measured adhesive pure modes traction-separation laws (e.g.  $E=250\text{MPa}$  and  $G=110\text{MPa}$ ). Both adherends are modeled as linear-elastic monolithic beams (e.g.  $E=66\text{GPa}$  and  $\nu=0.36$ ). Good agreement is shown in terms of initial stiffness of the specimen. However significant deviations are observed after the adhesive layer enters its non-linear domain (i.e. depending on the adhesive test specimen). In the second model, the adhesive layer is presumed as acting as a cohesive interface resuming the complete adhesive pure modes traction-separation laws characterized from Fig.96 and Fig.97. Both adherends are modeled as linear-elastic monolithic beams (e.g.  $E=66\text{GPa}$  and  $\nu=0.36$ ). Fulfilling agreement is shown for both DCB and SLJ adhesive specimens in terms of both stiffness and maximum load bearing capability. It then suggests that the adhesive degradation process (i.e. characterized by both pure mode I and pure mode II traction separation laws) is the main mechanism involved in the ruin of the studied DCB and SLJ specimens. However significant deviations are still observed in the case of both ENF and MMB adhesive specimens. In the

third semi-analytical model, the adhesive layer is presumed as acting as a cohesive interface resuming the complete adhesive pure modes traction-separation laws characterized from [Fig.96](#) and [Fig.97](#). However both adherends are this time modeled as nonlinear monolithic beams resuming the true traction-compression stress-strain relationship of the 6060 series aluminum alloy (see [Section 3.3.1](#)). Fulfilling agreement is shown for both ENF and MMB adhesive specimens in terms of both stiffness and maximum load bearing capability. It then suggests that the ENF (MMB) adhesive specimen experiences significant levels of adherends plasticity (i.e. sufficient to impact non-negligibly the predicted Applied Load versus Resulting Displacement evolution law).

– This page has been voluntarily left blank –

## **Chapter 4. Conclusion**

The field of computational mechanics and particularly Finite Elements (FE) methods have provided numerous techniques for modeling the mechanical behavior of adhesively bonded joints over the past few years. However these techniques generally involves high computational requirements and can lead to instability due to numerical convergence issues.

As a result, numbers of engineers and researchers have suggested working on simplified analyses of the mechanical equilibrium of the joint. The simplified 1D-beam adhesive stress analysis is inspired by the FE method and allows for the resolution of the system of governing differential equations of the bonded overlap at low computational costs. The displacements (forces) of both adherends as well as the adhesive stresses (strains) are then obtained from solving the local equilibrium of the adherends. The method then consists in meshing the structure. A fully bonded overlap is meshed using a unique 4-nodes macro-element. This macro-element, referred to as the BBe element, is specially formulated to allow for the resolution of the system of governing differential equations of the bonded overlap at low computational costs. The outer adherends, referred to as Beam elements, are in turn meshed using specifically formulated Euler-Bernoulli beam elements. The simplified 1D-beam adhesive stress analysis thus takes the advantage of the flexibility of FE methods and the robustness of theoretical approaches.

In this thesis:

(i) An original way of accounting for the effective behavior of adhesive layers within the formulation of a dedicated macro-element analysis, referred to as the simplified 1D-beam adhesive stress analysis, is presented and developed in view of its implementation. The suggested analysis is inspired by the FE method, and allows for the nonlinear behavior of the adhesive layer to be accounted for with no restriction on the specimen geometry (see [Sections 2.3 and 2.4 of Chapter 2](#)). The proposed adhesive material models are formulated under a two dimensional mixed-mode model that account for the possible interaction (interdependency) between both pure mode I and pure mode II adhesive stress-strain evolutions laws.

(ii) Then, the preceding iterative resolution procedure is adapted (upgraded) so that it allows for both adhesive and adherends material nonlinearities to be simultaneously accounted for.

Then, an original way of accounting for the effect of the surrounding adherends plasticization based on an adaptation of the classical theory of beam plasticity (see [Sections 2.5 and 2.6 of Chapter 2](#)) is presented and developed in view of its implementation.

(iii) The results obtained from the suggested solution procedure are then compared to those of both sandwich type analyses and Finite Element (FE) predictions involving cohesive interface elements. Good agreement is shown.

By the use of the presented simplified joint analysis, it is shown that the mechanical response of a large range of adhesively bonded joints can be investigated using a restricted number of specifically formulated elements. It has then conducted to the development of a simplified stress analysis tool allowing for the simulation of a large range of bonded assemblies at low computational costs (see [Appendix 7](#)).

The use (development) of such analyses (tool) has also highlighted the need of proper experimental protocols for measuring the true nonlinear behavior of adhesive layers sandwiched between two rigid or semi-rigid adherends.

Indeed, it is seen from [Chapter 2](#) that both FE and simplified 1D-beam adhesive stress analyses are based on the modeling of the adhesive interfacial strength through a set of adhesive cohesive properties (i.e. traction separation laws) in pure mode I, mode II and mixed-mode I/II. Accurate experimental protocols for the measurement of the effective adhesive cohesive properties are then essential for the strength prediction of adhesively bonded joints. As a result, numerous authors have worked on providing experimental protocols for characterizing the cohesive properties of thin adhesive layers.

In this thesis:

(i) The results obtained from three existing experimental protocols for the characterization of the constitutive relationships of thin adhesive layers are presented (see [Section 3.4 of Chapter 3](#)) and compared to numerical predictions (i.e. in terms of simplified 1D-beam adhesive stress analyses). Significant deviations as well as limitations are demonstrated.

(ii) Then, and due to the need for developing proper techniques that allow for the characterization of adhesive cohesive properties, three new protocols for the characterization of the effective cohesive relationships of thin adhesive layers are presented and developed in view of their implementation (see [Section 3.5 of Chapter 3](#)). Each of these techniques is based on the real time monitoring of the adherend-to-adherend displacement field nearby the adhesive crack tip of specifically designed specimens (i.e. DCB, ENF & MMB). The results obtained are then compared to numerical predictions (i.e. in terms of simplified 1D-beam adhesive stress analyses). Good agreement is shown.

(iii) Finally, the first results of an experimental test campaign on metal-to-metal adhesive bonding are provided so that the new characterization protocols are validated in the case of metal-to-metal adhesive joints.

– This page has been voluntarily left blank –

– This page has been voluntarily left blank –

**References**

(Adams & Wake 1997) Adams RD, Comyn J and Wake WC. Structural adhesive joints in engineering. Springer Science & Business Media. Chapman & Hall. ISBN 0412709201, 9780412709203. 1997.

(Adams & Peppiatt 1973) Adams RD and Peppiatt NA. Effect of Poisson's ratio strains in adherends on stress of an idealized lap joint. Journal of Strain Analysis. Volume 8, N°2, pages 134-139. 1973.

(Alfredsson *et al.* 2003) Alfredsson, Biel A and Leffler K. An experimental method to determine the complete stress-deformation relation for a structural adhesive layer loaded in shear. 9<sup>th</sup> International Conference on The Mechanical Behavior of Materials, Geneva. 2003.

(Alfredsson 2004) Alfredsson KS. On the instantaneous energy release rate of the end notched flexure adhesive joint specimen. International Journal of Solids and Structures. Volume 41, pages 4787-4807. 2004.

(Allman 1977) Allman DJ. A theory for elastic stresses in adhesive bonded lap joints. Quarterly Journal of Mechanics and Applied Mathematics. Volume 30, pages 415-436. 1977.

(Anderson *et al.* 2003) Andersson T and Stigh U. The stress-elongation relation for an adhesive layer loaded in peel using equilibrium of energetic forces. International Journal of Solids and Structures. Volume 41, pages 413-434. 2004.

(Anderson *et al.* 2006) Andersson T and Biel A. On the effective constitutive properties of thin adhesive layer loaded in peel. International Journal of Fracture. Volume 141, Issue 1, pages 227-246. 2006.

(Andrews & Patterson 1973) Andrews HC and Patterson CL. Singula value decomposition and digital image processing. IEEE Transactions on Accoustics, Speech and Signal Processing. Volume x, N°1, pages xx-xx. 1976.

(Anyfantis 2012) Anyfantis KN. Analysis and design of composite-to-metal adhesively bonded joints. PhD Thesis. National Technical University of Athens, School of Naval Architecture and Marine Engineering. 2012.

- (Bartczak 2010) Bartczak Z and Geleski A. Plasticity of semicrystalline Polymers. *Macromolecular Symposia*. Volume 294, Issue 1, pages 67-90. 2010.
- (Berthelot 1999) Berthelot JM. *Composite Materials: Mechanical behavior and structural analysis*. Springer Science & Business Media. ISBN 0387984267, 9780387984261. 1998.
- (Bigwood & Crocombe 1991) Crocombe AD and Bigwood DA. Nonlinear adhesive bonded joint design analyses. *International Journal of Adhesion and Adhesives*. Volume 10, N°1, pages 31-41. 1990.
- (Boussarie 2013) Boussarie N. *Analyse à la rupture de jonctions collées*. Sogeti High Tech, Confidential Note. MS Thesis, MATMECA. 2013.
- (Broughton 1999) Hinopoulos G and Broughton WR. Evaluation of the T-peel joint using the finite element method. Centre for Materials Measurement & Technology. National Physical Laboratory. ISBN 1361-4061. 1999.
- (Broughton 2001a) Broughton B and Gower M. *Measurement good practice guide n°47. Preparation and testing of adhesive joints*. NPL Material Centre. National Physical Laboratory. ISBN 1368-6550. 2001.
- (Broughton 2001b) Broughton WR, Croker LE and Urquhart JM. Project PAJex1. Report 3. *Strength of adhesive joints: A parametric study*. NPL Material Center. National Physical Laboratory. ISBN 1473-2734. 2001.
- (Campilho 2008) Campilho RDSG, DE Moura MFSF, Ramantani DA and Goncalves JPM. Obtaining the cohesive laws of a trapezoidal mixed-mode damage model using an inverse method. *Ciencia e Tecnologia dos Materials*. Volume 20, N°1-2, pages xx-xx. 2008.
- (Campilho 2013) Campilho RDSG, Banea MD, Neto JABP and Da Silva LFM. Modelling adhesive joints with cohesive zone models: Effects of the cohesive law shape of the adhesive layer. *International Journal of Adhesion and Adhesives*. Volume 44, pages 48-56. 2013.
- (Clarke *et al.* 2003) Clarke JL. *Structural design of polymer composites : Eurocomp design code and background document*. CRC Press. ISBN 0203475135, 9780203475133. 2003.
- (Crocombe 2009) Khoramishad H, Crocombe AD, Katnam KB and Ashcroft IA. A generalized damage model for constant amplitude fatigue loading of adhesively bonded joints. *International Journal of Adhesion and Adhesives*. Volume 30, pages 513-521. 2010.
- (Crocombe 2011) Khoramishad H, Crocombe AD, Katnam KB and Ashcroft IA. Fatigue damage modeling of adhesively bonded joints under variable amplitude loading using cohesive zone model. *Engineering Fracture Mechanics*. Volume 78, pages 3212-3225. 2011.
- (Cui *et al.* 2014) Cui H, Koussios S, Li Y and Beukers A. Constitutive law of adhesive layer measured with mixed-mode bending test. *Engineering Fracture Mechanics*. Volume 127, pages 235-251. 2014.

- (Cui 2014) Cui H. Delamination and debonding failure of laminated composite T-joints. PhD Thesis. Design and Production of Composite Structures Group. Delft University of Technology. 2014.
- (De Moura 2009) De Moura MFSF, Campilho RDSG and Goncalves JPM. Mixed-mode cohesive damage model applied to the simulation of the mechanical behavior of laminated composite adhesive joints. *Journal of Adhesion Science and Technology*. Volume 23, Issue 10-11, pages xx-xx. 2009.
- (De Moura 2014) De Moura MFSF and Goncalves JPM. Development of a cohesive zone model for fatigue/fracture characterization of composite bonded joints under mode II loading. *International Journal of Adhesion and Adhesives*. Volume 54, pages 224-230. 2014.
- (Da Silva 2009) Da Silva LFM, Das Neves PJC, Adams RD and Spelt JK. Analytical models of adhesively bonded joints. Part I: Literature survey. *International Journal of Adhesion and Adhesives*. Volume 29, pages 319-330. 2009.
- (Da Silva 2012) Da Silva LFM and Campilho RDSG. Advances in numerical modeling of adhesive joints. *SpringBriefs in Computational Mechanics*. DOI 10.1007/978-642-23608\_1. 2012.
- (Da Veiga 2009) Da Veiga A. Développement de modèles analytiques pour des assemblages collés et hybrides boulonnés-collés non équilibrés. Sogeti High Tech, Confidential Technical Note. MS Thesis, MATMECA. 2009.
- (Fernlund 2007) Fernlund G. Stress analysis of bonded lap joints using fracture mechanics and energy balance. *International Journal of Solids and Structures*. Volume 27, pages 574-592. 2007.
- (Fraisse 1993) Fraisse P and Schmit F. Use of J-integral as fracture parameter in simplified analysis of bonded joints. *International Journal of Fracture*. Volume 63, pages 59-73. 1993.
- (Gaubert 2011) Gaubert F. Modélisation bidimensionnelle du comportement élasto-plastique d'un joint collé. Sogeti High Tech, Confidential Technical Note. MS Thesis, MATMECA. 2011.
- (Gavoille 2014) Gavoille C. Modélisation simplifiée de jonctions collées sous chargement cyclique. Sogeti High Tech, Confidential Technical Note. MS Thesis, MATMECA. 2014.
- (Gift *et al.* 2013) Gift MDM, Selvakumar P and Alexis SJ. A review on the cohesive zone models for crack propagation analysis. *Elixir Mechanical Engineering*. Volume 55, pages 12760-12763. 2013.
- (Goland & Reissner 1944) Goland M and Reissner E. The stresses in cemented joints. *Journal of Applied Mechanics*. Volume 11, pages 11-27. 1944.

- (Hansson 2002) Hansson P. Fracture analysis of adhesive joints using the finite element method. Thesis for the degree of Master of Science. Lund Institute of Technology. Division of Solid Mechanics. 2002.
- (Hart-Smith 1973a) Hart-Smith LJ. Adhesive bonded single lap joints. NASA Technical Report. CR-112236. 1973.
- (Hart-Smith 1973b) Hart-Smith LJ. Adhesive bonded double lap joints. NASA Technical Report. CR-112235. 1973.
- (Hart-Smith 1980) Hart-Smith LJ. Adhesive bonding of aircraft primary structures. Society of Automotive Engineer, Inc. Aerospace Congress and Exposition, Los Angeles. 1980.
- (Higgins 2000) Higgins A. Adhesive bonding for aircraft structures. International Journal of Adhesion and Adhesives. Volume 20, pages 367-376. 2000.
- (Hogberg 2004) Hogberg JL. Mechanical behavior of single layer adhesive joints: An integrated approach. Thesis for the degree of Licentiate of Engineering. Chalmers University of Technology. ISSN 1650-8912 2004:3. 2004.
- (Hogberg 2006) Hogberg JL. Mixed-mode testing of adhesive layer. 27th International Symposium on Materials Science, Polymer Composite Materials for Wind Power Turbines, Riso. 2006.
- (Hogberg *et al.* 2007) Hogberg and Stigh U. Specimen proposals for mixed-mode testing of adhesive layer. Engineering Fracture Mechanics. Volume 73, pages 2541-2556. 2006.
- (Hogberg 2007) Hogberg JL, Sorensen BF and Stigh U. Constitutive behavior of mixed-mode loaded adhesive layer. International Journal of Solids and Structures. Volume 44, pages 8335-8354. 2007.
- (Igens 1993) Van Igen JW and Vlot A. Stress analysis of adhesively bonded single lap joints: Survey and evaluation of analyses. LR-740. Faculty of Aerospace Engineering. Structures and Materials Laboratory. Delft University of Technology. 1993.
- (Jones 1998) Jones RM. Mechanics of composite materials. CRC Press. ISBN 156032712X, 9781560327127. 1998.
- (Kamm 1998) Kamm JL. Singular value decomposition based methods for signal and image restoration. PhD Thesis. Faculty of the Dedman College. Southern Methodist University. 1998.
- (Kenane 1997) Kenane M and Benzeggagh ML. Mixed-mode delamination fracture toughness of unidirectional glass/epoxy composites under fatigue loading. Composites Science and Technology. Volume 57, pages 597-605. 1997.
- (Konstantinides *et al.* 1997) Konstantinides K, Natarajan B and Yovanof GS. Noise estimation and filtering using block based singular value decomposition. IEEE Transactions on Image Processing. Volume 6, N°3, pages 479-483. 1997.

- (Lachaud 2011) Lachaud F. Contribution à l'analyse multi échelle du comportement mécanique non linéaire matériau des structures composites. HdR. University of Toulouse. 2011.
- (Lang & Mallick 1998) Lang TP and Mallicj PK. Effect of spew geometry on stresses in single lap adhesive joints. *International Journal of Composite Materials*. Volume 33, pages 640-666. 1998.
- (Lees 1987) Lees AW. Bonding composites. *International Journal of Adhesion and Adhesives*. Volume 4, pages 591-602. 1986.
- (Leffler *et al.* 2006) Leffler K, Alfredsson KS and Stigh U. Shear behavior of adhesiv layers. *International Journal of Solids and Structures*. Volume 44, pages 530-545. 2007.
- (Leguillon 2002) Leguillon D. Strength or toughness? A criterion for crack onset at a notch. *European Journal of Mechanics and Solids*. Voulem 21, Issue 1, pages 61-72. 2002.
- (Li *et al.* 2005) Li S, Thouless MD, Waas AM, Schroeder and Zavattieri PD. Mixed-mode cohesive zone models for fracture of an adhesively bonded polymer matrix composite. *Engineering Fracture Mechanics*. Volume 73, pages 64-78. 2006.
- (Luo & Tong 2009) Luo Q and Tong L. Analytical solutions for nonlinear analysis of composite single lap adhesive joints. *International Journal of Adhesion and Adhesives*. Volume 29, pages 144-154. 2009.
- (Martin *et al.* 2016) Martin E, Vandellos T, Leguillon D and Carrère N. Initiation of edge debonding: Coupled criterion versus cohesive zone model. *International Journal of Fracture*. Volume x, pages 1-12. 2016.
- (Matlab 2014) MATLAB® R2012b. User's manual. 2014.
- (Mittal 2002) Mittal KL. Adhesive joints: Formation, characteristics and testing. VSP. ISBN 9067643718, 9789067643719. 2002.
- (Moonen *et al.* 1992) Moneen M, Van Dooren P and Vandewalle J. A singular decomposition updating algorithm for subspace tracking. *SIAM Journal on Matrix Analysis and Applications*. Volume 13, Issue 4, pages 1015-1038. 1992.
- (Mortensen 1997) Mortensen F. Development of tools for engineering analysis and design of high performance FRP composite structural elements. PhD Thesis. Institute of Mechanical Engineering. Aalborg University. ISBN 0905-2305. 1998.
- (Oudin 2011) Oudin H. Introduction à la plasticité. CEL-00483603, Version 1. Ecole Centrale de Nantes. 2010.
- (Paroissien 2006) Paroissien E. Contribution aux assemblages hybrides: Application aux jonctions aéronautiques. PhD Thesis. Univesrity of Toulouse. 2006.

- (Paoissien *et al.* 2013) Paoissine E, Lachaud F and Jacobs T. A simplified stress analysis of bonded joints using macro-elements. In: *Advances in Modeling and Design of Adhesively Bonded Systems*. By: Kumar S and Mittal KL. Wiley. Pages 93-146. 2013.
- (Pickthall & Heller 1997) Pickthall C, Heller M and Rose LRF. Finite element analysis of the double lap joint with elastic-plastic adhesive. Aeronautical and marine Research Laboratory. Airframes and Engines Division. DSTO-TR-0528. 1997.
- (Raydan 2011) Monsalve M and Raydan M. A secant method for nonlinear matrix problems. *Lecturas en Ciencias de la Computacion*. ISSN 1316-6239. Centro de Calculo Cientifico y Tecnologico de la UCV. Facultad de Ciencias. Universidad Central de Venezuela. 2011.
- (Reeder 1990) Reeder JR and Crews JR. Mixed-mode bending method for delamination testing. *AIAA Journal*. Volume 28, N°7, pages 1270-1276. 1990.
- (Reeder 1992) Reeder JR. An evaluation of mixed-mode delamination failure criteria. NASA Technical Report. 104210. 1992.
- (Rice 1968) Rice JR. A path independent integral and the approximate analysis of strain concentration by notches and cracks. *Journal of Applied Mechanics*. Volume 35, pages 379-386. 1968.
- (Sadek 2012) Sadek RA. SVD based image processing applications: State of the art, contributions and research challenges. *International Journal of Advanced Computer Science and Applications*. Volume 3, N°7, pages xx-xx. 2012.
- (Samcef 2013) SAMCEF® v14.1. User's manual. 2013.
- (Schwartz 2013) Schwartz S. Modélisation simplifiée d'une jonction collée sous chargement cyclique. Introduction de non linéarités matérielles. Sogeti High Tech, Confidential Technocal Note. MS Thesis, MATMECA. 2013.
- (Stapelton 2011) Stapelton SE and Wass AM. Modeling progressive failure of bonded joints using a single joint finite element. *AIAA Journal*. Volume 49, N°8, pages xx-xx. 2011.
- (Stapleton 2012) Stapelton SE. The analysis of adhesively bonded advanced composite joints using joint finite elements. PhD Thesis. University of Michigan. 2012.
- (Tong 1994) Tong L. Bond shear strength for adhesive bonded double lap joints. *International of Solids and Structures*. Volume 31, pages 2919-2931. 1994.
- (Tsai 1994) Tsai MY and Morton J. An evaluation of analytical and numerical solutions to the single lap joint. *International Journal of Solids and Structures*. Volume 31, pages 2537-2563. 1994.
- (Tsai *et al.* 1998) Tsai MY, Oplinger DW and Morton J. Improved theoretical solutions for adhesive lap joints. *International Journal of Solids and Structures*. Volume 35, N°12, pages 1163-1185. 1998.

- (Tsai & Morton 2010) Tsai MY and Morton J. An investigation into the stresses in double-lap adhesive joints with laminated composite adherends. *International Journal of Solids and Structures*. Volume 47, Issue 24, pages 3317-3325. 2010.
- (Valoroso 2004) Valoroso N and Champaney L. A damage model for simulating decohesion in adhesively bonded assemblies. *European Congress on Computational Methods in Applied Sciences and Engineering*, Jyvaskyla. 2004.
- (Volkersen 1938) Volkersen O. Die nietkraftverteilung in zugbeanspruchten nietverbindungen mit konstanten laschenquerschnitten. *Luftfahrtforschung*, Volume 15, pages 41-47. 1938.
- (Wahab 2012) Wahab MMA. Fatigue in adhesively bonded joints: A review. *International Scholarly Research Networ. Material Science*. DOI: 10.5402/2012/746308. Volume 2012, Article ID 746308, 25 pages. 2012.
- (Wegman & Van Twisk 2012) Wegman RF and Van Twisk J. Surface preparation techniques for adhesive bonding. Second Edition. Williams Andrew. ISBN 1455731285, 9781455731282. 2012.
- (Weissgraeber 2013) Weissgraeber P and Becker W. Finite fracture mechanics model for mixed-mode fracture in adhesive joints. *International Journal of Solids and Structures*. Volume 50, Issue 14-15, pages 2383-2394. 2013.
- (Weissgraeber 2014) Weissgraeber P, Stein N and Becker W. A general sandwich type model for adhesive joints with composite adherends. *International Journal of Adhesion and Adhesives*. Volume 55, pages 56-63. 2014.
- (Williams 1975) Williams JH. Stresses in adhesive between dissimilar adherends. *The Journal of Adhesion*. Volume 7, Issue 2, pages 97-107. 1975.



**List of PhD publications**

The work presented in this thesis has formed the basis of the following publications:

- Lelias G, Paroissien E, Lachaud F, Morlier J, Schwartz S and Gavaille C. An extended semi-analytical formulation for fast and reliable mode I/II stress analysis of adhesively bonded joints. *International Journal of Solids and Structures*. Volume 62, pages 18-38. 2015.
- Lelias G, Lachaud F, Morlier J and Paroissien E. On the experimental characterization of thin adhesive layers loaded in mode I, mode II and mixed-mode I/II. Submitted to: *International Journal of Solids and Structures* on the 27<sup>th</sup> of May 2016.

– This page has been voluntarily left blank –



**Appendix 1. Non-exhaustive review of simplified closed-form adhesive stress analyses of adhesively bonded joints (Da Silva 2009)**

	Material linearity			Adherends			Adhesive stresses			Solution	
	Adhesive		Adherent	Isotropic Composite			$\sigma_x$	$\sigma_y$	$\tau_{xy}$	Closed-form	Numerical
	Linear	Nonlinear	Linear	Nonlinear	Similar	Disimilar					
Volkersen [1]	X		X		X				X		
Goland and Reissner [2]	X		X		X			X	X		
Wah [21]	X		X	X	X				X		X
Hart-Smith [13,50]	X		X		X				X		X
Pirviets [22]	X		X		X				X		X
Grimes and Greimann [58]	X		X	X	X			X	X		X
Renton and Vinson [23-24]	X		X	X	X			X	X		X
Srinivas [25]	X		X	X	X			X	X		X
Allman [18]	X		X	X	X			X	X		X
Ojalvo and Eidinoff [16]	X		X	X	X			X	X		X
Delale et al. [32]	X		X	X	X			X	X		X
Bigwood and Crocombe [12]	X		X	X	X			X	X		X
Bigwood and Crocombe [51]	X		X	X	X			X	X		X
Cheng et al. [26]	X		X	X	X			X	X		X
Crocombe and Bigwood [59]	X		X	X	X			X	X		X
Adams and Mallick [31]	X		X	X	X			X	X		X
Tung [54]	X		X	X	X			X	X		X
Yang and Pang [27]	X		X	X	X			X	X		X
Frostig et al. [48]	X		X	X	X			X	X		X
Sawa et al. [28]	X		X	X	X			X	X		X
Mortensen and Thomsen [33]	X		X	X	X			X	X		X
Adams et al. [61]	X		X	X	X			X	X		X
Wang et al. [60]	X		X	X	X			X	X		X
Smeltzer and Kiang [56]	X		X	X	X			X	X		X

This page has been voluntarily left blank -

### Appendix 2. Supplementary material on the adherends constitutive equations

Thanks to the form of the classical Euler-Bernoulli beam kinematic it is possible to express the displacement field of both adherends in the form of (see [Section 2.5.1](#)):

$$\begin{cases} u^j(x, y) = u_j(x, y=0) - yw_{j,x}(x, y=0) \\ w^j(x, y) = w_j(x, y=0) \end{cases}, j=1,2 \quad (\text{A2.1})$$

where  $u^j(x,y)$  and  $w^j(x,y)$  respectively refer to the longitudinal and transverse displacement fields of adherend  $j$  ( $j=1,2$ ),  $u_j(x,y=0)$  and  $w_j(x,y=0)$  to the longitudinal and transverse displacements of the neutral fiber of adherend  $j$  ( $j=1,2$ ), and  $w_{j,x}(x,y=0)$  to the first derivative of  $w_j(x,y=0)$  with respect to  $x$ .

It is then possible to express the axial deformation in adherend  $j$  ( $j=1,2$ ) as:

$$\varepsilon^j(x, y) = u_{,x}^j(x, y) = u_{j,x}(x, y=0) - yw_{j,xx}(x, y=0) \quad (\text{A2.2})$$

And the axial stress in each ply of adherend  $j$  ( $j=1,2$ ) as:

$$\sigma_k^j(x, y) = \bar{\mathbf{Q}}_k^j \varepsilon^j(x, y) \quad (\text{A2.3})$$

Where  $\bar{\mathbf{Q}}_k^j$  refers to the reduced stiffness matrix of the  $k^{\text{th}}$  ply of adherend  $j$  ( $j=1,2$ ).

According to the Classical Laminates Theory (CLT), the normal force and the bending moment in adherend  $j$  ( $j=1,2$ ) are expressed as:

$$\begin{cases} N_j(x) = \int_{-e_{j/2}}^{e_{j/2}} \sigma^j dy dz = \sum_{k=1}^n \int_{y_k}^{y_{k+1}} \sigma_k^j dy dz \\ M_j(x) = \int_{-e_{j/2}}^{e_{j/2}} \sigma^j y dy dz = \sum_{k=1}^n \int_{y_k}^{y_{k+1}} \sigma_k^j y dy dz \end{cases} \quad (\text{A2.4})$$

By combining (A3.2) (A3.3) and (A3.4) it is then possible to express the normal force and the bending moment in adherend  $j$  ( $j=1,2$ ) as:

$$\begin{cases} N_j(x) = \sum_{k=1}^n \int_{y_k}^{y_{k+1}} \sigma_k^j dy dz = b \sum_{k=1}^n \left( \int_{y_k}^{y_{k+1}} \bar{\mathbf{Q}}_k^j u_{j,x}(x, y=0) dy - \int_{y_k}^{y_{k+1}} \bar{\mathbf{Q}}_k^j y w_{j,xx}(x, y=0) dy \right) \\ M_j(x) = - \sum_{k=1}^n \int_{y_k}^{y_{k+1}} \sigma_k^j y dy dz = -b \sum_{k=1}^n \left( \int_{y_k}^{y_{k+1}} \bar{\mathbf{Q}}_k^j y u_{j,x}(x, y=0) dy - \int_{y_k}^{y_{k+1}} \bar{\mathbf{Q}}_k^j y^2 w_{j,xx}(x, y=0) dy \right) \end{cases} \quad (\text{A2.5})$$

Then leading to the adherend  $j$  ( $j=1,2$ ) constitutive equations:

$$\begin{cases} N_j(x) = A_j u_{j,x}(x, y=0) - B_j w_{j,xx}(x, y=0) \\ M_j(x) = -B_j u_{j,x}(x, y=0) + D_j w_{j,xx}(x, y=0) \end{cases} \quad (\text{A2.6})$$

Where:

$$\begin{cases} A_j = \sum_{k=1}^n \bar{\mathbf{Q}}_k^j (y_k - y_{k-1}) \\ B_j = \frac{1}{2} \sum_{k=1}^n \bar{\mathbf{Q}}_k^j (y_k^2 - y_{k-1}^2) \\ D_j = \frac{1}{3} \sum_{k=1}^n \bar{\mathbf{Q}}_k^j (y_k^3 - y_{k-1}^3) \end{cases} \quad (\text{A2.7})$$

### **Appendix 3. On the effective peel modulus of sandwiched adhesive layers**

In numbers of recent closed-form stress analyses of adhesively bonded joints (Clarke *et al.* 2003, Stapelton 2011, Stapelton 2012, Weissgraeber 2014) the adhesive layer has been assumed to act as a plane-strain deformable material when subjected to through thickness deformations. Then leading to the definition of the effective tensile adhesive modulus:

$$E_a^* = \frac{E_a(1-\nu_a)}{(1+\nu_a)(1-2\nu_a)} \quad (\text{A3.1})$$

Where  $\nu_a$  refer to the adhesive Poisson's ratio and  $E_a$  to the adhesive tensile modulus determined from the bulk material properties.

This modeling of the adhesive elastic behavior when subjected to through thickness deformations lies on the assumption that when sandwiched the adhesive transverse deformations are constrained by the surrounded rigid (or semi-rigid) adherends (see Fig.A3-1). However adherends are in facts not infinitely rigid. This is particularly true when bonding thin adherends. It is then legitimate to think that real adherends will allow for small adhesive transverse deformations to occur (i.e. depending on the ability of both adherends to constrain the adhesive transverse deformations). This ability of the adherends to constrain the adhesive transverse deformations can be modulated by different parameters: the thickness (stiffness) of the surrounding adherends, the thickness (stiffness) of the adhesive layer itself, etc.

In (Hart-Smith 1973b) the author suggested that the effective tensile modulus of the adhesive layer was resulting from a complex interaction between the adhesive layer itself and the surrounding adherends. The author then suggested using an effective adhesive tensile modulus given by (see Fig.A3-2):

$$\frac{1}{E_a^*} = \frac{1}{E_a} + \frac{k_1}{E_1} + \frac{k_2}{E_2} \quad (\text{A3.2})$$

where  $E_1$  and  $E_2$  are the transverse tensile moduli of the inner (upper) and the outer (lower) adherends,  $k_1$  and  $k_2$  the number (or fraction) of adhesive layer thicknesses for which the adherends are affected by the applied peel stresses, and  $E_a$  the adhesive tensile modulus determined from the bulk material properties. The author finally suggested that this effective tensile modulus of the adhesive layer (equation (A3.2)) should be determined by transverse loading of an adhesive film bonded to blocks rather than from bulk material properties specimen.

Since the second definition of the adhesive tensile modulus makes more sense to the authors of the present thesis, it is decided to refer to this particular modulus as the effective *peel modulus* of the adhesive layer. This *peel modulus* has then to be determined experimentally

from bonded overlap specimens, and do apply to the effective tensile modulus of the adhesive layer measured when subjected to through thickness deformations.

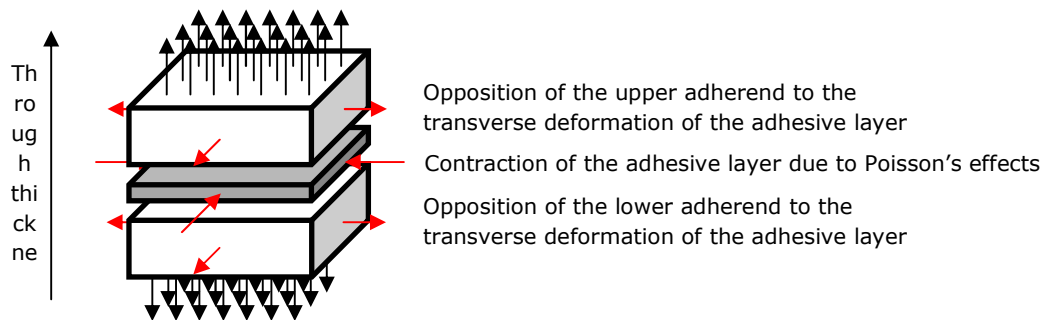


Figure A3-1. Schematic representation of the relative equilibrium between the adhesive layer transverse deformations (i.e. due to Poisson's effects) and the reactions/oppositions of the surrounding adherends. Through thickness adhesive loadings. Adhesive layer as a plane-strain deformation material. On the effective peel modulus of sandwiched adhesive layers.

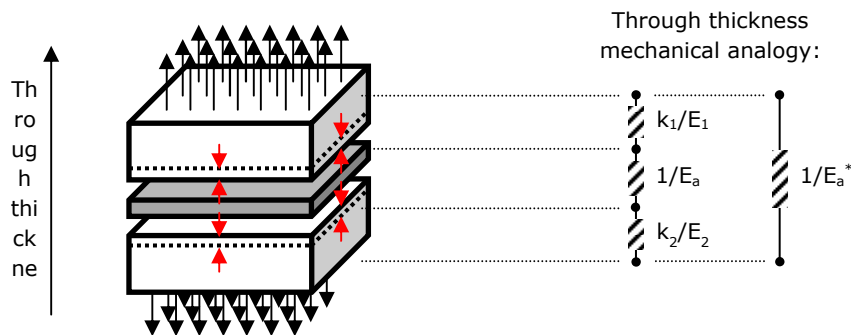


Figure A3-2. Schematic representation of the through thickness mechanical analogy of an adhesive layer sandwiched between two semi-rigid adherends. The peel modulus of sandwiched adhesive layers as a complex interaction between the adhesive layer itself and the surrounding adherends. On the effective peel modulus of sandwiched adhesive layers.

**Appendix 4. Expression of the adhesive shear (peel) stress distribution(s) depending on the nature of the roots of the characteristic polynomial**

1. Expression of the adhesive shear (peel) stress distribution(s) depending on the nature of the roots of the characteristic polynomial

As presented in [Chapter 2](#), the classical theory of homogeneous linear differential equations suggests that the analytical form of the adhesive shear (peel) stress distribution(s) as derived in ([Parioussien 2006](#), [Da Veiga 2009](#), [Parioussien et al. 2013](#)) can be completed by three additional expressions depending on the nature of the roots of the characteristic polynomial (A4.1):

$$P(R) = R^6 - k_1 R^4 + k_4 R^2 + (k_2 k_3 - k_1 k_4) = 0 \quad (\text{A4.1})$$

where:

$$\left\{ \begin{array}{l} k_1 = \frac{Gb}{e} \left[ \frac{D_1}{\Delta_1} \left( 1 + \frac{A_1 e_1 (e_1 + e)}{4D_1} \right) + \frac{D_2}{\Delta_2} \left( 1 + \frac{A_2 e_2 (e_2 + e)}{4D_2} \right) + \left( \frac{e_1 B_1}{\Delta_1} + \frac{e B_1}{2\Delta_1} - \frac{e_2 B_2}{\Delta_2} - \frac{e B_2}{2\Delta_2} \right) \right] \\ k_2 = \frac{Gb}{e} \left[ \frac{e_1 A_1}{2\Delta_1} - \frac{e_2 A_2}{2\Delta_2} + \left( \frac{B_1}{\Delta_1} + \frac{B_2}{\Delta_2} \right) \right] \\ k_3 = \frac{Eb}{e} \left[ \frac{(e_1 + e) A_1}{2\Delta_1} - \frac{(e_2 + e) A_2}{2\Delta_2} + \left( \frac{B_1}{\Delta_1} + \frac{B_2}{\Delta_2} \right) \right] \\ k_4 = \frac{Eb}{e} \left[ \frac{A_1}{\Delta_1} + \frac{A_2}{\Delta_2} \right] \end{array} \right. \quad (\text{A4.2})$$

and whose roots will be thereafter denoted  $R_1, R_2, R_3, R_4, R_5$  and  $R_6$ .

In ([Da Veiga 2009](#)), the author suggests relating the roots of equation (A4.1) to the roots of the 3<sup>rd</sup> order equivalent polynomial (A4.3):

$$P'(R') = R'^3 - k_1 R'^2 + k_4 R' + (k_2 k_3 - k_1 k_4) = 0 \quad \text{so that} \quad R' = R^2 \quad (\text{A4.3})$$

Which can be re-written in the form of the simpler canonical form:

$$P''(R'') = R''^3 + pR'' + q = 0 \quad \text{so that} \quad R'' = R' - k_1/3 \quad (\text{A4.4})$$

where:

$$\left\{ \begin{array}{l} p = -\frac{k_1^2}{3} + k_4 \\ q = -\frac{k_1}{27} (2k_1^2 - 9k_4) + (k_2 k_3 - k_1 k_4) \end{array} \right. \quad (\text{A4.5})$$

Then depending on the sign of the Cardano's discriminant  $\Delta=27q^2+4p^3$ , three specific cases can be distinguished: (i)  $\Delta>0$ , (ii)  $\Delta=0$  and (iii)  $\Delta<0$ .

For (i)  $\Delta>0$ , the polynomial  $P''$  is shown to have one real and two conjugate complex solutions, so that:

$$\begin{cases} R''_1 = u + v \\ R''_2 = ju + \bar{j}v \\ R''_3 = j^2u + j^2v \end{cases} \quad (\text{A4.6})$$

where:

$$\begin{cases} u = \sqrt[3]{(-q + \sqrt{\Delta/27})/2} \\ v = \sqrt[3]{(-q - \sqrt{\Delta/27})/2} \\ j = \bar{j}^2 = -1/2 + i\sqrt{3}/2 \\ j^2 = \bar{j} = -1/2 - i\sqrt{3}/2 \end{cases} \quad (\text{A4.7})$$

and where  $i$  refers to the imaginary unit so that  $i^2=-1$ .

Then depending on the sign of the roots  $R''_1$ ,  $R''_2$  and  $R''_3$ , the six roots  $R_1, R_2, R_3, R_4, R_5$  and  $R_6$  of the characteristic polynomial (A4.1) can be derived with respect to the variable substitutions introduced in equations (A4.4) and (A4.3), so that:

$$R_1 = +r \quad R_2 = -r \quad R_3 = (s+it) \quad R_4 = -(s+it) \quad R_5 = (s-it) \quad R_6 = -(s-it) \quad (\text{A4.8})$$

or:

$$R_1 = +ir \quad R_2 = -ir \quad R_3 = (s+it) \quad R_4 = -(s+it) \quad R_5 = (s-it) \quad R_6 = -(s-it) \quad (\text{A4.9})$$

depending on the sign of  $R'_1$ .

Similarly, for (ii)  $\Delta=0$ , the polynomial  $P''$  is shown to have two real solutions, one simple and one double, so that:

$$\begin{cases} R''_1 = 2\sqrt[3]{-q/2} = 3q/p \\ R''_2 = R''_3 = -\sqrt[3]{-q/2} = -3q/2p \end{cases} \quad (\text{A4.10})$$

Then depending on the sign of the roots  $R''_1$  and  $R''_2=R''_3$ , the six roots  $R_1, R_2, R_3, R_4, R_5$  and  $R_6$  of the characteristic polynomial (A4.1) can be derived with respect to the variable substitutions introduced in equations (A4.4) and (A4.3), so that:

$$R_1 = +ir_1 \quad R_2 = -ir_1 \quad R_3 = +r_2 \quad R_4 = -r_2 \quad R_5 = +r_2 \quad R_6 = -r_2 \quad (\text{A4.11})$$

or:

$$R_1 = +r_1 \quad R_2 = -r_1 \quad R_3 = +ir_2 \quad R_4 = -ir_2 \quad R_5 = +ir_2 \quad R_6 = -ir_2 \quad (\text{A4.12})$$

depending on the sign of the roots  $R''_1$  and  $R''_2=R''_3$ . It is worth noticing from equation (A4.10) that  $R''_1$  and  $R''_2=R''_3$  cannot be of the same sign, so that the roots  $R_1, R_2, R_3, R_4, R_5$  and  $R_6$  cannot be all real or all complex.

Finally, for (iii)  $\Delta < 0$ , the polynomial  $P''$  is shown to have three real solutions, so that:

$$\begin{cases} R''_1 = u + \bar{u} \\ R''_2 = ju + \overline{ju} \\ R''_3 = j^2u + \overline{j^2u} \end{cases} \quad (\text{A4.13})$$

where:

$$\begin{cases} u = \sqrt[3]{(-q + i\sqrt{-\Delta/27})/2} \\ j = \sqrt[3]{-1} = -1/2 + i\sqrt{3}/2 \end{cases} \quad (\text{A4.14})$$

So that  $R''_1, R''_2$  and  $R''_3$  can be expressed in their trigonometric form as:

$$R''_k = 2\sqrt{\frac{-p}{3}} \cos\left(\frac{1}{3} \arccos\left(\frac{-q}{2\sqrt{-p^3}}\right) + \frac{2k\pi}{3}\right) \quad \text{where } k=1,2,3 \quad (\text{A4.15})$$

Then depending on the sign of the roots  $R''_1, R''_2$  and  $R''_3$ , the six roots  $R_1, R_2, R_3, R_4, R_5$  and  $R_6$  of the characteristic polynomial (A4.1) can be derived with respect to the variable substitutions introduced in equations (A4.4) and (A4.3), so that:

$$R_1 = +r_1 \quad R_2 = -r_1 \quad R_3 = +r_2 \quad R_4 = -r_2 \quad R_5 = +ir_3 \quad R_6 = -ir_3 \quad (\text{A4.16})$$

or:

$$R_1 = +r_1 \quad R_2 = -r_1 \quad R_3 = +ir_2 \quad R_4 = -ir_2 \quad R_5 = +ir_3 \quad R_6 = -ir_3 \quad (\text{A4.17})$$

depending on the sign of the roots  $R''_1, R''_2$  and  $R''_3$ . Similarly to (ii)  $\Delta=0$ , it is worth noticing from equation (A4.15) that  $R''_1, R''_2$  and  $R''_3$  cannot be all of the same sign, so that the roots  $R_1, R_2, R_3, R_4, R_5$  and  $R_6$  cannot be all real or all complex.

Finally, it is possible to show that a total of four analytical expressions for the adhesive shear (peel) stress distribution(s) are derivable depending on the nature of the roots of the characteristic polynomial (A4.1), so that:

$$\begin{cases} S(x) = \begin{bmatrix} \overline{K_1}e^{sx} \sin(tx) + \overline{K_2}e^{sx} \cos(tx) + \overline{K_3}e^{-sx} \sin(tx) \\ + \overline{K_4}e^{-sx} \cos(tx) + \overline{K_5}e^{rx} + \overline{K_6}e^{-rx} \end{bmatrix} \\ T(x) = \begin{bmatrix} K_1e^{sx} \sin(tx) + K_2e^{sx} \cos(tx) + K_3e^{-sx} \sin(tx) \\ + K_4e^{-sx} \cos(tx) + K_5e^{rx} + K_6e^{-rx} + K_7 \end{bmatrix} \end{cases} \quad (\text{A4.18})$$

$$\begin{cases} S(x) = \begin{bmatrix} \overline{K_1}e^{sx} \sin(tx) + \overline{K_2}e^{sx} \cos(tx) + \overline{K_3}e^{-sx} \sin(tx) \\ + \overline{K_4}e^{-sx} \cos(tx) + \overline{K_5} \sin(rx) + \overline{K_6} \cos(rx) \end{bmatrix} \\ T(x) = \begin{bmatrix} K_1e^{sx} \sin(tx) + K_2e^{sx} \cos(tx) + K_3e^{-sx} \sin(tx) \\ + K_4e^{-sx} \cos(tx) + K_5 \sin(rx) + K_6 \cos(rx) + K_7 \end{bmatrix} \end{cases} \quad (\text{A4.19})$$

$$\begin{cases} S(x) = \begin{bmatrix} \overline{K_1} \sin(r_1x) + \overline{K_2} \cos(r_1x) + \overline{K_3} \sin(r_2x) \\ + \overline{K_4} \cos(r_2x) + \overline{K_5}e^{r_3x} + \overline{K_6}e^{-r_3x} \end{bmatrix} \\ T(x) = \begin{bmatrix} K_1 \sin(r_1x) + K_2 \cos(r_1x) + K_3 \sin(r_2x) \\ + K_4 \cos(r_2x) + K_5e^{r_3x} + K_6e^{-r_3x} + K_7 \end{bmatrix} \end{cases} \quad (\text{A4.20})$$

or:

$$\begin{cases} S(x) = \begin{bmatrix} \overline{K_1} \sin(r_1x) + \overline{K_2} \cos(r_1x) + \overline{K_3}e^{r_2x} \\ + \overline{K_4}e^{-r_2x} + \overline{K_5}e^{r_3x} + \overline{K_6}e^{-r_3x} \end{bmatrix} \\ T(x) = \begin{bmatrix} K_1 \sin(r_1x) + K_2 \cos(r_1x) + K_3e^{r_2x} \\ + K_4e^{-r_2x} + K_5e^{r_3x} + K_6e^{-r_3x} + K_7 \end{bmatrix} \end{cases} \quad (\text{A4.21})$$

2. Study of the sign of the Cardano's discriminant  $\Delta=27q^2+4p^3$  in the case of balanced monolithic (or symmetric) adherends

For simplification purpose, here is considered monolithic (or symmetric) adherends only, so that the upper and lower adherends coupling stiffnesses  $B_1$  and  $B_2$  are equal to zero. Additionally, the geometry as well as the extensional, coupling and bending stiffnesses of the upper and lower adherends are assumed as equals (i.e.  $e_1=e_2$ ,  $A_1=A_2=A$ ,  $D_1=D_2=D$  and  $B_1=B_2=B=0$ ).

Then, from equations (A4.2) fall:

$$\begin{cases} k_1 = \frac{2Gb}{Ae} \left( 1 + \frac{Ae_1(e_1 + e)}{4D} \right) \\ k_2 = k_3 = 0 \\ k_4 = \frac{2Eb}{De} \end{cases} \quad (\text{A4.22})$$

So that the Cardano's discriminant  $\Delta=27q^2+4p^3$  can be re-written in the form of:

$$\begin{aligned} \Delta &= 27q^2 + 4p^3 = 27 \left( -\frac{k_1}{27} (2k_1^2 - 9k_4) - k_1k_4 \right)^2 + 4 \left( -\frac{k_1^2}{3} + k_4 \right)^3 \\ &= \frac{8}{3} k_1^4 k_4 - 19k_1^2 k_4^2 + 4k_4^3 - \frac{4}{27} k_1^6 + \frac{12}{9} k_1^4 k_4 + 27k_1^2 k_4^2 + \frac{4}{27} k_1^6 \\ &= 4k_1^4 k_4 + 8k_1^2 k_4^2 + 4k_4^3 \end{aligned}$$

$$=4k_4(k_4+k_1^2)^2 \quad (\text{A4.23})$$

So that the Cardano's discriminant  $\Delta=27q^2+4p^3$  can be finally reduced to the following expression:

$$\Delta = \frac{8Eb}{De} \left[ \frac{2Eb}{De} + \left( \frac{2Gb}{Ae} \left( 1 + \frac{Ae_1(e_1+e)}{4D} \right) \right)^2 \right]^2 \quad (\text{A4.24})$$

Equation (A4.24) then suggests that for all physically acceptable choices of the parameters  $E$ ,  $G$ ,  $b$ ,  $e_1$ ,  $e$ ,  $A$  and  $D$  (i.e. strictly positive), the Cardano's discriminant  $\Delta=27q^2+4p^3$  will remain strictly positive (i.e.  $\Delta>0$ ).

Then studying the sign of  $R''_1$  provides:

$$R''_1 = \sqrt[3]{(-q + \sqrt{\Delta/27})/2} + \sqrt[3]{(-q - \sqrt{\Delta/27})/2} \quad (\text{A4.25})$$

$$\text{with } R''_1 > 0 \text{ if and only if } \begin{cases} -q > 0 \\ \sqrt{\Delta/27} > 0 \end{cases} \longrightarrow \text{Satisfied if } \Delta > 0 \quad (\text{A4.26})$$

Then studying the sign of  $-q$  provides:

$$\begin{aligned} -q &= \frac{k_1}{27} (2k_1^2 - 9k_4) + k_1k_4 = \frac{2}{27} k_1^3 + \frac{18}{27} k_1k_4 \\ &= \frac{2}{27} \left( \frac{2Gb}{Ae} \left( 1 + \frac{Ae_1(e_1+e)}{4D} \right) \right)^3 + \frac{18}{27} \frac{2Eb}{De} \frac{2Gb}{Ae} \left( 1 + \frac{Ae_1(e_1+e)}{4D} \right) \end{aligned} \quad (\text{A4.27})$$

So that equation (A4.27) finally suggests that for all physically acceptable choices of the parameters  $E$ ,  $G$ ,  $b$ ,  $e_1$ ,  $e$ ,  $A$  and  $D$  (i.e. strictly positive),  $-q$  will remain strictly positive (i.e.  $-q>0$ ).

Thanks to equations (A4.24) and (A4.27), it is finally shown that the analytical solutions of the adhesive shear (peel) stress distribution(s) derived in (Paoissien 2006, Da Veiga 2009, Paoissien *et al.* 2013) are fully legitimates in the case of balanced monolithic (or symmetric) adherends. However, in the case of unbalanced adherends and (or) if considering the possible coupling stiffnesses  $B_j$  of the upper (lower) adherend  $j$  ( $j=1,2$ ), the following demonstration is not straightforward so that counterexamples are easily identifiable.

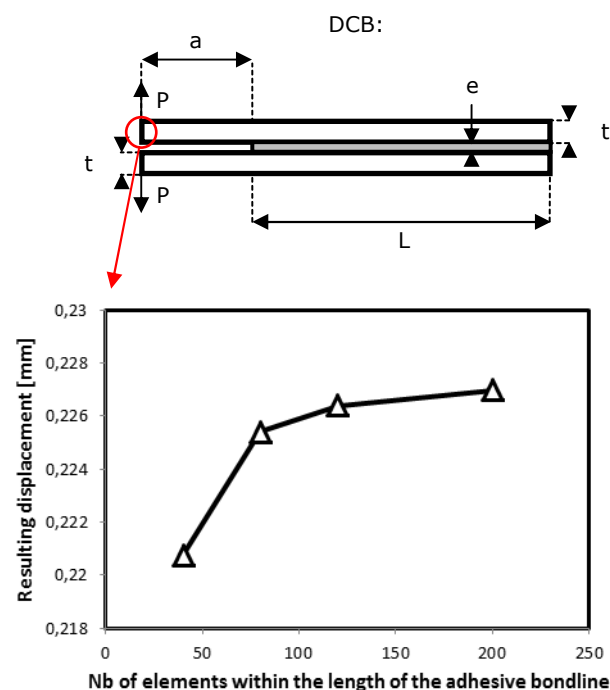
### Appendix 5. Convergence of the numerical analyses

#### 1. D

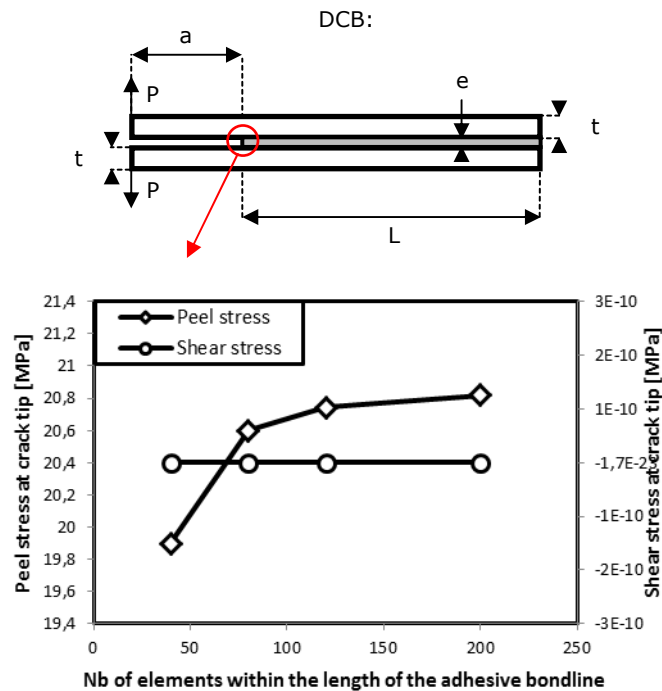
##### Double Cantilever Beam adhesive joint specimen (DCB)

##### 1.1. Convergence of the linear elastic Finite Element (FE) models

The DCB adhesive joint specimen consists in two adherends partially joined by a thin adhesive layer. The symmetric boundary and loading conditions of the specimen provide exclusively pure mode I solicitations of the adhesive layer. Since the DCB joint specimen is commonly recognized as the critical configuration in terms of convergence of the numerical analyses, its results are provided first. Both the adhesive layer and the surrounding adherends are considered as experiencing linear elastic deformations only. Here is presented the evolution of the resulting displacement (i.e. displacement that results from the applied load in N) as a function of the number of elements within the length of the adhesive bondline (see Fig.A5-1). Similarly, Fig.A5-2 presents the evolution of the adhesive peel (shear) stress at crack tip as a function of the number of elements within the length of the adhesive bondline. It is seen from Fig.A5-1 and Fig.A5-2 that the results of the linear elastic FE analyses are clearly depending on the mesh refinement. However the results are shown as rapidly converging towards an asymptote in terms of both resulting displacement and adhesive peel (shear) stress at crack tip.



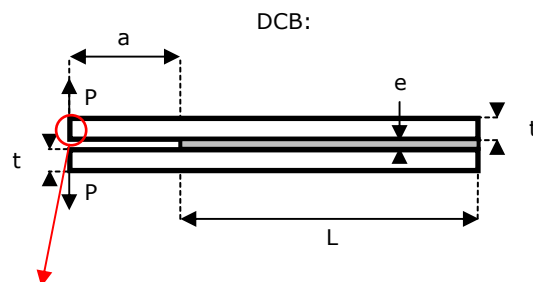
**Figure A5-1.** Evolution of Resulting Displacement as a function of the number of elements within the length of the adhesive bondline. Convergence of the linear elastic Finite Element (FE) models. Double Cantilever Beam adhesive specimen (DCB).



**Figure A5-2.** Evolution of adhesive peel and shear stresses at crack tip as a function of the number of elements within the length of the adhesive bondline. Convergence of the linear elastic Finite Element (FE) models. Double Cantilever Beam adhesive specimen (DCB).

### 1.2. Convergence of the nonlinear Finite Element (FE) models

Similarly to [Section 1.1 of Appendix 5](#), [Fig.A5-3](#) shows the evolution of the resulting displacement (i.e. displacement that results from the applied load in N) as a function of the number of elements within the length of the adhesive bondline in the case of nonlinear adhesive stress-strain evolution. Then, the adhesive is here loaded so that it experiences nonlinear adhesive deformations although the surrounding adherends are again considered as facing linear elastic deformations only. Similarly, [Fig.A5-4](#) shows the evolution of the adhesive peel (shear) stress at crack tip as a function of the number of elements within the length of the adhesive bondline. The results are also shown as converging toward an asymptote in terms of both Resulting Displacement and adhesive peel (shear) stress at crack tip.



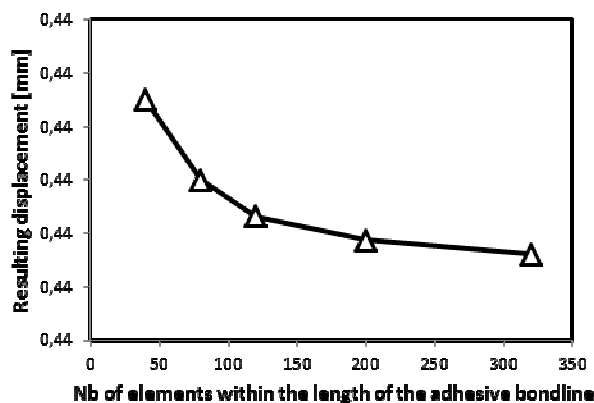


Figure A5-3. Evolution of Resulting Displacement as a function of the number of elements within the length of the adhesive bondline. Convergence of the nonlinear Finite Element (FE) models. Double Cantilever Beam adhesive specimen (DCB).

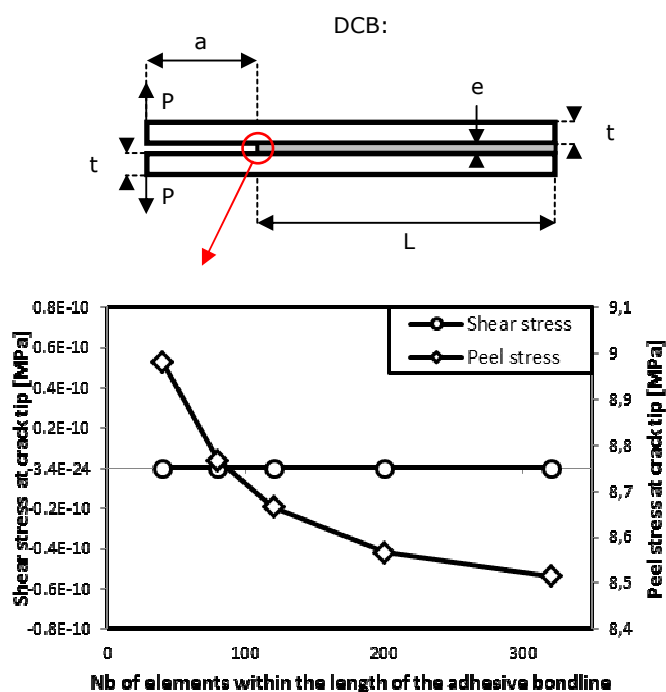


Figure A5-4. Evolution of adhesive peel and shear stresses at crack tip as a function of the number of elements within the length of the adhesive bondline. Convergence of the nonlinear Finite Element (FE) models. Double Cantilever Beam adhesive specimen (DCB).

### 1.3. Convergence of the linear elastic simplified 1D-beam adhesive stress analyses

Similarly to Sections 1.1 and 1.2 of Appendix 5, here is presented the evolution of the resulting displacement as a function of the number of elements within the length of the adhesive bondline in the case of the simplified 1D-beam adhesive stress analyses (see Fig.A5-5). Both the adhesive layer and the surrounding adherends are here considered as experiencing linear elastic deformations only. Similarly, Fig.A5-6 presents the evolution of the adhesive peel (shear) stress at crack tip as a function of the number of elements within the length of the adhesive bondline. Unlike Fig.A5-1 and Fig.A5-2, Fig.A5-5 and Fig.A5-6 show

the results obtained from the simplified 1D-beam adhesive stress analyses as independent on the mesh refinement (i.e. in the case of linear elastic adhesive stress-strain evolution). This property of the simplified 1D-beam adhesive stress analysis being due to the specific formulation of the BBe element, and allows for linear elastic bonded overlaps to be modeled using a unique 4-nodes BBe element only.

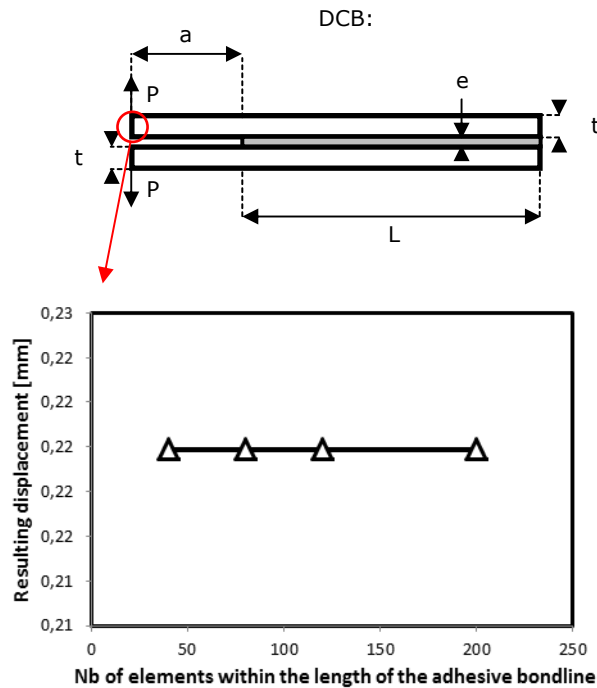


Figure A5-5. Evolution of Resulting Displacement as a function of the number of elements within the length of the adhesive bondline. Convergence of the linear elastic simplified 1D-beam adhesive stress analyses. Double Cantilever Beam adhesive specimen (DCB).

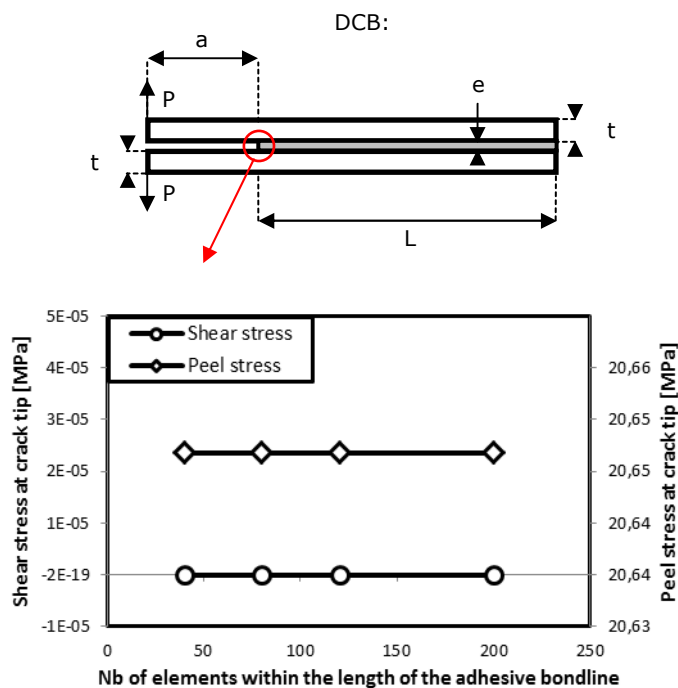


Figure A5-6. Evolution of adhesive peel and shear stresses at crack tip as a function of the number of elements within the length of the adhesive bondline. Convergence of the linear elastic simplified 1D-beam adhesive stress analyses. Double Cantilever Beam adhesive specimen (DCB).

#### 1.4. Convergence of the nonlinear simplified 1D-beam adhesive stress analyses

Similarly to Section 1.3 of Appendix 5, Fig.A5-7 shows the evolution of the resulting displacement as a function of the number of elements within the length of the adhesive bondline. The adhesive is here loaded so that it experiences nonlinear adhesive deformations while both adherends are considered as facing linear elastic deformations only. Similarly, Fig.A5-8 shows the evolution of the adhesive peel (shear) stress at crack tip as a function of the number of elements within the length of the adhesive bondline. The obtained results are here shown as depending on the mesh refinement, so that an adequate number of BBe elements has to be used to capture the local stress gradients within the adhesive bondline when facing nonlinear adhesive stress-strain evolution. This mesh dependency of the simplified 1D-beam adhesive stress analysis in the case of nonlinear adhesive stress-strain evolutions is due to the necessity of defining an integration strategy for integrating the right side and left side secant adhesive moduli into the computation of the secant stiffness matrix resulting from the projection of the adhesive shear (peel) stress onto the specified stress-strain evolution law (see Section 2.4 of Chapter 2). However it is shown that the results are rapidly converging towards an asymptote.

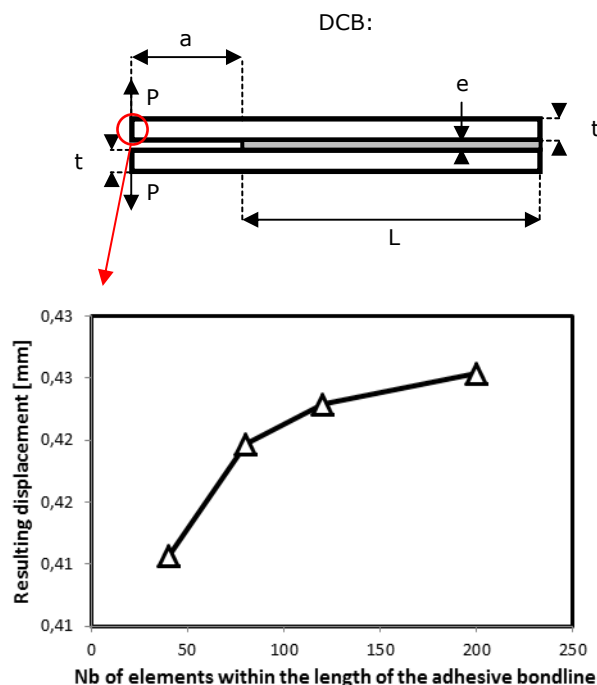


Figure A5-7. Evolution of Resulting Displacement as a function of the number of elements within the length of the adhesive bondline. Convergence of the nonlinear simplified 1D-beam adhesive stress analyses. Double Cantilever Beam adhesive specimen (DCB).

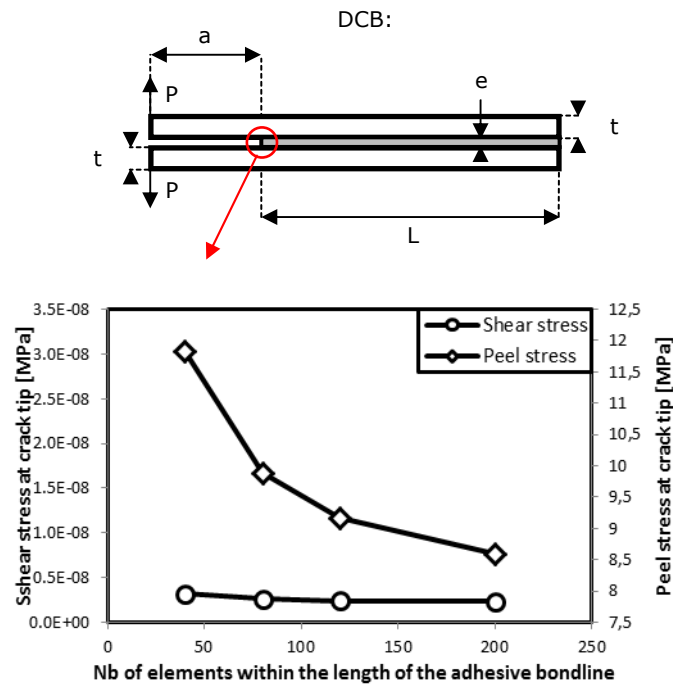


Figure A5-8. Evolution of adhesive peel and shear stresses at crack tip as a function of the number of elements within the length of the adhesive bondline. Convergence of the nonlinear simplified 1D-beam adhesive stress analyses. Double Cantilever Beam adhesive specimen (DCB).

2.

E

nd Notched Flexure adhesive specimen (ENF)

2.1. Convergence of the linear elastic Finite Element (FE) models

Similarly to the DCB adhesive joint specimen, the ENF joint specimen consists in two adherends partially joined by a thin adhesive layer. The modified antisymmetric geometry and loading conditions then provide essentially pure mode II solicitations of the adhesive layer. However, significant mode I adhesive stresses appear nearby center of the specimen. Both the adhesive layer and the surrounding adherends are here considered as experiencing linear elastic deformations only. Here is presented the evolution of the resulting displacement (i.e. displacement that results from the applied load in N) as a function of the number of elements within the length of the adhesive bondline (see Fig.A5-9) in the case of linear elastic adhesive stress-strain evolution. Similarly, Fig.A5-10 shows the evolution of the adhesive peel (shear) stress at crack tip as a function of the number of elements within the length of the adhesive bondline in the case of linear elastic adhesive stress-strain evolution. The results are shown as depending on the mesh refinement. However the results are shown as rapidly converging towards an asymptote in terms of both resulting displacement and adhesive peel (shear) stress at crack tip.

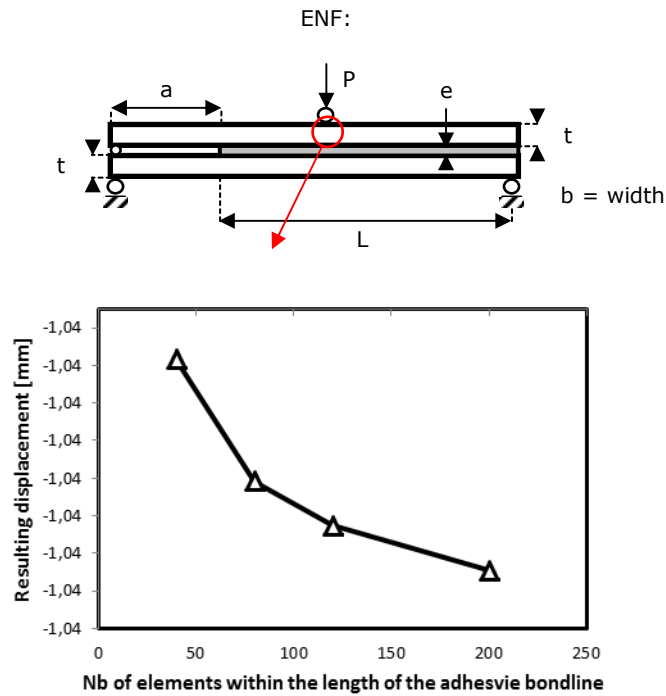


Figure A5-9. Evolution of Resulting Displacement as a function of the number of elements within the length of the adhesive bondline. Convergence of the linear elastic Finite Element (FE) models. End Notched Flexure adhesive specimen (ENF).

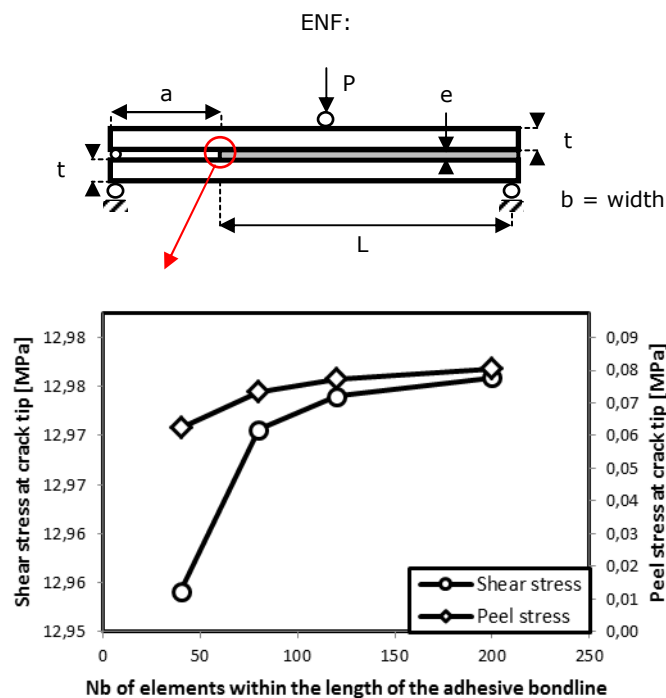


Figure A5-10. Evolution of Resulting Displacement as a function of the number of elements within the length of the adhesive bondline. Convergence of the linear elastic Finite Element (FE) models. End Notched Flexure adhesive specimen (ENF).

## 2.2. Convergence of the nonlinear Finite Element (FE) models

Similarly to Section 2.1 of Appendix 5, Fig.A5-11 shows the evolution of the resulting displacement as a function of the number of elements within the length of the adhesive bondline. The adhesive is here loaded so that it experiences nonlinear adhesive deformations while both adherends are considered as facing linear elastic deformations only. Similarly, Fig.A5-12 shows the evolution of the adhesive peel (shear) stress at crack tip as a function of the number of elements within the length of the adhesive bondline.

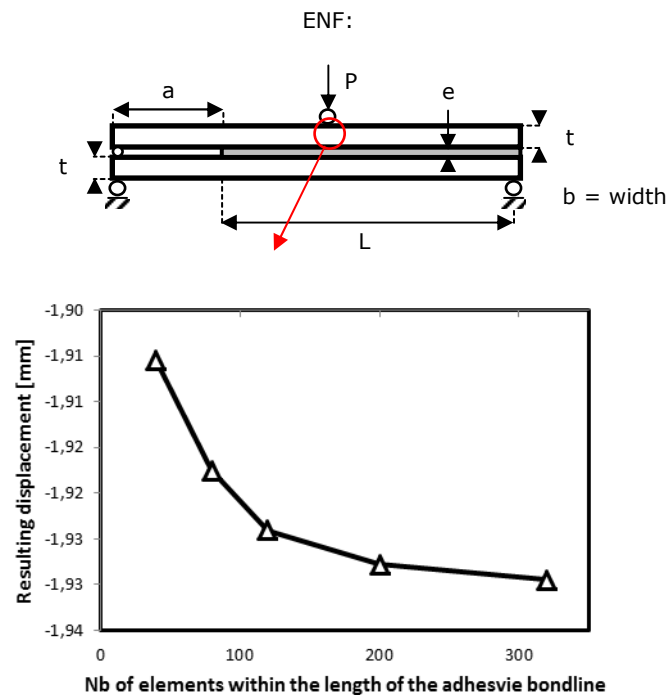
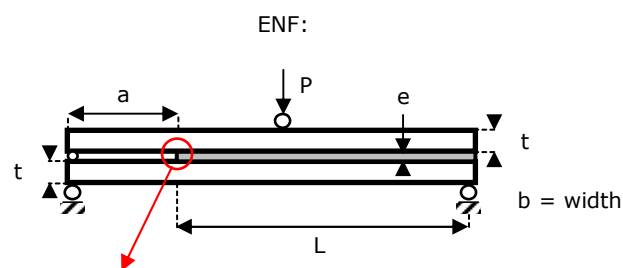


Figure A5-11. Evolution of Resulting Displacement as a function of the number of elements within the length of the adhesive bondline. Convergence of the nonlinear Finite Element (FE) models. End Notched Flexure adhesive specimen (ENF).



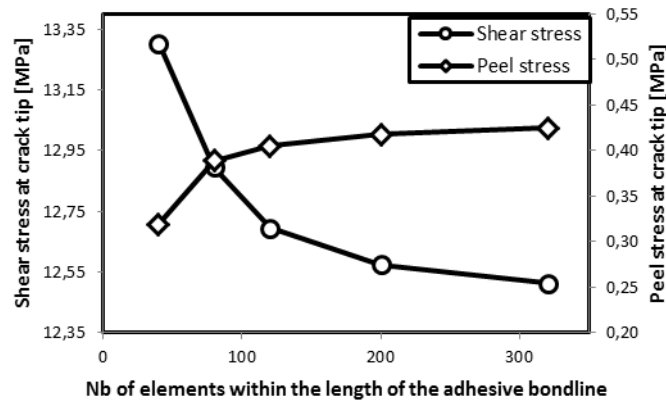


Figure A5-12. Evolution of Resulting Displacement as a function of the number of elements within the length of the adhesive bondline. Convergence of the nonlinear Finite Element (FE) models. End Notched Flexure adhesive specimen (ENF).

### 2.3. Convergence of the linear elastic simplified 1D-beam adhesive stress analyses

Similarly to Sections 2.1 and 2.2 of Appendix 5, here is presented the evolution of the resulting displacement as a function of the number of elements within the length of the adhesive bondline in the case of the simplified 1D-beam adhesive stress analyses (see Fig.A5-13). Both the adhesive layer and the surrounding adherends are here considered as experiencing linear elastic deformations only. Similarly, Fig.A5-14 presents the evolution of the adhesive peel (shear) stress at crack tip as a function of the number of elements within the length of the adhesive bondline.

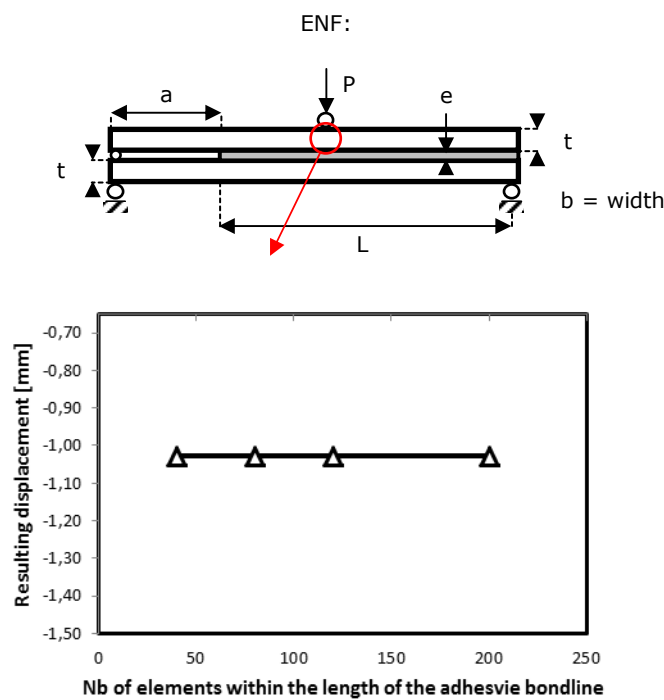


Figure A5-13. Evolution of Resulting Displacement as a function of the number of elements within the length of the adhesive bondline. Convergence of the linear elastic simplified 1D-beam adhesive stress analyses. End Notched Flexure adhesive specimen (ENF).

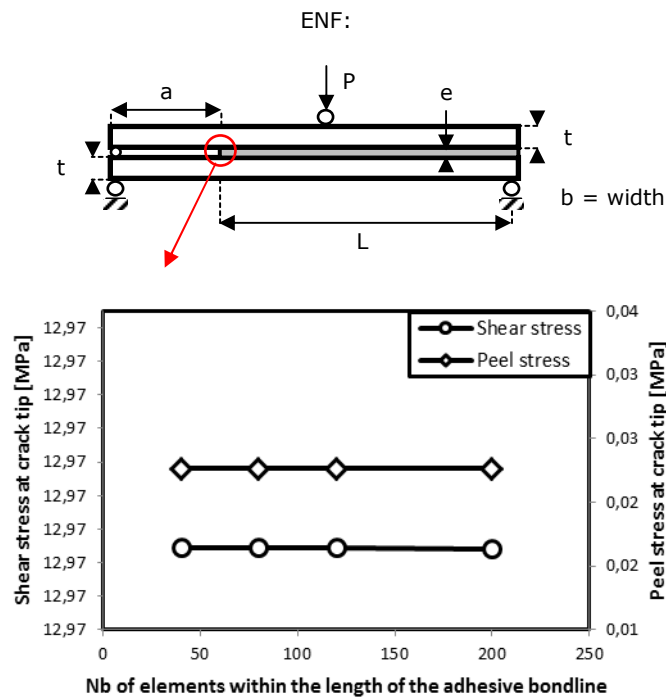
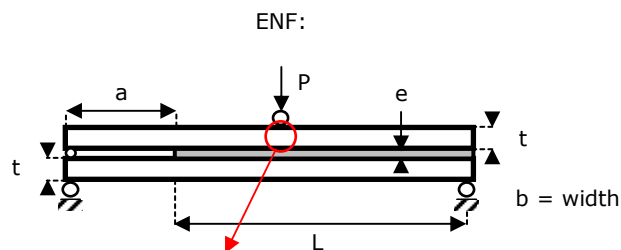


Figure A5-14. Evolution of Resulting Displacement as a function of the number of elements within the length of the adhesive bondline. Convergence of the linear elastic simplified 1D-beam adhesive stress analyses. End Notched Flexure adhesive specimen (ENF).

#### 2.4. Convergence of the nonlinear simplified 1D-beam adhesive stress analyses

Similarly to Section 2.3 of Appendix 5, Fig.A5-15 shows the evolution of the resulting displacement as a function of the number of elements within the length of the adhesive bondline. The adhesive is here loaded so that it experiences nonlinear adhesive deformations while both adherends are considered as facing linear elastic deformations only. Similarly, Fig.A5-16 shows the evolution of the adhesive peel (shear) stress at crack tip as a function of the number of elements within the length of the adhesive bondline.



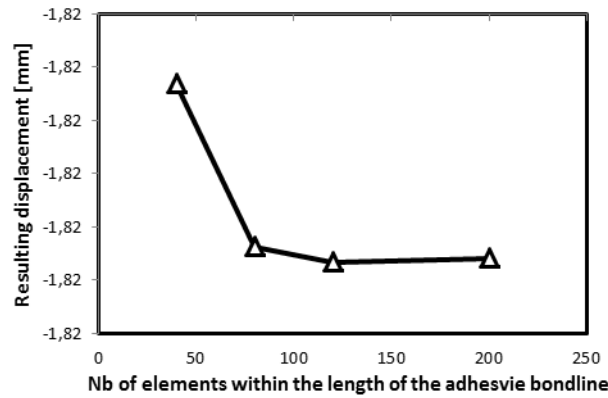


Figure A5-15. Evolution of Resulting Displacement as a function of the number of elements within the length of the adhesive bondline. Convergence of the nonlinear simplified 1D-beam adhesive stress analyses. End Notched Flexure adhesive specimen (ENF).

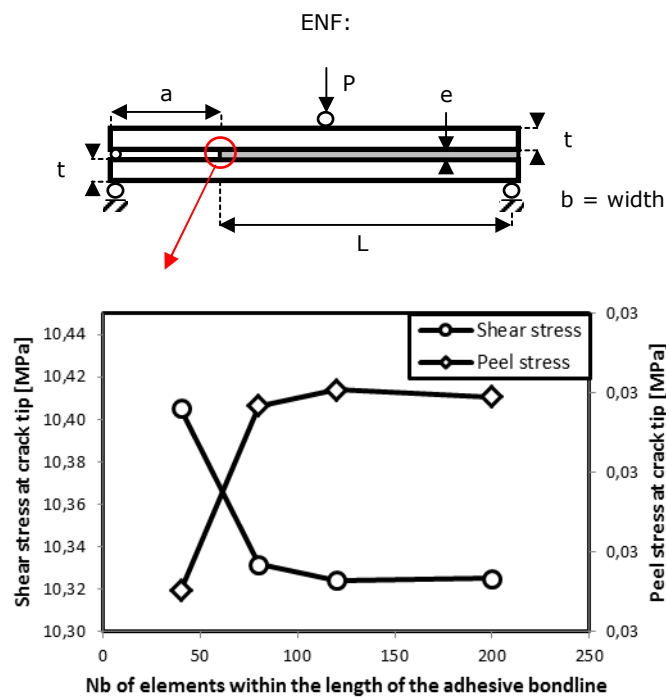


Figure A5-16. Evolution of Resulting Displacement as a function of the number of elements within the length of the adhesive bondline. Convergence of the nonlinear simplified 1D-beam adhesive stress analyses. End Notched Flexure adhesive specimen (ENF).

- 3. C  
 antilever beam in pure bending
- 3.1. C  
 onvergence of the linear elastic Finite Element (FE) models

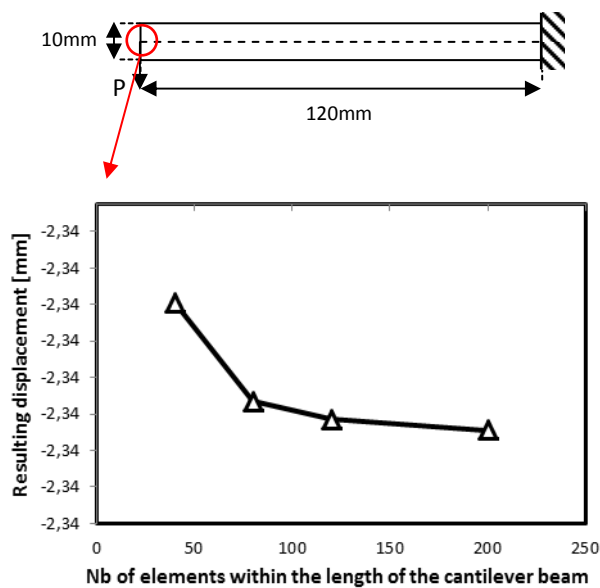


Figure A5-17. Evolution of Resulting Displacement as a function of the number of elements within the length of the cantilever beam. Convergence of the linear elastic Finite Element (FE) models. Cantilever beam in pure bending.

3.2.

C

convergence of the nonlinear Finite Element (FE) models

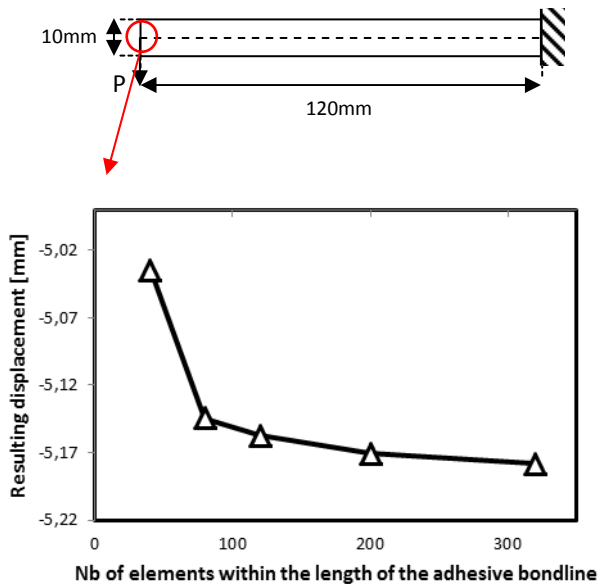


Figure A5-18. Evolution of Resulting Displacement as a function of the number of elements within the length of the cantilever beam. Convergence of the nonlinear Finite Element (FE) models. Cantilever beam in pure bending.

3.3. Convergence of the linear elastic simplified 1D-beam adhesive stress analyses

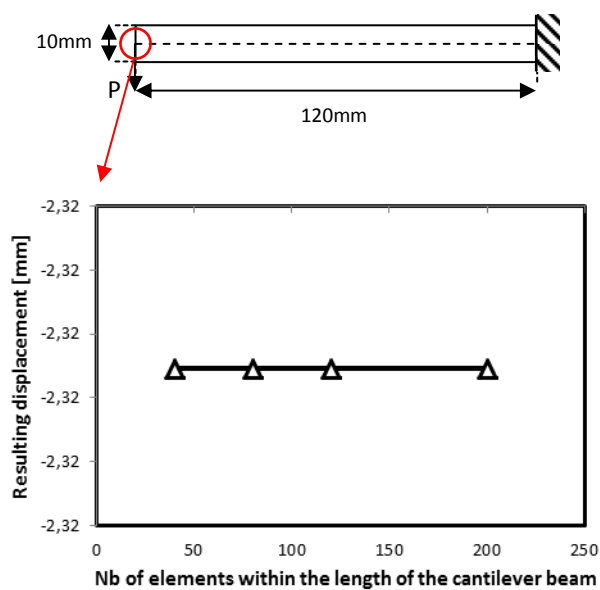


Figure A5-19. Evolution of Resulting Displacement as a function of the number of elements within the length of the cantilever beam. Convergence of the linear elastic simplified 1D-beam adhesive stress analyses. Cantilever beam in pure bending.

### 3.4. Convergence of the nonlinear simplified 1D-beam adhesive stress analyses

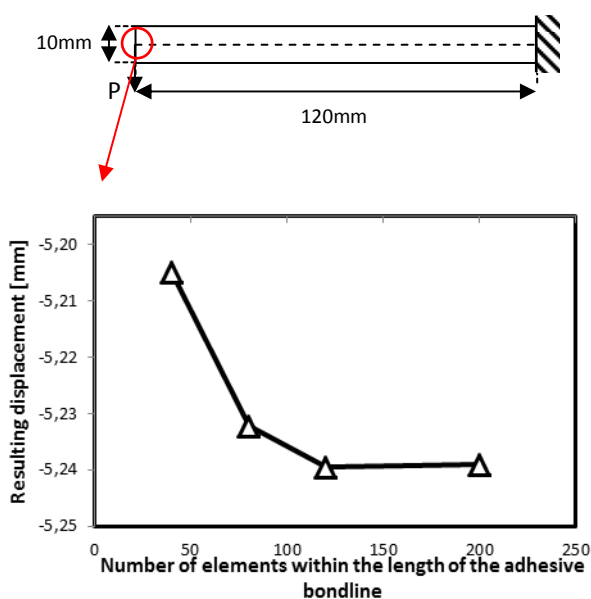


Figure A5-20. Evolution of Resulting Displacement as a function of the number of elements within the length of the cantilever beam. Convergence of the nonlinear simplified 1D-beam adhesive stress analyses. Cantilever beam in pure bending.



$$r_i = y_i - ax_i - b \quad (\text{A6.1})$$

The least squares minimization problem can be written the form of finding the correct set of parameters  $(a, b)$  that minimizes the objective function defined as:

$$E(a, b) = \sum_{i=1}^N r_i^2 = \sum_{i=1}^N (y_i - ax_i - b)^2 = \sum_{i=1}^N \left( y_i - [x_i \quad 1] \begin{bmatrix} a \\ b \end{bmatrix} \right)^2 \quad (\text{A6.2})$$

which can be written in the form of the simpler matrix system as:

$$E(\mathbf{C}) = \|\mathbf{Y} - \mathbf{XC}\|^2 = (\mathbf{Y} - \mathbf{XC})^T (\mathbf{Y} - \mathbf{XC}) = \mathbf{Y}^T \mathbf{Y} - 2(\mathbf{XC})^T \mathbf{Y} + (\mathbf{XC})^T (\mathbf{XC})^T \quad (\text{A6.3})$$

where  $\mathbf{Y}^T = [y_1, \dots, y_n]$  refers to the vector resuming the set of experimental data points,  $\mathbf{C}^T = [a, b]$  to the vector resuming the model fitting parameters and  $\mathbf{X}$  to the specifically formulated design matrix, so that:

$$\mathbf{X} = \begin{pmatrix} x_1 & 1 \\ \vdots & \vdots \\ x_n & 1 \end{pmatrix} \quad (\text{A6.4})$$

Minimizing finally gives:

$$\frac{\partial E}{\partial \mathbf{C}} = 2\mathbf{X}^T \mathbf{XC} - 2\mathbf{X}^T \mathbf{Y} = \mathbf{0} \quad (\text{A6.5})$$

So that the problem of optimizing the fitting parameters  $(a, b)$  in the sense of the least squares method can be finally written in the form of finding  $\mathbf{C}$  so that:

$$\mathbf{X}^T \mathbf{XC} = \mathbf{X}^T \mathbf{Y} \quad (\text{A6.6})$$

$$\mathbf{C} = (\mathbf{X}^T \mathbf{X})^{-1} \mathbf{X}^T \mathbf{Y} \quad (\text{A6.7})$$

and where  $(\mathbf{X}^T \mathbf{X})^{-1} \mathbf{X}^T$  refers to the Moore-Penrose pseudo inverse of the specifically formulated design matrix  $\mathbf{X}$ . It is indicated that providing that the total number of data points  $N$  is equal or exceeds the number of fitting parameters (i.e. overdetermined system of linear equations), the solution  $\mathbf{C}$  here appears as unique and fully determined by equation (A6.7).

2.

C

concatenation of linear least squares optimization problems

As discussed in [Section 2.3.4](#) of [Chapter 2](#), here is investigated the concatenation property of linear least squares optimization problems. Assuming two sets of uncorrelated experimental data points  $(x'_1, y'_1), (x'_2, y'_2), \dots, (x'_n, y'_n)$  and  $(x''_1, y''_1), (x''_2, y''_2), \dots, (x''_n, y''_n)$  and two linear

model equations  $y' = a'x' + b'$  and  $y'' = a''x'' + b''$  then provides the two guiding matrix systems, that are:

$$\mathbf{X}'^T \mathbf{X}' \mathbf{C}' = \mathbf{X}'^T \mathbf{Y}' \quad \text{and} \quad \mathbf{X}''^T \mathbf{X}'' \mathbf{C}'' = \mathbf{X}''^T \mathbf{Y}'' \quad (\text{A6.8})$$

and where  $\mathbf{Y}'^T = [y'_1, \dots, y'_n]$  and  $\mathbf{Y}''^T = [y''_1, \dots, y''_n]$  respectively refer to the vectors resuming the two sets of experimental data points,  $\mathbf{C}'^T = [a', b']$  and  $\mathbf{C}''^T = [a'', b'']$  to the vectors resuming the two models fitting parameters and  $\mathbf{X}'$  and  $\mathbf{X}''$  to the two specifically formulated design matrices, so that:

$$\mathbf{Y}' = \begin{pmatrix} y'_1 \\ \vdots \\ y'_n \end{pmatrix} \quad (\text{A6.11})$$

$$\mathbf{Y}'' = \begin{pmatrix} y''_1 \\ \vdots \\ y''_n \end{pmatrix} \quad (\text{A6.12})$$

$$\mathbf{C}' = \begin{pmatrix} a' \\ b' \end{pmatrix} \quad (\text{A6.13})$$

$$\mathbf{C}'' = \begin{pmatrix} a'' \\ b'' \end{pmatrix} \quad (\text{A6.14})$$

and:

$$\mathbf{X}' = \begin{pmatrix} x'_1 & 1 \\ \vdots & \vdots \\ x'_n & 1 \end{pmatrix} \quad (\text{A6.15})$$

$$\mathbf{X}'' = \begin{pmatrix} x''_1 & 1 \\ \vdots & \vdots \\ x''_n & 1 \end{pmatrix} \quad (\text{A6.16})$$

Then, the whole optimization problem can be concatenated in the form of the single matrix system, that is:

$$\begin{pmatrix} \mathbf{X}'^T \mathbf{X}' & \mathbf{0} \\ \mathbf{0} & \mathbf{X}''^T \mathbf{X}'' \end{pmatrix} \begin{pmatrix} \mathbf{C}' \\ \mathbf{C}'' \end{pmatrix} = \begin{pmatrix} \mathbf{X}'^T \mathbf{Y}' \\ \mathbf{X}''^T \mathbf{Y}'' \end{pmatrix} \quad (\text{A6.17})$$

So that  $(\mathbf{C}', \mathbf{C}'')$  can finally be computed as:

$$\begin{pmatrix} \mathbf{C}' \\ \mathbf{C}'' \end{pmatrix} = \begin{pmatrix} \mathbf{X}'^T \mathbf{X}' & \mathbf{0} \\ \mathbf{0} & \mathbf{X}''^T \mathbf{X}'' \end{pmatrix}^{-1} \begin{pmatrix} \mathbf{X}'^T \mathbf{Y}' \\ \mathbf{X}''^T \mathbf{Y}'' \end{pmatrix} \quad (\text{A6.18})$$

For simplification purpose, the design matrix obtained by the concatenation of  $\mathbf{X}'^T \mathbf{X}'$  and  $\mathbf{X}''^T \mathbf{X}''$  will be now referred to as  $\mathbf{X}^T \mathbf{X}$ . Similarly, the vector obtained by the concatenation of  $\mathbf{X}'^T \mathbf{Y}'$  and  $\mathbf{X}''^T \mathbf{Y}''$  and the vector obtained by the concatenation of  $\mathbf{C}'$  and  $\mathbf{C}''$  will be now referred to as respectively  $\mathbf{X}^T \mathbf{Y}$  and  $\mathbf{C}$ .

### 3. C unconstrained linear least squares optimization problems

As presented in [Section A7.1](#), the Moore-Penrose pseudo inverse technique arises from the minimization of the unconstrained optimization problem  $P$ , that is:

$$P: \left\{ \min_{\mathbf{C} \in \mathbb{R}^2} E(\mathbf{C}) = \mathbf{Y}^T \mathbf{Y} - 2(\mathbf{X}\mathbf{C})^T \mathbf{Y} + (\mathbf{X}\mathbf{C})^T (\mathbf{X}\mathbf{C}) \right\} \quad (\text{A6.19})$$

As presented in [Section 2.3.4](#) of [Chapter 2](#), introducing equality constraints between the model fitting parameters in the form of:

$$\mathbf{B}\mathbf{C} = \mathbf{C}^{\text{pilot}} \quad (\text{A6.20})$$

where  $\mathbf{C}$  is the vector resuming the model fitting parameters,  $\mathbf{B}$  a  $2xp$  coupling parameter matrix and  $\mathbf{C}^{\text{pilot}}$  the set of  $p$  equality constraints (i.e. not necessarily equal to zero).

result in  $(\mathbf{C}, \lambda)$  being the optimum of the equivalent minimization problem (see [Section 2.3.4](#) of [Chapter 2](#)):

$$P': \left\{ \min_{\mathbf{U} \in \mathbb{R}^n, \lambda \in \mathbb{R}^p} L(\mathbf{C}, \lambda) = E(\mathbf{C}) + (\mathbf{B}\mathbf{C} - \mathbf{C}^{\text{pilot}})^T \lambda \right\} \quad (\text{A6.21})$$

So that minimizing  $P'$  gives:

$$\frac{\partial L}{\partial \mathbf{C}} = -2\mathbf{X}^T \mathbf{Y} + 2\mathbf{X}^T \mathbf{X}\mathbf{C} + \mathbf{B}^T \lambda = \mathbf{0} \quad \frac{\partial L}{\partial \lambda} = \mathbf{B}\mathbf{C} - \mathbf{C}^{\text{pilot}} = \mathbf{0} \quad (\text{A6.22})$$

which can be re-written in the form of the *augmented* linear problem:

$$\begin{cases} \mathbf{X}^T \mathbf{X}\mathbf{C} + \mathbf{B}^T \lambda & = & \mathbf{X}^T \mathbf{Y} \\ \mathbf{B}\mathbf{C} + \mathbf{0} & = & \mathbf{C}^{\text{pilot}} \end{cases} \quad (\text{A6.23})$$

Where  $\mathbf{C}^T = [\mathbf{a}, \mathbf{b}]$  refers to the vector resuming the model fitting parameters,  $\mathbf{B}$  a  $2xp$  coupling parameter matrix and  $\lambda$  to the  $p$  undetermined Lagrange's multipliers.

Finally,  $(\mathbf{C}, \lambda)$  can be computed as:

$$\begin{pmatrix} \mathbf{C} \\ \lambda \end{pmatrix} = \begin{pmatrix} \mathbf{X}^T \mathbf{X} & \mathbf{B}^T \\ \mathbf{B} & \mathbf{0} \end{pmatrix}^{-1} \begin{pmatrix} \mathbf{X}^T \mathbf{Y} \\ \mathbf{C}^{\text{pilot}} \end{pmatrix} \quad (\text{A6.24})$$

4.

I

Illustration: Fitting simultaneously  $w(x)$  and  $\theta(x)=dw(x)/dx$

Assuming two sets of correlated experimental data points  $(x_1, w_1), (x_2, w_2), \dots, (x_n, w_n)$  and  $(x_1, \theta_1), (x_2, \theta_2), \dots, (x_n, \theta_n)$  and two linear model equations  $w=a'x+b'$  and  $\theta=a''x+b''$  then provides the two guiding matrix equations, as:

$$\mathbf{X}^T \mathbf{X} \mathbf{C} = \mathbf{X}^T \mathbf{W} \quad \text{and} \quad \mathbf{X}^T \mathbf{X} \mathbf{C} = \mathbf{X}^T \boldsymbol{\theta} \quad (\text{A6.25})$$

where:

$$\mathbf{X} = \begin{pmatrix} x_1 & 1 \\ \vdots & \vdots \\ x_n & 1 \end{pmatrix} \quad (\text{A6.26})$$

$$\mathbf{C}' = \begin{pmatrix} a' \\ b' \end{pmatrix} \quad (\text{A6.27})$$

$$\mathbf{C}'' = \begin{pmatrix} a'' \\ b'' \end{pmatrix} \quad (\text{A6.28})$$

and:

$$\mathbf{W} = \begin{pmatrix} w_1 \\ \vdots \\ w_n \end{pmatrix} \quad (\text{A6.30})$$

$$\boldsymbol{\theta} = \begin{pmatrix} \theta_1 \\ \vdots \\ \theta_n \end{pmatrix} \quad (\text{A6.31})$$

Then, concatenating the two linear least squares optimization problems provides the main guiding linear equation, that is:

$$\begin{pmatrix} \mathbf{X}^T \mathbf{X} & \mathbf{0} \\ \mathbf{0} & \mathbf{X}^T \mathbf{X} \end{pmatrix} \begin{pmatrix} \mathbf{C}' \\ \mathbf{C}'' \end{pmatrix} = \begin{pmatrix} \mathbf{X}^T \mathbf{W} \\ \mathbf{X}^T \boldsymbol{\theta} \end{pmatrix} \quad (\text{A6.32})$$

Finally, ensuring the models fitting parameters to satisfy the additional condition  $\theta(x)=dw(x)/dx$  is achieved by introducing the two equality constraints, that are:

$$\begin{cases} a'' = a' \\ b'' = 0 \end{cases} \quad (\text{A6.33})$$

So that:

$$\mathbf{BC} = \mathbf{C}^{\text{pilot}} \quad (\text{A6.34})$$

where:

$$\mathbf{B} = \begin{pmatrix} 1 & 0 & -1 & 0 \\ 0 & 0 & 0 & 1 \end{pmatrix} \quad (\text{A6.35})$$

$$\mathbf{C} = \begin{pmatrix} \mathbf{C}' \\ \mathbf{C}'' \end{pmatrix} \quad (\text{A6.36})$$

and:

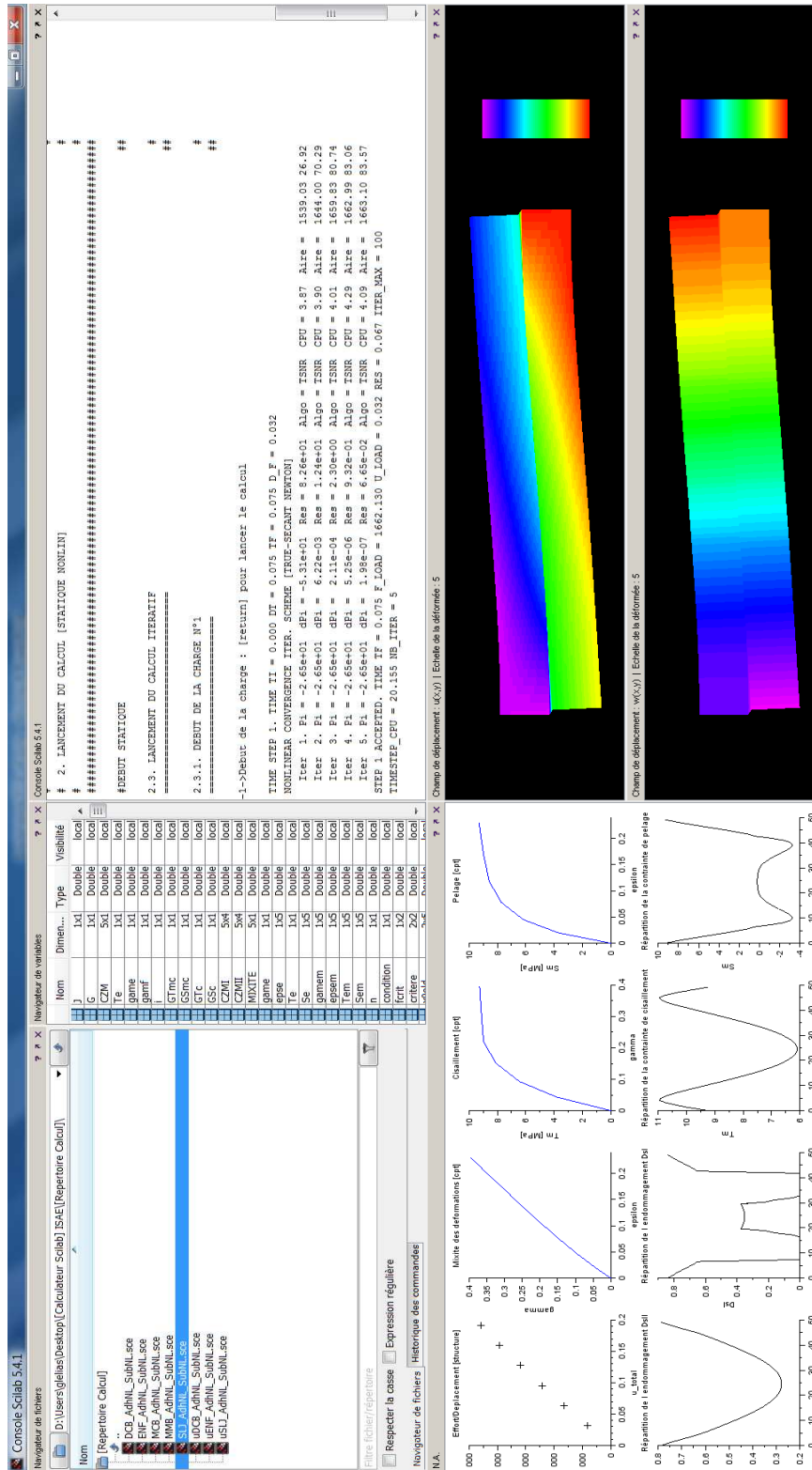
$$\mathbf{C}^{\text{pilot}} = \begin{pmatrix} 0 \\ 0 \end{pmatrix} \quad (\text{A6.37})$$

So that the problem of optimizing the fitting parameters  $(\mathbf{C}', \mathbf{C}'')$  in the sense of the least squares method can be finally written in the form of finding  $(\mathbf{C}', \mathbf{C}'', \lambda)$  so that:

$$\begin{pmatrix} \mathbf{X}^T \mathbf{X} & \mathbf{0} & \mathbf{B}^T \\ \mathbf{0} & \mathbf{X}^T \mathbf{X} & \mathbf{0} \\ \mathbf{B} & \mathbf{0} & \mathbf{0} \end{pmatrix} \begin{pmatrix} \mathbf{C}' \\ \mathbf{C}'' \\ \lambda \end{pmatrix} = \begin{pmatrix} \mathbf{X}^T \mathbf{W} \\ \mathbf{X}^T \boldsymbol{\theta} \\ \mathbf{0} \end{pmatrix} \quad (\text{A6.38})$$

$$\begin{pmatrix} \mathbf{C}' \\ \mathbf{C}'' \\ \lambda \end{pmatrix} = \begin{pmatrix} \mathbf{X}^T \mathbf{X} & \mathbf{0} & \mathbf{B}^T \\ \mathbf{0} & \mathbf{X}^T \mathbf{X} & \mathbf{0} \\ \mathbf{B} & \mathbf{0} & \mathbf{0} \end{pmatrix}^{-1} \begin{pmatrix} \mathbf{X}^T \mathbf{W} \\ \mathbf{X}^T \boldsymbol{\theta} \\ \mathbf{0} \end{pmatrix} \quad (\text{A6.39})$$

**Appendix 7. Joint Stress Analysis Tool (JoSAT)**



– This page has been voluntarily left blank –

### **Abstract:**

In the frame of an internal research program called JoSAT (Joint Stress Analysis Tool), Sogeti High Tech has suggested developing since 2008 a simplified tool for the stress analysis of adhesively bonded joints. This tool allows for the distribution of both the internal forces and displacements in the adherends as well as the adhesive stresses along the overlap to be estimated from specified loads and boundary conditions, and has the advantage of being extremely time saving compared to conventional Finite Element (FE) analyses.

In 2011, this tool was extended to support adhesive material nonlinearities in the form of specified adhesive stress-strain evolution laws. However the theory developed was demonstrated as valid for the Single-Lap Joint (SLJ) configuration only, and limited to small levels of adhesive material nonlinearities.

In this context, the objective of the thesis is double. First, extend and validate the simplified tool for the analysis of adhesively bonded joints in the case of nonlinear adhesive as well as adherends stress-strain constitutive behaviors. Then, develop new experimental protocols for the characterization of the cohesive properties of thin adhesive layers.

**Keywords:** Adhesive, Bonding, Modeling, Simplified analysis, Finite-Element, Experimental Characterization

---

### **Résumé:**

Dans le cadre d'un projet de recherche interne nommé JoSAT (Joint Stress Analysis Tool), Sogeti High Tech a développé depuis 2008 un outil de simulation simplifié d'analyse de joints collés. Cet outil permet d'obtenir à la fois la répartition des efforts internes dans chacun des substrats mais également la répartition des contraintes adhésives le long du recouvrement, tout en ayant l'avantage d'être beaucoup moins chronophage que la méthode des Eléments-Finis (EF).

En 2011, cet outil a été étendu de sorte à supporter différents comportements adhésifs non-linéaires sous la forme de relations contrainte-déformation spécifiée par l'utilisateur. Cependant, le champ d'application de cette nouvelle théorie fut démontré comme limitée aux jonctions en simple recouvrement, et dans le cas de faible non-linéarité uniquement.

Dans ce contexte, l'objectif de la thèse est double. Premièrement, étendre et valider l'outil d'analyse simplifiée aux cas de comportement non-linéaire adhésif mais également des substrats. Deuxièmement, proposer et développer de nouvelles méthodes visant à caractériser le comportement non-linéaire d'un film adhésif.

**Mots clés:** Adhésif, Collage, Simulation, Analyse Simplifiée, Eléments-Finis, Caractérisation Expérimentale